THESIS

SIMULATED TROPICAL CONVECTION

Submitted by

Matthew Garcia

Department of Atmospheric Science

In partial fulfillment of the requirements

for the Degree of Master of Science

Colorado State University

Fort Collins, Colorado

Fall 1999

COLORADO STATE UNIVERSITY

September 24, 1999

WE HEREBY RECOMMEND THAT THE THESIS PREPARED UNDER OUR SUPERVISION BY MATTHEW GARCIA ENTITLED SIMULATED TROPICAL CONVECTION BE ACCEPTED AS FULFILLING IN PART REQUIREMENTS FOR THE DEGREE OF MASTER OF SCIENCE.

Committee on Graduate Work

Advisor

Department Head

ABSTRACT OF THESIS

SIMULATED TROPICAL CONVECTION

A two-dimensional, finite-element, nonhydrostatic, primitive equation model developed by Dr. K.V. Ooyama of NOAA/AOML/HRD is described in detail. Numerous unpublished experiments oriented toward the evaluation of numerical constructs are described in brief. The focus of discussion is the maritime tropical squall line system. A detailed review of previous observational and numerical modeling efforts is included, and provides a basis for a detailed qualitative evaluation of model results through other unpublished, and new, simulations. These analyses conclude with a favorable assessment of Dr. Ooyama's model with respect to the proper simulation of observed and previously modeled tropical squall line system development and structure. The author's participation in SCSMEX provided numerous data with which the model was initialized for further experiments involving the examination of cumulus growth and decay on smaller scales, and at higher resolutions, than the previous squall line system simulations. A analysis of these new simulations also provides a favorable assessment of this model with respect to the simulation of convective-scale phenomena.

Matthew Garcia
Department of Atmospheric Science
Colorado State University
Fort Collins, Colorado 80523-1371
Fall 1999

ACKNOWLEDGEMENTS

I would most like to thank Wayne, for providing the time and support required for an effort of this magnitude. Great thanks to Dr. Ooyama, for the model and some direction(s). Also, thanks to Scott Hausman and Dr. Johnson for reviewing various aspects of this work, and to Dr. Johnson again for sending me to the SCS—now I know what to expect next time! Thanks to Erica Loechl for ECMWF analyses, to Rick Taft for computer help and satellite images, to Paul Ciesielski for talking data, and to Gail Cordova for keeping us in line. Thanks also to my lovely wife and my persistent parents.

The author's participation in SCSMEX was supported by NOAA, Grant NA67RJ0152, Amendment 13. The author's work at CSU was supported by NOAA, Grant NA67RJ0152, Amendment 17, and the National Science Foundation, Grant ATM-9729970. Computing time used in this research was provided by Dr. Montgomery's group and by the National Center for Atmospheric Research, which is sponsored by the National Science Foundation.

> "Many roads lead to the Path, but basically there are only two: Reason, and Practice. To enter by Reason means to realize the Essence through instruction..."
>
> — Bodhidharma
> *Outline of Practice*

CONTENTS

FIGURES

TABLES

Chapter 1

INTRODUCTION

In addition to observational efforts, atmospheric scientists rely on mathematical and numerical models in order to more fully understand natural phenomena. These numerical models come in all shapes and sizes, from global spectral models for numerical weather predition to one-dimensional finite-difference models for the examination of cloud growth and decay. The construction of a model typically depends on the scale of interest, such that global models of synoptic-scale phenomena might rely more on spectral methods for accuracy over a large (finite, but unbounded) domain, while models of convective-scale processes might rely more on finite difference methods in order to more accurately simulate dynamic, thermodynamic and microphysical processes in a much smaller region of space. Models which focus on the mesoscale regime of atmospheric motions, between the synoptic and convective scales, must consider large-scale, slowly-evolving ("slow-manifold") dynamical processes as well as convective-scale thermodynamic and microphysical processes which operate on much faster time scales.

Over a period of several years, Dr. K.V. Ooyama of NOAA's Hurricane Research Division (HRD) has devised a finite-element model of the atmosphere which is based on the equations of motion in their primitive form and an original thermodynamic formulation which has been derived from first principles of thermodynamics. While a bulk microphysical parameterization is still employed, limiting the small-scale resolution of this model to processes which operate on a scale of tens of meters, a resolution of 100 m to 200 m is commonly sufficient to simulate convective processes and their effects on mesoscale convective

systems and circulations. Several experiments performed by Ooyama with this model have been published in conference literature (Ooyama, 1984, 1991, 1995, 1997). This thesis represents an important step in the development and verification of this model as a useful and important tool in the detailed examination of convective-scale and mesoscale atmopsheric phenomena.

The verification of this model has begun, in conference literature (Ooyama, 1995, 1997), with simulations of tropical squall line systems, a distinctly mesoscale phenomena which is highly dependent on convective-scale processes for its development, maturity, and eventual decay. Accordingly, Chapter 2 of this thesis provides a detailed review of tropical squall line system observational and numerical modeling efforts. Many of the earlier sources included here examined the large-scale structure of observed tropical squall line systems, and are employed accordingly in the formulation of a conceptual model of cumulonimbus initiation and development and of the tropical squall line system which results from the proper organization of successive convective events.

This review of observational efforts includes many maritime squall line system observations during GATE, which was undertaken in the tropical eastern Atlantic Ocean during the summer of 1974, and from which numerous analyses and numerical simulations of tropical convective systems have arisen. Observational efforts which have focused on continental squall line systems, in the tropics and mid-latitudes, are included where their findings significantly contribute to our understanding of maritime squall line system development and structure. Along these lines, several numerical efforts directed at the simulation of specific tropical and mid-latitude, maritime and continental squall line systems are reviewed in some detail.

Chapter 3 introduces the reader to the history and formulation of Ooyama's model. Following a brief historical account of publications and developments leading up to and through the formulation of this model, the dynamical and thermodynamical formulation of the model as published by Ooyama (1990, 1995) is described in detail. Slightly less detailed

discussions of the numerical (due to its complexity) and microphysical (due to the brevity of bulk formulations and the detail of their sources) formulations in the model are also included.

Results from this model are first evaluated in Chapter 4. Analyses of the model results presented by Ooyama (1995, 1997) are included here, followed by a detailed analysis of unpublished model simulations which have been formulated for this purpose. Included in these simulations are several which have been devised solely for the testing of certain numerical constructs and parameters, and are analysed briefly. The bulk of these unpublished simulations are oriented toward the variation of initial conditions and perturbations in the examination of tropical squall line system development and structure. These simulations are analyzed in Chapter 4 with the detailed review of such processes in Chapter 2 always in mind. Favorable comparisons are drawn between the observational and numerical efforts presented in Chapter 2 and the results of tropical squall line simulations presented in Chapter 4.

In the course of evaluating the numerous tropical squall line simulations presented in Chapter 4, several hypotheses are formulated regarding the "optimal" state of tropical squall line system growth and maturity. These hypotheses are posed near the end of Chapter 4, and are evaluated in Chapter 5 with a new tropical squall line simulation which was formulated to complement those simulations analyzed previously and to allow for further exploration of the convective outflow and regeneration structures which are commonly observed in multicellular convective systems such as squall lines and are successfully simulated in this experiment. A detailed analysis of outflow dynamics and the process of convective regeneration is included in the first section of Chapter 5.

The remainder of Chapter 5 is devoted to the exploration of new experiments which rely on data collected by the author as a shipboard scientist on the R/V *Kexue 1* during the South China Sea Monsoon Experiment (SCSMEX), which was undertaken in the region of Southeast Asia during the summer of 1998. The second section of Chapter 5 describes,

in detail, the SCSMEX data which are employed in the definition of the initial atmosphere for numerous new experiments with this model. In the process of formulating these new experiments, several portions of the domain initialization procedure were modified in order to accomodate some of these data which were to be employed. These new experiments were oriented toward an examination of convective-scale processes, and as such involve a domain of greater spatial and temporal resolution than previously employed in experiments with this model.

Following a description of the SCSMEX data employed, a discussion of model results for several simulations is included. Favorable results are demonstrated and analyzed for most of the simulations discussed, including those simulations for which little convection was observed in the vicinity of the *Kexue 1* during data collection. A brief analysis of simulations which employed SCSMEX data collected at the time of a tropical squall line passage over the position of the *Kexue 1* is included here. Finally, a highly successful simulation of moderate cumulus growth is analyzed in detail, with careful attention to previously published theoretical, observational and numerical efforts at the analysis of cumulus growth and entrainment processes. A favorable comparison is drawn between this simulation and the development of precipitating cumuli observed in the vicinity of the *Kexue 1* during SCSMEX.

Chapter 6 concludes this thesis with a general assessment of the model results discussed earlier, and further discussion is oriented toward numerous possibilities for the validation and improvement of this model. Throughout this thesis, previously published efforts which are abbreviated may be referenced through Appendix A. Scientific field experiments mentioned in the course of various discussions are listed in Appendix B. Mathematical notation and variables employed in discussions of the model formulation and in the description of various experiments and simulations are listed in Appendix C.

Chapter 2

TROPICAL SQUALL LINE SYSTEMS

Squall line systems have been observed and documented in tropical oceanic regions such as the eastern Atlantic during GATE (Houze, 1977; Frank, 1978; Gamache and Houze, 1982; Johnson and Nicholls, 1983), the eastern Caribbean during the 1968 Barbados Experiment (Zipser, 1977), the central Pacific during the Line Islands Experiment (Zipser, 1969), and the western Pacific during TOGA COARE (Jorgensen et al., 1997). In tropical continental regions, Betts et al. (1976) studied squall lines over Venezuela during VIMHEX-1972, while squall line systems over tropical western Africa were examined closely during COPT81 (Roux, 1988; Chalon et al., 1988) and have been studied since the work of Hamilton and Archibold (1945). Midlatitude continental squall line systems observed during several field experiments, including CCOPE (Matejka and Stossmeister, 1986) and the Oklahoma-Kansas PRE-STORM experiment (Smull and Houze, 1987b; Rutledge et al., 1988; Sun et al., 1993), have been examined. A trailing-stratiform midlatitude squall line system observed over Oklahoma during 22 May, 1976, was examined in detail by Smull and Houze (1985, 1987a, 1987b).

This synthesis is oriented primarily toward a two-dimensional line-perpendicular view of a maritime tropical squall line system. In its mature stage, the system is typically composed of a strong leading convective line and a large trailing stratiform precipitation region. Squall line systems quite often fulfill the size and duration criteria for classification as mesoscale convective systems (MCSs; Maddox, 1980). Although some three-dimensional aspects are discussed here, such aspects may pose problems in the proper simulation of

tropical squall lines systems using the limited capabilities of two-dimensional models.

2.1 Background

Data from the Global Atmospheric Research Program's (GARP) Atlantic Tropical Experiment (GATE) during the summer of 1974 is presented by Houze (1977, hereafter H77), and forms the basis for one of the most widely accepted conceptual models of tropical squall line structure. This model was qualitatively similar to the structure presented by Zipser (1977), and has been further detailed in later experiments with regard to processes such as convective initiation, squall line propagation, convective scale and mesoscale organization, and thermodynamic and microphysical processes. The structural model of a tropical squall line system presented in H77 is supported through observations and modeling of airflow patterns by Zipser (1969, 1977) and sounding and satellite data obtained during GATE. Some observations of structure and conditions during the late stages of the life cycle of a tropical squall line system and the effects of the residual stratiform precipitation region on the tropical environment have been presented by Zipser (1969, hereafter Z69). Zipser (1977, hereafter Z77) studied a Caribbean squall line system which passed over the Windward Islands during August, 1968, and found a line-perpendicular structure nearly identical to that presented in H77.

The tropical squall line system studied in H77 formed during GATE on 4-5 September, 1974, on the west side of an African easterly wave trough, as was found by Payne and McGarry (1977) for most GATE squall line systems. Frank (1978) recounted that the speed of the African Easterly Jet, which drives tropical easterly waves over the Atlantic Ocean, induces divergence at midlevels ($\sim$ 600 hPa) westward of the trough axis. This preconditions the lower levels of the troposphere by creating a region of weak ascent, sometimes with as much as 2.5 cm s^{-1} of vertical motion near the 800 hPa level.

A similar synoptic field is described for the Caribbean squall line system presented in Z77, although the causative connection between the easterly wave and the formation

of a squall line is declared much less distinctly in that study. There is ample reason for ambiguity in this case, as Yamasaki (1984) states that convective systems found in the western regions of tropical oceanic basins, as in the Caribbean Sea, commonly occur to the east of easterly wave troughs due to evolution of dynamic and thermodynamic structures of the waves as they cross the ocean basin, while the mere presence of the jet at midlevels ensures convective activity to the west of the trough axis. Although the structural evolution recounted by Yamasaki may include a weakening of the African Easterly Jet, such that easterly wave systems derive less of their energy from barotropic instability and more from the diabatic heating of tropospheric midlevels by cumulus convection, the consideration of low-level wind shear induced by a finite jet strength in an atmosphere which is conditionally unstable on a consistent basis may allow all of these factors to apply to the squall line system examined in Z77.

In H77, evidence was presented which indicates that the initial stages of the 4-5 September, 1974, GATE squall line had developed and organized along the boundary of a low-level cold pool which remained after an earlier disturbance had dissipated upon exiting the African coast. Payne and McGarry found that many more squall line systems occurred over the African continent than over the adjacent northern tropical Atlantic Ocean. Such systems are commonly observed during the summer months, as strong convective systems embedded in easterly waves over the African continent move over the Atlantic coastline and quickly dissipate upon the loss of their continental source of surface heating.

Some convective systems which exit the African coast may, however, undergo a successful transition to maritime-based systems, such that the dissipation of the continental convection is not so pronounced as for the system presented in H77. These systems, which maintain some continuity of convective activity during their transitions, are often regarded as possible precursor systems for tropical cyclones, depending on numerous other environmental and dynamic conditions. Convective systems which, for any number of reasons, do not make a successful transition to a maritime structure may develop a spreading cold pool

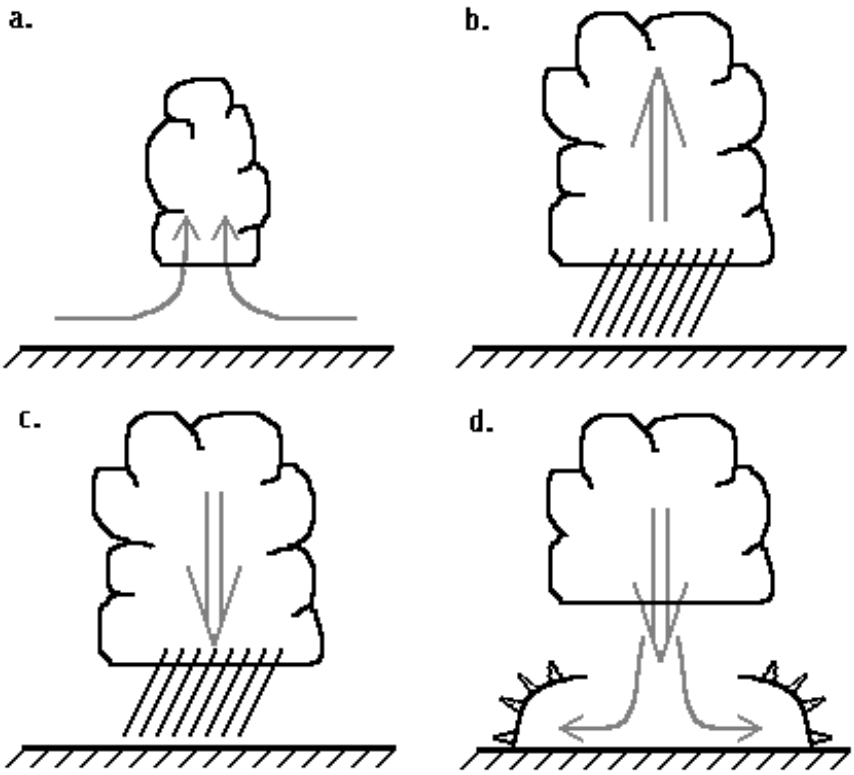

Figure 2.1: Schematic view of downdraft and outflow development beneath a cloud or system following the demise of convective activity, after RKW88.

of low-level air while the continental-based clouds and precipitation continue to dissipate, as demonstrated in Figure 2.1. Along the lateral boundaries of this spreading low-level cold pool, new convection may develop through the lifting of warm, moist environmental air from the surface, as in Figure 2.2, in a manner similar to that explained below for the propagation of the subsequent squall line system. In these Figures, large arrows indicate buoyant ascent (descent), which commonly follows forced ascent for moist convection near the surface of the Earth. The process of generating moist convection will be discussed further in Chapter 5.

The dynamics of low-level convective outflows as a gust front have been studied by Mitchell and Hovermale (1977), as well as by Mueller and Carbone (1987) under the density current analogue suggested by Charba (1974). The initiation of deep convection by density currents in the form of continental thunderstorm outflows has been examined by Purdom

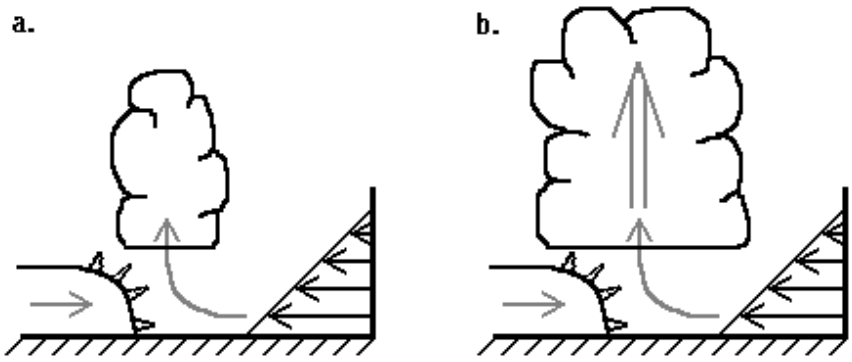

Figure 2.2: Schematic view of moist convective generation on an outflow boundary, after RKW88.

(1979) and by Purdom and Marcus (1982). This process was explored by Nakajima and Matsuno (1988) as an essential mechanism in the development of mesoscale tropical cloud clusters under seemingly self-organizing conditions. The dynamics of density currents have been examined by many methods, including laboratory tank simulations and numerical experiments by Simpson (1969) and Simpson and Britter (1980), and the idealized numerical experiments of Klemp et al. (1994) and Xue et al. (1997). The dynamics and effects on the surrounding environment of a surface outlfow which has separated from its parent convective system have been examined by Purdom (1976), who suggested the interaction of multiple density currents in the initiation of convection long after the demise of the parent systems, and Wakimoto (1982), who demonstrated a surface outflow life cycle in a composite radar analysis of continental thundersotrm gust fronts. The interaction of a density current, such as a low-level convective outflow pool, with a sheared low-level flow has been examined by Xu (1992) and by Moncrieff and Liu (1999), who found that a configuration in which the density current propagates upshear produces a jump updraft, which is favorable to squall line structure and longevity (Moncrieff, 1992; Kingsmill and Houze, 1999), and that low-level shear contributes more to the dynamical organization of the convection than to its originating low-level convergence field. By similar processes, an organized maritime convective system may develop from the demise of a preceeding continental convective

system.

Thorpe et al. (1982, hereafter TMM82) concluded that some degree of low-level vertical wind shear is necessary for the development of long-lived convection such as a tropical squall line system. These conclusions were carried further by Rotunno et al. (1988, hereafter RKW88), who suggested that the convection which produced the results presented in TMM82 represents a single two-dimensional long-lived cell, though not necessarily a supercell system (Browning, 1964) as commonly found in midlatitude continental regions during the spring and summer. In the tropics, a similarly-structured supercell-like system was observed and studied by Lewis et al. (1998) during the Tropical Ocean-Global Atmosphere (TOGA) Coupled Ocean-Atmosphere Response Experiment (COARE). Takeda (1971) examined various configurations of a cloud's updraft and downdraft cycle which would produce a single, long-lived precipitating convective cloud. Takeda considered the interaction between various profiles of two-dimensional vertical shear, which included a jet at a particular level, with various heights of two "critical levels," defined by thermodynamic (downdraft penetration depth) and microphysical (droplet growth rate) considerations. For simulations in which the jet was prescribed at a height between these two critical levels, long-lasting cumulonimbi were observed.

Instead, typical tropical squall line systems have been observed to be long-lived multicellular convective systems. It was also concluded in RKW88 that the persistence of a tropical squall line system depends upon relative inflow at all levels ahead of the system, whereas midlatitude systems may exist with some degree of upper-level relative outflow ahead of the squall line. The low-level shear necessary for the long life of the system is often provided by the environment of the initial convective cells, but later contributions to the low-level vertical wind shear by the convective line itself become substantial factors in the continued growth or ultimate dissipation of the system. In a study of TOGA COARE convective systems displaying some degree of linear organization, LeMone et al. (1998) reiterated that convection organized into bands, such as squall lines, reinforce and will

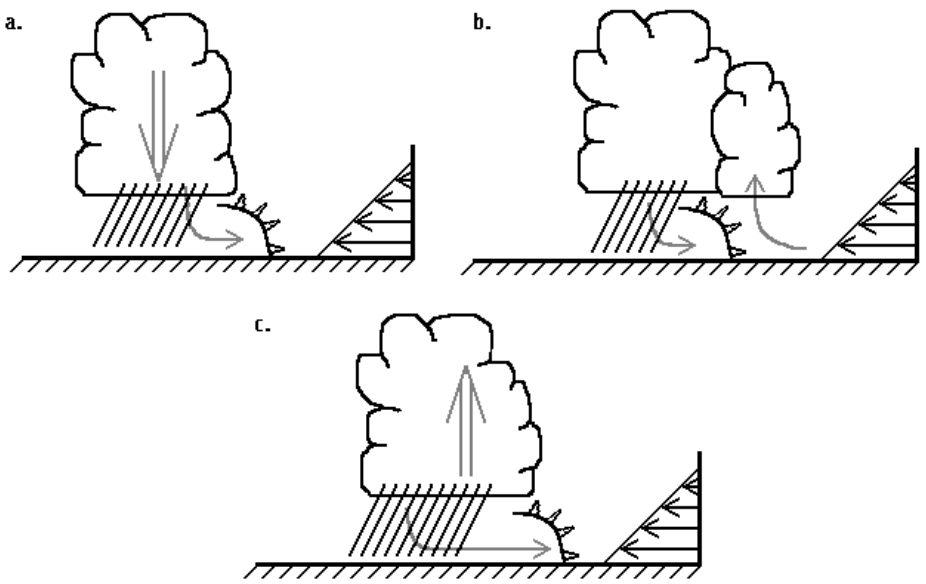

Figure 2.3: Schematic view of the continuous propagation of a single cumulus cell in the direction of environmental LLS, after RKW88.

often increase the low-level line-normal vertical wind shear. The tropical squall line system presented in H77 developed on the southwest edge of a low-level pool of relatively cold air, left behind by a preceeding system, which propagated in a direction perpendicular to the surface environmental flow. Regional soundings presented in H77 show that the low-level (surface to ~850 hPa) vertical wind shear (LLS) is oriented toward the southwest, indicating the direction of propagation of the squall line cumuli in their initial stages of growth as demonstrated in Figure 2.3.

While the LLS may determine the direction of initial cumulus motion, further consideration of the middle layer (~850 to ~500 hPa) vertical wind shear (MLS) is required for the determination of convective updraft tilting and the eventual formation of a trailing stratiform region down-MLS of the convective line. Consideration of a tilted convective updraft helps to determine the placement of convective precipitation and downdrafts, as shown in Figure 2.4, which further affect the continued maintenance of adequate surface forcing mechanisms for squall line propagation. A convective line which deposits its precipitation and subsequent low-level convective cold pool up-MLS in its region of significant

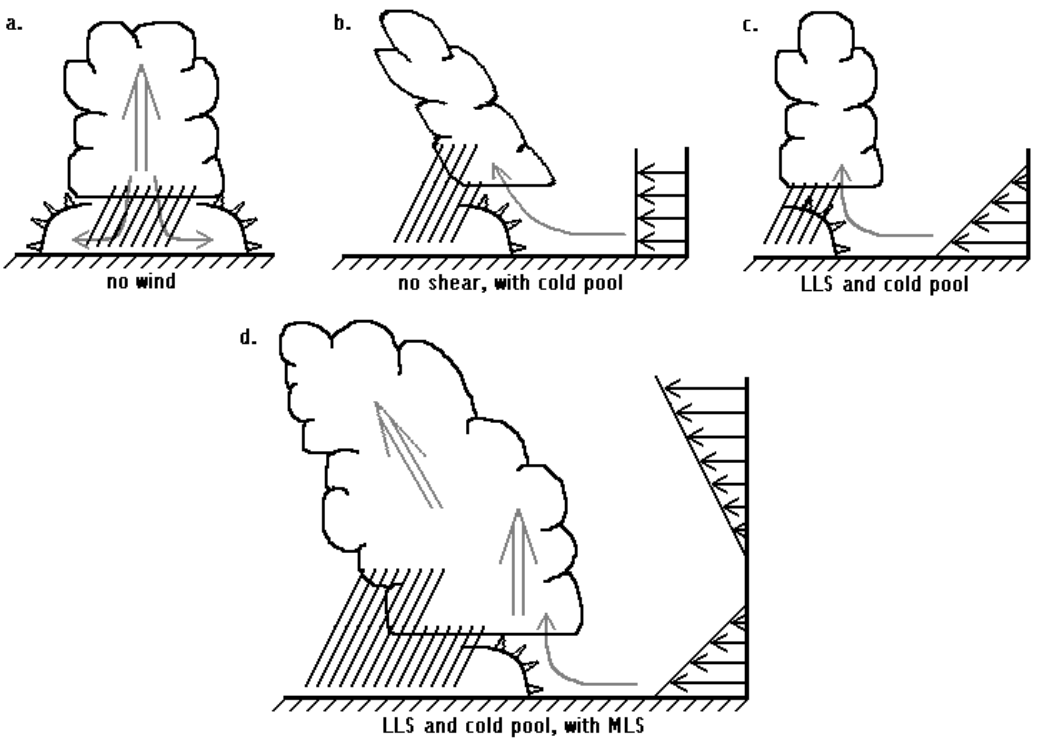

Figure 2.4: Schematic view of various cases for precipitation and downdraft placement, depending on local sources of shear and vorticity, after various precedents.

low-level inflow and moisture supply, i.e. down-LLS, is likely to move more slowly than the archetypal trailing stratiform squall line system and may be extinguished within a short period of time.

As well, it may be important to consider upper-level winds in the placement of squall line precipitation and its effects on the strength of the convective line. Grady and Verlinde (1997) examined a continental squall line system which developed in the lee of the Rocky Mountains in northeast Colorado and found that strong mid- and upper-level shear not only forced the convective updrafts into a more upright position, but also dictated the flow of upper-level convective debris into a pre-squall overhanging anvil region. Grady and Verlinde found that the melting and evaporation of precipitation beneath this overhanging anvil may have served to create a "suppression zone" ahead of the convective line and above the low-level gust front near the southern end of the system, such that only sporadic discrete

propagation events resulted.

Aloft, the formation of a trailing stratiform region is determined by the ability of the MLS and the mid- to upper-level environmental winds to tilt the convective updrafts rearward, to precondition the environment down-MLS of the convective line by the detrainment of moist turbulent air (Ackerman, 1958; Perry and Hobbs, 1996), and then to displace the mature and dissipating convective cells from the leading convective line toward the rear of the system. For this last process, some amount of relative flow directed from the front toward the rear of the system is required in the upper levels, reinforcing the necessity of a deep inflow layer ahead of the squall line system. Houze and Rappaport (1984) examined the 28 June, 1975, GATE squall line system, which demonstrated a flow pattern in the 400-to-200 hPa layer later in its life cycle which deposited upper-level squall line outflows and precipitation ahead of the convective line. Although evidence was not entirely conclusive in designating this pre-squall overhanging precipitation as the mechanism for the eventual demise of a portion the squall line system, it was concluded by Houze and Rappaport that this arrangement presented a "self-destructive" structure for squall line systems. Under the influence of midlevel pre-squall inflow, the airflow and precipitation schematic presented by Smull and Houze (1985) may be interpreted as forcing overhanging pre-squall precipitation to re-enter the convective line. While such a mechanism may allow for the formation of large graupel and hail particles to form by the recycling of hydrometeors in some midlatitude continental convective systems such as supercell thunderstorms, the implications of this recycling for tropical maritime system dynamics which are influenced more by warm-rain processes are unclear.

It was explained in Z77 that as the convective cells of the squall line develop regions of heavy precipitation, evaporatively cooled air initiates convective-scale downdrafts in the lower levels of the convective line which begin to form a cold pool and then spread laterally upon meeting the ground, as shown in Figure 2.1. In experiments involving various microphysical parameterizations in a two-dimensional cloud model, Nakajima and Matsuno

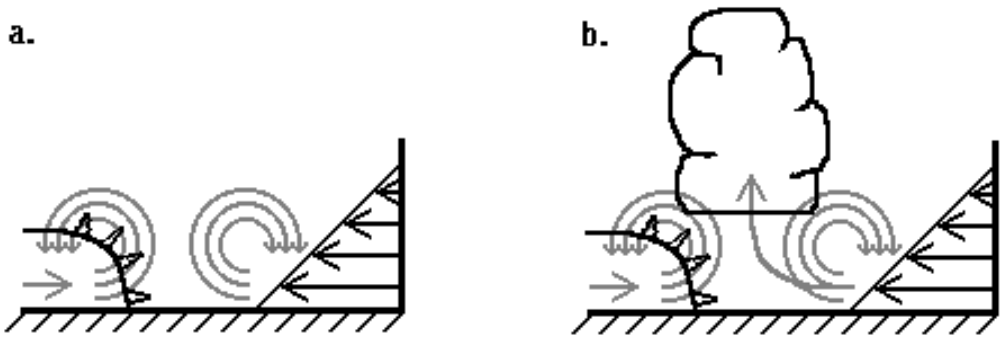

Figure 2.5: Schematic view of roll-like circulations created by a propagating gust front and opposing LLS, after RKW88 and FT98.

(1988) found that raindrop formation, subsidence, and evaporation played primary roles in the formation of the low-level cold pool. Nakajima and Matsuno also concluded that the first two of these processes contribute to sustained convection by removing moisture form the air at midlevels in the cloud, allowing the cloudy region to remain conditionally unstable, while raindrop evaporation contributes to the humidification of the regions adjacent to the precipitating cloud, preconditioning the environment there for new convection.

The portion of the convective cold pool which attempts to propagate from beneath the squall line against the mean low-level wind will develop roll-like (solenoidal) circulations on its leading edge as a result of internal vertical wind shear and local baroclinicity, as shown in Figure 2.5. These circulations assist the low-level convergence of dense convective outflow air and the warm, moist environment inflow, lifting the inflow air to form a new convective cell some distance down-LLS of the pre-existing convective line. Weckwerth and Wakimoto (1992) have suggested that the strongest lifting and most successful generation of new convective cells may occur at regions in which constructive interference is greatest between Kelvin-Helmholtz waves generated atop the outflow head (Droegemeier and Wilhelmson, 1985, 1986) and internal gravity waves which exist along the upper surface of the cold outflow layer and are generated by convective motions near the gust front. In unstable environments, solenoidal circulations on the leading edge of the cold pool may be aided

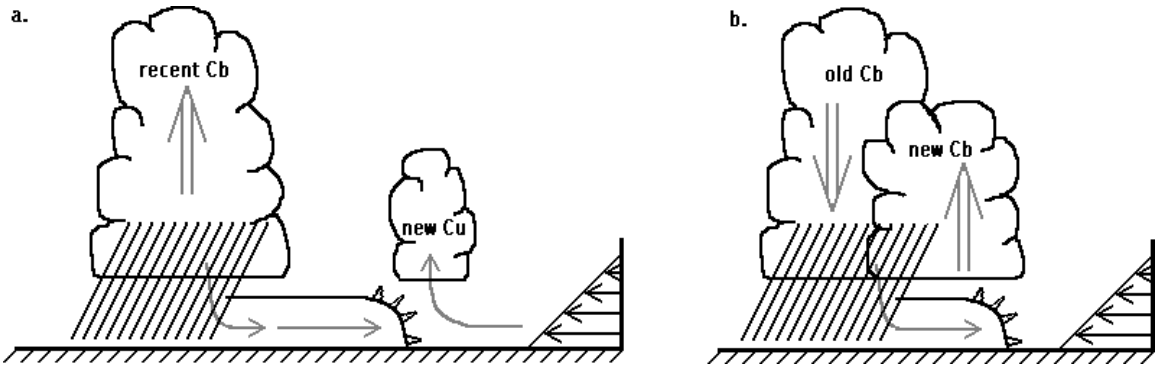

Figure 2.6: Schematic view of the mechanism of discrete squall line propagation, after RKW88.

by lifting in forward-propagating gravity waves induced by the initial deep convection, as found by Matejka and Stossmeister (1986). The relation of deep convection to gravity waves and the propagation of a convective cell has been examined by Cram et al., (1992) and Mapes (1993). Yamasaki (1988) emphasized the importance of gravity waves in convective dynamics, despite an obvious dissimilarity between mesoscale and gravity wave dynamics.

A squall line system may exhibit two modes of propagation, depending on the time period over which the system is observed. Over short time periods, the convective cells in the squall line may propagate continuously, as demonstrated in Figure 2.3. By this mechanism, the cloud mass is continually displaced downwind from the location of the core updraft within the cloud, such that the strongest updrafts continually penetrate an inflow of pre-squall environmental air. Thus, a solitary cumulus cloud may seem to move more slowly than its environmental flow by propagating up-MLS. This mechanism has been studied in detail with regard to the entrainment and mixing of environmental air into the cloud, and will be discussed further in Chapter 5.

Over longer time periods of observation, as in H77, the formation of new cells on the gust front immediately ahead of the mature convective region allows for a discrete propagation of the system as demonstrated in Figure 2.6. As the convective cells age and are carried upward and rearward into the trailing stratiform region, the leading edge of the squall line seemingly "jumps" to the new convective cells and re-forms there. The

dynamic interaction between the convective and stratiform regions of the tropical squall line system is important in the evolution to and duration of the mature stage of the system life cycle, and will be discussed further in the next section. By this mechanism of discrete propagation, the demise of the squall line system in H77 seems to have been brought about as the leading convective line propagated sufficiently quickly enough so as to eventually separate it from the trailing stratiform region, limiting this dynamic interaction and its benefits to the maintenance of the system.

It has been observed that classification of squall line systems according to the speed of convective line propagation provides valuable insight into differences in convective structure and the two-dimensionality of the overall system and its environment. Houze and Rappaport (1984) examined the early GATE squall line system of 28 June, 1974, which was considered distinctive for its pre-squall overhanging stratiform precipitation region. In RKW88, such a structure is attributed to weak LLS in relation to the MLS, which is typically oriented opposite the LLS in wind profiles of the undisturbed environment of tropical squall lines. As discussed earlier, a convective line which deposits its outflow and precipitation in its region of primary inflow has developed a self-destructive structure under the influence of the local MLS and upper-level winds in relation to the direction of system propagation. Due to the disturbance of the pre-squall environment by precipitation-cooled downdraft air, the majority of the squall line system of 28 June, 1974, was observed to propagate continuously and slowly, at approximately 7 m s^{-1}, instead of discretely and more quickly ($\sim$10-14 m s^{-1}) as was observed for several of the more long-lived GATE squall line systems (Z77, H77; Frank, 1978; GH82; Tao and Simpson, 1989).

Although observations of the GATE squall line system of 28 June, 1974, demonstrate largely two-dimensional structure, including the late-stage trailing stratiform growth on the southern end of the convective line observed by Houze and Rappaport (1984), the orientation and structure of a late GATE squall line system on 14 September, 1974, are documented by Zipser et al. (1981) and present a more complicated three-dimensional structure than earlier

systems. The 14 September, 1974, squall line system was actually observed to propagate eastward while embedded in the southerly wind region of a tropical easterly wave, while the system itself was seemingly oriented south-southeast to north-northwest from the front to the rear. To complicate the description of this system further, only east-west cross sections of the system were presented in the analysis of Zipser et al. Although the system was observed to propagate at only $\sim$1 m s^{-1}, LeMone et al. (1998) concluded that even such slow-moving convective lines experience significant low-level inflow from the pre-squall environment, despite differences in convective line and LLS orientations. However, such a complicated example presents a poor archetype of two-dimensional squall line system structure.

Barnes and Seickman (1984) presented a comparative analysis of slow- and fast-moving GATE tropical convective lines which can be understood with the information on initial squall line environment and structure already presented here. Slow-moving systems were observed to form behind the trough of a tropical easterly wave and propagated eastward, as in Zipser et al. (1981), in a slightly warmer and moister midlevel environment than faster moving lines, and with a leading edge approximately parallel to weak LLS. These slow-moving systems possessed an average propagation speed of $\sim$2 m s^{-1}, and developed low-level pre-squall convective outflows which were less than 1 km deep. However, the fast-moving systems, which propagated westward ahead of the tropical easterly wave trough with average speeds of $\sim$11 m s^{-1}, were observed to form with leading convective lines perpendicular to strong LLS in an environment which was slightly cooler and drier in the 850-to-450 hPa layer than that of the slow-moving systems. These fast-moving systems were found to produce deeper low-level pre-squall convective outflows ($\sim$1.6 km) than their slow-moving counterparts. Similar results, with regard to the orientation of slow- and fast-moving squall lines compared to the direction of LLS, were found in simulations of TOGA COARE convective systems by Skamarock et al. (1996). Systems which propagated at intermediate speeds, $\sim$3-7 m s^{-1}, were not examined by Barnes and Seickman, although

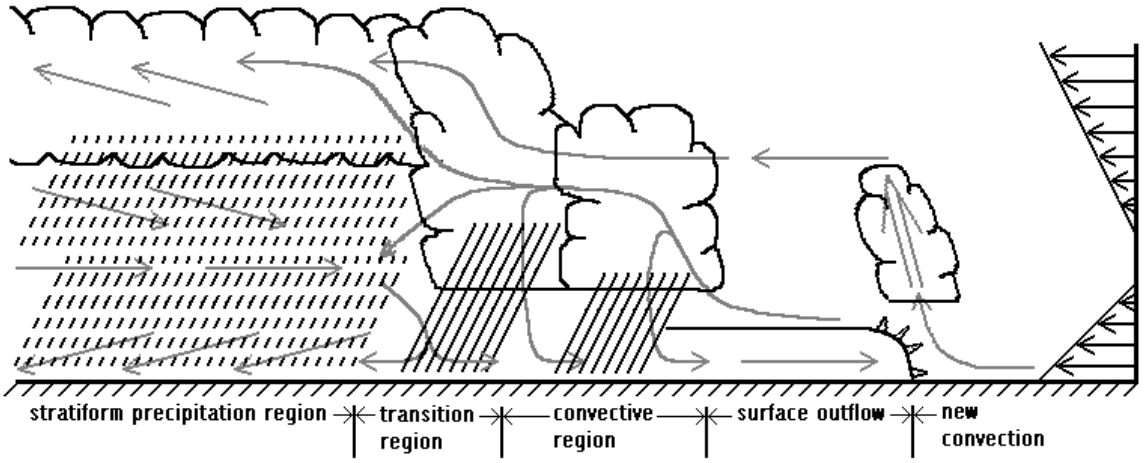

Figure 2.7: Schematic view of tropical squall line system convective, precipitation and system-relative flow structures, after various precedents. The vertical scale is exaggerated in the lower levels to show detail.

it may be concluded that squall lines systems such as the one on 28 June, 1974 presented by Houze and Rappaport (1984) may fall into a class of systems which require more detailed analyses, as do the slowest convective systems, than the notably two-dimensional fast-moving squall line systems.

Once the convective line has developed in a region of adequate moisture and LLS, the MLS and mean flow contribute to the large-scale structure of the tropical squall line as presented in H77 and reproduced here in Figure 2.7. The line-perpendicular structure of a mature, quasi-steady state squall line system is discussed in greater detail in the next section.

2.2 Structure

Figure 2.7 can be employed to illustrate the fundamental two-dimensional structure of a successfully long-lived squall line system. During the early stages of growth, the relative environmental wind ahead of the system is directed into the squall line from the front at all levels, such that the relative wind field in the early stages of the squall line life cycle is directed from the front to the rear of the system. A convective updraft on the leading edge of the squall line tilts slightly down-MLS, as observed for GATE convective lines by

LeMone et al. (1984), depositing its convective precipitation and associated convective cold pool slightly to the rear (up-LLS) of the pre-existing convective updraft as in Figure 2.4. The forward portion of this descending and spreading cold pool will tend to move in a direction against the low-level wind, such that a solenoidal circulation is developed in a region of low-level convergence, where moist inflow air is then lifted over the advancing cold outflow and, if the lifting is strong enough, develops a new convective cell down-LLS of the pre-existing convective line. With the formation of enough new cells ahead of the pre-existing squall line, the leading convective line will re-establish itself on the locations of the new cells, while the mature and older cells ascend and are transported toward the rear of the system by the MLS and the deep-layer environmental flow. Matejka and Stossmeister (1986) found for midlatitude squall line systems that the main convective line typically joins new pre-squall convective elements within 1 hour of their initiation.

Lifting of pre-squall environmental air by the advancing convective cold pool tends to produce a low-level double maximum in the vertical velocity field for the convective system, as found by Jorgensen et al. (1997, hereafter JLT97) in studies of a tropical squall line system in the western Pacific region during TOGA COARE. In JLT97, it was noted that the two low-level vertical velocity maxima occurred for different reasons: one low-level pre-squall vertical velocity maximum was due to external forcing by the advancing cold pool, while a low-level vertical velocity maximum within the convective region was due to buoyant convection. Another vertical velocity maximum was found in the upper troposphere above the freezing level within the convective line. Separating the two vertically-oriented maxima within the convective region, a distinct minimum in vertical velocity was found around the freezing level, actually spread over an altitude range of 4-9 km, in the convective updrafts. This minimum in vertical velocity may be attributed to several factors, not the least of which may be a layer of increased static stability, or possibly a temperature inversion, produced by the release of latent heat on the freezing of cloud droplets and precipitation within the cumulonimbus (Johnson et al., 1996). Another factor may involve interaction of

the squall line convective updraft with midlevel inflow which has been found to pass through the convective line and toward the rear of the system (Fankhauser, 1971; Smull and Houze, 1985, 1987a).

Advection of the mature and older cells aloft and rearward in the system serves several purposes, among which are: the displacement of convective precipitation from mature cells toward the rear of the convective updraft such that the moisture source for the new cells developing in the leading convective line is not extinguished as demonstrated in Figure 2.4, the allowance of continued convective growth in the leading edge of the squall line by lateral removal of moist and more stable air aloft (Taylor and Baker, 1991), and development of the trailing stratiform region of clouds and precipitation. Low rainfall rates in the stratiform region, as compared to the preceeding convective line, allow for the slow formation of a significantly larger and slightly deeper cold pool in the low-level stratiform region due to the melting and evaporation of less substantial but longer-lived precipitation.

It may be deduced that, in the trailing stratiform region, mesoscale ascent in the upper-level cloudy region and mesoscale subsidence in the sub-cloud region will require compensating inflow from the sides of the stratiform region in the middle levels of the system. These stratiform mesoscale regions of ascent and subsidence and the presence of compensating mid-level convergence, most prominent at approximately the 650 hPa level, have been observed in composite analyses of the 12 September, 1974, GATE squall line system by Gamache and Houze (1982, hereafter GH82) and for a midlatitude continental squall line system by Smull and Houze (1987a). While detrainment of moist air and convective debris from and ventilating flow through the leading convective line may provide some inflow in the forward portions of the trailing stratiform region, more substantial compensating mid-level inflow to the trailing stratiform region has been observed to originate from the rear of the squall line system by Betts et al. (1976) and in Z77, as well as in several studies of mid-latitude continental squall line systems. Smull and Houze (1985, 1987a) observed midlevel inflow which formed a notch at the rear of the stratiform cloud region, a

feature also observed by Rutledge et al. (1988, hereafter RHBM88). During PRE-STORM, in RHBM88 a rear-to-front flow was observed in a developed squall line system which descended from the middle levels while becoming shallower and weaker as it approached the convective line from behind.

Divergence in the leading convective line, which leads to detrainment from the convective cells, is noted in GH82 for levels above approximately 650 hPa. Enhanced divergence at this level is supported by the observation of marginally enhanced stability near the freezing level by Johnson et al. (1996). Immediately behind the leading convective cells, a transition region (Smull and Houze, 1987a) is formed where the loss of buoyant and mechanical upward momentum and the effects of compensating subsidence behind the leading convective line force air detrained down-MLS to descend sharply. This transition region immediately behind the convective line was also found in the continental system presented in RHBM88 as well as in analyses presented in Z77, for which temperature anomalies of $T' = +4°C$ and low saturation ratios around the 850 hPa level were observed, conditions which can be attributed to adiabatic warming and drying due to strong deep-layer subsidence in the region. In Z77 it was proposed that the downdraft-dominated transition region is composed of inflow at middle levels of the system from both the front, through the convective updrafts, and the rear of the system. Sun et al. (1993) agreed with earlier researchers (Heymsfield and Schotz, 1985; Smull and Houze, 1987a) that upper-level transition region downdrafts may actually be forced by detrainment from the preceeding convective line, since thermodynamic analyses of PRE-STORM squall line system showed positively buoyant upper-level downdrafts there. At lower levels in the transition region, where precipitation-induced cooling and negative buoyancy perturbations may occur, the rear-to front flow observed in analyses presented in RHBM88 was found to descend more sharply in the region immediately behind the convective updrafts, while also turning parallel to the leading convective line according to radar observations.

Of all the air motions considered in this two-dimensional line-perpendicular treat-

ment of tropical squall line systems, the front-to-rear flow which originates in the midlevels ahead of the squall line may be the most complicated. Radar and satellite observations of cumulonimbus cell spacing in the leading convective line indicate that a significant portion of midlevel pre-squall inflow may actually pass through the leading edge of the system and around the individual cumulonimbus cells, as found by Fankhauser (1971), instead of being fully incorporated into the convective updrafts. Mid-level front-to-rear flow through the leading convective line was also observed and examined by Smull and Houze (1985, 1987a). The additional consideration of discrete propagation may ensure that large quantities of low-moisture front-to-rear flows in the pre-squall middle troposphere never take part in the convective updrafts, but rather find themsleves suddenly to the rear of the leading line and immediately part of the post-squall transition region. A structure which includes inflow through the leading convective line was suggested by observations of continental squall line systems during the second Venezuelan International Meteorological and Hydrological Experiment (VIMHEX-1972), as reported by Betts et al. (1976), and is supported by observations of maritime squall line systems presented in Z77. Upon encountering downdrafts in the transition region, the front-to-rear flow may descend toward the surface, crossing the steeply descending rear-to-front flow in this region. Airflow schematics presented by Betts et al. (1976) and in Z69 and Z77 demonstrate this descending flow which passes through the leading convective line and extends toward the rear of the system as a low-level front-to-rear flow.

However, where the midlevel pre-squall inflow may encounter the strong updrafts in the leading convective line, some finite entrainment and mixing interaction of the convective updrafts with this ventilating flow may contribute to the midlevel vertical velocity minimum in the convective line observed in JLT97. It is noted in Z77 that some degree of entrainment and mixing of the inflow air into the cumulonimbus cells of the leading convective line must occur, although convective scale undilute updraft cores may still exist as found by Heymsfield et al. (1978). Those updrafts which entrain the least low-moisture air from their

mid-level environment are expected to produce the strongest convective cells in the leading edge of the squall line system. Midlevel front-to-rear inflow which receives some amount of upward momentum from the convective updrafts, causing the midlevel convective vertical velocity minimum, will then ascend through the transition region, advecting mature and older convective cells, cumulonimbus debris, and hydrometeors aloft and rearward into the trailing stratiform precipitation region. The tropical squall line system airflow schematics presented in GH82 and here in Figure 2.7 demonstrate this ascending flow which passes through the leading convective line at midlevels, crosses the transition zone downdraft region, and joins the post-squall stratiform region as an upper-level front-to-rear flow.

While the convective cold pool spreads quickly ahead of the leading convective line and contributes to the propagation and eventual dissipation of that line, the stratiform cold pool affects a deeper layer of the lower troposphere and spreads more slowly forward than rearward, possibly affecting maintenance of the convective line by forcing air from the warm and dry transition region into the convective precipitation and updraft source regions as suggested by Smull and Houze (1987b). However, the presence of adequate MLS through the system is expected to dominate low-level effects of the mesoscale cold pool on the leading convective line. These processes may be considered components of the dynamic interactivity between convective and stratiform regions, as discussed earlier. Johnson and Nicholls (1983, hereafter JN83) performed composite analyses of rawindsonde and surface data beneath the 12 September, 1974, GATE squall line system, complementing the analyses in GH82, to examine marine boundary layer modification and recovery to pre-squall conditions. Using these composite analyses and further modeling studies, Nicholls and Johnson (1984) found that the stratiform region low-level cold pool which remains after dissipation of the system is of such high thermodynamic stability, as found in JN83, that it greatly affects the time required by the marine boundary layer and lower troposphere to return to convectively neutral or unstable conditions and for that region to be conducive to later convective disturbances. These results agree with conclusions presented in Z69, in

which it was found that the residual modified boundary layer is unlikely to participate in sustained deep convection for six to twelve hours after the formation of the low-level cold pool.

Convective cells are often observed to remain active while embedded within the trailing stratiform cloud region long after the leading convective line is estimated to have passed their position, as indicated by satellite imagery in H77 and similar observations by other researchers. The upper vertical velocity maximum observed for the leading convective line of the system presented in JLT97 was found to increase in height with distance from the leading convective line, supporting the idea that mature and older cells are advected upward and rearward while they remain convectively active. These observations, in addition to radar and rainfall data as presented in H77, lend support to the idea that the stratiform region is not composed exclusively of dynamically inactive cumulonimbus debris advected rearward from the convective line. It is widely accepted that a mesoscale area of weak ascent forms within the cloudy upper troposphere of the stratiform region, above the precipitation melting level and the slowly-forming stratiform cold pool with its associated mesoscale region of weak downdrafts. For dynamically inactive cloud regions, little vertical motion would be observed, and the cloudy region would be expected to dissipate (Haman and Pawlowska, 1995) over a time period much shorter than that observed for the stratiform regions of squall line systems. Some of the mixing mechanisms which may allow the stratiform region of a tropical squall line system to remain dynamically active, in some cases partially convective, and long-lived will be discussed in further detail in Chapter 5.

2.3 Thermodynamics and Microphysics

Although many aspects of cumulonimbus growth and squall line propagation will be discussed individually in Chapter 5, some of these subjects are worthy of immediate note due to their pertinence in the present discussion. It may be sufficient to state here that the entrainment of and mixing with low-moisture air from the environment ahead of

the squall line is inherently detrimental to the maintenance of buoyancy and precipitation production within existing convective cells, and is therefore detrimental to the maintenance of the strength of the leading convective line and possibly to the persistence of the squall line system.

The mixing of relatively dry environmental air into a cloud has the effect of reducing cloud water mixing ratios in the cloud through the evaporation of cloud and precipitation droplets. Differential evaporation rates for cloud droplets of various sizes effectively alter the cloud droplet size distributions, as explored in many observational and laboratory experiments (Stith and Politovich, 1989; Hicks et al., 1990; Brenguier and Grabowski, 1993; Politovich, 1993). A similar effect is observed when precipitation falls into a subsaturated region, again altering the precipitation droplet size distribution through differential evaporation rates for various droplet sizes (Kamburova and Ludlam, 1966). It may be noted here that smaller droplets, of either the cloud or precipitation type, are known to evaporate more quickly due to a larger ratio of surface area to volume than larger droplets, while these larger droplets may experience some degree of evaporation and size reduction but are not as likely as smaller droplets to evaporate completely. The remaining large droplets in the mixed parcel may play a role in the production of bimodal cloud droplet size distributions (Stith and Politovich, 1989; Hicks et al., 1990) and the formation of precipitation droplets (Baker et al., 1980) through later parcel motions and repeated episodes of condensation growth (Telford and Chai, 1980).

While the leading convective cells of the squall line system are oriented vertically and typically cover a horizontal scale of 10-20 km from front to rear, the trailing stratiform region becomes increasingly horizontally oriented toward the rear of the system. The advection of older convective cells from the leading edge of the system toward the transition region and further rearward may allow for some evidence of convective motions, such as heavy, convective-like precipitation and vertical velocities at typical convective intensities well behind the leading convective line as found in H77. Precipitation measurements be-

neath the trailing stratiform region seem to indicate, as in H77, that aging convective cells which are advected into the trailing stratiform region may remain dynamically active. This conclusion is supported by radar observations of strong precipitation echoes in the upper levels of the transition and stratiform regions, while the strong precipitation echoes of the lower levels of the trailing stratiform region are physically separated from the the strong echoes indicative of the leading convective line by a weak-echo region, indicating the lower levels of the intermediate transition region (Smull and Houze, 1987a).

Low-level subsidence observed beneath the trailing stratiform region in Z69, Z77 and H77 may be attributed to several processes, most of which involve the thermodynamic cooling of the region by the evaporation of precipitation. Leary and Houze (1979, hereafter LH79) found that cooling rates in the subcloud region due to the evaporation of precipitation are comparable, in observed squall line cases, to cooling rates in the lower portion of the stratiform cloud layer due to the melting of ice precipitation near the 0°C level. Kamburova and Ludlam (1966) found that effects on buoyancy induced by cooling in the subcloud region, in addition to water-loading effects on parcel density, contributed most to the development of downdrafts in the lower levels of precipitating systems. Despite careful consideration of purely warm-rain processes and the development of mesoscale downdrafts in the stratiform regions of convective systems, and the ability of many models to reproduce these downdraft structures solely through the evaporation of precipitation, in LH79 it is suggested that the cooling effects of melting precipitation may contribute to the initiation of these downdrafts in the mid-levels of the system.

Airborne measurements discussed in Z77 indicate that downdrafts in the convectively active region of the squall line consist of cool air which is saturated but has relatively low water content when compared with moist low-level air in the undisturbed pre-squall environment. Mesoscale downdrafts beneath the trailing stratiform region may consist of unsaturated air, with precipitation, that may actually be slightly warmer than air surrounding the squall line system at similar levels. As reported in Z77, the percentage of area beneath

the stratiform cloud region which is occupied by these unsaturated downdrafts increases with altitude below the stratiform clouds, age of the squall line system, and distance from the leading convective line.

A radar bright band denotes the level of melting precipitation in the stratiform region of the squall line system, as in LH79, and is found to slope slightly downward toward the rear of the system in H77. This may be indicative of the influence of post-convective transition region descent in the warming of low-level air, but it is more likely that the sloping 0°C isotherm is an artifact of cooling in the middle and low levels by the melting and evaporation of precipitation. Near the rear of the system, depression of the 0°C isotherm is expected where the cooling effects of precipitation have accumulated over the length of the trailing stratiform region.

The precipitation itself is expected to play a role in the initiation of the mesoscale downdraft in the middle and lower levels of the troposphere according to two factors: first, melting and evaporation of the precipitation particles cools the surrounding air, which causes a positive density perturbation and negative buoyancy (Kamburova and Ludlam, 1966); second, there exists a downward drag force on the air surrounding the falling precipitation (Das, 1964; Takeda, 1966; Srivastava, 1967; Clark and List, 1971) which is generally greater for liquid precipitation particles than for most types of ice due to greater terminal fall speeds for liquid precipitation under most conditions (Böhm, 1992). Density perturbations in the melting region, and subsequent evolution to an equilibrium state, may contribute to the melting-level stable layers observed by Johnson et al. (1996). That precipitation fall speeds increase on melting has been suggested by Doppler radar profiles of stratiform precipitation regions, such as those analyzed in LH79, and has been incorporated into the bulk microphysical diagnoses of precipitation fall speeds in the model of Ooyama (1995).

2.4 Surface Observations

It was concluded in Z77 that the characteristics of the lowest 200-400 m of the troposphere, the lower portion of the boundary mixed layer, in the stratiform precipitation region behind the leading convective line of the system are considerably different from those of the convective line itself or the intervening transition region of saturated downdraft air. Some characteristics of the surface streamline and divergence fields have been found in composite analyses of aircraft data in GH82 and in analyses of ship-based surface and rawindsonde data in JN83. These results exhibit regions of strong surface convergence under the leading convective line, with correspondingly weak horizontal system-relative surface winds beneath the region of strongest convective updraft, and surface divergence of comparable magnitude beneath the trailing stratiform region with correspondingly strong surface winds beneath the strongest observed mesoscale downdraft regions. Although these divergence fields are of largely three-dimensional character, some of these aspects can be identified in the two-dimensional near-surface winds denoted in Figure 2.7, especially upon consideration of the local wind field in the vicinity of a rotor which is formed in the lower levels of the squall line system from larger-scale system-relative winds.

Observations of a Caribbean squall line presented in Z77 indicated a post-squall mesoscale region of high surface pressure, typically of $p' \approx +2$ hPa, centered on the forward portion of the stratiform region behind the active convective line. This post-squall mesohigh likely lends its formation to cool, saturated convective downdraft air in the transition region immediately behind the convective updrafts and to cool, descending inflow from the rear of the trailing stratiform region. However, the surface mesohigh as discussed in the composite analyses of JN83 is not necessarily co-located with the region of greatest surface divergence. The post-squall mesohigh is often accompanied by a following mesoscale region of low pressure, of $p' \approx -2$ hPa as found in JN83, farther toward the rear of the squall line system. This trailing mesolow is likely formed by the slow descent and warming of subsaturated air in the lower levels beneath the stratiform cloud region induced by low-level divergence

in response to the preceeding mesohigh (Haertel, 1998). Evidence of the pressure gradient between surface mesohigh and mesolow areas beneath the stratiform region of the squall line system was presented in Z77 by way of airborne observations. Similar features were observed and discussed by Johnson and Hamilton (1988) and Loehrer and Johnson (1995) for midlatitude squall line systems.

It was also found in Z77, and again in JN83, that the surface air temperature decreases considerably with the passage of the squall line convective region, then recovers to and sometimes exceeds its pre-squall value with the procession of the trailing stratiform region. However, it was found in Z77 that the dew point trace experiences two minima during the passage of the system, the first with the passage of the squall line and its associated saturated downdrafts in the convective cold pool, and the second with the passage of the unsaturated downdrafts beneath the stratiform region approximately 3-5 hours after the passage of the leading convective line. The dew point minimum farther behind the convective region was found between the post-squall mesohigh and the trailing stratiform mesolow in JN83 and corresponded to a specific humidity perturbation of $q' \approx -3$ g kg^{-1}. A similar feature was observed in a central Pacific squall line system and was documented in Z69. These low-level unsaturated downdraft regions occur well behind the saturated downdrafts of the transition region near the convective line. This later specific humidity depression is often observed to increase in magnitude with height up to about 900 hPa and then to decrease with height on approaching the cloudy levels of the stratiform precipitation region, producing the "onion" sounding which is demonstrated in Z77 and reproduced here in Figure 2.8 as a common characteristic of the trailing stratiform region in tropical squall line systems.

Results presented in JLT97 suggest that recovery of the low-level mixed layer beneath the squall line system occurs rapidly immediately behind the convective line but more slowly behind the entire squall line system. From these results, it may be concluded that the cool unsaturated downdrafts of the trailing stratiform region exert a much more detrimental effect on the depth and humidity of the surface boundary layer beneath the squall line

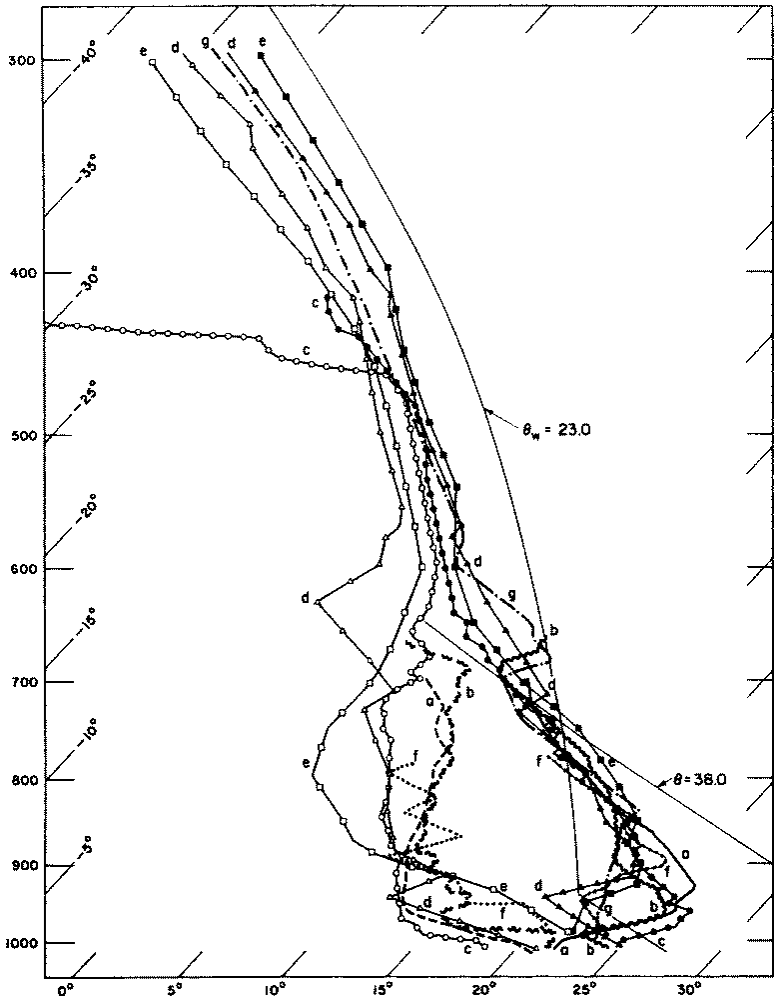

Figure 2.8: The post-squall stratiform precipitation region "onion" sounding, from Zipser (1977).

system than the saturated downdrafts in the post-squall transition region. Barnes and Seickman (1984) found that fast-moving tropical squall line systems observed during GATE developed much greater convective inhibition in the low-level system wake that their slow-moving, sometimes eastward-propagating counterparts. Using primarily surface ship and rawindsonde data, the squall line system boundary layer composite analyses presented in JN83 exhibit a significantly shallower mixed layer depth beneath the stratiform region of the system than the undisturbed boundary layer ahead of the leading convective line. From a minimum near the leading edge of the stratiform region of the squall line system, the mixed

layer depth recovered to approximately undisturbed conditions several hundred kilometers behind the system in an asymmetric wake. Asymmetry of the squall line system wake in JN83 was attributed to differential convective line strength and intensity of downdrafts in the trailing stratiform region. Modification of the boundary mixed layer in the stratiform region of the squall line system and the recovery of the system's wake was explored with further analyses and modeling efforts by Nicholls and Johnson (1984).

2.5 Squall Line System Modeling Efforts

Numerous efforts at numerical modeling of midlatitude and tropical squall line systems are summarized in Tables 2.1 and 2.2. Listed models are identified in the text and in Appendix A; field experiments are described in Appendix B. Models which include two- or three-dimensional ("2D" or "3D") simulations are noted with a filled circle in the appropriate column, while models which include quasi-three-dimensional simulations are denoted with an open circle in the "3D" column. In a discussioon of the one model for which this is the case, the framework of quasi-three-dimensionality, as different from strict two- or full three-dimensionality, is briefly outlined. In another instance, a model described by its authors as "quasi-three-dimensional" is shown to be fully three-dimensional upon further consideration of this framework. Grid spacings included in model descriptions by the appropriate authors are included; when a range of grid spacings is listed, the model was described to include variable resolution in the method noted on the corresponding axis. Those models listed which include thermodynamics and microphysics for only the liquid phase of cloud droplets and precipitation are considered "warm rain" models, while those which include both the liquid and ice phases of cloud and precipitation droplets are considered "mixed phase" models. Because different models may be employed for similar simulations, or vice versa, the initial conditions for model simulations, also provided in model descriptions by the appropriate authors, are included. All models discussed here incorporated some finite LLS in their simulations. However, variations in the strength and depth of the LLS and its

Table 2.1: Several modeling efforts for continental squall line systems. In the descriptions of model grid spacing, (s) denotes a stretched (i.e. variable) grid spacing and (n) denotes nested grids of constant spacing in the appropriate direction.

Model	2D	3D	grid spacing	microphysics	initial conditions
Midlatitude squall line systems					
KW78		•	$\Delta x, y = 1$ km $\Delta z = 500$ m	warm rain	original sounding dry above 700 mb
TMM82	•		$\Delta x = 0.5$ km $\Delta p = 50$ mb	condensate only	Miller (1978) United Kingdom
RKW88	•	•	$\Delta x, y = 2$ km $\Delta z = 700$ m	warm rain	Bluestein and Jain (1985) midlatitude composite
FO88, FD95	•		$\Delta x = 1 - 158$ km (s) $\Delta z = 200 - 940$ m (s)	mixed phase	Ogura and Liou (1980) 22 May, 1976, Oklahoma sndg
FO89	•		$\Delta x = 1 - 158$ km (s) $\Delta z = 200 - 940$ m (s)	warm rain	Ogura and Liou (1980) 22 May, 1976, Oklahoma sndg
F91		○	$\Delta x = 1 - 67$ km (s) $\Delta z = 200 - 940$ m (s)	warm rain	Ogura and Liou (1980) 22 May, 1976, Oklahoma sndg
FT98	•	•	$\Delta x, y = 1$ km $\Delta z = 200 - 940$ m (s)	warm rain	Ogura and Liou (1980) 22 May, 1976, Oklahoma sndg
COPT81 squall line systems					
DMS87	•		$\Delta x = 1$ km $\Delta p = 50$ mb	warm rain	22-23 and 23-24 June, 1981 Korhogo nocturnal soundings
RL88		•	$\Delta x, y = 1.25$ km $\Delta z = 200 - 1400$ m (s)	warm rain	23-24 June, 1981 Korhogo composite soundings
LM89	•		$\Delta x = 1 - 6$ km (n) $\Delta z = 500 - 1000$ m (n)	mixed phase	22-23 and 23-24 June, 1981 Korhogo composite soundings
CY93		•	$\Delta x, y = 1 - 59$ km (s) $\Delta z = 120 - 920$ m (s)	warm rain	22-23 and 23-24 June, 1981 Korhogo composite soundings
CRL94, CLR95	•		$\Delta x = 1.25$ km $\Delta z = 220 - 1400$ m (s)	mixed phase	23-24 June, 1981 Korhogo composite soundings
LMZ97	•		$\Delta x = 1 - 6$ km (n) $\Delta z = 500 - 1000$ m (n)	mixed phase	22-23 and 23-24 June, 1981 Korhogo composite soundings

effects on convection are the sole subjects of several modeling and analysis efforts.

2.5.1 Continental Squall Line System Simulations

Table 2.1 outlines several efforts in the modeling of continental squall line systems. A short discussion is included here regarding insights into system dynamics derived from these simulations, as well as the place of each publication in this review of squall line system modeling efforts. Several three-dimensional models, and models of midlatitude squall line systems, are discussed here, although the focus of this study will remain on the two-dimensional representation of tropical squall line systems. The reader is referred to the publications listed for further details on the respective modeling efforts and their results.

Although the model of Klemp and Wilhelmson (1978, hereafter KW78) and its further use in the modeling efforts presented in RKW88 simulated midlatitude continental squall line systems, as defined by the initial environmental soundings employed, and employed only warm rain thermodynamics and microphysics based on the parameterizations of Kessler (1969), these efforts have contributed greatly to the study of shear-influenced convective systems and the understanding of dynamic and thermodynamic structures in both midlatitude and tropical squall line systems. Given most early efforts at two-dimensional modeling with moderate spatial and temporal resolution, it may be considered that the three-dimensional modeling effort presented in KW78 was quite ambitious for its time. In TMM82 a two-dimensional numerical model was presented in which the development of somewhat unicellular continental convective systems in a sheared flow was based on a dynamical model of dry convective downdrafts presented by Thorpe et al. (1980). In TMM82, moisture is included in the model by the use of midlatitude thermodynamic profiles from Miller (1978), although condensation and evaporation processes are not addressed explicitly in TMM82. In a conceptual model of the simulated system, the convective overturning updraft and post-squall downdraft were found to initiate a low-level rotor structure in the region of the squall line.

The 22 May, 1976, Oklahoma squall line system examined by Smull and Houze (1985, 1987a, 1987b) was simulated in a series of experiments by Fovell and Ogura (1988, hereafter FO88; 1989, hereafter FO89) and Fovell and Dailey (1995, hereafter FD95). In FO88, FO89, and FD95, the same two-dimensional model, described by Soong and Ogura (1980), was employed, with only slight numerical modifications by the time of FD95. These efforts successfully simulated a multicellular continental squall line system, yielding a structure similar to that observed by Smull and Houze. Due to the design of the model, the system was unable to modify its pre-squall environment sufficiently enough to induce an eventual decay phase in the squall line life cycle, resulting in a squall line system which eventually reached a mature quasi-equilibrium state. Quasi-regular cycles of pre-squall cell generation

and realistic squall line propagation speeds were enhanced in their realism by the inclusion of ice processes, which also promoted the formation of a trailing stratiform-like region of light precipitation.

In a refinement of the work presented in FO88, in FO89 it was found that more strongly-sheared systems developed greater propagation speeds as well as longer periods of pre-squall cell generation cycles, while also exhibiting larger and less distinctly separate convective cells, stronger rear inflow, and greater amounts of convectively-generated precipitation. Fovell (1991, hereafter F91) performed quasi-three-dimensional simulations, using the same model as that presented in FO88 and FO89 but including the v component of the horizontal wind (although no actual distance in the y-direction was included, such that $\partial/\partial y = 0$ everywhere) in order to examine the effects of rotation on the simulated squall line system. In F91, the inclusion of Coriolis accelerations appropriate for midlatitude simulations led to the eventual decay of the simulated system "for physically realistic rather than numerical reasons."

The oscillatory nature of convective cell generation and structure in the simulations presented in FO88, FO89, and F91 was examined in further detail in FD95, in which it was found that systems in weak or shallow environmental LLS displayed nonperiodic (chaotic) convective behavior, while LLS of moderate depth and strength induced simple periodic behavior, and simulations employing strong and deep LLS displayed complex periodic behavior with overlapping oscillations of differing convective strengths. Fovell and Tan (1998, hereafter FT98) extended this analysis of the temporal behavior of convective systems to include another model, the University of Oklahoma Advanced Regional Prediction System (ARPS), in two- and three-dimensional simulations of the 22 May, 1976, Oklahoma squall line system. In FT98, a conceptual three-stage life cycle of convection, enhanced with expected vertical velocity and equivalent potential temperature profiles, was proposed for short-lived convective cells embedded in a multicellular squall-type system. The results presented in FT98 were considered directly applicable to multicellular squall-type systems

which propagate by the spreading of a low-level cold pool, and were directly contrasted with unicellular or supercell-like systems such as that presented in TMM82 or systems which may propagate by other mechanisms, such as by gravity-wave propagation as discussed by Cram et al. (1992).

Dudhia et al. (1987, hereafter DMS87) simulated continental tropical squall line systems observed over West Africa during COPT81 on 22-23 June and 23-24 June, 1981, using a model modified from that presented by Miller and Pearce (1974). The earlier of these two systems was examined in detail by Roux (1984, 1985) and Chong et al. (1987), while an examination of the latter system was performed by Roux (1988). For the model presented in DMS87, only warm rain thermodynamics and microphysics were employed, and only the nocturnal soundings for these systems were employed as initial conditions. In DMS87, it was found that downdrafts play a crucial role in the ultimate organization of the convective system. The leading convective updraft and downdraft structure and the trailing low-level mesoscale downdraft structure were found to generate a low-level rotor similar to that described in TMM82 and included in Figure 2.7 at the forward end of the convective region. This low-level rotor structure is expected to be found directly beneath the leading cumulonimbus line and is thought to participate in vigorous boundary layer mixing processes immediately behind the convective line.

The earlier of the two COPT81 squall line systems listed above was simulated by Lafore and Moncrieff (1989, hereafter LM89) using a nested two-dimensional mixed-phase model which was described by Clark (1977) and Clark and Farley (1984). In the results presented in LM89, the sub-convective rotor is clearly evident. Three-dimensional models were employed by Redelsperger and LaFore (1988, hereafter RL88) and in the later efforts of Chang and Yoshizaki (1993, hereafter CY93) who employed a model based on several precedents, including KW78. In RL88, only the 23-24 June, 1981, COPT81 squall line system was simulated using a three-dimensional model, described by Redelsperger and Sommeria (1986), with stretched vertical resolution and only warm rain thermodynamics

and microphysics. The sub-convective rotor is not explicitly identified or examined in CY93, although a similar but weak low-level flow structure is evident in the wind field of results presented in CY93.

While convection in the model of RL88 was triggered using a density current in a process similar to that suggested for continental thunderstorm initiation by Purdom (1979) and by Purdom and Marcus (1982), and similar to the GATE case study presented in H77, a warm bubble was employed for the initiation of convection in the model of CY93. Objections to this latter method of convective initiation have been presented in DMS87 and in LM89, and will be discussed further in Chapter 5. Despite their differences, the three-dimensional models of RL88 and CY93 both achieved qualitatively accurate results for their simulations of the COPT81 squall line of 23-24 June, 1981. Quantitatively, both models produced low precipitation rates in comparison with the actual system, although the inclusion of a rear inflow jet induced by the stratiform region, as discussed earlier, in experiments presented in RL88 did allow the results for squall line convective intensity to approach observational values. Due to the exclusion of ice thermodynamic and microphysical processes, the squall line stratiform region was not accurately simulated in the model of CY93, and that the convective system simulated in the model was found to move more slowly and to have a lesser convective intensity than the observed system was attributed to this lack of stratiform precipitation and thermodynamic forcing.

Caniaux et al. (1994, hereafter CRL94; 1995, hereafter CLR95) employed a two-dimensional version of the model for anelastic deep convection which was described by Redelsperger and Sommeria (1986) to simulate the 23-24 June, 1981, COPT81 tropical squall line system. The simulations presented in CRL94 were found to agree well overall and in detail with Doppler radar observations of this system presented by Chalon et al. (1988), while the simulations of this system presented in CLR95 were oriented more toward an explanation of scale and regional interactions within the squall line system. In CLR95, it was found that inclusion of ice phase thermodynamics and microphysics was essential in the

proper simulation of the trailing stratiform region of the squall line system. The simulation of convective motions well behind the leading convective line in these experiments and in other COPT81 case studies support the idea that persistent convective cells may become embedded in the trailing stratiform region of the tropical squall line system.

Liu et al. (1997, hereafter LMZ97) successfully simulated the 22-23 June and 23-24 June, 1981, COPT81 squall line systems. Using a nonhydrostatic anelastic cloud model, described by Clark and Farley (1984) and Clark and Hall (1991), in LMZ97 it was found that the inclusion of ice phase thermodynamics and microphysics was of marginal importance in the proper simulation of the overall squall line system dynamics, and was also of little importance in dynamics on the convective scale, in an atmosphere which was already strongly unstable to convection. However, for an environment which is weakly unstable and is nearly saturated in the lowest levels, the inclusion of ice phase thermodynamics and microphysics is highly important in the proper simulation of the convective regions of the tropical squall line system.

2.5.2 Maritime Squall Line System Simulations

Table 2.2 outlines several efforts in the modeling of maritime squall line systems. The simulation of maritime tropical squall lines has generally been focused on systems observed during Phase III of GATE, which was based in the eastern Atlantic Ocean during the summer of 1974. Although only six squall-type convective lines were observed during this period, very few have been examined in greater detail than the 4-5 September and 12 September, 1974, systems. Analyses of the earlier of these two systems can be found in LH79, GH83, and JN83. The latter of these systems has been analysed in H77 and LH79.

Early models of maritime tropical squall line systems focused on the GATE system of 12 September, 1974. Yoshizaki (1986, hereafter Y86) employed mixed-phase thermodynamics and microphysics in an original two-dimensional model to simulate the convective

Table 2.2: Several modeling efforts for maritime squall line systems. In the descriptions of model grid spacing, (s) denotes a mathematically stretched grid spacing, (v) denotes an otherwise varied grid spacing, (e) denotes an experiment-dependent grid spacing which is constant within the experiment, and (n) denotes nested grids of constant spacing in the appropriate direction.

Model	2D	3D	grid spacing	microphysics	initial conditions
GATE squall line systems					
Y86	•		$\Delta x = 0.5 - 8.0$ km (s) $\Delta z = 100 - 500$ m (s)	mixed phase	12 September, 1974 composite sounding
N87, NJC88	•		$\Delta x = 0.5$ km $\Delta z = 350 - 900$ m (v)	mixed phase	12 September, 1974 composite sounding
NW88	•	•	$\Delta x = 0.5 - 1.0$ km (e) $\Delta z = 350 - 1000$ m (v)	mixed phase	12 September, 1974 composite sounding
TS89	•	•	$\Delta x, y = 1.0 - 1.5$ km (e) $\Delta z = 200 - 1000$ m (s)	mixed phase	composite of GATE squall systems
CFBM95	•		$\Delta x = 1.5 - 115$ km (s) $\Delta z = 200 - 600$ m (s)	mixed phase	4 September, 1974 06 UTC sounding
CW98		•	$\Delta x, y = 1.5$ km $\Delta z = 100 - 700$ m (s)	warm rain	3-4 September, 1974 various soundings
TOGA COARE squall line systems					
TSLPJ96		•	$\Delta x, y = 1 - 9$ km (n) $\Delta z = 100 - 700$ m (s)	mixed phase	February 1993 composite sounding

and stratiform regions of this system. The results presented in Y86 display squall line system features similar to those described in Z77 and H77, presented here in Figure 2.7, and discussed in detail above. Nicholls (1987, hereafter N87) simulated the same squall line system in a two-dimensional framework using the Colorado State University Regional Atmospheric Modeling System (RAMS), which employs a nonhydrostatic compressible system of dynamical and thermodynamical equations along with an extensive set of microphysical equations for the treatment of mixed phase cloud and precipitation droplets. Nicholls et al. (1988, hereafter NJC88) began with the model and initial conditions employed in N87 and performed experiments to determine the sensitivity of the two-dimensional squall line system to changes in initial wind and thermodynamic profiles. The results discussed in NJC88 were consistent with those presented in RKW88 with regard to the existence of an optimum level and magnitude of vertical shear which allows for a long-lived system, and

demonstrate the importance of mid-level moisture, found often in tropical environments but seldom in the environments of midlatitude systems, in the maintenance of convective updraft strength, the formation of convective downdrafts, and the evolution of the low-level cold pool.

Several discrepancies between the two-dimensional simulations presented in N87 and the observed tropical squall line system were discussed in NJC88, and include simulated features such as greater tropospheric warming due to compensating subsidence ahead of the leading convective line, a more shallow tilt of the leading convective line, weaker convective updrafts, a persistent warm layer in the mid-levels of the stratiform region, a weaker mesoscale downdraft structure in the trailing stratiform region, and comparatively low liquid water contents throughout the system. Nicholls and Weissbluth (1988, hereafter NW88) employed RAMS to compare two-dimensional and three-dimensional simulations of the same 12 September, 1974, GATE tropical squall line system. In this three-dimensional framework, called "quasi-three-dimensional" in NW88, the along-line axis (y) was just long enough to accomodate a single large convective cell, but incorporated cyclic boundary conditions to produce a seemingly infinite distance along the resulting squall line. Locally, i.e. within the experimental domain, convective motions could be expected to exhibit fully three-dimensional character in this framework. It was noted in NW88 that the simulations presented in N87 may have included convective motions embedded in the stratiform region which were exaggerated in comparison with the observations. This exaggeration may have been due to a lack of convergence in other parts of the stratiform region which are typically included in a three-dimensional simulation. In NW88 it was also noted that the earlier two-dimensional simulations could not account for inflow between laterally adjacent cells in the convective line to the transition and trailing stratiform regions, as observed by Betts et

al. (1976) and in Z77.

Tao and Simpson (1989, hereafter TS89) employed a composite squall-type system environment and a cloud ensemble model derived from those described by Soong and Ogura (1980), Soong and Tao (1980), and Tao and Soong (1986) to simulate the overall structure and dynamics of tropical squall line systems. In TS89, it was found that ice phase thermodynamics and microphysics were crucial to the accurate simulation of the trailing stratiform precipitation region, in agreement with the conclusions presented in Y86, N87, and FO88. It was also found in TS89 that the stratiform region was better reproduced in two-dimensional simulations than in three-dimensional simulations, due to a smaller domain and shorter time integrations for the latter experiments. Both two- and three-dimensional experiments accurately reproduced the initiation of new convective cells on the cold pre-squall convective outflow boundary, as well as the discrete propagation of the squall line system.

Chin et al. (1995, hereafter CFBM95) improved upon the model presented by Chin and Ogura (1989) and utilized a 06 UTC 4 September, 1974, sounding from the northeast corner of the GATE region to simulate the 4-5 September, 1974, GATE squall line system. In addition to using a warm bubble for the initiation of convection, a large-scale forcing was employed in CFBM95 which lifted a large region of the atmosphere to near-saturated conditions in order to initiate and sustain the deep convection required for squall line formation. A similar theory was discussed by Mapes (1993), in which deepening of the boundary mixed layer by convergence of heat and moisture over a large area supported sustained deep tropical convection. However, in CFBM95 it was suggested that this saturation forcing by large-scale lifting precludes the need for mechanical lifting by the convective outflow to maintain the convective system. While gregarious tropical convection and tropical convective complexes with little degree of linear organization, such as those described by

Nakajima and Matsuno (1988) and by Mapes (1993), may thrive with such a background forcing mechanism, the dismissal in CFBM95 of the commonly-observed and extensively-studied squall line convective outflow as a necessary mechanism of convective initiation and squall line propagation is somewhat suspect.

Chin and Wilhelmson (1998, hereafter CW98) employed a three-dimensional version of the model presented by Chin and Ogura (1989), as well as various GATE soundings prior to the time of the 4-5 September, 1974, GATE squall line system, to investigate the properties of individual squall line convective cells. Since the squall line stratiform region was not a focus of these experiments, only warm rain thermodynamics and microphysics were employed. Futhermore, possibly in consideration for the low latitude of the GATE region, Coriolis accelerations were not included in the simulations presented in CW98. In addition to using a large-scale saturation forcing similar to that employed in CFBM95, a low-level convergence line similar to that observed by Ogura et al. (1979) prior to this system was employed to initiate convection. The resulting convective systems presented in CW98, however, resembled right- and left-moving midlatitude supercell-like systems, with associated rotating updrafts, which displayed eventual cell merger episodes as well as system decay for lack of a multicell-related mechanism of discrete propagation.

Few modeling efforts oriented toward the more recent TOGA COARE field experiment have appeared in the literature as yet. Most notably, Trier et al. (1996, hereafter TSLPJ96) performed both warm rain and mixed-phase experiments with a three-dimensional model which accurately reproduced the general features of the same 22 February, 1993, TOGA COARE squall line system which was later examined in JLT97. In TSLPJ96, it was found that ice microphysics and surface fluxes were not necessary for an adequate simulation of the gross features of a maritime tropical squall line system, but that

the thermodynamic effects of these processes greatly enhance the accuracy of simulation in reproduction of low-level cold pools and in the evolution of the squall line system altogether. While most other modeling efforts concentrated on the importance of ice-phase thermodynamics and microphysics in the formation and maintenance of the trailing stratiform region, it was found in TSLPJ96 that the inclusion of ice processes produced more realistic convective updraft strengths and maximum heights, likely through enhanced latent heating which occurs on the freezing of cloud and precipitation droplets at middle levels in the convective updrafts.

Chapter 3

A TWO-DIMENSIONAL, PRIMITIVE EQUATION MODEL

A summary is presented here detailing developments which led to the publication by Ooyama (1995, 1997) of a nested, two-dimensional, nonhydrostatic numerical model of the atmosphere which employs the primitive equations and explicit, mixed-phase, moist thermodynamics with precipitation. This brief history is followed by a description of the dynamic, thermodynamic, microphysical and selected numerical constructs employed in the model. For ease of reference, a complete listing of all variables employed here is included in Appendix C. An abbreviated assessment of model accuracy in the simulation of a tropical squall line system was presented by Ooyama (1995, hereafter O95), and more detailed results were presented following larger-scale experiments by Ooyama (1997, hereafter O97). This assessment of model accuracy in relation to observed tropical squall line system characteristics will be expanded here with particular attention to the review of observation and simulation studies presented in Chapter 2. Detailed conclusions will be drawn regarding the accuracy of this model in high-resolution simulations of tropical squall line systems, followed by a discussion of the applicability of this model to variable-scale dynamic processes, especially the numerical representation of moist convection on finer scales than in previous experiments with this model.

3.1 Historical Background

In early work, Ooyama (1969a) presented a simulation of the life cycle of a balanced, axisymmetric tropical cyclone. In the position of that thesis, Ooyama considered that moist convection presented major challenges in the consistency and accuracy of numerical methods, which are quite necessary in the study of dynamics in convective systems. Despite these challenges, Ooyama concluded that some effort must be made to include the effects of moist thermodynamics and cumulus clouds, since without these processes the tropical cyclone would not exist. In the simulations presented by Ooyama (1969a), an original parameterization of moist convection was developed. This parameterization was an approximation which, under the contemporary temporal and physical constraints of computing resources, could reasonably be substituted for a complete examination of explicit moist thermodynamics. During this work, Ooyama also recognized that conflicts may arise between the available resolution of numerical models and the scales of dynamical interest, especially in the accurate representation of smaller-scale cumulus convection processes and larger-scale dynamic features in a single consistently-formulated numerical model. Under these considerations, cumulus parameterization was a reasonable solution at the time, but was still only an approximation of important and still interesting convective-scale processes.

Ooyama (1969b) presented an updated version of the balanced axisymmetric model detailed by Ooyama (1969a), including an unbalanced treatment of winds in the boundary layer based on the original primitive equations. Although results of the updated model were considered better than those of the earlier version, the conclusions reached by Ooyama lent support to other axisymmetric models of contemporary researchers (Syōno and Yamasaki, 1966; Yamasaki, 1968) which fully employed the primitive equations of motion instead of a hybrid, or mixed-balance, model formulation.

Calculation of detail in individual clouds for any large-scale model was severely limited by the availability of resources for some time during the technological development of digital computers. For the explicit models available, desired spatial resolutions would have required an increase of time resolution so as to make the models far too impractical for their limited increases in accuracy. Ooyama (1971) proposed a theoretical, hydrostatic model for further tropical cyclone simulations which included significantly more moist thermodynamic considerations than previous methods. By this cumulus parameterization method the vertical transport effects of cumulus convection, including entrainment and detrainment, were included in the large-scale model. However, this method was eventually superceded in general use by the Arakawa-Schubert method of cumulus parameterization (Arakawa and Schubert, 1974), and was never employed by Ooyama in a numerical model for the simulation of tropical cyclones.

Through a continued commitment to the improvement of high-resolution numerical modeling, a conceptual model of the tropical cyclone life cycle was developed by Ooyama (1982) which included a brief discussion of cyclogenesis processes as well as discussions of convective-scale thermodynamic processes and large-scale dynamics. However, numerical modeling of these important processes in the life cycle of a tropical cyclone remained limited by computing resources, as well as by the formulation of viable and economical mathematical representations for these processes. Although numerical modeling of tropical cyclogenesis has yet to culminate, simulations of the growth, mature, and dissipating phases of tropical cyclone systems have advanced considerably.

A method of numerical construction for models was proposed by Ooyama (1984) which employed specific finite elements of physical representation in a framework of spectral transforms on nested horizontal domains. This method was further developed by Ooyama

(1987, hereafter O87) for use in the representation of irregularly distributed data, notably from the GATE field experiment, within a finite domain. The refinement of domain nesting capabilities for this framework advanced its applicability in the simulation of dynamical systems which span a range of physical scales, and finally the method based on Spectral Application of Finite Element Representation (SAFER) was applied by Shapiro and Ooyama (1990), using an explicit method of time integration, to a simulation of the two-dimensional evolution of a tropical cyclone-like vortex in a barotropic environment.

In related work, Ooyama (1989, 1990) proposed the separation of dynamics and thermodynamics in model formulation, such that each could be treated in their "primitive" forms without parameterizations on the scales of moist convection or larger-scale processes. Although pressure gradients are a driving mechanism in the primitive equations of motion, by this method the prognostic equations would be applied through the use of purely conservative variables, which do not include pressure itself. The pressure would then be diagnosed by thermodynamic calculations which employ the conservative variables as their input, followed by the diagnosis of local pressure gradients for feedback into the dynamic prognostic equations. Although this separation of processes was intended to simplify the theoretical structure of numerical models, consideration of explicit moist thermodynamics in such a model added numerical complexity in the number of variables to be accounted. Ooyama (1990) explored only reversible moist thermodynamic processes in equilibrium, neglecting irreversible precipitation processes.

Ooyama (1991) synthesized these numerical, dynamic and thermodynamic advances, as well as the semi-implicit method of time integration (Robert, 1969) to allow longer time steps than acoustic waves normally allow, in a one-dimensional test of this method for the accurate thermodynamic calculation of pressure. In O95, the thermodynamic model struc-

ture was extended to include microphysical processes for precipitation in the liquid and ice phases, and the physical domain became two-dimensional for a vertical plane representation of the system environment. Simulations presented in O95 employed composite West Indies (Caribbean) soundings compiled by Jordan (1958), as well as variations of that profile in the temperature and moisture structure for experimental purposes. As a larger-scale test, this two-dimensional nonhydrostatic quasi-spectral numerical model, employing semi-implicit methods of time integration on multiple interactive nested domains, was applied to the simulation of a long-lived tropical squall line system. In O95 it was concluded that results produced by this model "generally" agreed with observational and theoretical results presented in RKW88. The model domain was expanded and capabilities for nesting of multiple domains became more refined for the simulations presented in O97, which "more convincingly depicted" near-surface precipitation and cold pool dynamics. However, for more accurate representation of tropical squall line system structures discussed in Chapter 2, greater spatial resolution than the experiments presented in O95 and O97 will be required.

3.2 Model Description

3.2.1 Prognostic Equations: Applied Formulation

A moist air parcel will include dry air and some amount of moisture, which theoretically may be treated separately. The airborne moisture includes water vapor and condensate, which are assumed to move with the air without form drag or other resistance, and precipitation, which falls through the advective flow. Thus, the total mass density of moist air is

$$\rho = \rho_a + \rho_m + \rho_r \tag{3.1}$$

for which ρ_a, ρ_m, and ρ_r are the densities of dry air, airborne moisture (vapor and airborne condensate), and precipitation, respectively. Correspondingly, the entropy density σ is

$$\sigma = \rho_a s_a + \rho_m s_m + \rho_r s_r, \tag{3.2}$$

the density-weighted sum of the specific dry air entropy, s_a, the specific airborne moisture entropy, s_m, and the specific precipitation entropy, s_r, all of which are defined thermodynamically.

As presented in O95 and O97, the six prognostic equations for this model, in flux form, include two momentum equations, three mass conservation equations for dry air, airborne moisture and precipitation, and one equation for the total entropy:

$$\partial_t(\rho u) + \partial_x(\rho u u) + \partial_z(\rho u w) + \partial_x p = D_{\rho u}, \tag{3.3}$$

$$\partial_t(\rho w) + \partial_x(\rho w u) + \partial_z(\rho w w) + \partial_z p + \rho g = D_{\rho w}, \tag{3.4}$$

$$\partial_t \rho_a + \partial_x(\rho_a u) + \partial_z(\rho_a w) = D_{\rho_a}, \tag{3.5}$$

$$\partial_t \rho_m + \partial_x(\rho_m u) + \partial_z(\rho_m w) = -Q_r + D_{\rho_m}, \tag{3.6}$$

$$\partial_t \rho_r + \partial_x(\rho_r u) + \partial_z\left[\rho_r(w + w_r)\right] = Q_r + D_{\rho_r}, \tag{3.7}$$

$$\partial_t(\sigma) + \partial_x(\sigma u) + \partial_z(\sigma w) + \partial_z(\rho_r s_r w_r) = D_\sigma, \tag{3.8}$$

for which ∂_i is the partial derivative with respect to the independent variable i, w_r and Q_r are the terminal fall speed of precipitation and the source term for precipitation, both of which will be defined through bulk microphysical parameterizations in Section 3.2.3, and D_j represents computational sources or sinks of the quantity j, which may be analogous to a subgrid-scale diffusive term or other non-conservative processes.

In an hydrostatic model, the terms $\partial_z p$ and ρg in the equation of vertical motion would be the only terms retained for the determination of altitude on a given pressure

surface or pressure at a given altitude. In a general form, the hydrostatic equation may be written as

$$\epsilon \equiv \partial_z p + g\rho, \tag{3.9}$$

for which, if a parcel is indeed in hydrostatic balance, $\epsilon = 0$. The use of hydrostatic balance in dynamic models requires maintenance of this balance throughout the period of prediction, such that $\partial_t \epsilon = 0$ with $\epsilon = 0$ as an initial condition. This formulation was explored in great detail by DeMaria (1995). The imposition of hydrostatic balance would replace the original prognostic equation for vertical velocity (3.4), leading to the determination of vertical motion diagnostically through prediction of the horizontal motion and knowledge of the temporal and spatial distribution of entropy and pressure. Since neither this analysis, nor those in O95 and in O97, considers a system in which strict hydrostatic equilibrium is prescribed, the reader is referred to Ooyama (1990) and DeMaria (1995) for further details on the application of and problems with hydrostatic equilibrium in the present numerical model.

3.2.2 Thermodynamic Formulation

Using values of ρ_a, ρ_m, ρ_r, and σ for a point in space, found by the prognostic equations above, the total pressure p, temperature T and the related quantities p_a, p_v, ρ_v, and ρ_c for a parcel of moist air with precipitation can then be determined.

Basic assumptions

It is assumed that this analysis is applied to a moist parcel which is small enough to assume thermodynamic homogeneity and equilibrium. Both dry air and water vapor are treated as ideal gases without mutual interference within the volume. The volume of con-

densate is considered negligible compared to the volume of dry air and water vapor in the parcel, and may therefore also be excluded from the assumption of thermodynamic homogeneity. The effects of condensate surface geometry and the presence of cloud condensation nuclei and dry air on the vapor pressure are also thus ignored, such that the saturation vapor pressure is defined as a function only of the temperature and will be discussed below.

Total airborne moisture density is the sum of vapor and airborne condensate densities:

$$\rho_m = \rho_v + \rho_c. \tag{3.10}$$

The total pressure is the sum of partial pressures for dry air and water vapor in the fixed-volume parcel:

$$p = p_a + p_v. \tag{3.11}$$

The equations of state for dry air and water vapor follow the Ideal Gas Law:

$$p_a = \rho_a R_a T, \tag{3.12}$$

and

$$p_v = \rho_v R_v T. \tag{3.13}$$

The Clausius-Clapeyron equation is considered as the definition of the latent heat of vaporization for water, $L(T)$, by

$$\frac{dE(T)}{dT} = \frac{L(T)E(T)}{R_v T^2}, \tag{3.14}$$

while the Kirchhoff equation is considered as the definition of the specific heat of condensate, $c_c(T)$, by

$$\frac{dL(T)}{dT} = c_{pv} - c_c(T), \tag{3.15}$$

for which $c_c(T)$ remains a function of temperature due to consideration of ice-phase condensate. The specific heats of dry air are related by

$$c_{pa} = c_{va} + R_a, \tag{3.16}$$

while the specific heats of vapor are related by

$$c_{pv} = c_{vv} + R_v. \tag{3.17}$$

The saturation vapor pressure of moist air over a plane surface of water in units of hPa, $E_w(T)$, is calculated using the Goff-Gratch formula (List, 1949):

$$\begin{aligned} \log_{10} E_w(T) &= -7.90298\left(\tfrac{T_b}{T} - 1\right) + 5.02808\log_{10}\left(\tfrac{T_b}{T}\right) \\ &\quad -1.3816\times 10^{-7}\left(10^{11.344\left(1-\frac{T}{T_b}\right)} - 1\right) \\ &\quad +8.1328\times 10^{-3}\left(10^{-3.49149\left(\frac{T_b}{T}-1\right)} - 1\right) + \log_{10} p_b, \end{aligned} \tag{3.18}$$

for which $T_b = 373.16$ K and $p_b = 1013.246$ hPa at the boiling point for water. The saturation vapor pressure of moist air over a plane surface of ice, $E_i(T)$, is calculated using

$$\begin{aligned} \log_{10} E_i(T) &= -9.09718\left(\tfrac{T_t}{T} - 1\right) - 3.56654\log_{10}\left(\tfrac{T_t}{T}\right) \\ &\quad +0.876793\left(1 - \tfrac{T}{T_t}\right) + \log_{10} p_t, \end{aligned} \tag{3.19}$$

for which $T_t = 273.16$ K and $p_t = 6.1071$ hPa at the triple point for water. These formulas are widely accepted for highly accurate pure thermodynamic calculations of saturation vapor pressure, but are not often used in high resolution numerical models because of their computational inefficiency. For the purposes considered here, vapor pressure "lookup tables" are pre-calculated in the initiation of the numerical model, such that later use in calculation is speeded considerably.

Entropy, temperature and pressure

For a given set of predicted values $(\rho_a, \rho_m, \rho_r, \sigma)$ for a parcel, or in this case a grid volume, at a particular time, two different temperatures may be found depending on the presence of condensate in the volume. The calculation of entropy density for a parcel is given by (3.2). For a parcel in which condensation has occurred, at which temperature the

parcel is also considered marginally saturated and in liquid-vapor (or ice-vapor) equilibrium, the entropy density is given by

$$\sigma = \rho_a c_{va} \ln\left(\frac{T_2}{T_0}\right) - \rho_a R_a \ln\left(\frac{\rho_a}{\rho_{a0}}\right) + \rho_m C(T_2) + D(T_2). \tag{3.20}$$

The entropy of a unit mass of condensate at a particular temperature, $C(T)$, can be shown to be

$$\begin{aligned} C(T) = \int_{T_0}^{T} \frac{c_c(T)}{T} dT &= c_{pv} \ln\left(\frac{T}{T_0}\right) - R_v \ln\left[\frac{E(T)}{E_0}\right] - \Lambda(T) + \Lambda_0, \\ &= c_{vv} \ln\left(\frac{T}{T_0}\right) - R_v \ln\left[\frac{\rho_*(T)}{\rho_{*0}}\right] - \Lambda(T) + \Lambda_0 \end{aligned} \tag{3.21}$$

for which $T_0 = 273.15\text{K}$ is the reference temperature, $E_0 \equiv E(T_0)$, $\rho_{*0} \equiv \rho_*(T_0)$, and $\Lambda_0 \equiv \Lambda(T_0)$. The density of vapor in a saturated parcel, $\rho_*(T)$, can be found from the equation of state for vapor as

$$\rho_*(T) \equiv \frac{E(T)}{R_v T}. \tag{3.22}$$

The increase of entropy of a parcel due to the evaporation of a unit mass of water at a particular temperature, $\Lambda(T)$, can be derived from the Clausius-Clapeyron equation and is found to be

$$\Lambda(T) \equiv \frac{L(T)}{T} = R_v T \frac{d[\ln E(T)]}{dT}. \tag{3.23}$$

The increase of entropy of a parcel due to the evaporation of enough water to saturate the parcel at a particular temperature, $D(T)$, is defined as

$$D(T) \equiv \rho_*(T)\Lambda(T) = \frac{dE(T)}{dT}. \tag{3.24}$$

In models involving moisture and condensation processes, the ice phase of water is commonly ignored in order to simplify the model thermodynamics. As explained in the previous chapter, models which exclude ice phase thermodynamic and microphysical processes are commonly called "warm rain" models, while models which do include such processes

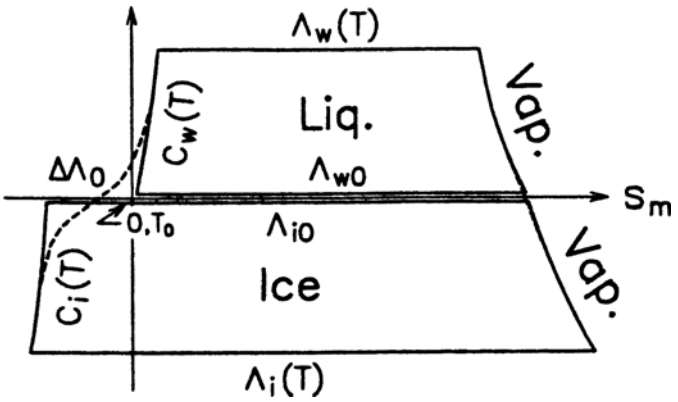

Figure 3.1: Ooyama (1990), Figure 1.

are considered "mixed phase" models. In mixed phase models, highly involved parameterizations are commonly employed to take the frozen precipitation into account. At this point in the theoretical development, Ooyama proposed a synthesis of precipitation phases by an adjustment of the thermodynamic behavior of water, such that a single condensate is produced which takes on the properties of water above a freezing temperature and the properties of ice below that temperature. For this hypothetical condensate, the freezing temperature is prescribed by the modeler, as is the width of the "freezing zone" of temperatures through which the condensate makes a smooth transition between water and ice properties. Instead of using a direct synthesis of $E_w(T)$ and $E_i(T)$ to derive the entropy functions needed for calculation of temperature and pressure, which would require more assumptions and explicit microphysical considerations than are economically feasable, an anomaly of the specific heat of the assumed condensate is considered as the basis of this synthesis. Figure 3.1, reproduced here from Ooyama (1990), shows the integrated forms of the Kirchhoff equation graphically. In this figure, a proper synthesis of the solid and liquid states for the hypothetical condensate would be represented by the dashed curve. It is the goal of formulating the hypothetical condensate to reproduce this dashed curve as

accurately as possible.

The synthesis of condensate states (liquid water and ice) is performed directly on $C(T)$ from (3.21) as an hyperbolic smoothing function, such that

$$C(T) \equiv \Omega_w(T) C_w(T) + \Omega_i(T) C_i(T) \tag{3.25}$$

for which

$$\left.\begin{aligned} \Omega_w(T) &\equiv \tfrac{1}{2}\left[1 + \tanh\left(\tfrac{T-T_f}{\Delta T_f}\right)\right], \\ \Omega_i(T) &\equiv 1 - \Omega_w(T), \end{aligned}\right\} \tag{3.26}$$

where ΔT_f is the prescribed temperature range of the freezing zone and T_f is the prescribed central temperature of that range. The smoothing coefficients are functions of temperature only, so as to reduce the number of assumptions or other factors which may influence the derivation of the synthesized $C(T)$. Equation (3.25) is then used in (3.21), and the resulting expression produces a synthesized $E(T)$, using the reference state of liquid water to avoid ambiguity in the use of state variables, as

$$\frac{d}{dT}\left[T \ln\left(\frac{E(T)}{E_{w0}}\right)\right] = \Omega_w(T)\frac{d}{dT}\left[T \ln\left(\frac{E_w(T)}{E_{w0}}\right)\right] + \Omega_i(T)\frac{d}{dT}\left[T \ln\left(\frac{E_i(T)}{E_{i0}}\right)\right]. \tag{3.27}$$

Integration of this equation requires only one boundary condition, at higher temperatures, where a condition is imposed by which the vapor pressure of the synthesized condensate approaches that of pure water at the same temperature, or $E(T) \to E_w(T)$ for $T \gg T_f$, for which the temperature T may be set at a high value since $E(T)$ and $E_w(T)$ converge rapidly by this method. Imposition of a lower boundary condition at $T < T_f$ is neither required nor allowed due to natural convergence of $E(T)$ to $E_i(T)$ at subfreezing temperatures. Outside the smoothing zone, the vapor pressure behaves as it is calculated by the Goff-Gratch formulas, while inside the zone specified by T_f and ΔT a smooth transition in $E(T)$ and $C(T)$ between the water and ice phases occurs. Figure 3.2, reproduced from Ooyama (1990), shows this smoothed function.

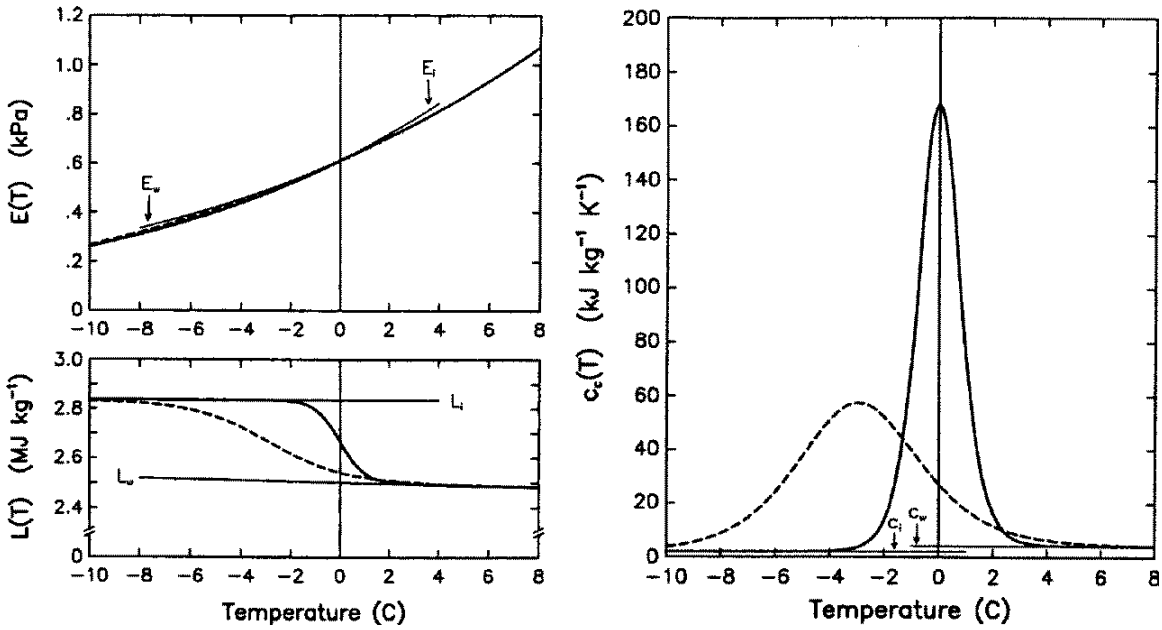

Figure 3.2: Ooyama (1990), Figures 2 and 3.

Once the synthesized $E(T)$ is obtained, the thermodynamic functions $C(T)$, $D(T)$, and others introduced here which are functions of $E(T)$ are redefined for the synthesized condensate without additional modifications or assumptions. For a model which includes precipitation processes, the precipitating water must then be excluded from the parcel in order to find the alternate non-condensate state. The specific entropy for a parcel which may contain precipitation and is otherwise unsaturated, marginally saturated, or supersaturated as long as no cloud droplet condensate is present, is then

$$\sigma = (\rho_a c_{va} + \rho_m c_{vv}) \ln\left(\frac{T_1}{T_0}\right) - \rho_a R_a \ln\left(\frac{\rho_a}{\rho_{a0}}\right) - \rho_m R_v \ln\left(\frac{\rho_m}{\rho_{*0}}\right) + \rho_m \Lambda_0 - \rho_r s_r(T_2), \quad (3.28)$$

in which the last term represents the exclusion of precipitation from the parcel.

In application, the order of computation is (3.20) before (3.28), such that T_2 is calculated first. Then (3.28) is solved explicitly for T_1. Equation (3.20) is a more complicated function, however, such that prepared tables of $C(T)$ and $D(T)$ are used to facilitate the calculation of T_2. In both cases, prepared tables of $E(T)$ for water and ice are employed to

speed the computation.

To determine which of the calculated temperatures, T_1 or T_2, represents the proper parcel conditions, we must consider the assumptions under which each function was derived and would therefore apply. For a parcel in which no cloud droplet condensation has occurred but precipitation may be present, (3.28) is valid. If the calculated T_1 satisfies the condition $\rho_m \leq \rho_*(T_1)$, the parcel is correspondingly unsaturated or marginally saturated, and T_1 is considered the actual parcel temperature. If $\rho_m > \rho_*(T_1)$, the parcel is supersaturated and a conflict arises: although supersaturation does indeed occur in the atmosphere as a metastable state, only equilibrium thermodynamics is considered here, eliminating the possibility for supersaturation to persist. Any disturbance of the parcel would expose the tendency of the air toward condensation of excess vapor until liquid-vapor equilibrium and marginal saturation are reached, in which case the calculated temperature T_2 is the correct temperature of the parcel. This condensation of excess vapor releases latent heat into the parcel, causing T_2 to be greater than T_1 for the same set of conditions $(\rho_a, \rho_m, \rho_r, \sigma)$.

The conditions assumed in the derivation of (3.20) included marginal vapor saturation, or $\rho_v = \rho_*(T_2)$. If the calculated temperature T_2 satisfies the condition $\rho_m \geq \rho_*(T_2)$, then T_2 is considered the actual parcel temperature, since the parcel also contains condensate in the amount $\rho_c = \rho_m - \rho_*(T_2)$. If, however, $\rho_m < \rho_*(T_2)$, the apparent negative condensate represents the amount of water which must be evaporated for the parcel to reach marginal saturation. For this unsaturated state, (3.28) represents the correct function for the calculation of temperature, and the use of (3.20) demonstrates that evaporation of water removes heat from the parcel, causing a lesser T_2 than the corresponding T_1 for the same parcel. By this reasoning, T_2 maintains physical significance for the unsaturated parcel as the wetbulb temperature of the air. It is for this reason that the entropy of the precipitation

in (3.28) is considered at T_2, the temperature of the water in the parcel, instead of at T_1, the temperature of the air itself.

Therefore, it may be stated that the correct temperature for a parcel is the greater of T_1 and T_2. If, after calculation of both states and selection of the proper temperature, $T_1 > T_2$, the parcel is considered unsaturated: $T = T_1$, $\rho_v = \rho_m$, $\rho_c = 0$, and the partial pressure of vapor in the parcel may be calculated by (3.13). If, however, $T_2 > T_1$, the parcel is saturated: $T = T_2$, $\rho_v = \rho_*(T)$, $\rho_c = \rho_m - \rho_v$, and $p_v = E(T)$. If $T_1 = T_2$, the parcel could be considered marginally saturated, and the calculations of ρ_v, ρ_c and p_v by both methods would produce identical results. The total pressure is then calculated by (3.11), using (3.12) and (3.13) for the partial pressures of dry air and water vapor, respectively, in the parcel. For use in the dynamical equations, pressure gradients are then calculated by a spectral transform method which employs the finite element representation discussed earlier.

3.2.3 Microphysical Formulation

For the above prognostic equations, the microphysical quantity Q_r is defined by

$$Q_r = Q_{auto} + Q_{col} + Q_{evap}. \tag{3.29}$$

Due to their complexity, these irreversible microphysical processes of autoconversion to, collection of, and evaporation of falling precipitation typically require parameterizations of some form. For these, in O95 and O97 the microphysical parameterizations developed in KW78 were selected. By this parameterization method, the components of Q_r are given by:

$$Q_{auto} = \begin{cases} 0.001(\rho_c - 0.001\rho_a) & \text{if } \rho_c > 0.001\rho_a \ , \\ 0 & \text{if } \rho_c \leq 0.001\rho_a \ , \end{cases} \tag{3.30}$$

$$Q_{col} = 2.20\rho_c \left(\frac{\rho_r}{\rho_a}\right)^{0.875}, \tag{3.31}$$

$$Q_{evap} = \frac{f_{vent} \cdot [\rho_*(T) - \rho_v]\, \rho_r^{0.525}}{\left[2.03\rho_*(T) + \frac{3.337}{T}\right] \cdot 10^4}, \tag{3.32}$$

for which the ventilation factor is defined by

$$f_{vent} = 1.6 + 30.39\rho_r^{0.2046}, \tag{3.33}$$

and for which ρ_* is again the saturation vapor density. If $\rho_m - \rho_*(T)$ is found to be negative, indicating a subsaturated state, all of the microphysical quantities are set to zero in the model calculations. The terminal fall speed of water or ice precipitation is defined by

$$w_r = -f_{ice} \cdot 14.164\rho_r^{0.1364} \left(\frac{\rho_{a0}}{\rho_a}\right)^{0.5}, \tag{3.34}$$

for which f_{ice}, which accounts for reduced terminal velocities of frozen precipitation, is given by

$$f_{ice} = \begin{cases} 0.2 + 0.8 \text{ sech}\left(\frac{T_0 - T}{5.0}\right) & \text{if } T < T_f \text{ ,} \\ 1.0 & \text{if } T \geq T_f \text{ ,} \end{cases} \tag{3.35}$$

for which, again, T_f is the freezing zone central temperature specified by the model user.

3.2.4 Methods of Numerical Integration

In O95 and in O97, an extended version of the SAFER method of numerical representation was employed. The development of the SAFER method can be traced through several steps. After its introduction by Ooyama (1984), refinements in data assimilation made the method suitable for use as an objective analysis tool by Franklin et al. (1985) and in O87. The SAFER method was first employed in prognostic modeling efforts by Shapiro and Ooyama (1990), and was later used for the analysis and forecasting of hurricane tracks by DeMaria et al. (1992, hereafter DAOL92). After further testing along with the thermodynamic structure discussed earlier by Ooyama (1991), the SAFER method was

finally applied to the two-dimensional single-domain model presented in O95 and in its multiple-domain version presented in O97.

The user of this model is given a choice of two explicit methods of time integration: the three-level Leapfrog scheme with an initial Euler step, or the three-level Adams-Bashforth scheme of second-order accuracy, also with an initial Euler step. The Euler method, also known as the Forward method, is a first-order Adams-Bashforth scheme. This method has been found to be absolutely unstable for extended periods of time integration (Mesinger and Arakawa, 1976), despite its lack of a computational mode of solution as a two-level scheme. However, the Euler method has been found to be quite useful for single time steps in conjunction with three-level schemes which do exhibit a computational mode of solution. While the three-level second-order Adams-Bashforth scheme provides some advantage, such as a damped computational mode, over the Leapfrog scheme for time integrations past time $t = 1\Delta t$, the Leapfrog scheme provides a desirable neutral physical mode and a slightly less desirable neutral computational mode. Although the damped computational mode of the second-order Adams-Bashforth scheme is expected to remove its own effects over a short period within the time integration, the physical mode of the second-order Adams-Bashforth scheme is weakly unstable, leading to amplification of the discrete solution with time. This instability has been demonstrated in unpublished simulations formulated by Ooyama which test the sensitivity of several numerical parameters. Several of these experiments were discussed briefly in O97, and corresponding results will be examined later in this analysis.

As mentioned above, the Leapfrog scheme for time integrations exhibits a neutral computational mode. This neutral mode has been found to cause the complete solution to oscillate on successive time steps. While the magnitude of oscillation may not increase significantly past a certain point in time, it is still undesirable. The oscillating computational

mode of the Leapfrog scheme is commonly treated in one of two ways in order to maintain accuracy over long periods of time. One method of treatment involves the use of a two-level time integration scheme, such as the Euler scheme as explained above, for a single time step at predetermined intervals in the time integration, effectively eliminating the computational mode and its oscillations in that step. After a two-level step, the time integration proceeds using the normal three-level scheme until another designated point at which the two-level scheme is again applied to remove the computational oscillations which have accumulated over that interval. Another method of treatment for the oscillating computational mode of the Leapfrog scheme involves numerical filtering, effectively combining the results of successive time steps in a weighted average. This latter method has been selected by Ooyama, for which a Robert-Asselin time filter (Asselin, 1972) was chosen. This construct acts as a low-pass filter, removing signals of high frequency such as the computational mode which causes the solution of the nonlinear equations of motion to oscillate on alternating time steps. The filter is employed by Ooyama with a typical Asselin (weighting) parameter of $\nu = 0.3$, well below the value of $\nu = 0.5$ beyond which stability of the solution decreases dramatically as noted by Haltiner and Williams (1980).

It is well known that, in models such as this which allow acoustic waves as a solution to the compressible prognostic equations, the chosen method of explicit time integration is subject to the Courant-Friedrichs-Lewy (CFL) condition for computational stability which appropriately relates the chosen spatial and temporal resolutions and the speed of acoustic waves in the model. For a two-dimensional model in the vertical plane, the CFL condition for explicit methods of time integration is traditionally written, as by Haltiner and Williams (1980), as

$$\left| \frac{c\Delta t}{\Delta(x,z)} \right| \leq 1, \tag{3.36}$$

for which c represents the prescribed or calculated speed of sound in the model, Δt is the length of a single model time step, and $\Delta(x, z)$ is the least of the grid spacings in the horizontal and vertical directions. For a vertical coordinate in which stretched resolution is employed, the least grid spacing for both directions in any region of the domain is chosen.

The use of semi-implicit methods of time integration (Robert, 1969) relaxes the CFL requirement of a fully explicit method. Semi-implicit methods allow for longer time steps in comparison with less than 0.66 seconds by explicit time integration methods for a grid spacing of 0.5 km and an acoutsic velocity of approximately $c = 331$ m s^{-1} at $T_0 = 273.15$K, with nearly the same results. In practice, the prognostic equations described earlier are solved explicitly for the specified time step on the appropriate domains, allowing acoustic waves to emerge in the solution. The results for each domain are then isolated, while still at the same time step, and any acoustic waves in the domain are then filtered from the physical domain. In the use of a semi-implicit method of time integration, the effects of the high-wavenumber instabilities which may form at each time step are eliminated by "tilting" the integration forward in time with each step, effectively damping the high-wavenumber portion of the solution for the prognostic equations.

The development of multiple nested domains for this model by Ooyama allows greater spatial resolution in the region of interest, commonly near the center of the overall model domain, while still representing the physically important but less dynamically interesting outer regions of the model domain with lesser spatial resolution. In addition to the economical use of spatial resolution, the nesting developed by Ooyama also applies to the temporal resolution. Dynamics of interest are simulated with shorter time steps, while time steps commonly increase at domain interfaces with changes in grid spacing toward the outer regions of the model domain. Thus, a domain with resolution Δx may have a specified time

step of $\Delta t = 2.5$ s, while the next coarser domain with resolution $2\Delta x$ has a time step of $2\Delta t = 5$ s. Because of these differences in temporal resolution, the use of the SAFER method with the semi-implicit method of time integration on a nested model domain follows a recursive order of computation, within which several steps for the proper calculation of physical and thermodynamic/microphysical parameters are required by the numerical mechanics of these domains. This order of computation was outlined in DAOL92, with significant attention given to the representation of physical parameters as quasi-spectral cubic spline basis functions and the numerical algorithms required in the use of these basis functions for representation on domains with different spatial resolutions and therefore different temporal resolutions.

3.2.5 Domain Structure, Boundary and Initial Conditions

The model presented in O95 and O97 which incorporates the SAFER method is two-dimensional, in the $x - z$ plane, and allows any horizontal grid-spacing specified by the user. With the version of this model which was presented in O97, the user also specifies as input to the model the number of nested domains, domain sizes of the smallest and largest grids, and grid-spacing ratios for the purposes of grid nesting. A typical experiment could specify a spacing of 1 km over a high-resolution domain of 96 km, a grid spacing ratio of 2 for five nested domains, such that the next coarser domains would have grid spacings of 2 km, then 4 km, and so on to the coarsest domain with a grid spacing of 16 km, and an outer domain size of 1440 km. Vertical grid spacing is also specified by the user, without nesting specifications, such that a typical vertical spacing of 750 m would apply throughout the given number of horizontally-nested domains.

As explained in O87, DAOL92, and O97, the incorporation of local (cubic spline) basis

functions, instead of global basis functions as in a full spectral model, in the development of the SAFER method of numerical representation allowed the specification of homogeneous or inhomogeneous lateral boundary conditions. At the outer boundaries of the largest and coarsest domain, homogeneous conditions such as those listed in O87 may be applied to allow the passage of signals out of the model domain to the non-simulated external atmosphere without reflection, or inhomogeneous periodic or cyclic boundary conditions may be applied there as in the model simulations presented in O95 and O97. For the model known as VICBAR, which employed the SAFER method and was presented in DAOL92, data fields on the outermost domain were prescribed by a global spectral model which served as a forcing-type inhomogeneous boundary condition for the higher-resolution subdomains.

At the interfaces between domains of differing resolution, the overlap of area between a coarse domain and its finer subdomain was constructed to allow the free passage of resolvable signals in both directions, while restricting the Gibbs effects of signals from the fine domain which are unresolvable on the coarse domain side of each interface. In order to remove these signals which would become unresolvable upon passage into the next coarser domain, a numerical construct called the "derivative constraint" was formulated in O87 and in DAOL92 to gradually filter signals of shorter, but still resolvable, wavelengths over a limited distance near the edges of the fine domain such that only those signals which could be resolved in the coarser domain on the far side of the interface would actually reach that interface. Mechanics of the interactions at domain interfaces, including a schematic diagram of grid spacing in fine and coarser domains, the accurate representation of information exchange between domains in the region of their overlap, and the derivative constraint, were detailed in DAOL92.

The vertical coordinate used in this model is the physical altitude z, and usually

extends from a flat surface at $z = 0$ km to a user-specified height, typically $z = 18$ km. The model presented in O95 and O97 has no special surface boundary layer or surface flux formulation, such that the lowest levels are affected only by thermodynamic structures in the initial sounding, by an optional low-level shear layer specified in the initial conditions, and by surface boundary conditions specified by the user. The specification of a tropopause by including an upper-level layer of high static stability in the initial sounding would be expected to affect significantly the model dynamics in the upper region of the domain. Typically, free-slip conditions are specified at the lower boundary, such that no surface friction exists, and a rigid lid is specified at the upper boundary of the model domain.

Chapter 4

NUMERICAL TESTING AND EVALUATION OF THE MODEL

4.1 Background

Snapshots of several simulations performed by Ooyama have been included and analyzed in biannual American Meteorological Society (AMS) *Conference on Hurricanes and Tropical Meteorology* preprint publications (O95, O97). Although these snapshots may provide some degree of insight into the dynamics of the model, including the dynamics of the cumulus cloud or squall line system in the simulation, full computer animations of model results are more useful and commonly more accurate for the basis of such analyses. Included here are analyses of the simulation snapshots provided in O95 and, in results of a much improved and expanded model, in O97. Results of experiments with the same version of the model which produced the simulation snapshots presented in O97 were later provided to us during Dr. Ooyama's visit in the summer of 1998. A detailed analysis of these results, which include numerical as well as physical experiments, also follows.

4.2 Experiments and Results: Ooyama (1995)

For the application of this model to the real atmosphere, in O95 the observations and conceptual understanding of squall line convective storms detailed in RKW88 were used as guides. As discussed in the previous chapter, in RKW88 the microphysical pa-

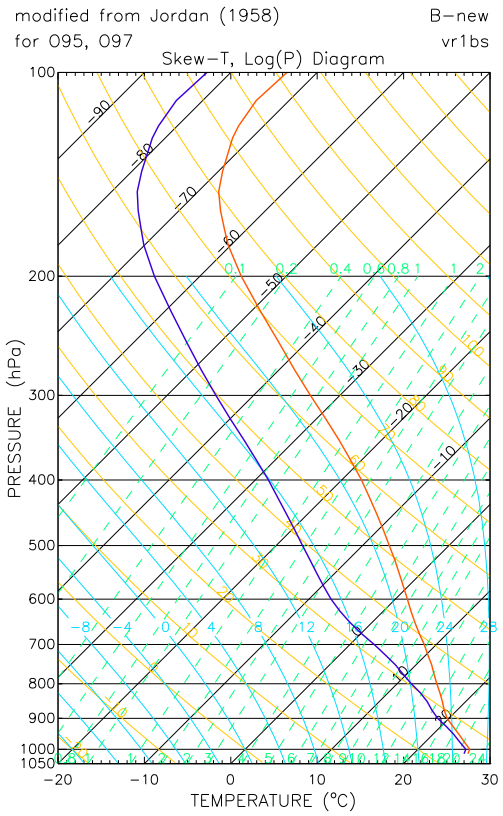

Figure 4.1: Thermodynamic profile employed in the experiments of O95 and O97, modified from Jordan (1958).

rameterizations developed in KW78 were also employed. For the experiments presented in O95, horizontal grid spacing of $\Delta x = 1$ km was chosen for a single (non-nested) 300 km domain with periodic boundary conditions. Vertical grid spacing of $\Delta z = 750$ m was applied throughout this domain. A widely-accepted tropical stratification of the atmosphere compiled by Jordan (1958), with increased (decreased) relative humidity in the lower (middle) levels of the troposphere, was assumed for the basic initial sounding. This sounding is included here in the Skew T, Log P diagram displayed in Figure 4.1. An initial horizontal wind was specified as a function of physical height, with a vertical profile at time $t = 0$

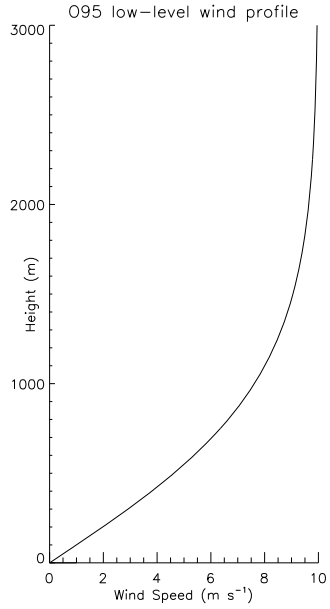

Figure 4.2: Near-surface initial wind profile employed in the experiment of O95.

given by

$$u(z) = u_c \tanh\left(\frac{z}{z_s}\right), \tag{4.1}$$

for which u_c represents the constant uniform flow aloft and z_s represents the depth scale of the shear zone above the lower boundary. A typical set of shear conditions near the lower boundary of the model domain, following (4.1), is displayed in Figure 4.2. For the experiments presented in O95, convection in the model was initiated by a semi-elliptical warm bubble of $T' = +3$ K centered in the domain at the lower boundary, and the x-coordinate moved with u_c such that the convective region of the squall line system should remain near the center of the domain during propagation. The consideration of free-slip conditions at the surface boundary allowed only subsequent convective and outflow processes to alter the initial low-level shear.

The primary experiment presented in O95 demonstrated a squall-type system which

was initiated with a deep-layer environmental flow of $u_c = 10$ m s^{-1} and a surface shear layer depth scale of $z_s = 1$ km. Snapshots of the main convective region of the system presented by Ooyama are reproduced here in Figure 4.3 for simulation times of 1h 50m (a) and 4h 35m (b). By the time of the first snapshot, accounting for the movement of the horizontal coordinate with the initial environmental wind, the leading edge of the convective region had actually propagated 80 km from its position of initiation. This early propagation speed of approximately 12 m s^{-1} decreased only slightly, by about 1 m s^{-1}, by the time of the second snapshot. While the convection itself continued, consistently regenerated by the propagation of a cool surface layer which was maintained by downdrafts just behind the convective updraft region, it can be seen that the area of precipitating water had contracted to the immediate region of the convective updrafts over that period. In the latter snapshot, reproduced in Figure 4.3b, the generation of the latest convective updraft was indicated by an area of high specific entropy (analogous to equivalent potential temperature, θ_e) at approximately the 3.5 km level along with strong velocity vectors directed upward and toward the previous convective cell from the front.

The shear conditions of the primary squall line simulation presented in O95 were compared with stronger and weaker environmental flow conditions. The results of these experiments are reproduced here in Figure 4.4. This Hovmöller diagram includes precipitation traces for several six-hour simulations with deep-layer initial environmental flows of $u_c = 0$, 5, 8, 10, 12, 15, and 20 m s^{-1}. The initial surface shear layer depth scale for each of these experiments was $z_s = 1$ km. For the case of no environmental flow ($u_c = 0$ m s^{-1}), disconnected convective cells were noted in the precipitation trace at sporadic intervals, possibly demonstrating the development of new cells from weak surface outflow forcing after the demise and dissipation of earlier cells. These experiments demonstrated that, under

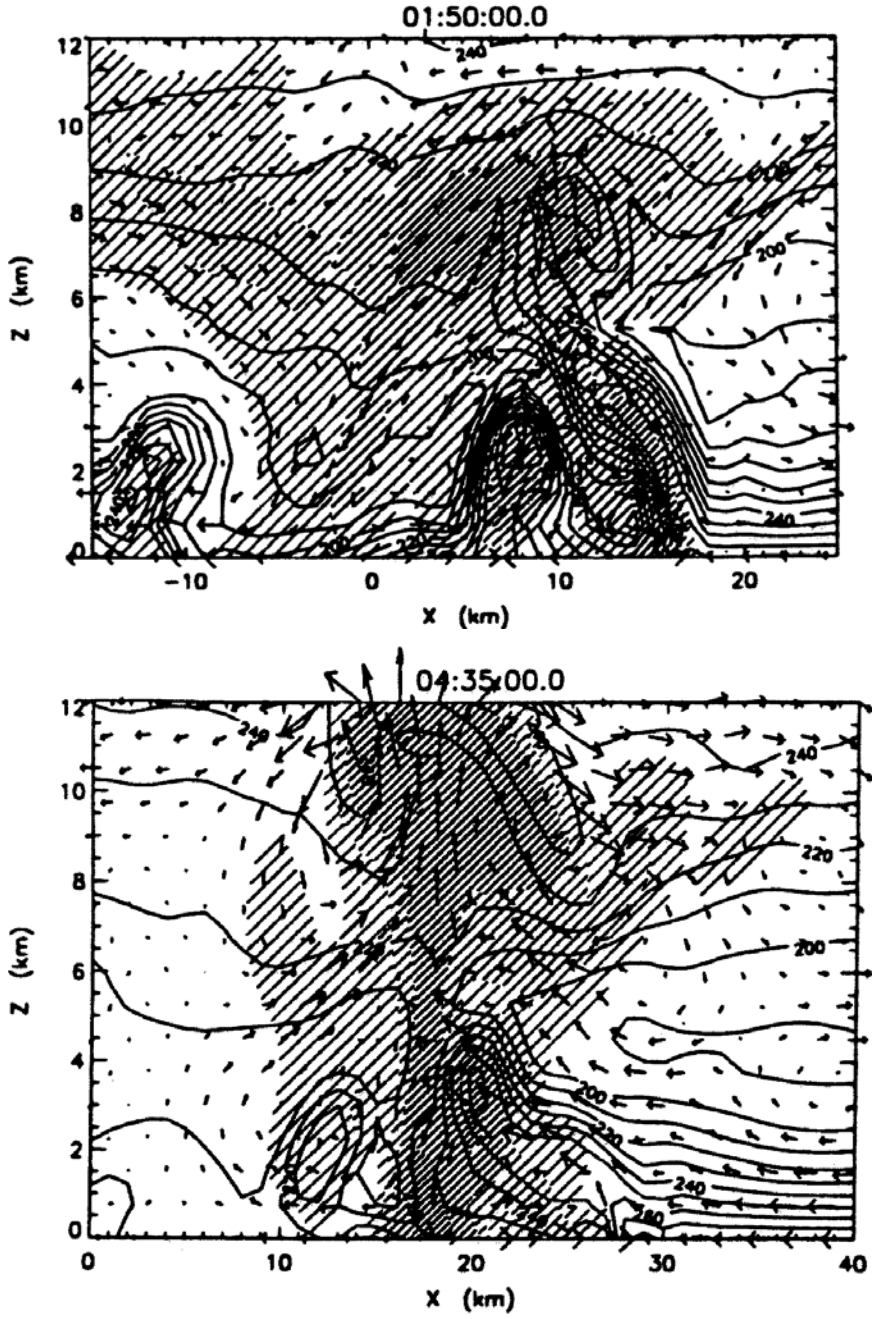

Figure 4.3: Results of the $u_c = 10$ m s^{-1} tropical squall line experiment presented in O95.

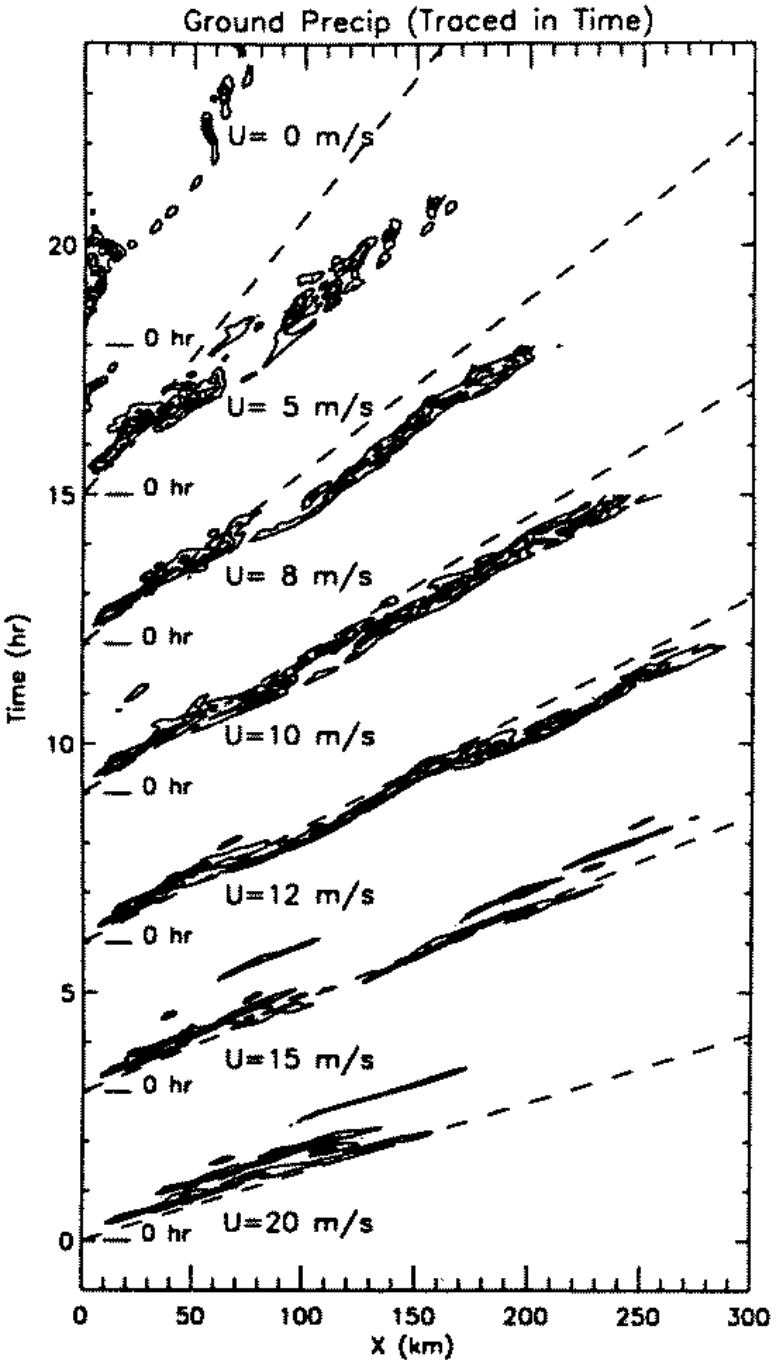

Figure 4.4: Hovmöller diagram of various experiments presented in O95.

most conditions of weak to moderate environmental flow ($u_c = 5$ to 12 m s^{-1}), the squall line convection began to propagate at a speed slightly slower than the mean environmental flow, but within two hours had exceeded the initial environmental flow speed and was propagating forward in the moving domain.

Although some organization was demonstrated by the case of $u_c = 5$ m s^{-1}, greater consistency in the maintenance of a continual convective region was achieved in the $u_c = 8$, 10, and 12 m s^{-1} simulations. For the cases of stronger environmental flow ($u_c = 15$ to 20 m s^{-1}), Ooyama found that the difficulty of convective organization had increased so as to induce slower propagation speeds and the early demise of the squall line convection altogether. In O95, experiments with a deeper shear zone ($z_s = 2$ km) were also reported. These experiments with a greater shear layer depth demonstrated weak convective organization and propagation for even weak and moderate environmental wind profiles, similar to the results for experiments involving strong initial environmental winds with a shallow surface shear layer.

Results of the numerical experiments published in O95 displayed typical growth and decay of squall line precipitation cells, as well as the birth of new cells and the propagation of the convective line. These results were in close agreement with the ideas presented in RKW88. Of great importance may be the demonstration of an optimal shear configuration for the experiments performed with the model presented in O95, as shown by the results reproduced in Figure 4.4. For a shear layer depth scale of $z_s = 1$ km, which is similar to the typical depth of the atmospheric boundary layer, in O95 it was found that an initial environmental wind of $u_c = 12$ m s^{-1} produced the most consistent, longest-lasting and therefore farthest-reaching of the simulated squall lines. In fact, the Hovmöller diagram for this simulation demonstrated two jump-like advances of the leading edge of the precipitation

region, at approximately 1.5 and 3.5 hours into the simulation, after each of which the propagation speed of the squall line seemingly decreased slightly and approached the speed of the initial environmental flow. Similar but more protracted jump-like features may be found in the precipitation traces for environmental flow speeds of $u_c = 10$ m s^{-1}, at approximately 1.5 hours into the simulation, and $u_c = 8$ m s^{-1}, at approximately 2 hours. For an initial environmental wind speed of $u_c = 12$ m s^{-1}, these alternating jumps and reductions in the forward speed of the squall line may have demonstrated the oscillatory nature of convective growth and propagation as examined in detail in FD95.

4.3 Experiments and Results: Ooyama (1997)

The model version presented in O97 was similar in setup and initial conditions to that discussed in O95. The reader is referred to Figures 4.1 and 4.2 for the typical initial environmental conditions for these simulations. However, the simulation presented in O97 employed five nested domains covering 1,100 km in the horizontal direction, with a finest central domain of $\Delta x = 1$ km over 96 km. Snapshots of simulations were included in O97 which demonstrated the accuracy of the domain nesting procedures developed for this model. In those snapshots, not included here, squall line convection which remained near the center of the domain which was moving at the speed of the constant environmental wind, and therefore remained entirely within the domain of highest resolution in the model, was compared with squall line convection which propagated through a domain which was fixed relative to the Earth and was beginning to enter the next coarser domain of $\Delta x = 2$ km. The snapshots at time 0h 40m for each simulation were compared, and displayed remarkable similarities in convective strength and shape, including updraft tilt. Only a slight loss of detail on the $\Delta x = 2$ km side of the domain interface was found.

Despite the lack of a clearly defined trailing stratiform region in these early snapshots, rear inflow near the surface was evident some distance behind the squall line convection in both simulations. Midlevel rear inflow immediately behind the convective line was found to be stronger and more horizontal in the simulations which held the convection entirely within the finest domain. It should be stressed again that the finest domain was initialized with $\Delta x = 1$ km, at which resolution many features of the tropical squall line convective region, itself only a small portion of the overall system, which were discussed earlier may remain unresolved.

Ooyama noted that in these simulations a convective cold pool began to form approximately two to three hours after generation of the initial convective cells, and that eventually the simulation settled into a quasi-steady mode of cyclic convective generation at the cold pool gust front where it met the environmental inflow near the surface. A snapshot of another model simulation, similar to the moving-domain experiment discussed above, at 4h 55m was included in O97, and is reproduced here in Figure 4.5. This simulation demonstrated the advance of the convective cold pool, which at the time of this snapshot had just crossed the interface between the finest and next coarser domains. The seemingly cyclic generation of new convective cells on the surface outflow layer is clearly evident in the contours of cloud water density, as is the advection of convective cells upward and rearward through the system after generation.

For the simulation snapshot presented in Figure 4.5, it may be speculated that the formation of a pre-squall overhanging precipitation region seems to have created a significantly stable layer between approximately 8.5 km and 10.5 km at about $x = 50$ km, demonstrated in the accompanying profiles of specific entropy (analogous to equivalent potential temperature, θ_e) in the lower panel of Figure 4.5, which may suppress the growth of new convective

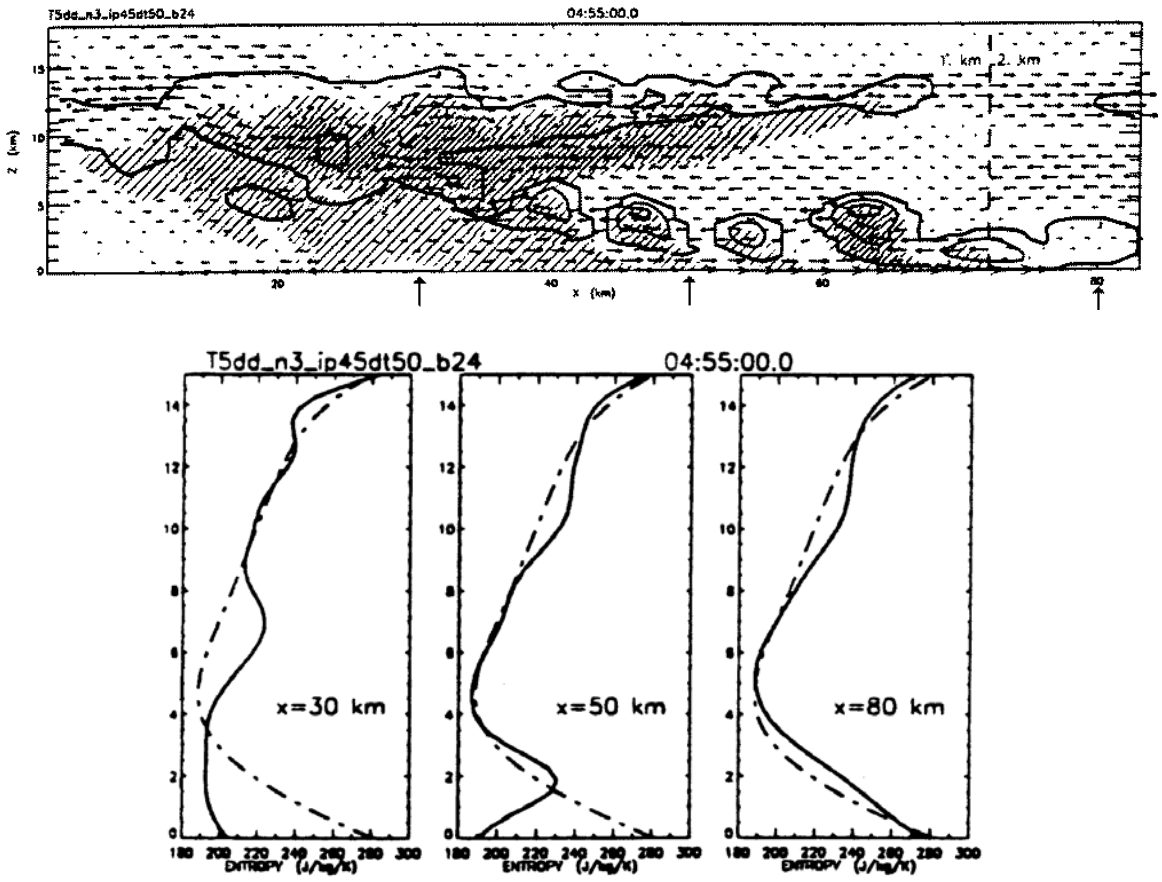

Figure 4.5: Results of the tropical squall line experiment presented in O97. Arrows in the model domain snapshot denote approximate locations of the specific entropy profiles included in the bottom panel.

cells into the middle and upper levels of the troposphere. Although the low-level cold pool seems to have advanced beyond the influence of this upper-level convective inhibition by the time of the snapshot included here, and has generated a new convective cell which looks to be stronger than those visible which were generated before, the presence of significant upper level pre-squall outflow may demonstrate that the overhanging precipitation region and its stable layer will persist, influencing the strength of the convective region further.

At $x = 30$ km, in the region of heavy precipitation behind the gust front, the profile of specific entropy included here in Figure 4.5 demonstrates that a deep layer of stable air has

formed, especially in the subcloud layer between 4 km and 7 km, with significant instability only in the layer between 7 km and 9 km where new convective cells are incorporated into this region. At $x = 80$ km, by the time of this snapshot the surface cold pool gust front had just begun to affect the profile of initial or pre-squall specific entropy, designated by the dotted-line profile for each of the selected locations. A layer slightly more stable than the initial sounding has developed at this location between 8 km and 10 km, ahead of and below the upper level pre-squall outflow region which is clearly evident in the profile at $x = 50$ km. The placement of the slightly weaker stable layer at $x = 80$ km may demonstrate the advection and evaporation of cumulus debris in the upper level outflow layer and the subsequent descent of evaporation-cooled air ahead of the squall line convective region.

Differences between the specific entropy profiles which are included in Figure 4.5 may demonstrate the effects of convection on the mixing of unstable air in the low levels of the initial environment and the establishment of a neutral or positively-stable layer there. The procession of the profiles from a deep unstable layer up to approximately $x = 5$ km in the pre-squall environment at $x = 80$ km, to a shallow but strongly stable layer at $x = 50$ km in the region beneath the rising cumuli up to 2 km and a significantly unstable profile in the cloud layer between 2 km and approximately 4.5 km, and finally to a deep neutral-to-significantly-stable profile up to 7 km in the region of heavy convective rainfall at $x = 30$ km may demonstrate the optimum redistribution of stability by the squall line convection. This redistribution leads to the overall reduction of instability in the low- and midlevels, as found by Asai and Nakasuji (1977, 1982), and eventually to buoyancy equilibrium in a manner similar to the buoyancy sorting mechanism for mixing in convection which was proposed by Telford (1975) and developed further by Taylor and Baker (1991).

4.4 Experiments and Results: Unpublished Simulations

Many other experiments with this model were performed by Ooyama around the time of those simulations which were included in O97. Although these simulations have not been published, a large quantity of these results in the form of model output data and computer animations were recently provided to us. Many of the model results and animations represent important tests of model sensitivity to prescribed numerical parameters, such as spatial resolution and length of time steps, and more technical parameters such as the derivative constraint, applied near domain interfaces, and the Asselin filter for the Leapfrog time integration scheme. Several simulations compare the two available methods of time integration, the Leapfrog and the second-order Adams-Bashforth schemes, as well as the effects of the forward tilt of these semi-implicit methods as discussed earlier. Many of the provided results and simulations address various strengths of the specified shear as initial physical conditions for the model domain, including several high-resolution experiments with an initial environment without wind or near-surface shear. Some of these results which compare low-level shear intensities will be associated favorably with earlier model results presented in O95 and discussed above.

Several of the simulations provided by Ooyama compare the development of convection from identical initial conditions in domains of different spatial resolution. These experiments employed the same initial thermodynamic profiles and shear conditions as the simulations presented in O97. The reader is again referred to Figures 4.1 and 3.4 for a display of typical initial environmental conditions for these numerical experiments. In each of these simulations, the direction of the vertical shear of the initial low-level horizontal wind is toward the right of the model domain snapshot; this direction will commonly be referred to as "downshear". Convection was initiated in the same manner as those experiments

presented in O97 and examined above. The location at which the initial warm bubble is placed, usually $x = 0$ km, will commonly be referred to as the "initial convective point". Experiments which did not compare model resolutions employed $\Delta x = 1$ km on the finest domain, with few exceptions, while variations in other model parameters were examined. In the results which follow, cloud water and precipitation content is represented by the shaded regions. The outermost of the shaded contours in most diagrams corresponds to cloud liquid water in any concentration (lighter shade) or precipitation liquid water content in concentrations between 0 and 0.5 g m^{-3} (slightly darker shade). The line contours superimposed on the diagram are of the "dry-air-specific" entropy of moist air,

$$s = \frac{\sigma}{\rho_a}, \tag{4.2}$$

as in section 6 of O90, at intervals of 10 J kg^{-1} K^{-1}. The dry-air-specific entropy of moist air in a parcel is analogous to the equivalent potential temperature of the parcel, and is (approximately) conserved following dry-adiabatic (pseudoadiabatic) parcel motions. This analogy is explored further in Appendix D.

4.4.1 Resolution Experiments

An experiment was performed by Ooyama to compare the development of convection in domains of $\Delta x = 1$, 2, and 4 km using a time step on the finest domain of $\Delta t = 5$ s for all of these resolutions. Snapshots of these simulations are presented here in Figure 4.6. It may be clearly noted that the warm bubble placed in the initial conditions has initiated convection earliest in the $\Delta x = 1$ km simulation. By the integration time of 0h 30 m, convection in the simulation of highest resolution has reached the tropopause.

A similar state is noted at 0h 40m (Figure 4.6a) for the convection in the $\Delta x = 2$ km simulation, while the convective updraft in the $\Delta x = 1$ km domain exhibits a distinct

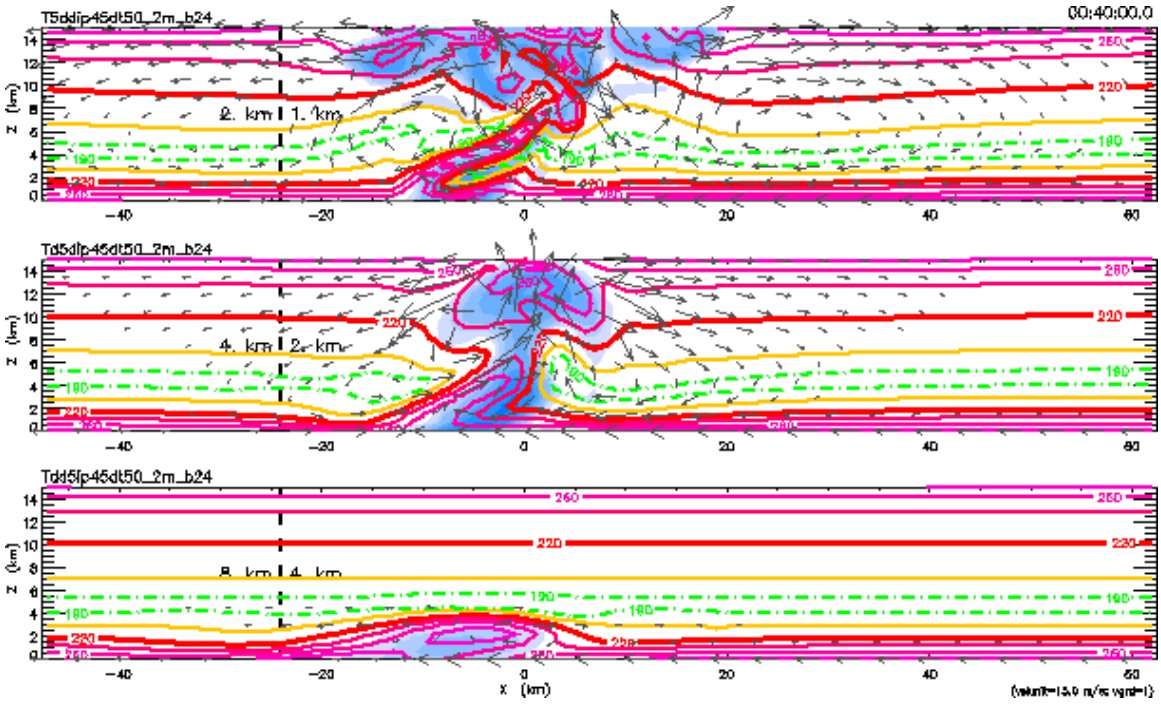

Figure 4.6a: Convection in $\Delta x = 1$, 2, and 4 km domains, at 0h 40m.

downshear tilt with strong downdrafts evident at midlevels ahead of the convective line. In the $\Delta x = 4$ km simulation, convection finally reaches the tropopause around 1h 16m, while the other simulations already exhibit some degeneration of the convection at low levels.

At 1h 52m (Figure 4.6b), convective regeneration begins in the $\Delta x = 1$ km simulation slightly downshear of the original convection, while weak evaporative cooling and subsidence in the $\Delta x = 2$ km simulation across the initial convective region seems to induce a weak convective bubble some distance upshear. Also at this time, convection in the $\Delta x = 4$ km simulation exhibits strong downshear tilt but a weak possibility for regeneration or development of new convection near the surface. By 3h 10m (Figure 4.6c), a gust front begins to form in the finest simulation, with some evidence of a jump updraft ahead of the cold low-level convective outflow, while downshear convective regeneration finally occurs in the $\Delta x = 2$ km simulation. In the $\Delta x = 4$ km simulation, slow subsidence of evaporatively-cooled air following the initial convective activity has formed a deep cold pool near the

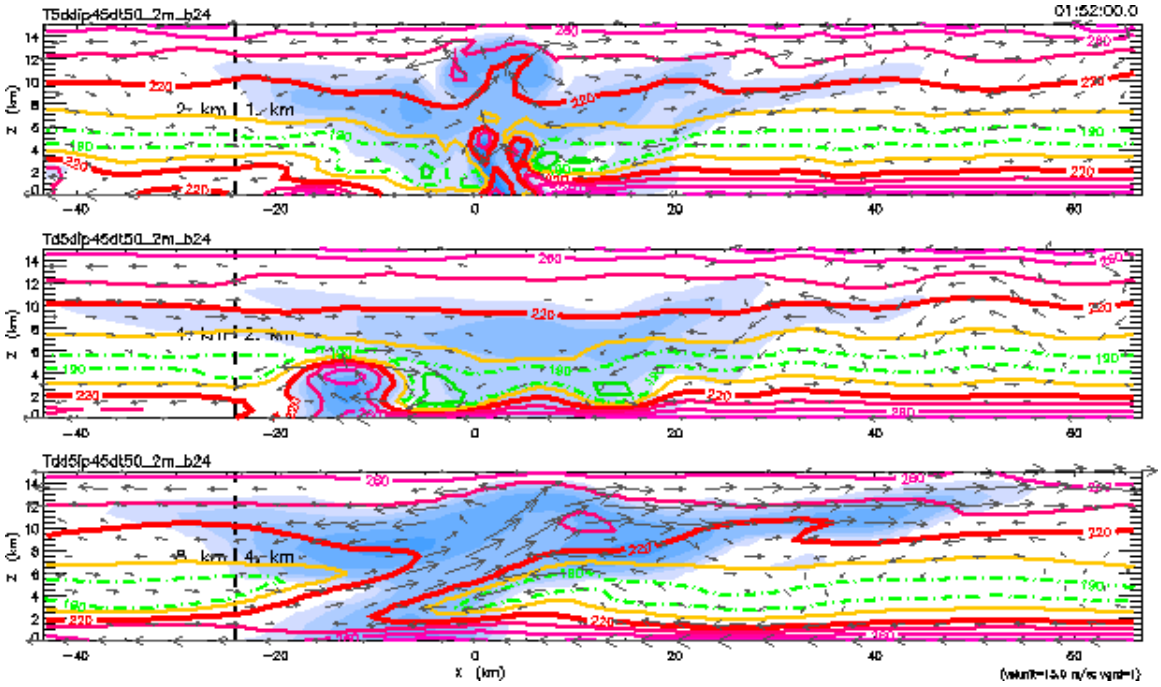

Figure 4.6b: Convection in $\Delta x = 1$, 2, and 4 km domains, at 1h 52m.

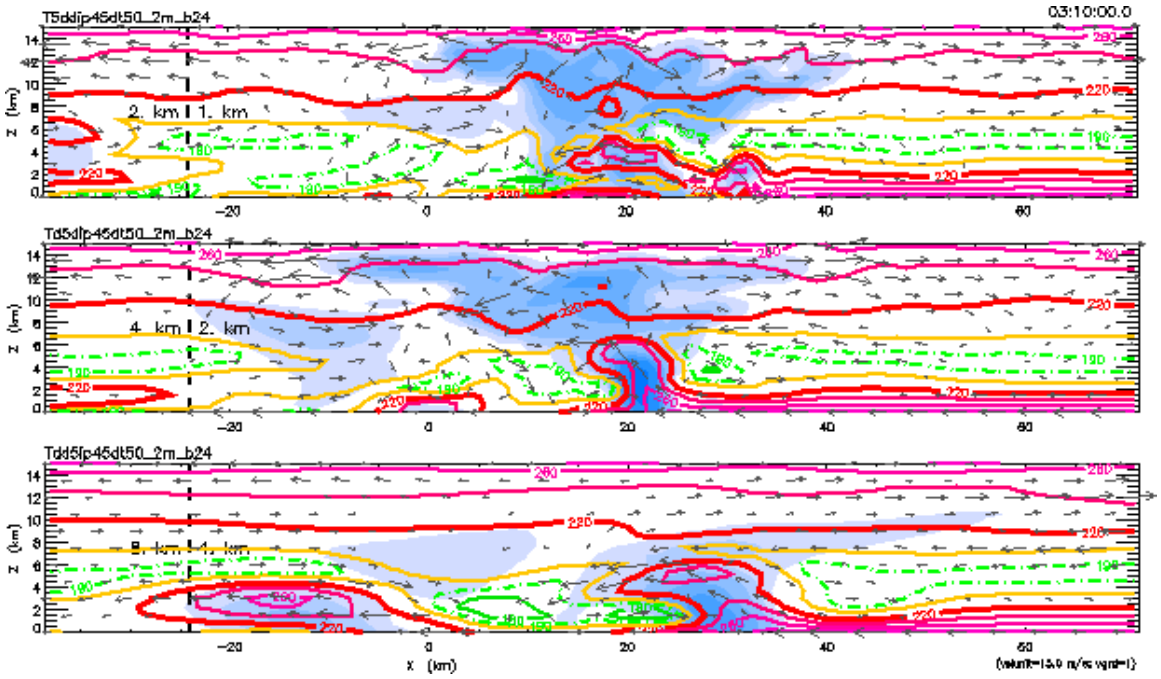

Figure 4.6c: Convection in $\Delta x = 1$, 2, and 4 km domains, at 3h 10m.

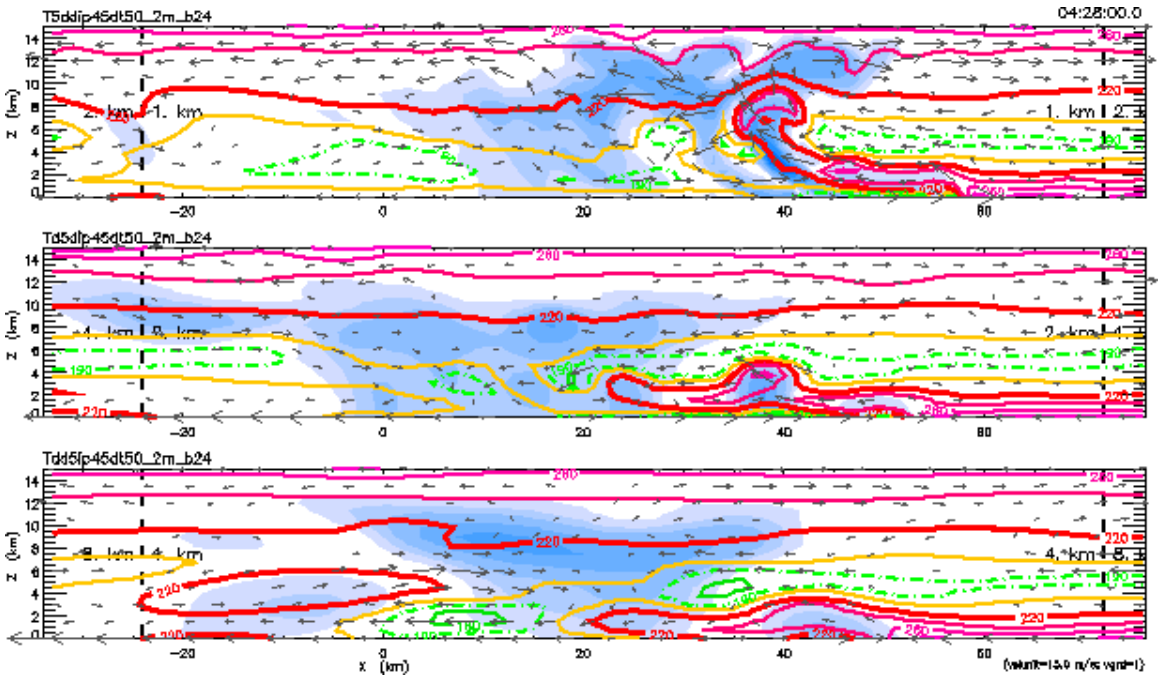

Figure 4.6d: Convection in $\Delta x = 1$, 2, and 4 km domains, at 4h 28m.

surface downshear of the initial convective point, and some weak derivative convection is evident upshear and downshear of the cold pool.

By 4h 28m (Figure 4.6d), this derivative convection has placed a significant amount of moisture in the midlevels of the domain, but the evaporation of this moisture only serves to strengthen the low-level cold pool by 5h 00m (Figure 4.6e) and initiates another weak convective plume slightly downshear. In the finer simulations, however, by 4h 28m a low-level gust front of cool convective outflow air has formed in both the $\Delta x = 1$ and 2 km domains, although the depth of the cold outflow and the strength of subsequently generated convection seems greater in the $\Delta x = 1$ km simulation. Pre-squall overhanging moisture evident in this snapshot seems not to have acted to suppress the convective plume over the low-level outflow in the simulation of highest resolution, possibly because of the proximity of this new convective plume to the pre-disturbed midlevels of the convective line.

By 5h 00m (Figure 4.6e), however, it is evident that convection generated slightly

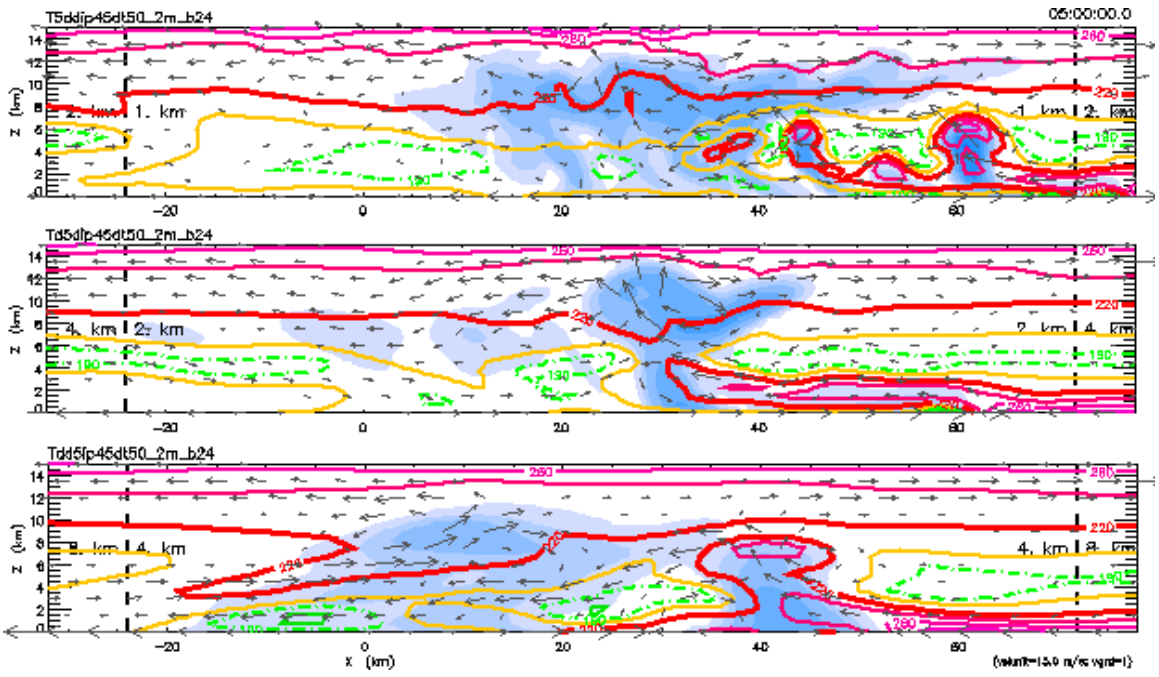

Figure 4.6e: Convection in $\Delta x = 1$, 2, and 4 km domains, at 5h 00m.

further ahead of the main convective region by the strong pre-squall low-level outflow is prevented from reaching its full potential by weak evaporation-induced downdrafts from the overlying moist layers. Far ahead of the main convective region, near the limits of the upper-level moist region, a strong convective plume has formed by 5h 00m behind the leading edge of the gust front in the $\Delta x = 1$ km simulation, while no new convective updrafts have been initiated by the shallow convective outflow in the $\Delta x = 2$ km simulation. The development of new convection approximately 20-25 km ahead of the main convective region, as in the $\Delta x = 1$ km simulation around 5h 00m, may demonstrate the discrete propagation of a mesoscale convective system such as a squall line.

Another experiment was performed to compare the development of convection on domains of $\Delta x = 0.5$ and 1 km. Snapshots of these simulations are included here in Figure 4.7. Although the semi-implicit formulation of this model is designed to allow time steps longer than those allowed by the CFL condition, discussed above, for explicit methods of

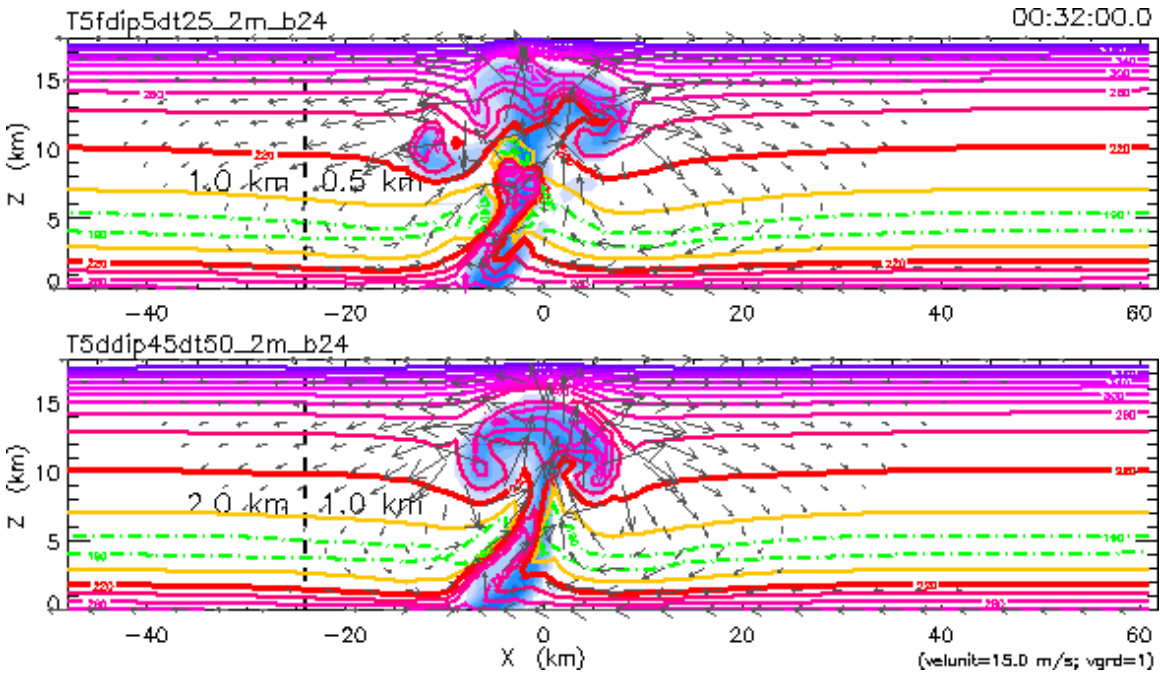

Figure 4.7a: Convection in $\Delta x = 0.5$ and 1 km domains, at 0h 32m.

time integration, in the interests of accuracy the time step for the $\Delta x = 0.5$ km model simulation was reduced to $\Delta t = 2.5$ s. In this way, the $\Delta x = 0.5$ km simulation is not only more finely resolved spatially, but also temporally.

The initial convection reaches the tropopause for each simulation at about 0h 32m (Figure 4.7a), although the cap of the convective bubble seems more symmetrical in the $\Delta x = 1$ km simulation. In the higher-resolution simulation, a sharp downdraft immediately upshear of the bubble cap has cut off a small region of midlevel moisture from the main convective plume. Additionally, wind vectors in the updraft of the $\Delta x = 0.5$ km simulation are oriented more downshear that in the coarser simulation, but with a similar upper-level outflow structure ahead of the initial convective bubble.

A snapshot at 1h 00m (Figure 4.7b) demonstrates the regeneration of weak convection immediately upshear of the initial convective point in both simulations, although the upper-level moisture region remains more symmetric about the initial convective point in the

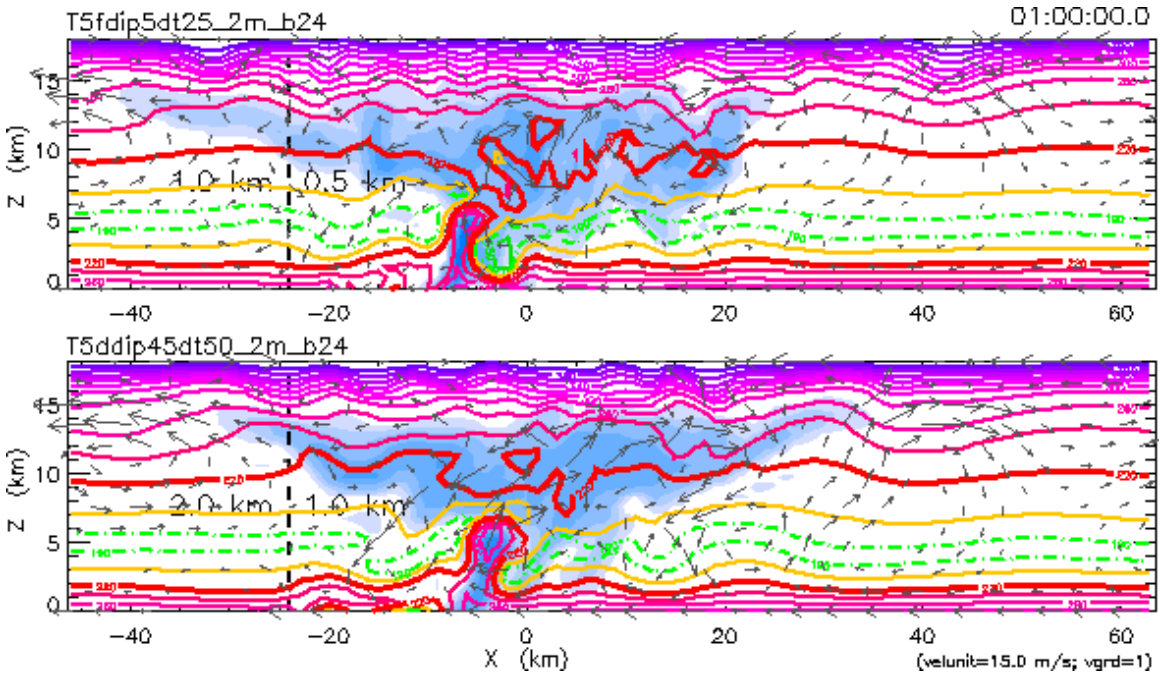

Figure 4.7b: Convection in $\Delta x = 0.5$ and 1 km domains, at 1h 00m.

$\Delta x = 1$ km simulation. In the finer simulation, upper-level convective outflow toward the rear (left) of the initial convective bubble is more pronounced, as is a significant shortening of the upper-level pre-squall convective outflow by the environmental winds.

Evaporatively-cooled downdrafts, which are more evident in the finer simulation, become more important by 1h 54m (Figure 4.7c), at which time some convective regeneration has occurred over the initial convective point while a significant cold pool has begun to form and descend into the lower levels around the main convective plume. In both simulations, the convective cold pool forms more strongly and deeply upshear of the initial convective point, which drives the convective downdraft and outflow downshear by 3h 00m (Figure 4.7d). At this time, a slightly stronger low-level cold pool and a more discrete convective initiation and updraft structure is evident in the finer simulation, as well as a slightly weaker upper-level layer of convective outflow moisture which could prevent the full development of new convective cells on the pre-squall gust front.

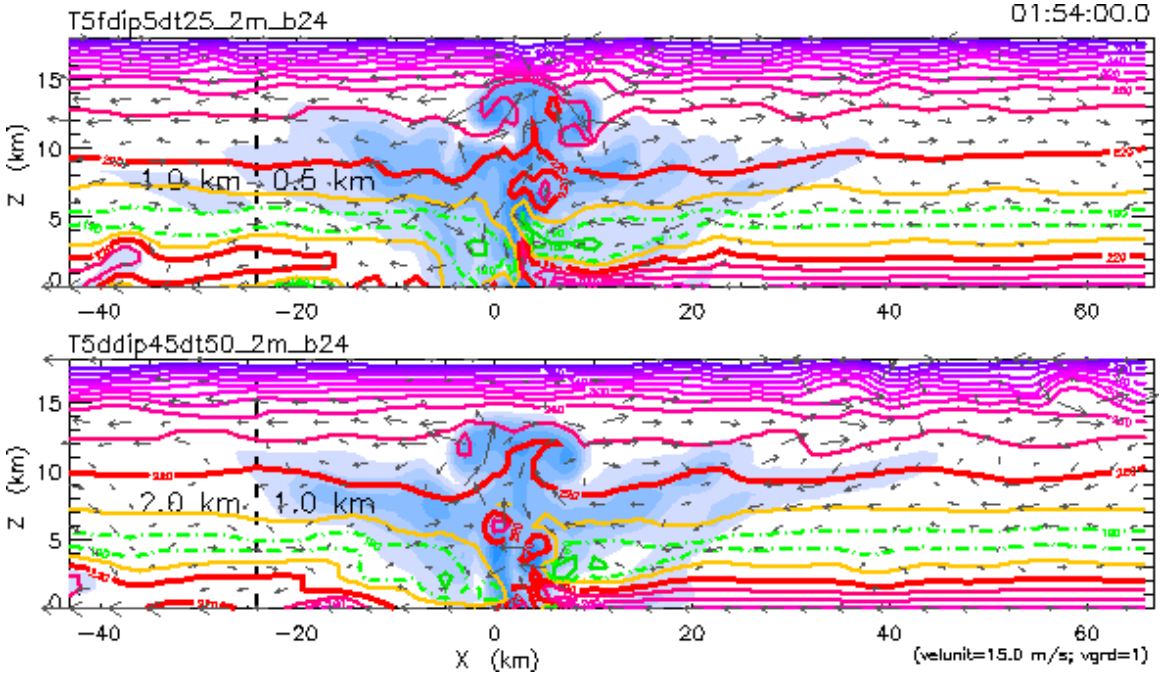

Figure 4.7c: Convection in $\Delta x = 0.5$ and 1 km domains, at 1h 54m.

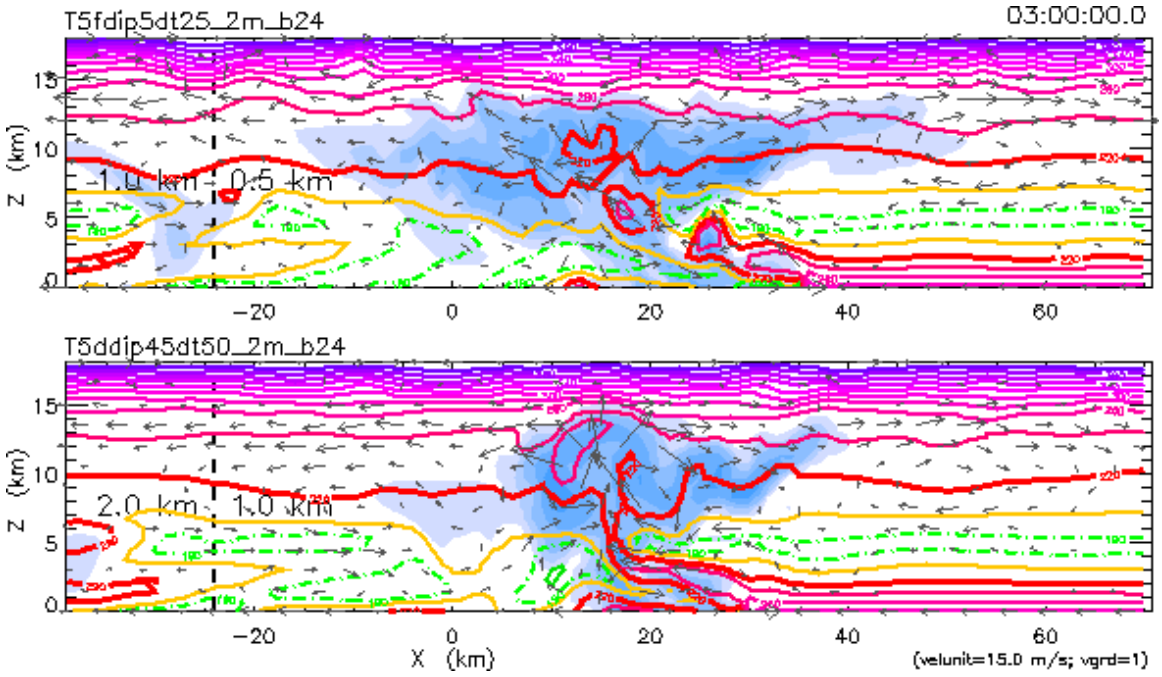

Figure 4.7d: Convection in $\Delta x = 0.5$ and 1 km domains, at 3h 00m.

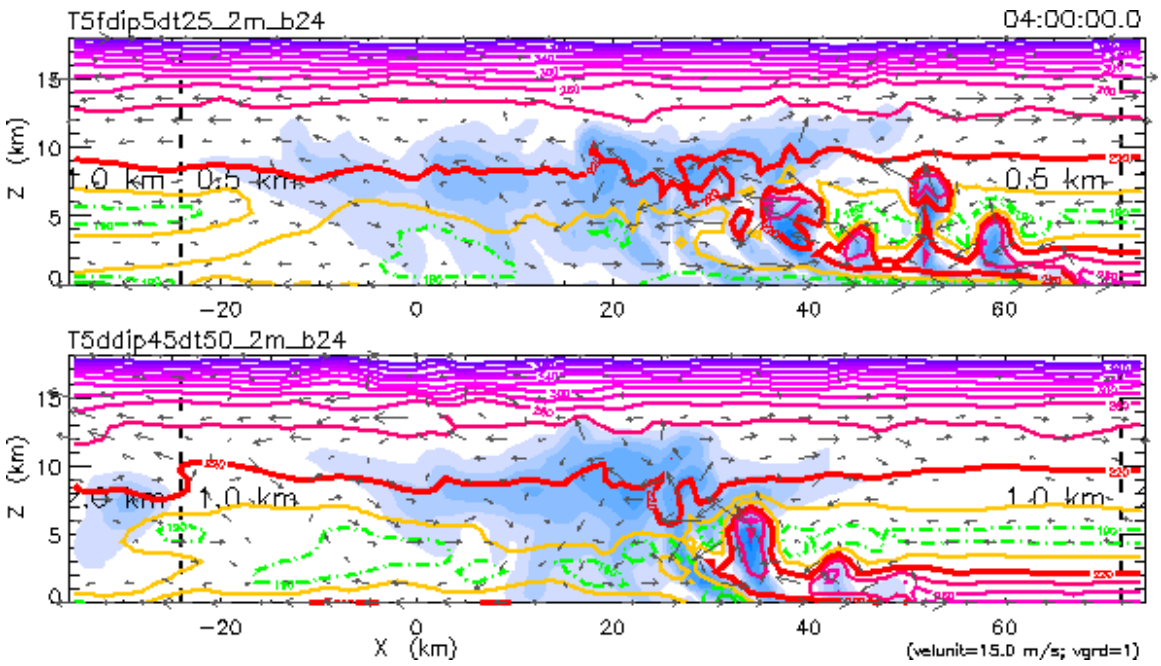

Figure 4.7e: Convection in $\Delta x = 0.5$ and 1 km domains, at 4h 00m.

By 4h 00m (Figure 4.7e), it is clearly evident that a stronger and more active low-level convective outflow has formed in the $\Delta x = 0.5$ km simulation, with the formation of new convective cells at regular intervals out to its downshear boundary. The coarser simulation, however, displays a more limited regeneration of convection on the outflow boundary, which continues through 5h 00m (Figure 4.7f). By this time, the low-level convective outflow in the $\Delta x = 0.5$ km simulation has already entered the next coarser model domain and has begun to generate seemingly strong convective cells there, while the outflow of the $\Delta x = 1$ km simulation is just reaching the interface between model domains and has generated pre-squall convective cells of similar strength.

4.4.2 Convection on a Domain Interface

As discussed in the earlier analysis of simulations presented in O97, convection which is initiated on the interface between model domains of differing resolution meets no numer-

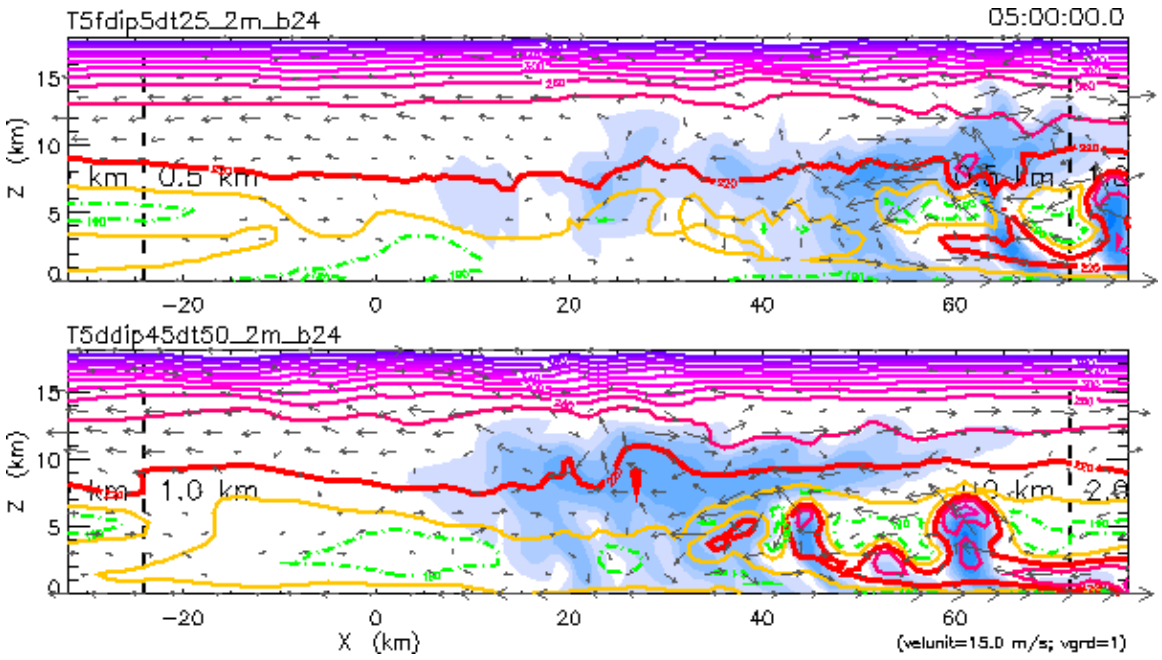

Figure 4.7f: Convection in $\Delta x = 0.5$ and 1 km domains, at 5h 00m.

ical difficulties in the accuracy of simulation. However, it was noted that these conditions may result in a slightly asymmetrical convective plume in the simulations, which could itself contribute to the forcing and propagation of the initial and subsequent convection. The effects of resolution differences in the representation of detailed convective structure have been demonstrated in the above analysis of comparative simulations. Simulations in which a surface temperature anomaly was placed across a domain interface were performed using a finest central domain of $\Delta x = 0.5$ km, such that the resultant convection developed on the domain interface at the left side of the finest domain. For simplicity in the examination of the asymmetry which develops in this interface convection, the simulations presented here included no initial wind field or surface shear. The case of convective development in an atmosphere at rest will be discussed further in a later section. In Figure 4.8, this interface convection at an early stage of development is compared to convection initiated in the center of the finest domain.

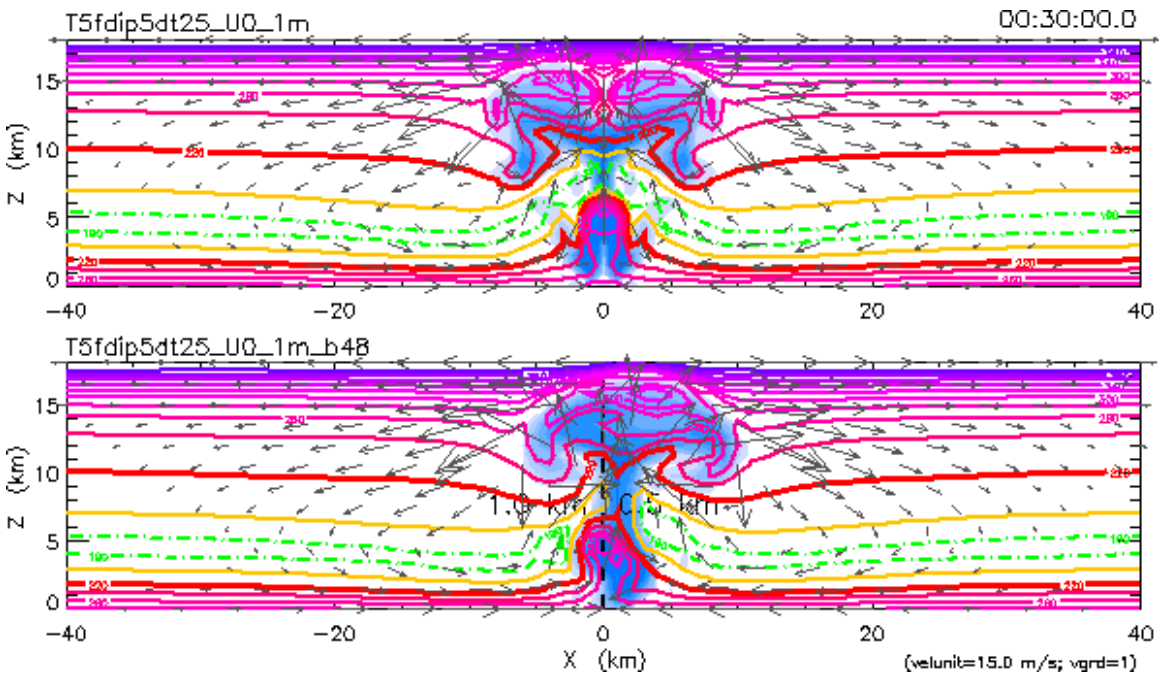

Figure 4.8a: Convection in the center of a domain and at a domain interface, at 0h 30m.

The symmetry of the convection which began in the center of the finest model domain is clearly evident throughout the simulation, whereas convection initiated on the domain interface demonstrates significant asymmetry in the rising thermal bubble by 0h 27m. By the time the convection reaches the tropopause and begins to spread through the upper troposphere at 0h 30m (Figure 4.8a), it may be noted that the moist convective updraft has preferentially formed on the high-resolution side of the domain interface, although wind vectors about the cumulus appear to remain quite symmetric about the axis of updraft. Extensive asymmetry develops in the interfacial convection by 0h 45m, and a low-level updraft which is tilted toward the high-resolution domain with height may be noted at this time in the simulation.

This tilted updraft becomes slightly weaker but more vertically homogeneous by 1h 00m (Figure 4.8b), while a region of cold downdraft air begins to form in the center of the original updraft in the symmetric simulation. Low-level cold pools begin to strengthen in

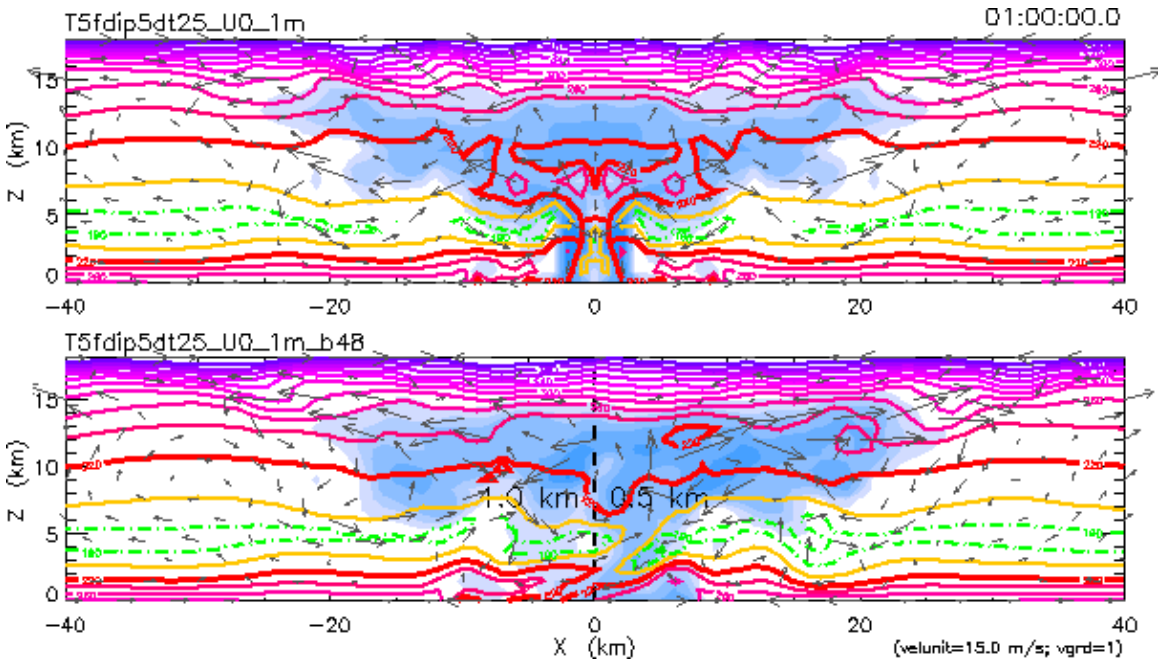

Figure 4.8b: Convection in the center of a domain and at a domain interface, at 1h 00m.

both simulations by 1h 15m, accompanied by sporadic residual convection on both sides of the system in the symmetric simulation but on only the high-resolution side in the interfacial simulation.

By 1h 30m (Figure 4.8c), a large central cold pool has begun to drive convective development in the low levels in the symmetric simulation, while warm low levels persist in the high-resolution domain where new convection begins to develop in the interfacial simulation. This new convection is forced by a complex stratification of low-level air in the interfacial simulation by 1h 45m, at which time a cool layer formed by the evaporation of moist air in weak convective downdrafts overlies a thin surface layer of warm moist air which remains from the original convective environment. The propagation of the convective system toward the high-resolution domain from its starting point on the domain interface may be distinctly noted by this time, as well as by 2h 00m (Figure 4.8d). By this time, the thin warm layer near the surface has nearly disappeared, while a layer of cool convective

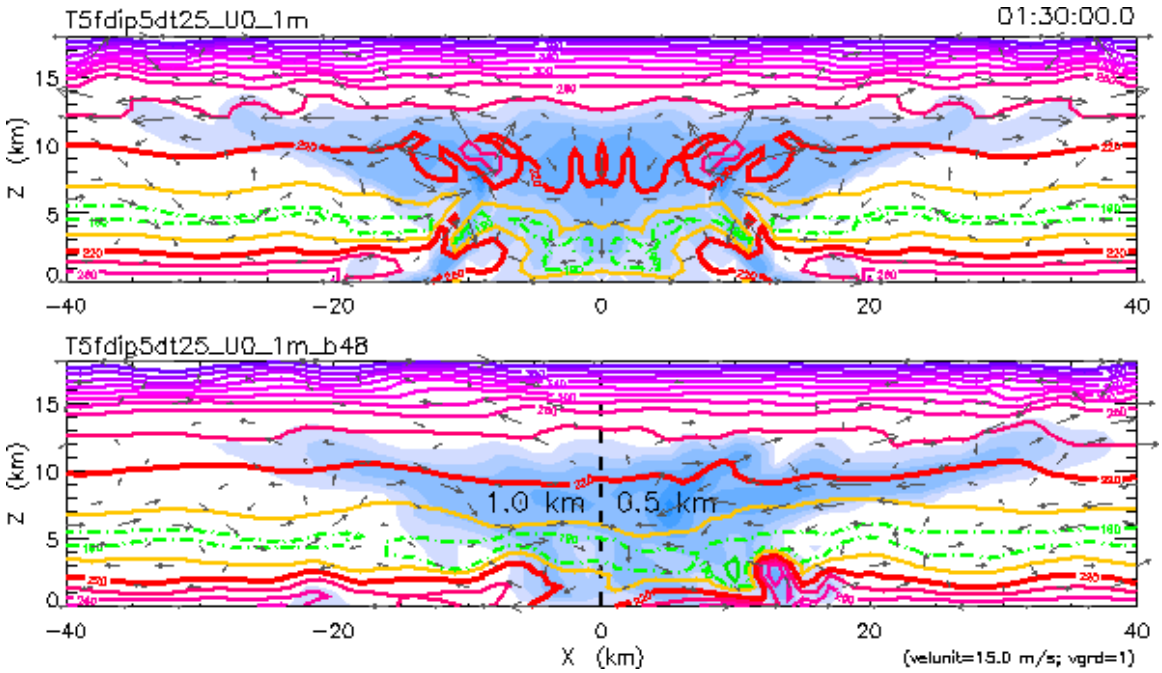

Figure 4.8c: Convection in the center of a domain and at a domain interface, at 1h 30m.

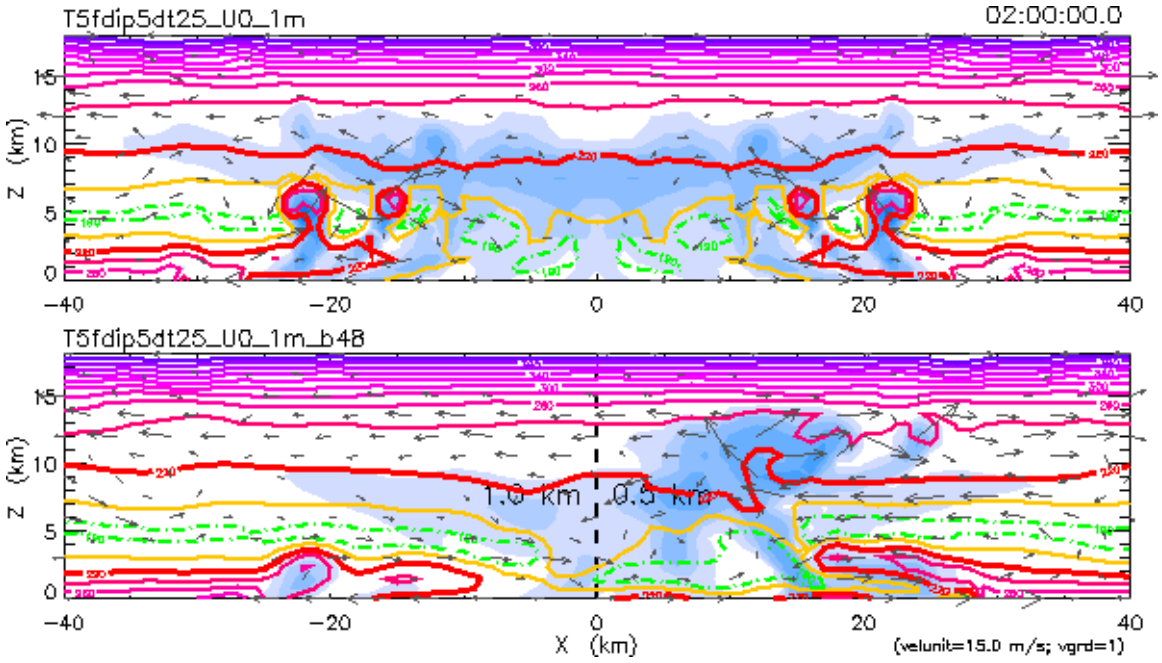

Figure 4.8d: Convection in the center of a domain and at a domain interface, at 2h 00m.

downdrafts continues to descend slowly into the lower levels, preferentially on the high-resolution side of the domain interface.

4.4.3 Length of Time Steps

With the simulations available, an evaluation of the effects of different time step lengths is difficult, as most simulations which employ a finest domain of $\Delta x = 1$, 2, or 4 km use the same base time step of $\Delta t = 5$ s, whereas a simulation with a finest domain of $\Delta x = 0.5$ km employs a time step of $\Delta t = 2.5$ s. It is clear that the greater accuracy of convective representation found in simulations of greater spatial and temporal resolution is more desirable, but these desires must be weighed against computational efficiency and limitations. Additionally, the limitations of the physical representation of nature which this model employs are unclear, as we may find problems in the representation of motion on very small scales in an atmosphere with no frictional dissipation. It may have been for computational efficiency that Ooyama chose to perform most numerical tests on a finest domain of $\Delta x = 1$ km and with a base time step of $\Delta t = 5$ s, but a true measure of the accuracy of simulation would be the realism of dynamic and thermodynamic reproduced by the model on a desired scale and with adequate resolution. Later, simulations which employ much greater resolutions will be discussed in the context of convective-scale motions. Such experiments will be intended to simulate phenomena which occur on much shorter spatial and temporal scales than the mesoscale convective system.

4.4.4 Strength of the Asselin Filter

The Asselin filter is another parameter which may be defined by the user of this model, and is a parameter which displays a slightly more noticeable effect on the attempted

simulations than the strength of the derivative constraint, which will be examined later. As discussed earlier, the Asselin parameter dictates the strength of a low-pass filter which is intended to neutralize the destabilizing effects of the computational mode of the solution which is produced by the three-level Leapfrog method of time integration. Simulations provided by Ooyama which examine the variations of this parameter employ select values within a range of $\nu = 0.01$ to $\nu = 0.4$, beyond which the filtered solution would be expected to become quite noisy and potentially unstable due to a greater dependence on the average of solutions at surrounding time steps than on the solution at the current time step. Within this range, the provided integrations and simulations remain quite stable, and as such provide few differences between them to compare and determine optimal values of ν. For this reason, snapshots of these simulations are not included here.

It may be sufficient to state here that the value of the Asselin parameter chosen for the majority of experiments is $\nu = 0.3$. This value provides a reasonable filtering of the oscillating computational mode without being large enough to allow high-frequency computational noise from the forecast solution at time $t + \Delta t$ to appear in the solution at time t, or small enough to remove valuable small-scale forecast information from the solution at the current time. It should be understood by the reader that these attributes of the Asselin filter have no bearing on the use of the second-order Adams-Bashforth method of time integration, which was also discussed earlier. These two methods, the Leapfrog with an Asselin filter and the second-order Adams-Bashforth, are compared in a set of simulations provided by Ooyama which will be discussed below.

4.4.5 Methods of Time Integration

As described above, two methods of time integration were included in the construction of this model. The method of primary usage in the experiments performed by Ooyama and presented here is the three-level Leapfrog method, which is considered accurate to an order $O(\Delta t^2)$. The second-order Adams-Bashforth method comprises the alternate option which is available to the model user. The advantages and disadvantages of each of these methods, especially with regard to the computational mode which arises in second-order methods of time integration, have been discussed above. However, the usefulness of these methods is likely best assessed in a comparative demonstration of their results, presented here in Figure 4.9. Simulations for each of these methods began with identical initial conditions, and the differences in convective development in each simulation are traced here. In each part of Figure 4.9, the upper panel represents the simulation which employed the Leapfrog-Asselin method of time integration, and the lower panel displays the results of the simulation which employed the second-order Adams-Bashforth method of time integration.

At 0h 30m (Figure 4.9a), the initial convective plume in each simulation has just begun to reach the upper levels of the model domain where a tropopause-like stable layer has been included in the initial conditions. Results at this time are nearly identical, and convective downdrafts are clearly evident on either side of a strong and moist updraft which tilts downshear. By 1h 00m (Figure 4.9b), differences between the simulations have begun to appear, as secondary convective development in the region of the initial updrafts is slightly further advanced in the Leapfrog simulation, which also displays a greater downshear spreading of the upper-level convective outflow. This spreading seems to be hindered by more horizontal than vertical motion immediately downshear of the system in the middle and upper levels of the Adams-Bashforth simulation.

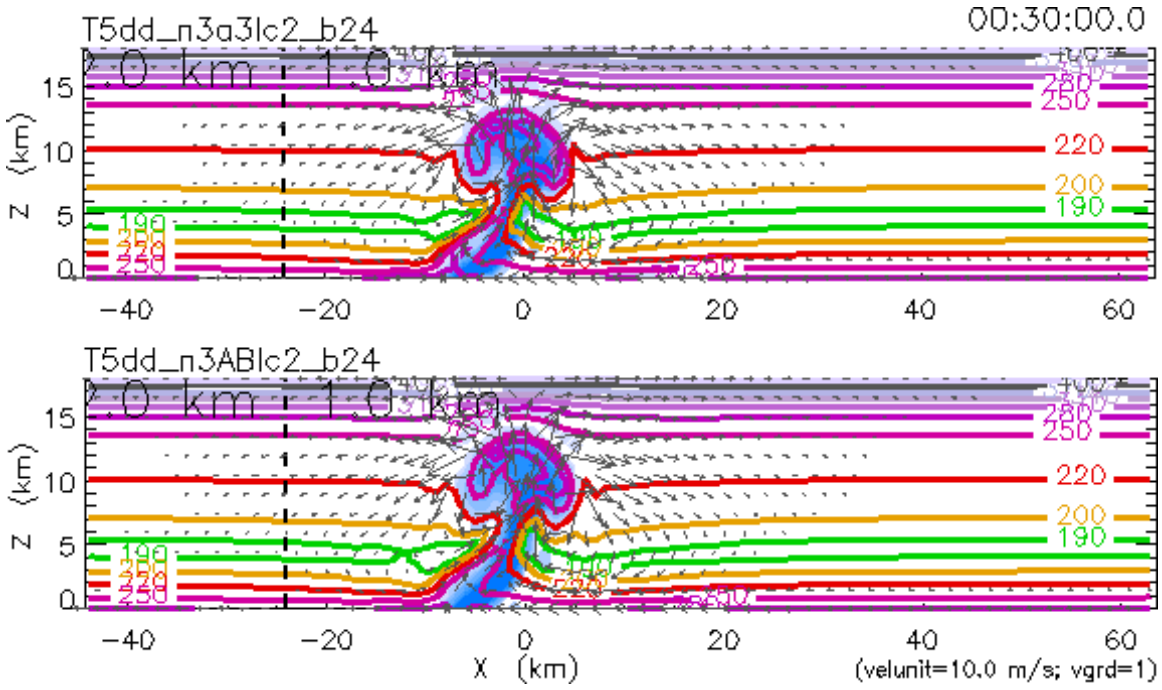

Figure 4.9a: Comparison of methods of time integration, at 0h 30m.

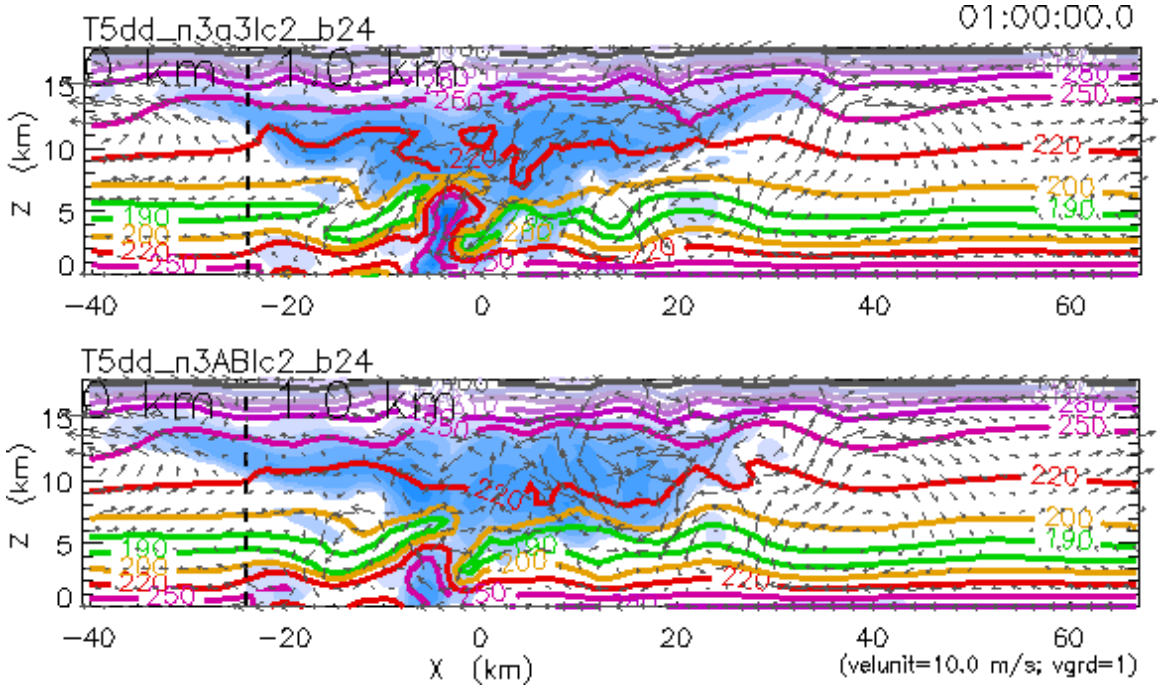

Figure 4.9b: Comparison of methods of time integration, at 1h 00m.

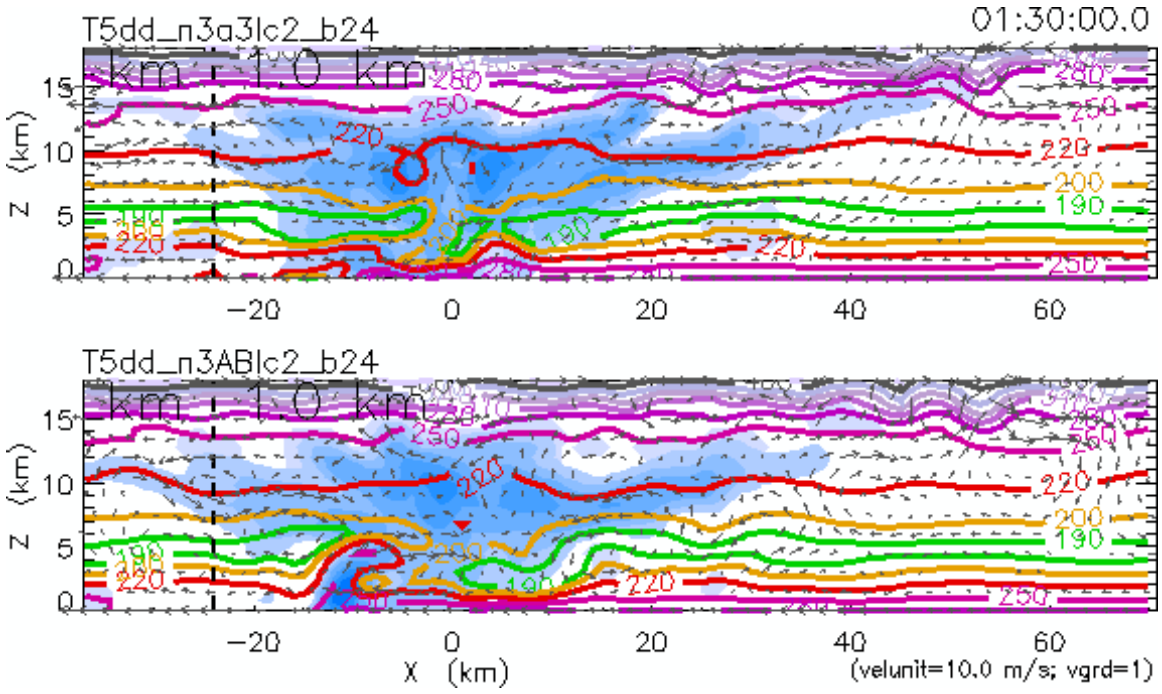

Figure 4.9c: Comparison of methods of time integration, at 1h 30m.

By 1h 30m (Figure 4.9c), updraft activity in the main convective region has waned slightly, although a new derivative cell is evident at this time immediately upshear of the initial convective point in the Adams-Bashforth simulation. By 2h 00m (Figure 4.9d) the cloud and precipitation system seems to have contracted further in both simulations, although evidence of a strong secondary updraft cell is evident in the central region of the convection in the upper levels of the Leapfrog simulation. Weak low-level secondary convection seems to persist in the Adams-Bashforth simulation, while a low-level cold pool has begun to develop more strongly in the Leapfrog simulation upshear of the initial convective point.

By 2h 30m (Figure 4.9e), the initial convective development has seemingly died in both simulations while a strong new cell has begun to form downshear, although more quickly in the Leapfrog simulation. Neither of the new convective cells seems to be driven by the developing low-level cold pool, which finally reaches the surface and begins

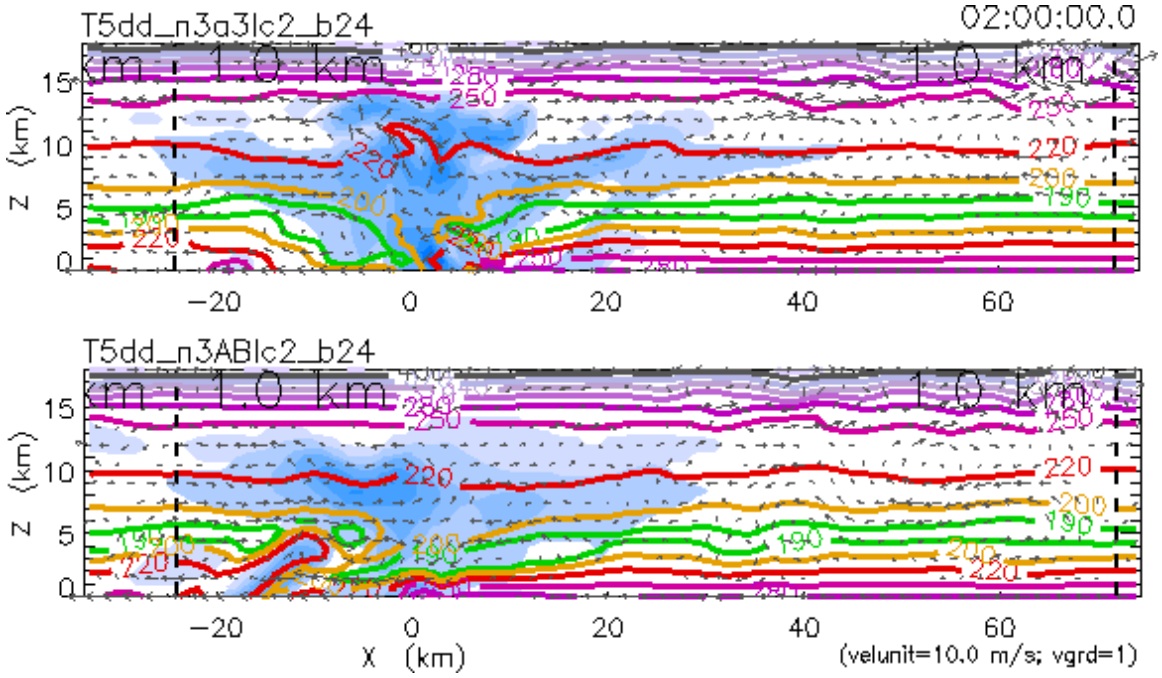

Figure 4.9d: Comparison of methods of time integration, at 2h 00m.

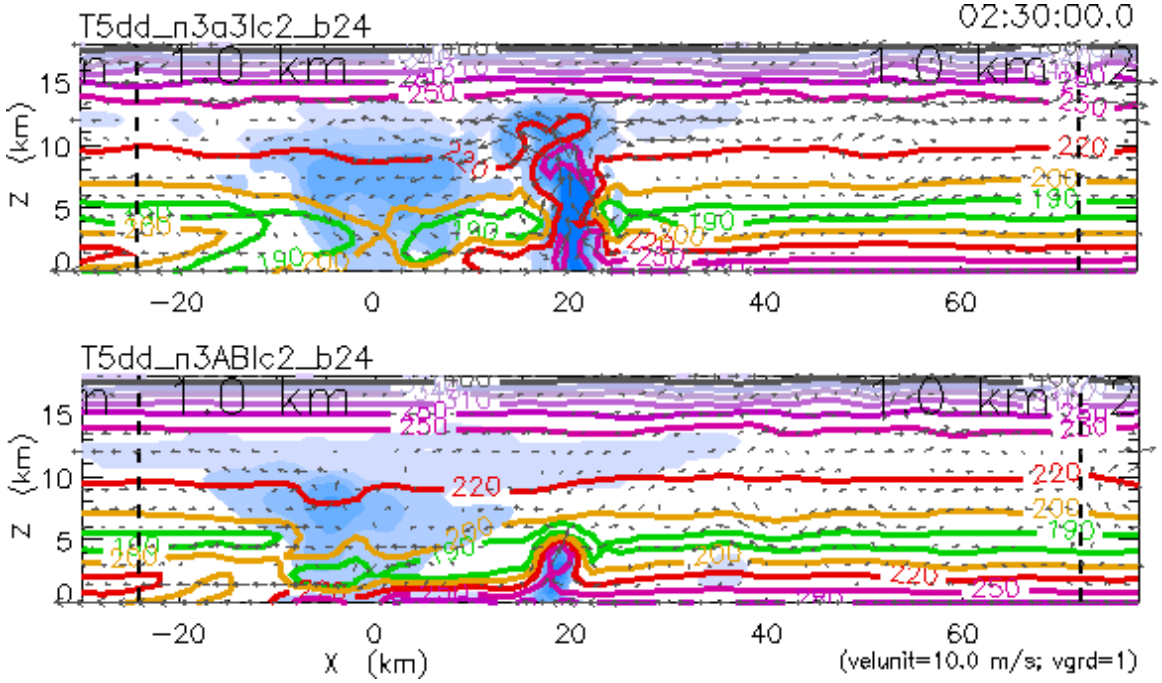

Figure 4.9e: Comparison of methods of time integration, at 2h 30m.

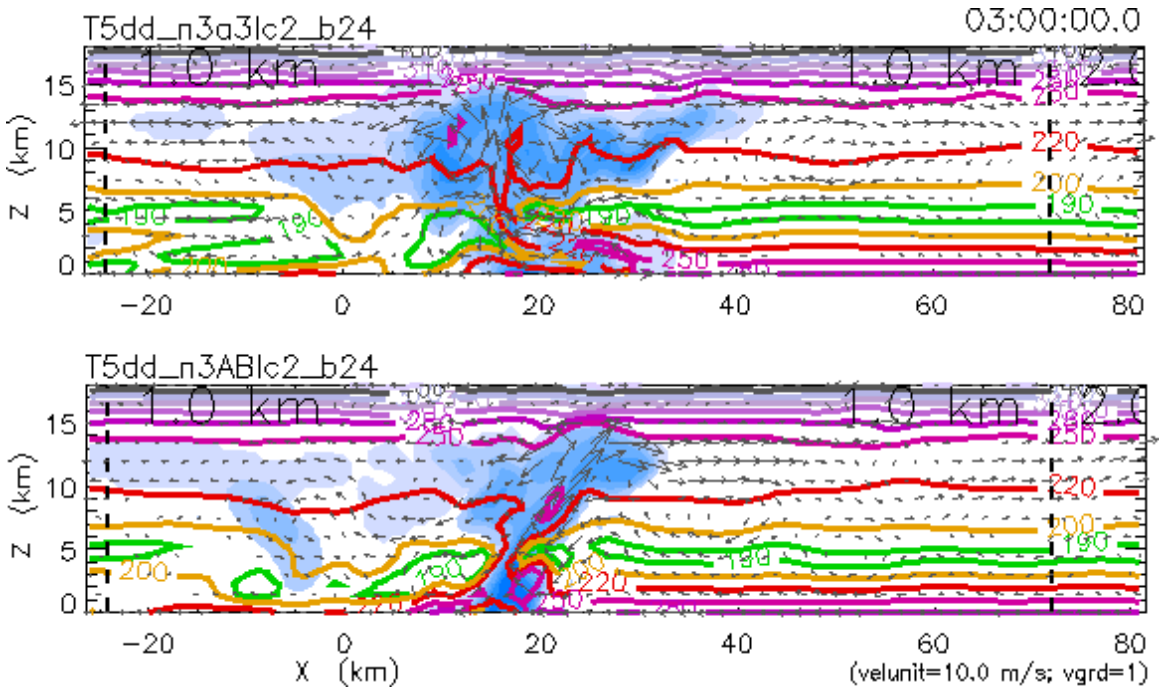

Figure 4.9f: Comparison of methods of time integration, at 3h 00m.

to propagate downshear in the Leapfrog simulation by 3h 00m (Figure 4.9f). By this time, it is evident that convective development occurs more quickly in the Leapfrog simulation than in the Adams-Bashforth simulation. While the low-level cold pool and gust front have begun to advance ahead of the main convective region by 3h 00m in the Leapfrog simulation, strongly-tilted secondary convection persists in the Adams-Bashforth simulation with still no indication of a developed propagating convective cold pool in the lower levels.

While the low-level convective cold pool seems to consolidate in the Leapfrog simulation by 3h 30m (Figure 4.9g), the secondary convective cell looks to be regenerating near its initial convective point in the Adams-Bashforth simulation. The low-level cold pool has yet to establish itself in the Adams-Bashforth simulation by 4h 00m (Figure 4.9h), while the advancing gust front and the initiation of forced convective updrafts are visible immediately downshear of the main convective region in the Leapfrog simulation by this time. By 4h 30m (Figure 4.9i), a self-sustaining or long-lived cinvective structure seems

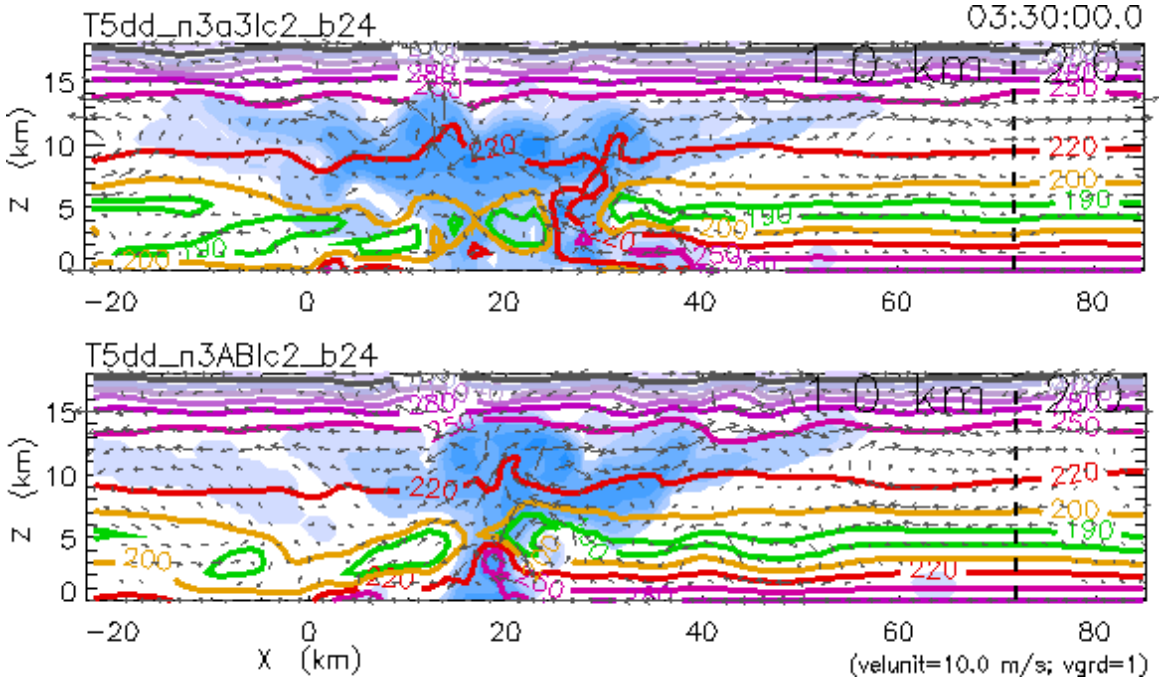

Figure 4.9g: Comparison of methods of time integration, at 3h 30m.

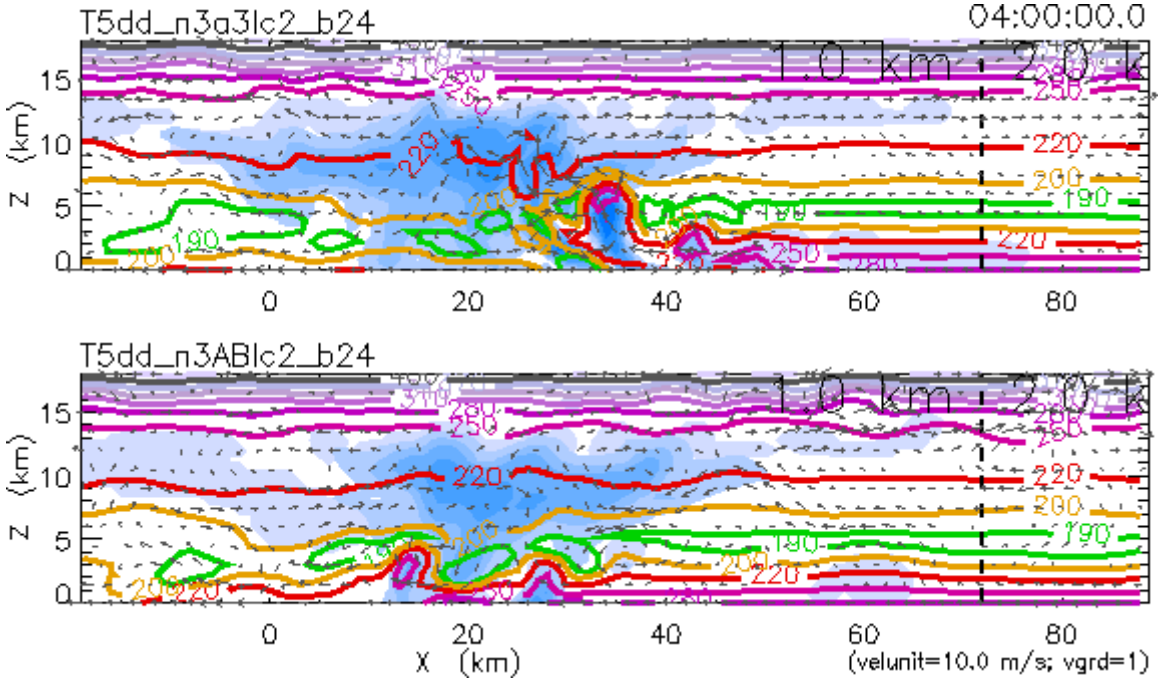

Figure 4.9h: Comparison of methods of time integration, at 4h 00m.

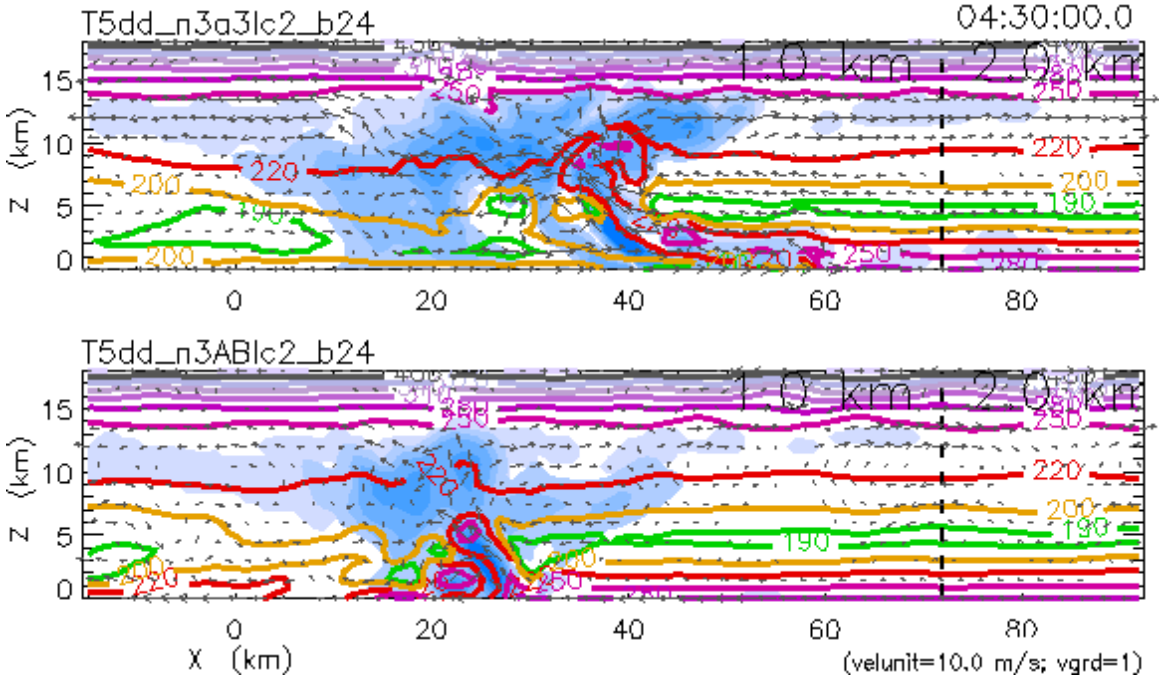

Figure 4.9i: Comparison of methods of time integration, at 4h 30m.

to have been established in the Leapfrog simulation, with new convection forced by the advancing gust front being advected rearward by the environmental flow to join the main convective region and produce convective and larger-scale downdrafts which feed the low-level cold pool and the continually-advancing pre-squall gust front. However, convection in the Adams-Bashforth simulation has yet to reach a self-sustaining long-lived phase by 5h 00m (Figure 4.9j), although by this time the convective cold pool of the Adams-Bashforth simulation does finally seem to have reached the surface by descending slowly through the warm low-levels in several small regions immediately downshear of the initial convective point.

By 5h 30m (Figure 4.9k), convection in the Adams-Bashforth simulation seems to have finally settled into a self-sustaining yet small-scale configuration, while the squall line in the Leapfrog simulation seems to have passed out of its long-lived mature phase with the rapid advance of the gust front far ahead of the main convective region and into the next

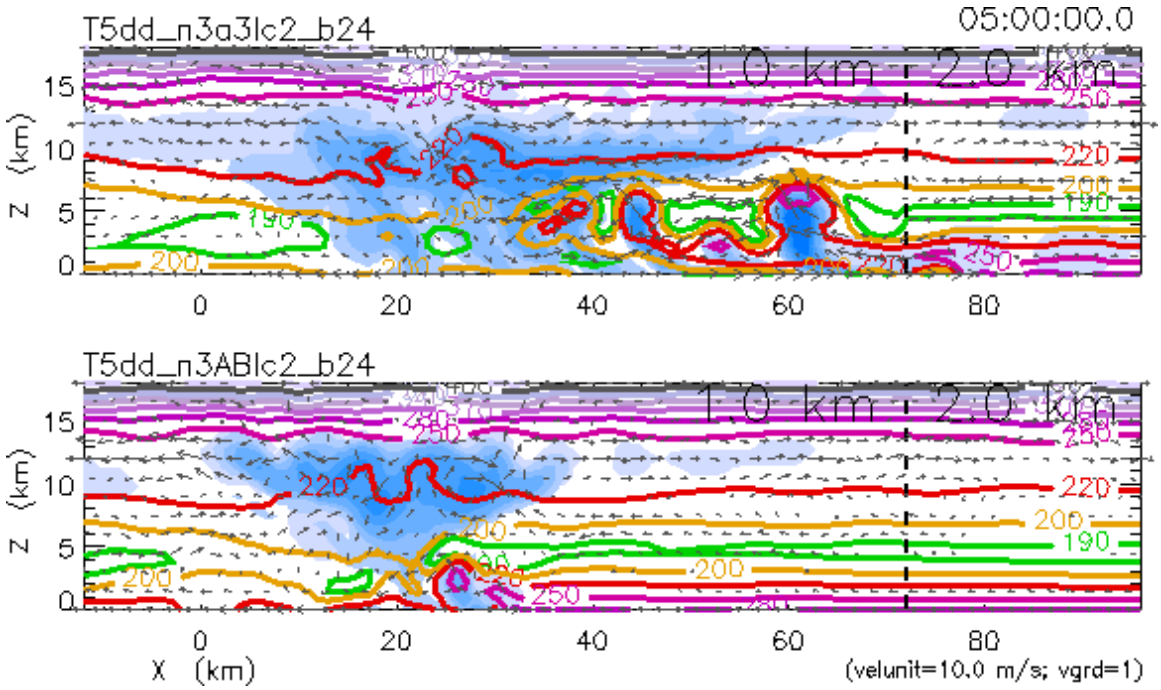

Figure 4.9j: Comparison of methods of time integration, at 5h 00m.

coarser domain of $\Delta x = 2$ km. The reader will note the smooth transition of fields between the fine and coarser domains at this interface, which is most evident with the presence of convective updrafts and moisture there and has been demonstrated in O97 (Figure 4.5). The development of new convective cells forced by the advancing gust front continues on both sides of this domain interface in the Leapfrog simulation through 6h 00m (Figure 4.9l), by which time a low-level cold pool has been established in the Adams-Bashforth simulation while new convective development remains slow.

4.4.6 Strength of the Derivative Constraint

In the SAFER method of numerical representation on nested domains, the derivative constraint is a parameter which ensures the continuity of fields across domain interfaces by effectively damping the amplitudes of signals which have wavelengths of a scale too small for accurate representation on the coarser domain. Thus, the derivative constraint is highly

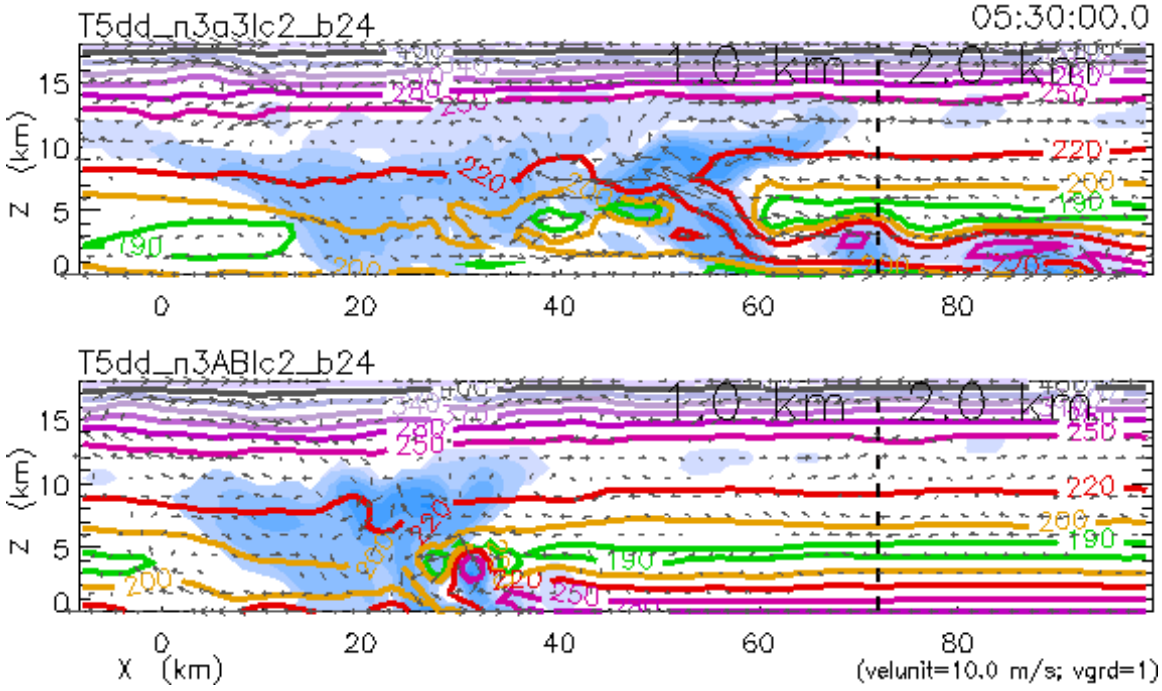

Figure 4.9k: Comparison of methods of time integration, at 5h 30m.

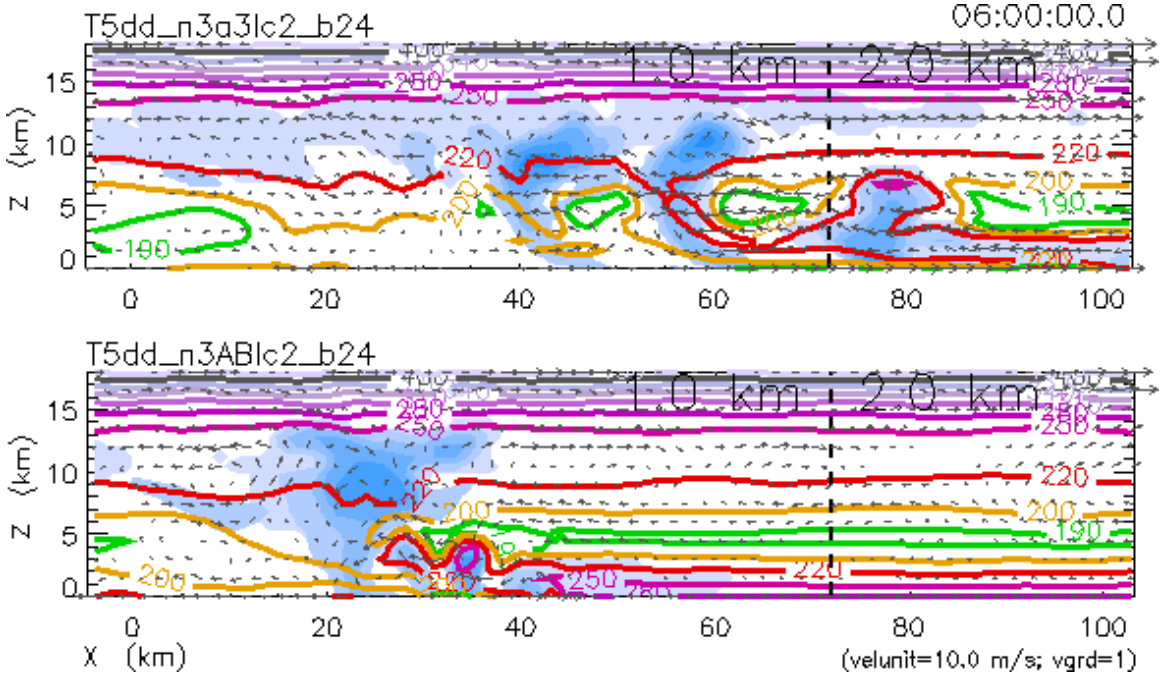

Figure 4.9l: Comparison of methods of time integration, at 6h 00m.

dependent upon the ratio of spatial resolution between adjacent domains. Commonly, this ratio is set by the user at 2, such that the finest domain of $\Delta x = 1$ km has outer interfaces with a domain of $\Delta x = 2$ km, as discussed earlier. For a signal which approaches the interface from the side of the finer domain, the wavelength of the signal must be great enough that it may be resolved on the coarser side of the interface. These considerations were discussed in detail in O87 and in DAOL92, and it may be sufficient to report here that the optimum value of the derivative constraint utilized by Ooyama is also 2, corresponding to the resolution ratio between adjacent domains.

Although the removal of signals which could produce noise in a domain of coarser resolution is the primary goal of this construct, a derivative constraint which is too strong would instead remove valuable small-scale information from the fields of interest. The removal of small-scale information by a derivative constraint which is too strong produces a simulation similar to the heavily-filtered results in which the Asselin parameter is less than optimal.

This effect can be noted in snapshots of simulations for both methods of time integration which are presented in Figure 4.10. The optimal value of the derivative constraint is represented by the middle frame in each snapshot, while weaker and stronger derivative constraints are represented by the upper and lower frames, respectively. Figure 4.10a presents snapshots at 3h 30m for the Leapfrog method of time integration for which the results of a strong derivative constraint may also be considered representative of results for an Asselin parameter which is less than the optimal value as described above. The second-order Adams-Bashforth method produces results similar to those of the Leapfrog method for strong derivative constraints (Figure 4.10b). These snapshots exhibit a distinct lack of detail for strong derivative constraints at later stages of convective development, such as

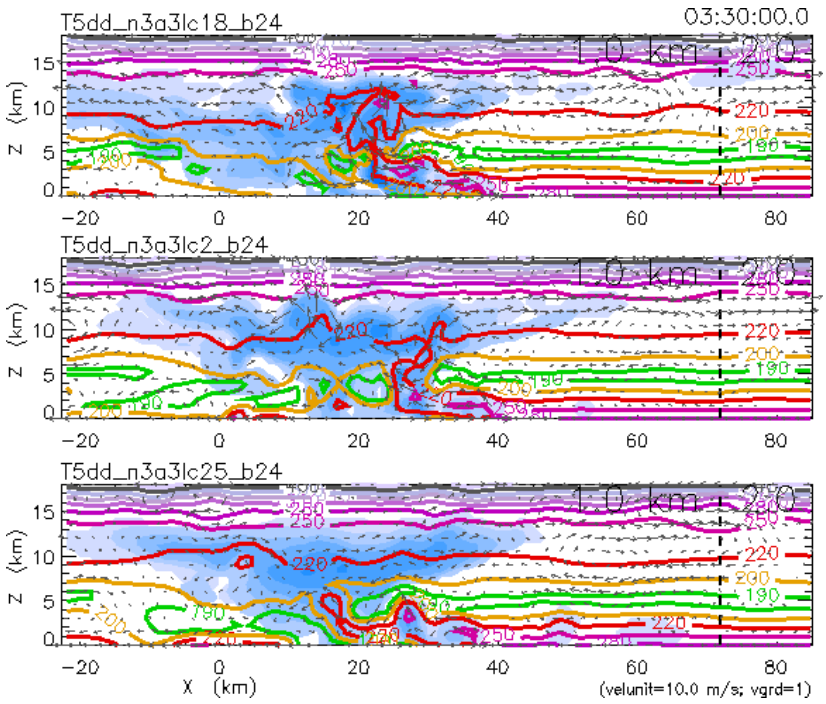

Figure 4.10a: Comparison of various strengths of the derivative constraint for the Leapfrog method of time integration, at 3h 30m.

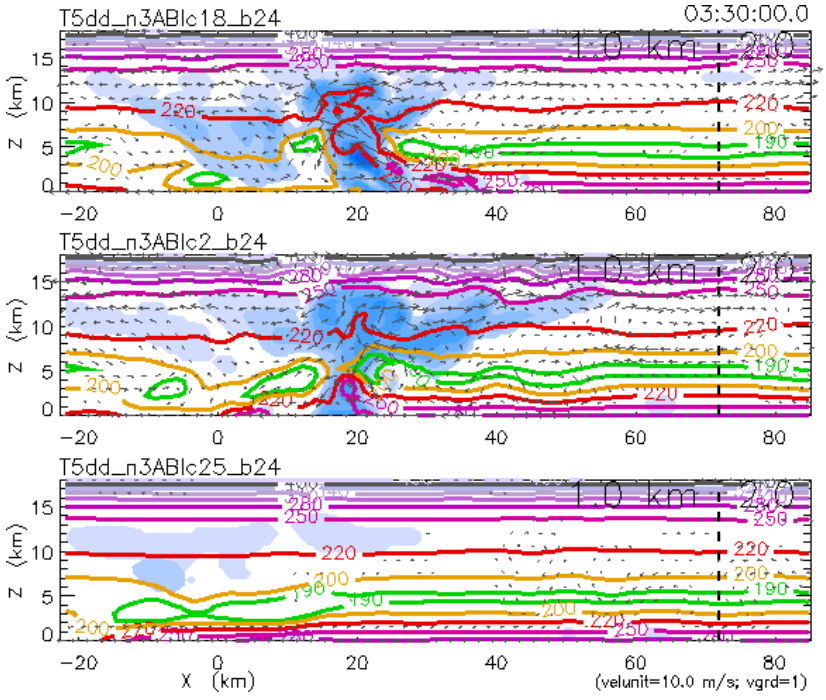

Figure 4.10b: Comparison of various strengths of the derivative constraint for the second-order Adams-Bashforth method, at 3h 30m.

around 3h 30m, when compared to simulations which employed a derivative constraint of optimal or weaker values.

4.4.7 Weak-to-Moderate Initial Shear

For ease of analysis, the unpublished experiments performed by Ooyama which examine the effects of various strengths of the initial low-level shear are divided into two regimes. Simulations which were initialized with a weak-to-moderate initial low-level shear layer will be discussed first, and are displayed in Figure 4.11. These are simulations for which shear strengths of 2, 5, 8, and 10 m s^{-1} were prescribed over a surface layer of depth scale $z_s = 1$ km, and which may be compared to the upper half of the Hovmöller diagram which was presented in O95 and is reproduced here in Figure 4.4. Precipitation traces in the lower half of Figure 4.4 may be compared with simulations presented here for initial conditions of moderate-to-strong low-level shear layers, for which shear strengths of 10, 12, 15, and 20 m s^{-1} were prescribed over a surface layer of depth scale $z_s = 1$ km. Snapshots of these simulations are displayed in Figure 4.12.

At 0h 20m (Figure 4.11a), convective updrafts initiated by the prescribed warm bubble at the lower boundary already exhibit a downshear tilt in the simulations which employ a moderate low-level shear layer. The updraft in the simulation which employs a shear layer strength of 2 m s^{-1} is nearly vertical. This may also be noted in the snapshots at 0h 30m (Figure 4.11b), by which time all of the weak-to-moderate shear simulations have developed a convective updraft through nearly the full depth of the troposphere with compensating downdrafts on both the upshear and downshear sides. By this time, the 8 and 10 m s^{-1} simulations demonstrate noticeably more downshear tilt in their convective updrafts than the weakly-sheared simulations. Updrafts which have developed under the

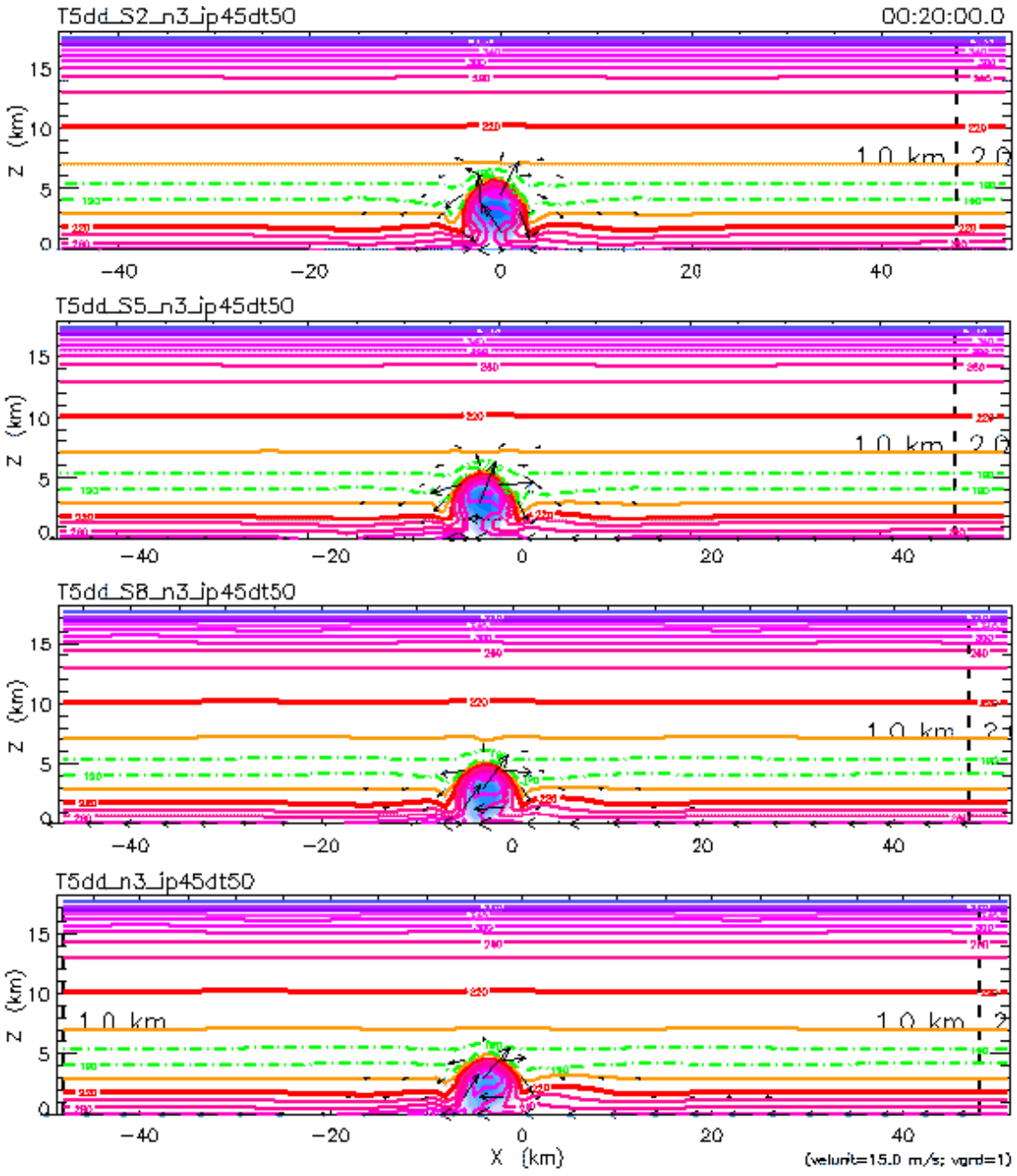

Figure 4.11a: Simulations for initial shears of 2, 5, 8, and 10 m s^{-1} for $z_s = 1$ km, at 0h 20m.

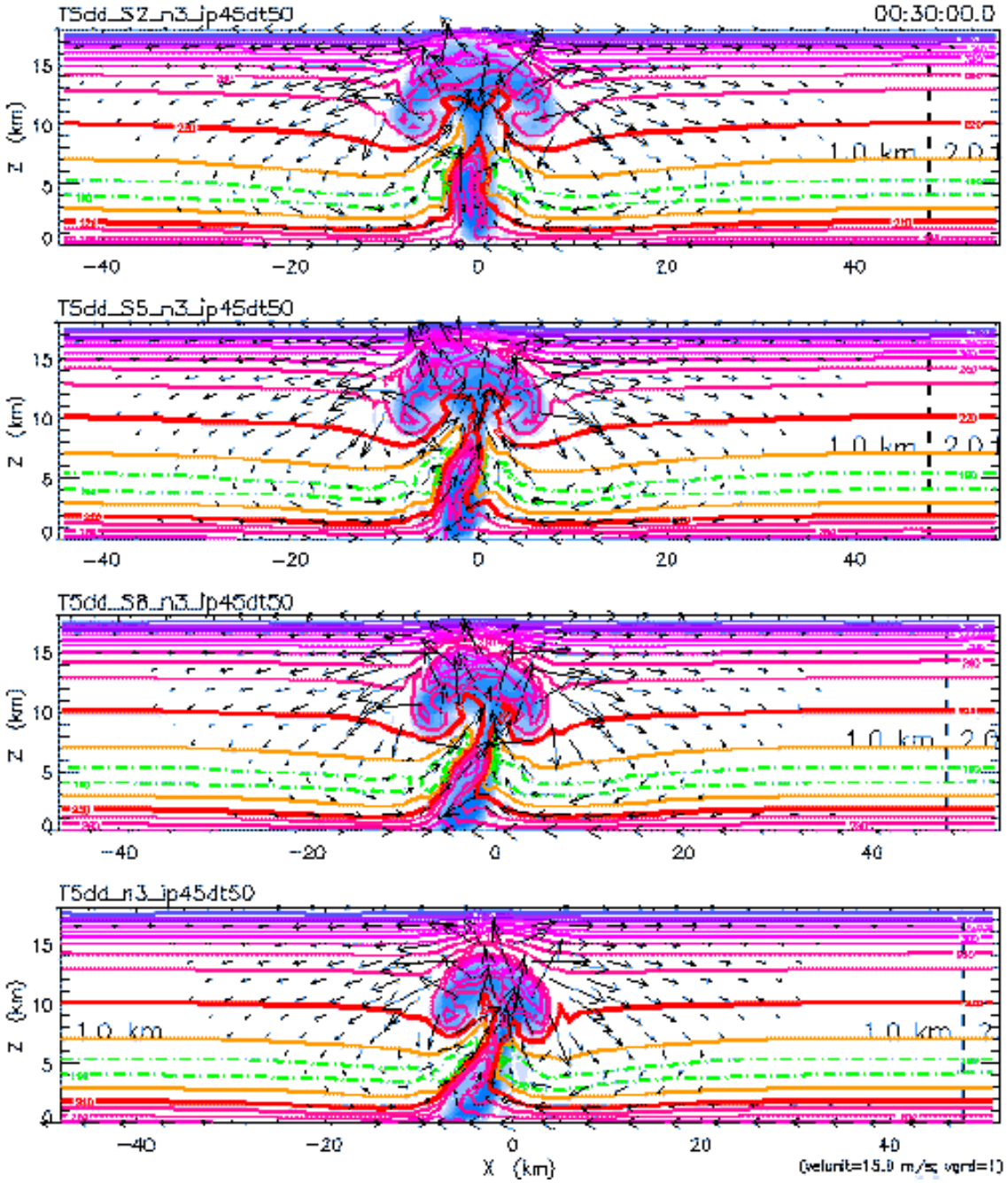

Figure 4.11b: Simulations for initial shears of 2, 5, 8, and 10 m s^{-1} for $z_s = 1$ km, at 0h 30m.

influence of weaker shear remain quite vertical through 0h 40m (Figure 4.11c), while the downshear tilt of the updraft plumes in the moderately-sheared simulations has become more pronounced by this time.

By 0h 50m (Figure 4.11d), the updraft plumes in the weakly-sheared simulations have become less coherent, and the moisture fields remain quite vertically oriented throughout the depth of the troposphere while showing only marginal influence of the ambient vertical shear and environmental flow fields. The 10 m s^{-1} simulation has maintained a downshear-tilted updraft through this time, with evidence of strong convective downdrafts ahead (downshear) of the updraft region and beneath the pre-squall upper-level outflow region. However, by 1h 15m (Figure 4.11e) the initial convective updrafts in each of these weak-to-moderate shear simulations has all but died out completely, although some evidence of continued weak convective motions are evident in the entropy field for the 5 and 8 m s^{-1} simulations.

At 1h 40m (Figure 4.11f), the regeneration of convection on the edges of the low-level convective outflow region is evident in the weakly-sheared simulations, while weak convective motions persist in the low levels immediately upshear of the initial convective point in the moderately-sheared simulations. In the 2 and 5 m s^{-1} simulations, new convection which is initiated immediately downshear of the low-level convective outflow is tilted upshear, back toward the convective debris which remains in the middle and upper levels from the initial convective event. This upshear tilt of the secondary convection in the weakly-sheared simulations has become more pronounced by 2h 05m (Figure 4.11g), while secondary convection has just become evident on the downshear edge of the low-level convective outflow region in both of the moderately-sheared simulations.

Downdrafts due to melting and evaporation seem to have significantly strengthened

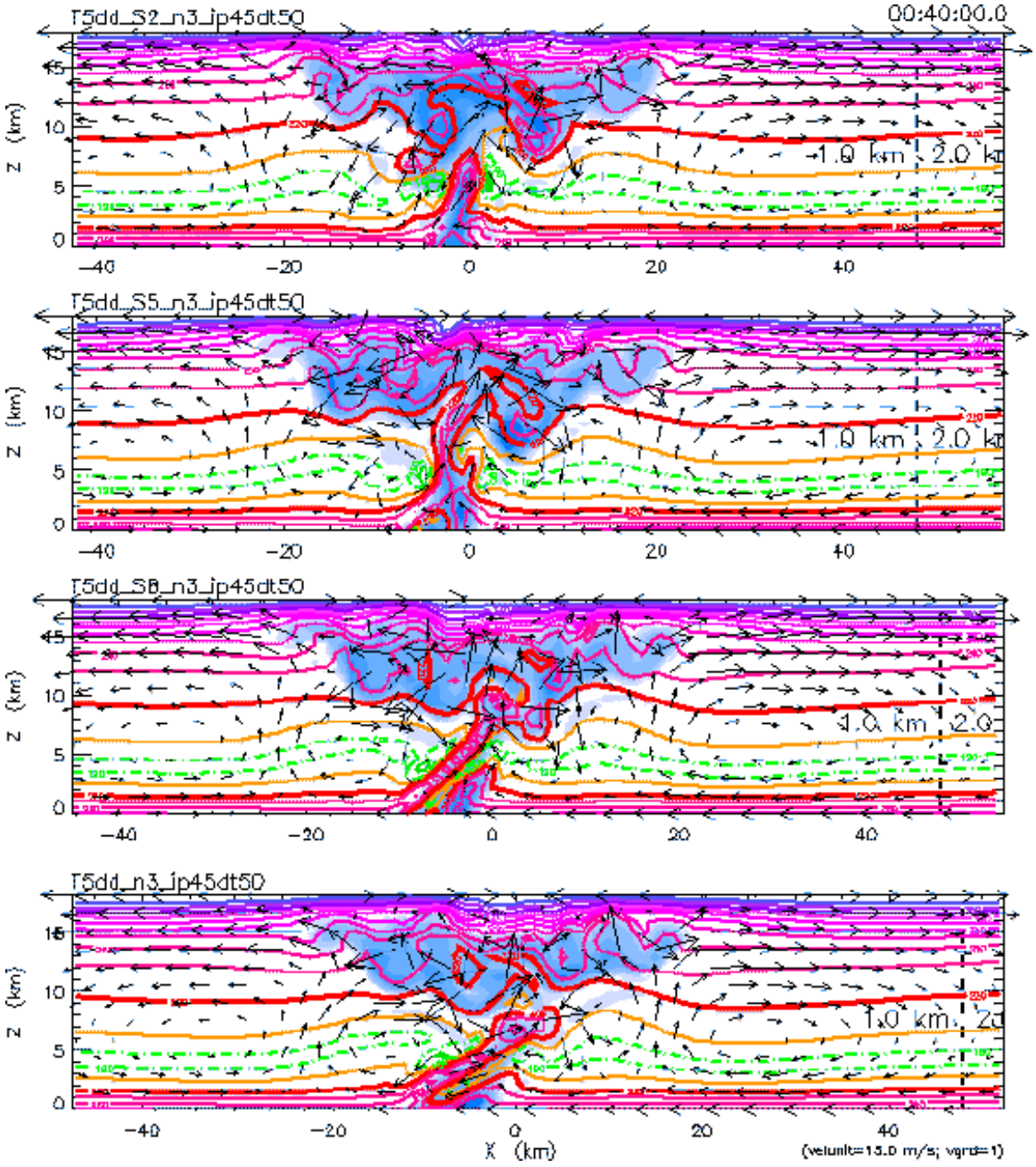

Figure 4.11c: Simulations for initial shears of 2, 5, 8, and 10 m s^{-1} for $z_s = 1$ km, at 0h 40m.

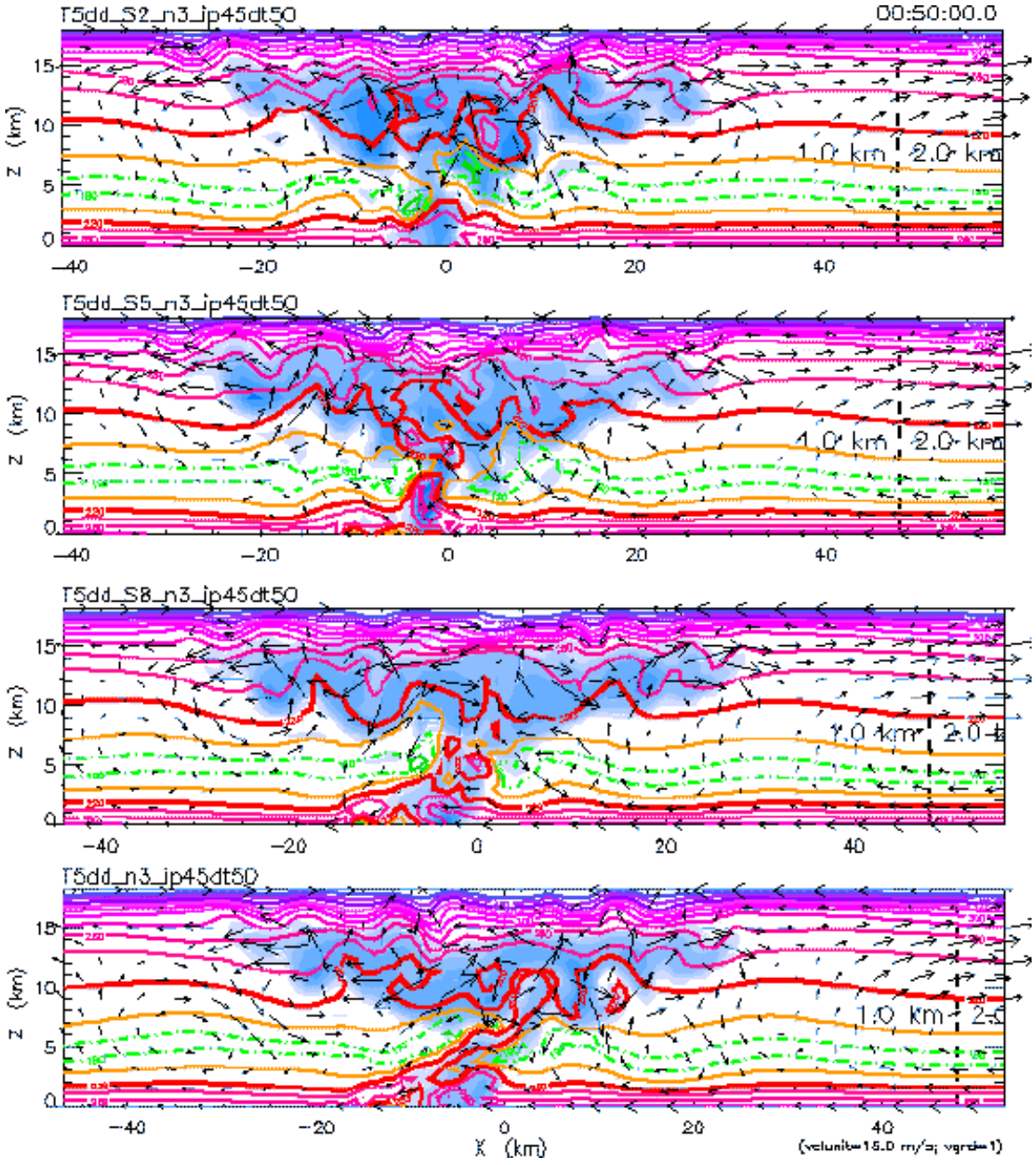

Figure 4.11d: Simulations for initial shears of 2, 5, 8, and 10 m s^{-1} for $z_s = 1$ km, at 0h 50m.

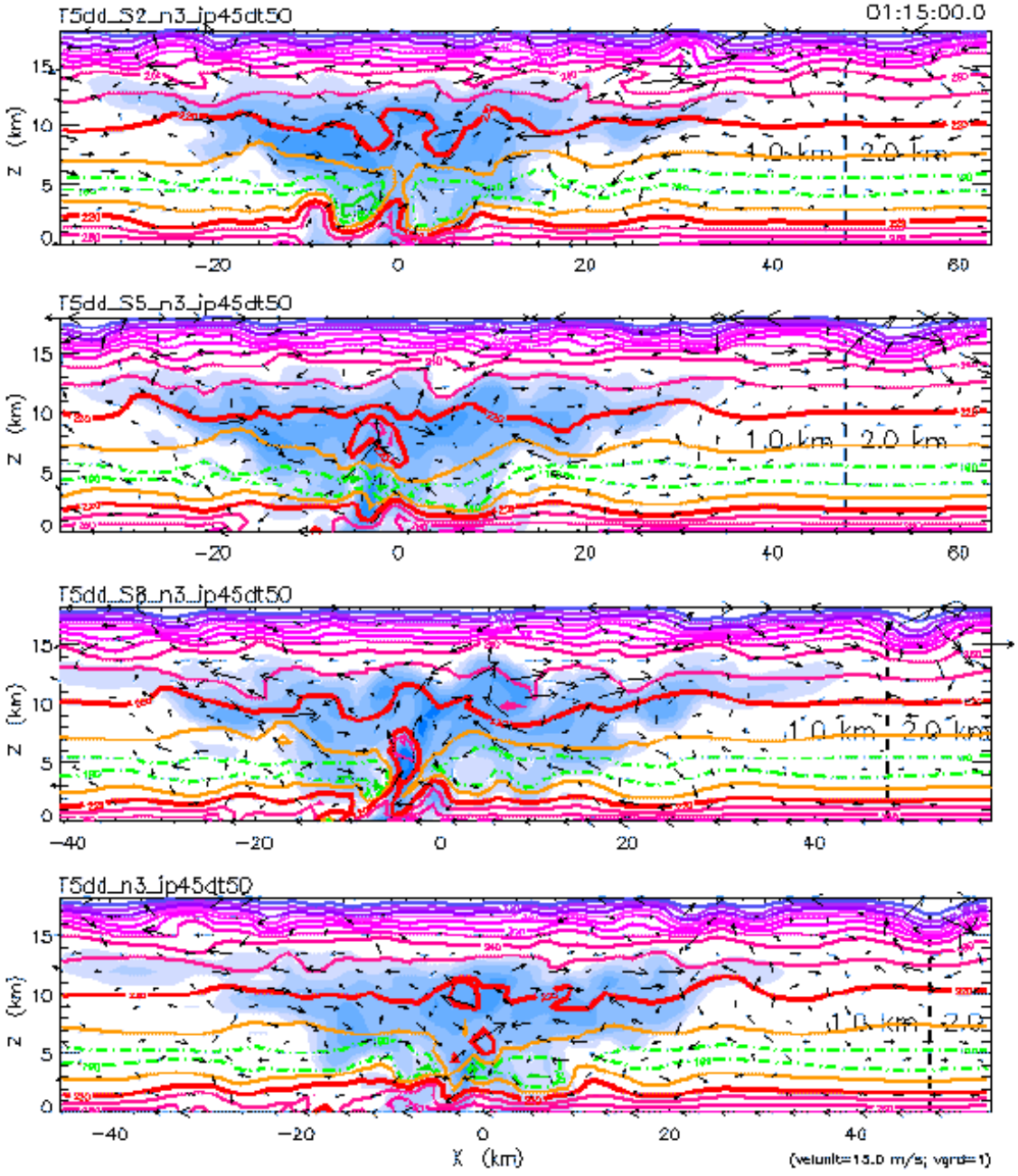

Figure 4.11e: Simulations for initial shears of 2, 5, 8, and 10 m s^{-1} for $z_s = 1$ km, at 1h 15m.

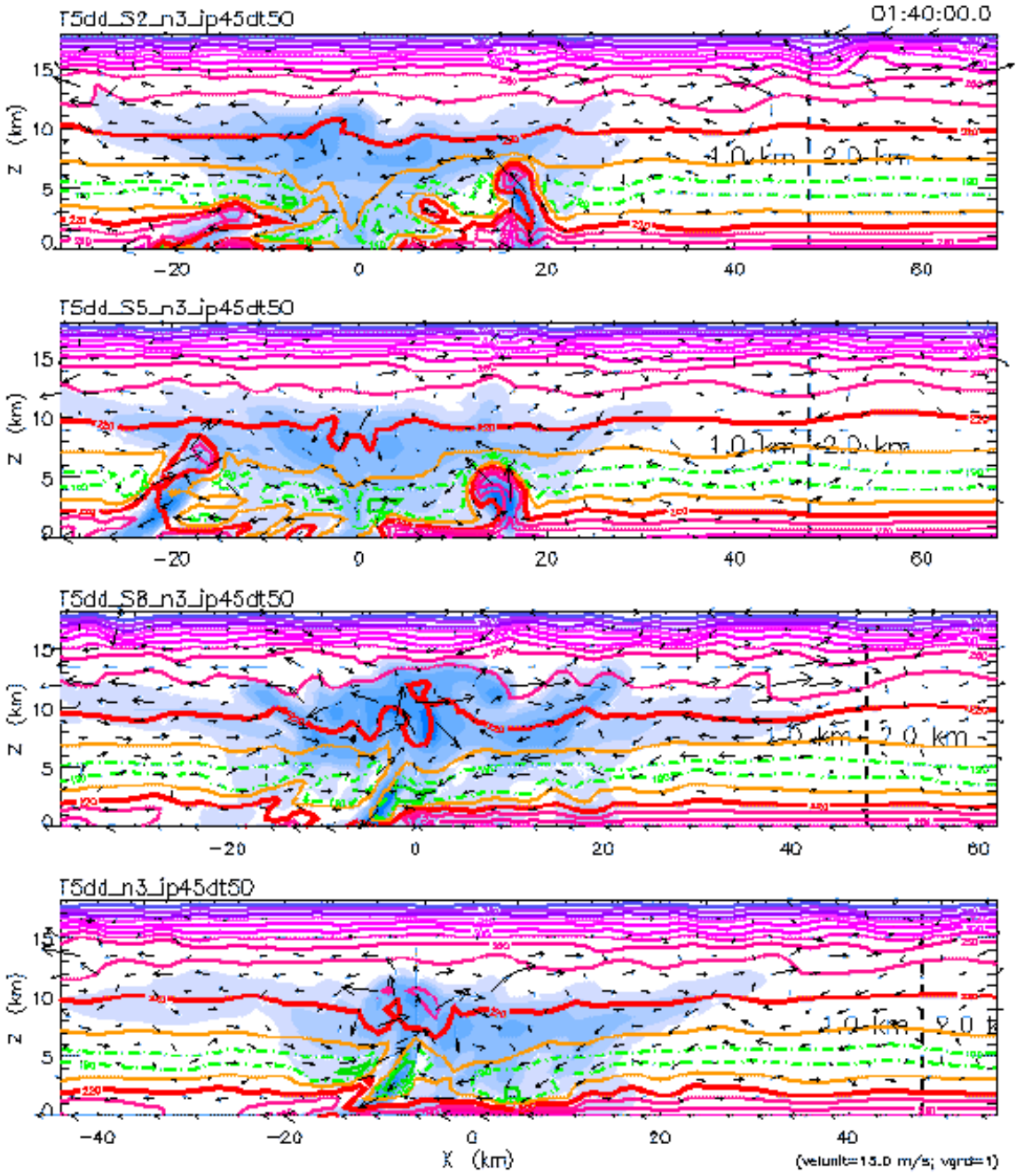

Figure 4.11f: Simulations for initial shears of 2, 5, 8, and 10 m s^{-1} for $z_s = 1$ km, at 1h 40m.

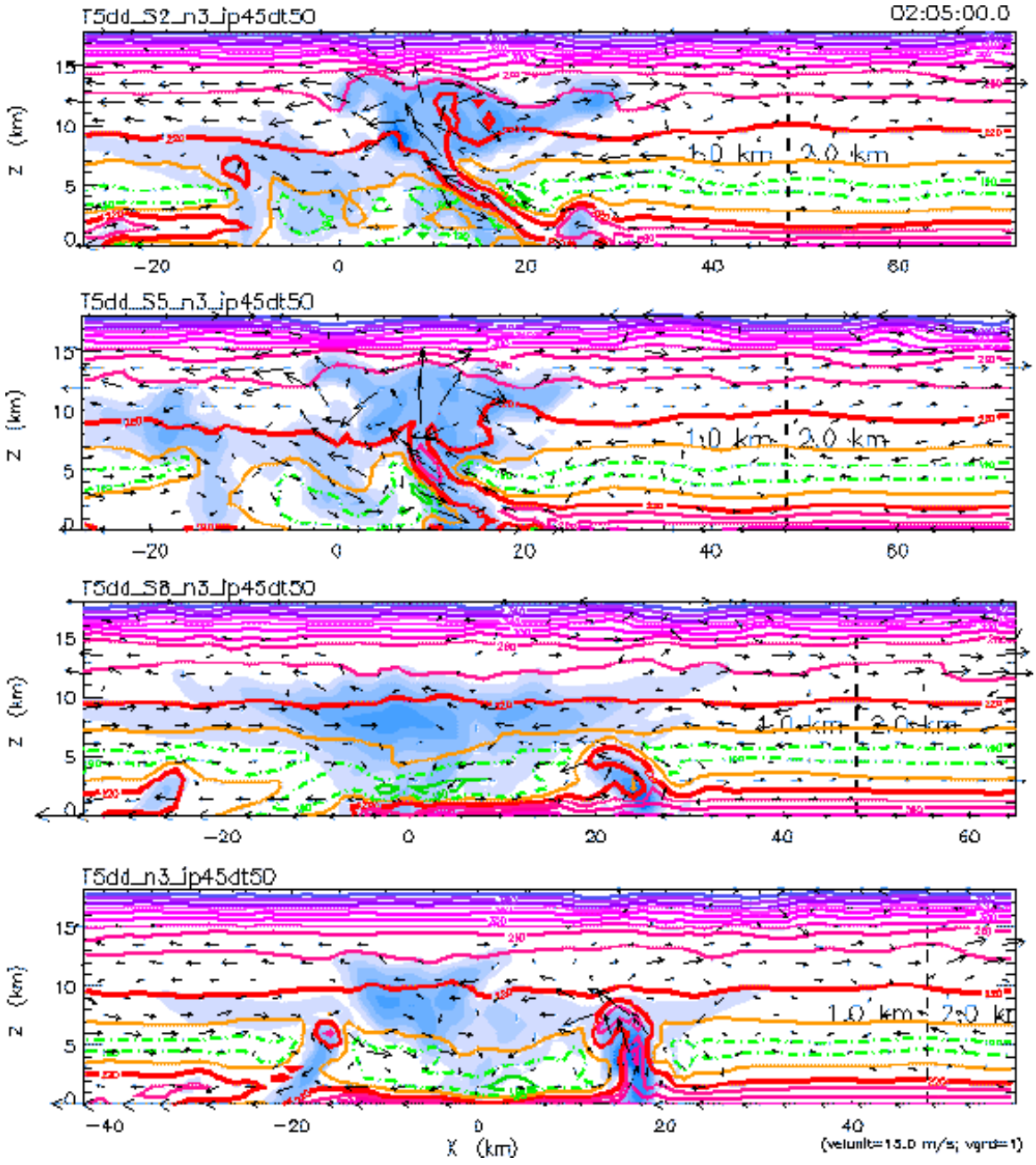

Figure 4.11g: Simulations for initial shears of 2, 5, 8, and 10 m s^{-1} for $z_s = 1$ km, at 2h 05m.

the low-level convective cold pool in the weakly-sheared simulations by 2h 30m (Figure 4.11h), which demonstrate little further regeneration of strong convection between this time and when the low-level convective outflows in the 2 and 5 m s^{-1} simulations cross the interface with the next coarser domain around 3h 45m (Figure 4.11i). Over this period, secondary convection in the moderately-sheared simulations has fully developed with a slight upshear tilt in each of these simulations, and demonstrates a slightly more rapid cycle of convective growth and dissipation in the 10 m s^{-1} simulation while a coherent upshear-tilted convective plume persists in the 8 m s^{-1} simulation through the snapshot at 3h 45m.

By 5h 00m (Figure 4.11j), the low-level convective outflow has crossed the interface with the next coarser domain in each of these weak-to-moderate shear simulations. Although sporadic convective regeneration is evident by this time in the 2, 5, and 8 m s^{-1} simulations, the 10 m s^{-1} simulation displays a remarkable structural similarity with the observations of tropical squall lines which were discussed extensively in Chapter 2. After the following discussion of the moderate-to-strong shear simulations, this particular simulation will be revisited with further evidence supporting these structural similarities.

4.4.8 Moderate-to-Strong Initial Shear

In agreement with the conclusions presented in O95, convection is seemingly inhibited by moderate-to-strong strengths of the initial environmental shear. At 0h 20m (Figure 4.12a), this inhibition is already evident in a simulation which employs 20 m s^{-1} initial environmental shear over a surface layer of depth scale $z_s = 1$ km. Despite the strong upshear advection of the initial temperature/moisture bubble introduced to the domain as a convective trigger, by 0h 30m (Figure 4.12b) a strong convective updraft has begun to

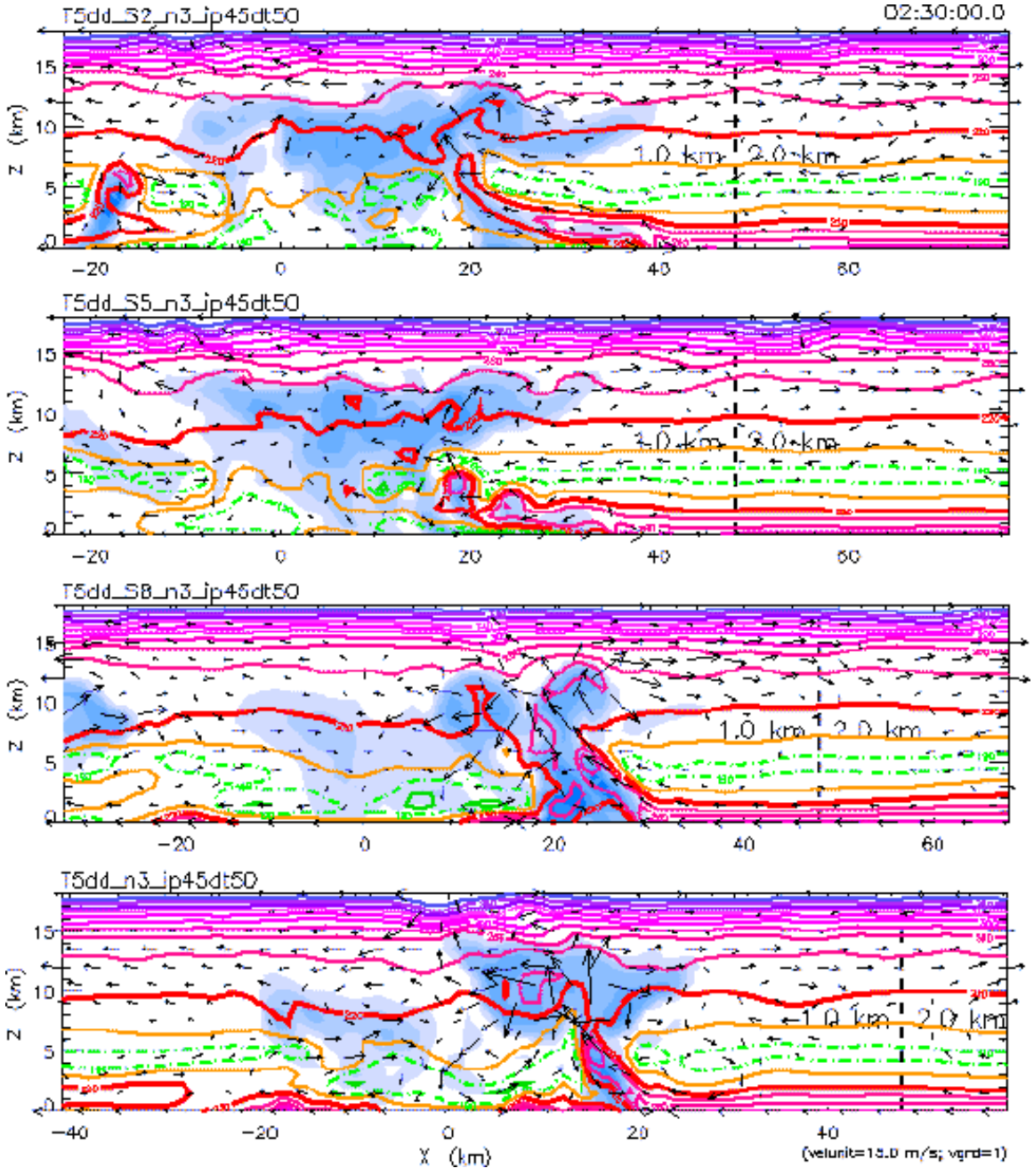

Figure 4.11h: Simulations for initial shears of 2, 5, 8, and 10 m s^{-1} for $z_s = 1$ km, at 2h 30m.

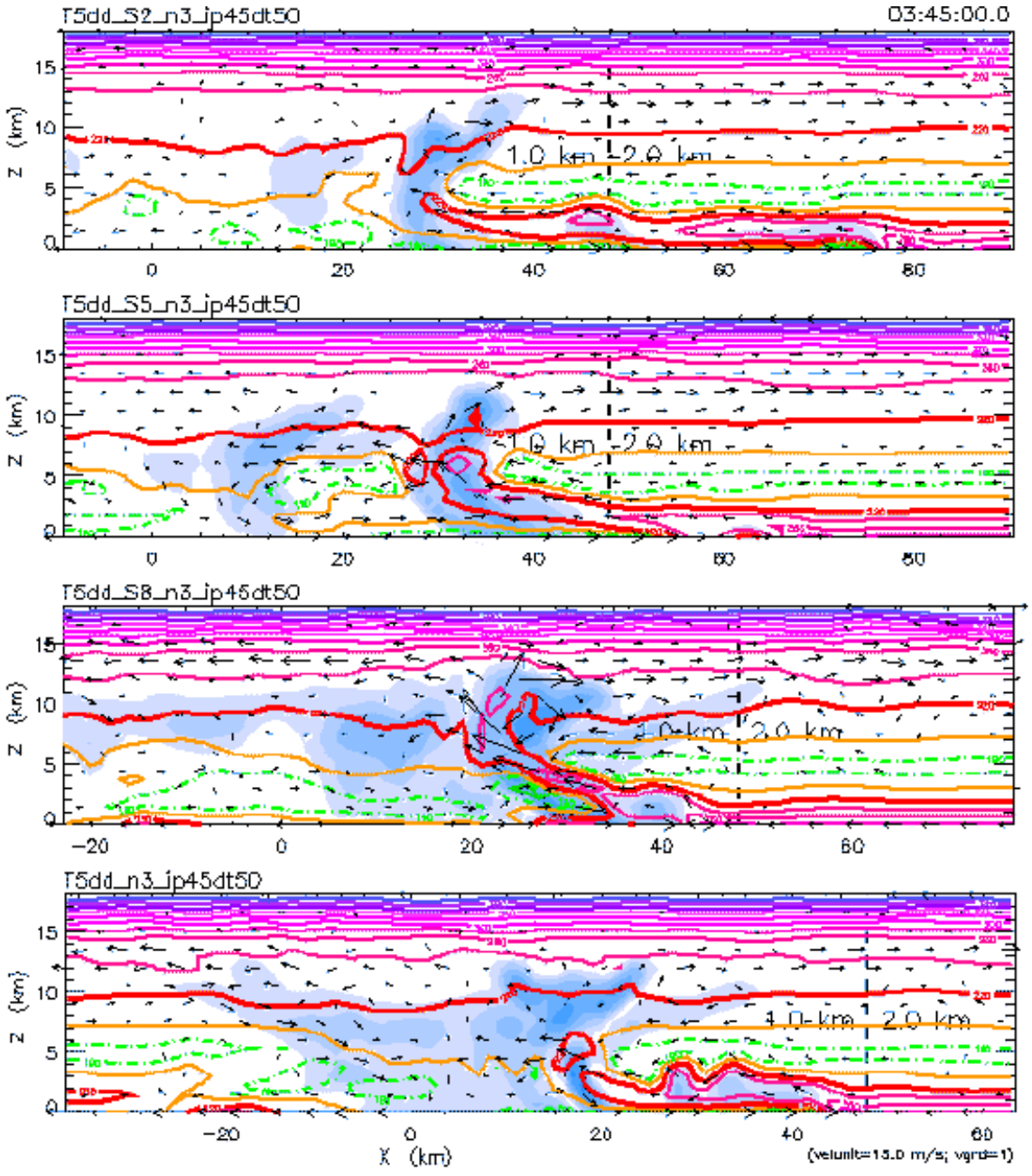

Figure 4.11i: Simulations for initial shears of 2, 5, 8, and 10 m s^{-1} for $z_s = 1$ km, at 3h 45m.

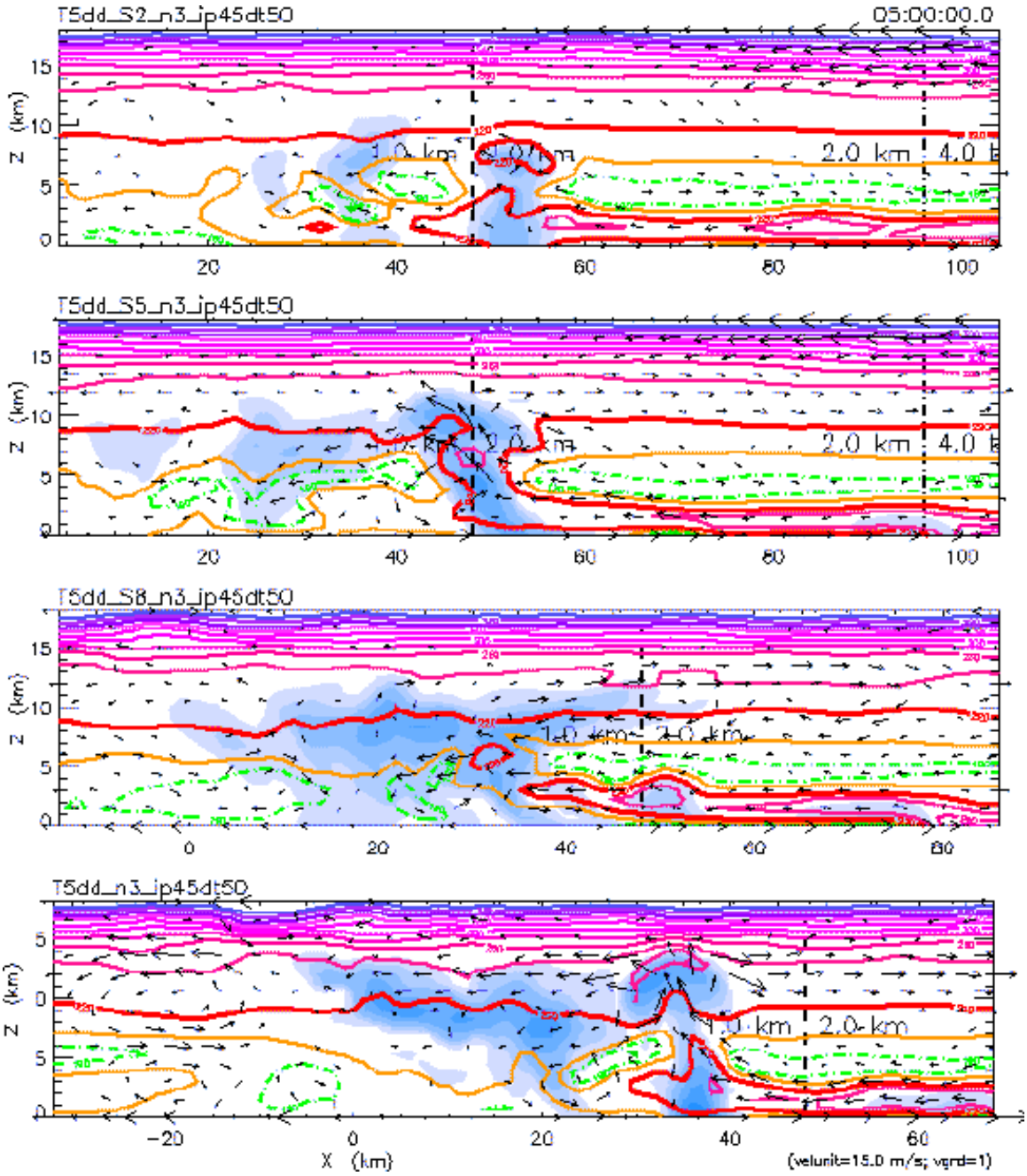

Figure 4.11j: Simulations for initial shears of 2, 5, 8, and 10 m s^{-1} for $z_s = 1$ km, at 5h 00m.

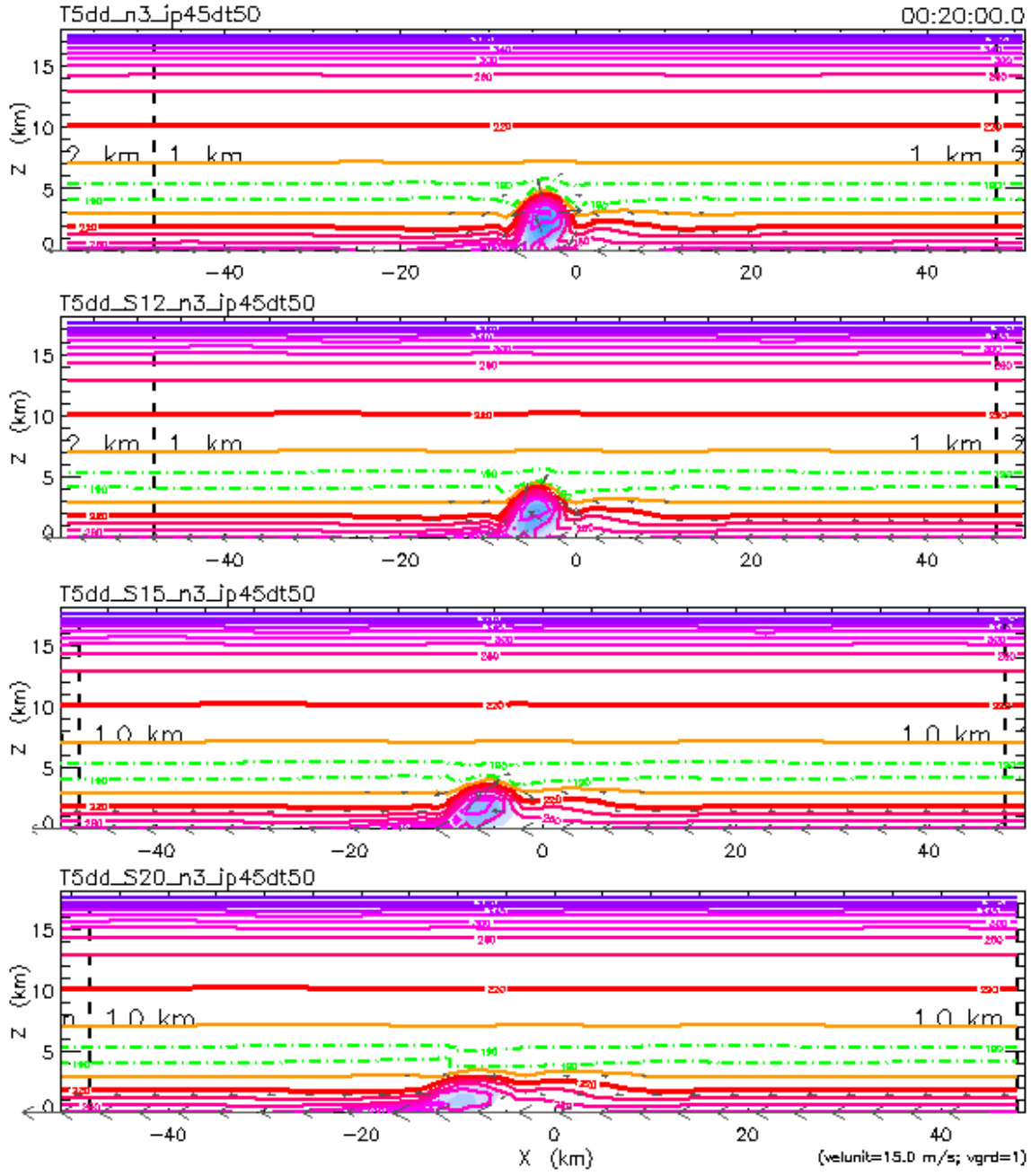

Figure 4.12a: Simulations for initial shears of 10, 12, 15, and 20 m s^{-1} for $z_s = 1$ km, at 0h 20m.

develop in all but the strongest of the shear conditions. While convection in the 10 m s^{-1} simulation proceeds as discussed above, less coherent downshear-tilted initial convective plumes are evident in the 12 and 15 m s^{-1} simulations by 0h 40m (Figure 4.12c).

By 0h 50m (Figure 4.12d), convection in the 20 m s^{-1} simulation has finally fully developed, although the lowest levels of the convective updrafts in the two strongly-sheared simulations demonstrate some of the detrimental effects of this strong ambient low-level flow in the upshear advection of the low-level moisture and temperature fields. Through 1h 15m (Figure 4.12e) and 1h 40m (Figure 4.12f), the strong downshear advection of the mid- and upper-level convective outflow becomes increasingly evident, and the formation of a middle- and low-level convective cold pool from the descent and evaporation of moisture-laden convective debris can be followed through 2h 05m (Figure 4.12g). By this time, secondary convection has developed on the downshear side of the low-level convective cold pool in all but the most strongly-sheared simulations.

The development of secondary convection slightly more ahead of the initial convective region in the 15 m s^{-1} simulation than in the more moderately-sheared simulations becomes more significant with time. By 2h 30m (Figure 4.12h), it is evident that this more distant jump in the convective activity has diminished the ability of the cold pool, which was left behind by the initial convective activity and debris, to assist in the formation of a low-level region of convergence between the environmental flow and the advancing low-level cold pool. Such a region of low-level convergence is given the opportunity to form in the moderately-sheared simulations, and may be shown to be vital to the sustenance of subsequent convective events.

Such assistance to the development of secondary convection is most absent from the 20 m s^{-1} simulation, which by 3h 45m (Figure 4.12i) has developed a secondary plume

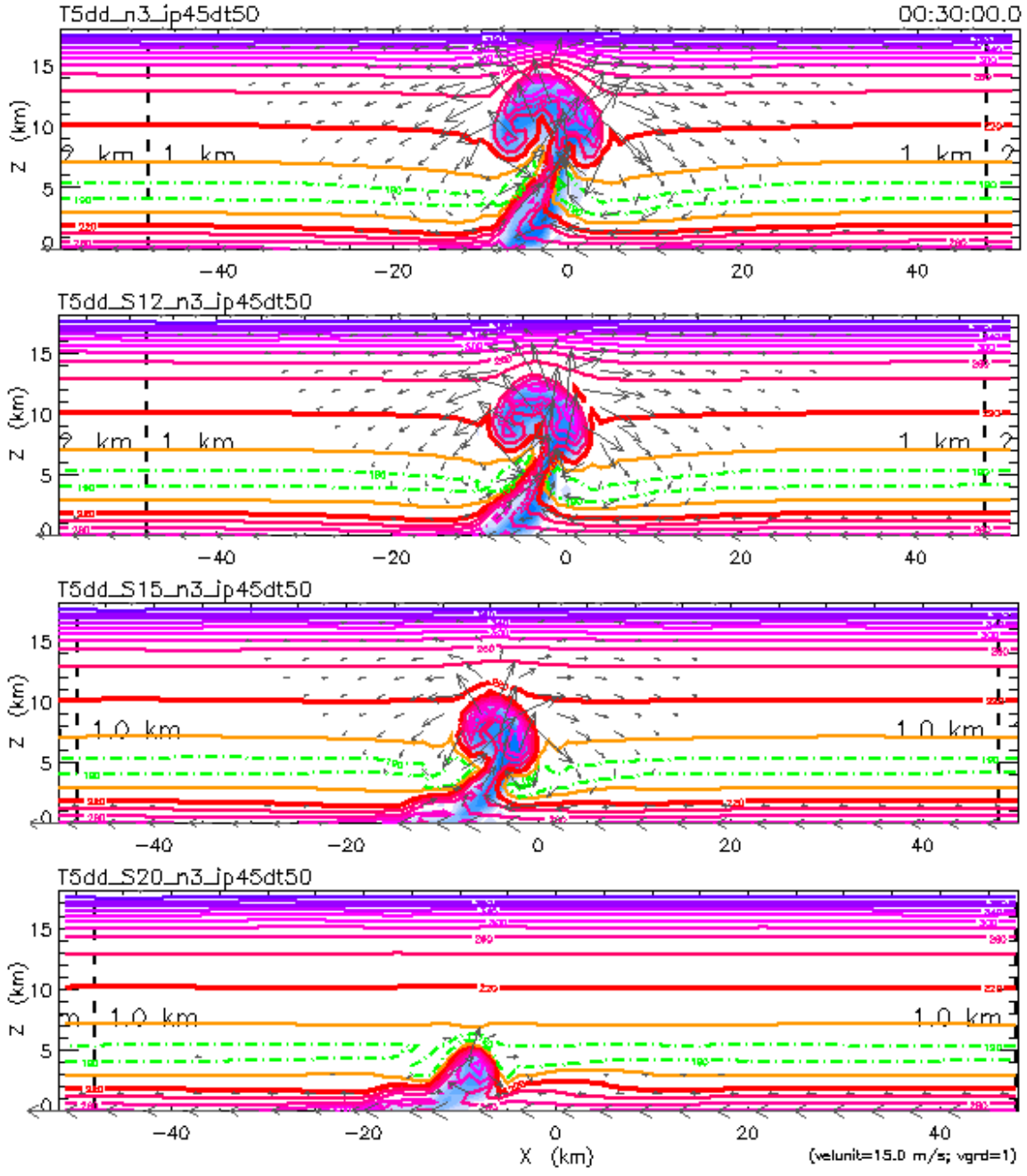

Figure 4.12b: Simulations for initial shears of 10, 12, 15, and 20 m s^{-1} for $z_s = 1$ km, at 0h 30m.

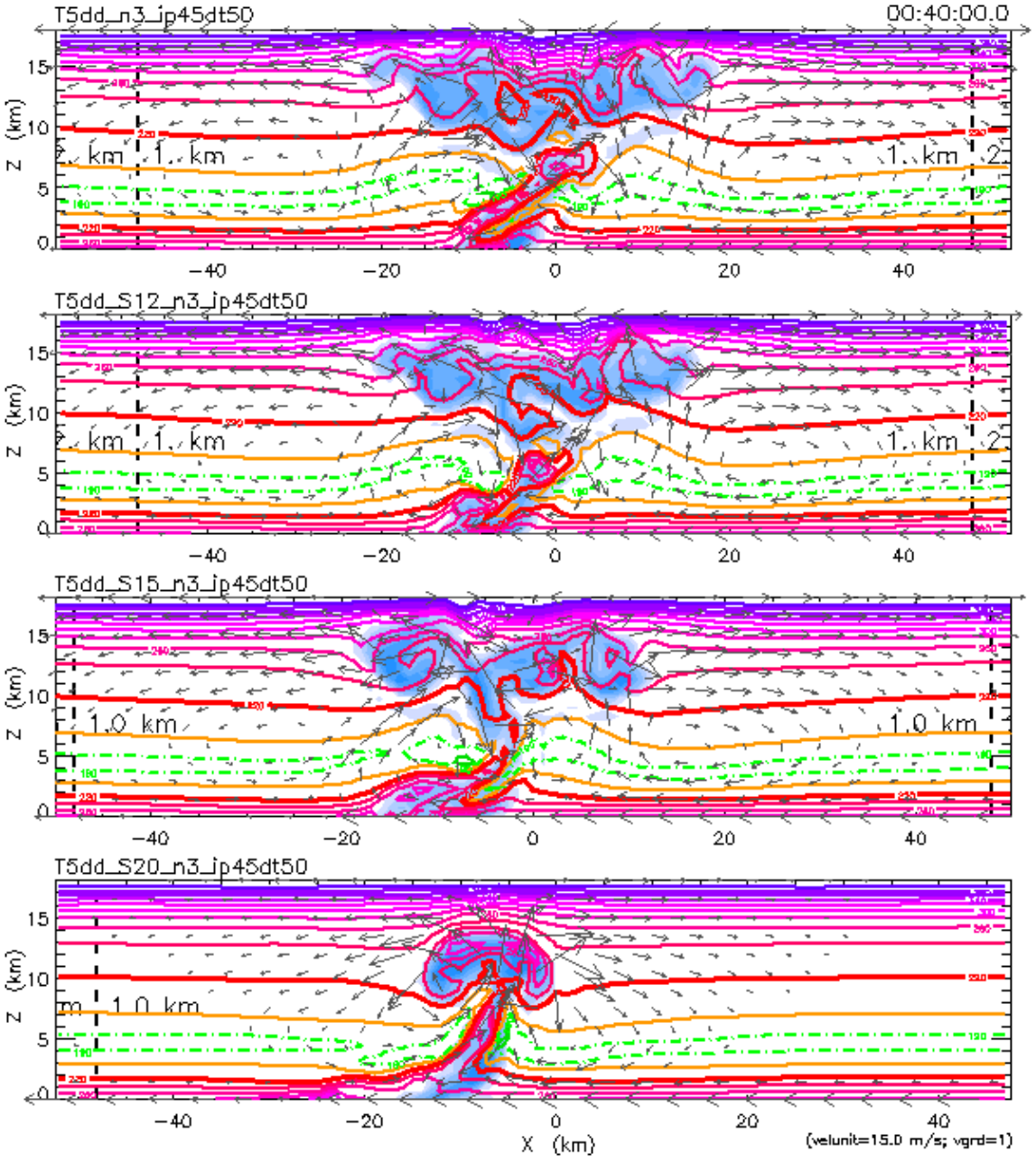

Figure 4.12c: Simulations for initial shears of 10, 12, 15, and 20 m s^{-1} for $z_s = 1$ km, at 0h 40m.

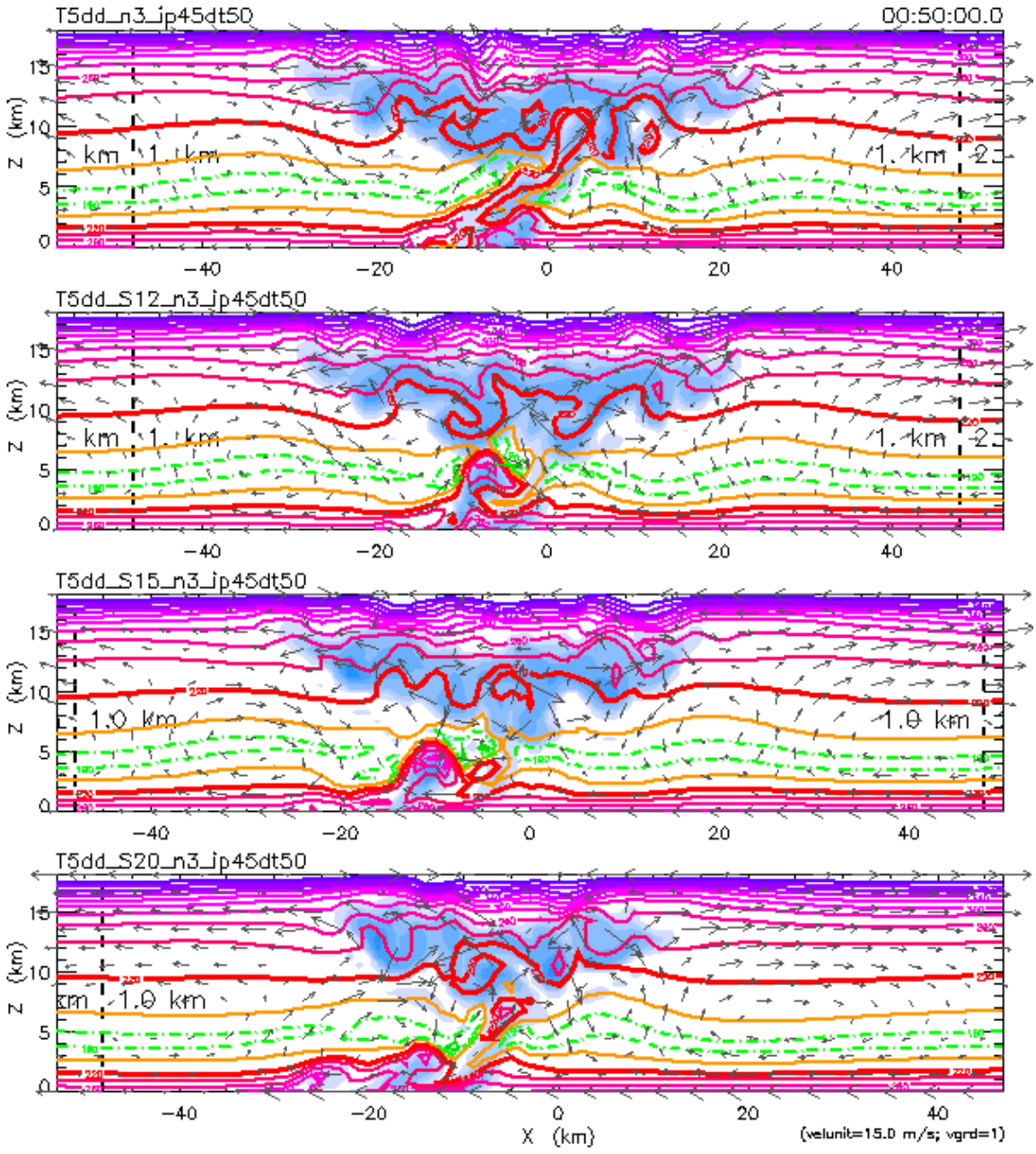

Figure 4.12d: Simulations for initial shears of 10, 12, 15, and 20 m s^{-1} for $z_s = 1$ km, at 0h 50m.

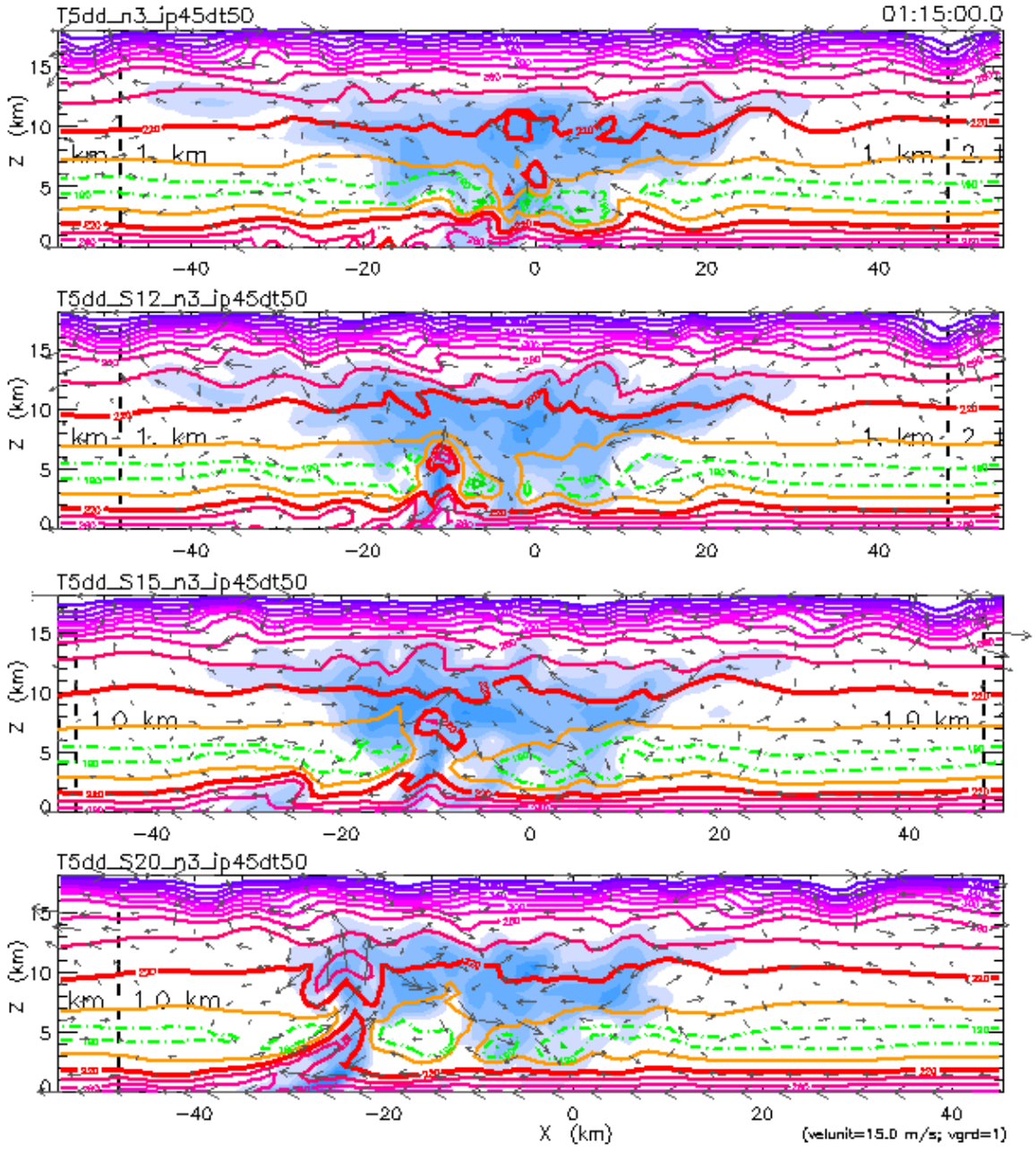

Figure 4.12e: Simulations for initial shears of 10, 12, 15, and 20 m s^{-1} for $z_s = 1$ km, at 1h 15m.

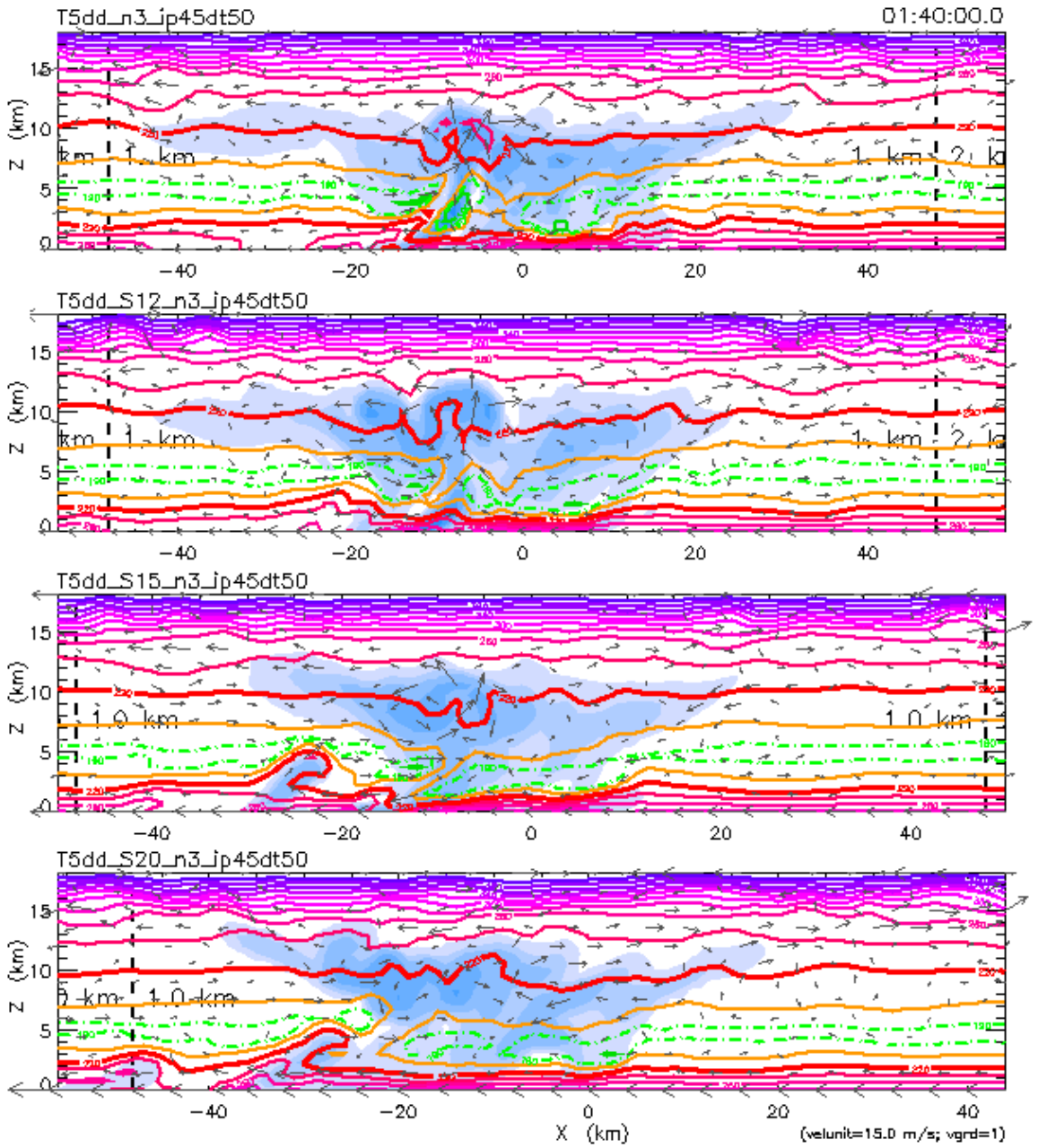

Figure 4.12f: Simulations for initial shears of 10, 12, 15, and 20 m s^{-1} for $z_s = 1$ km, at 1h 40m.

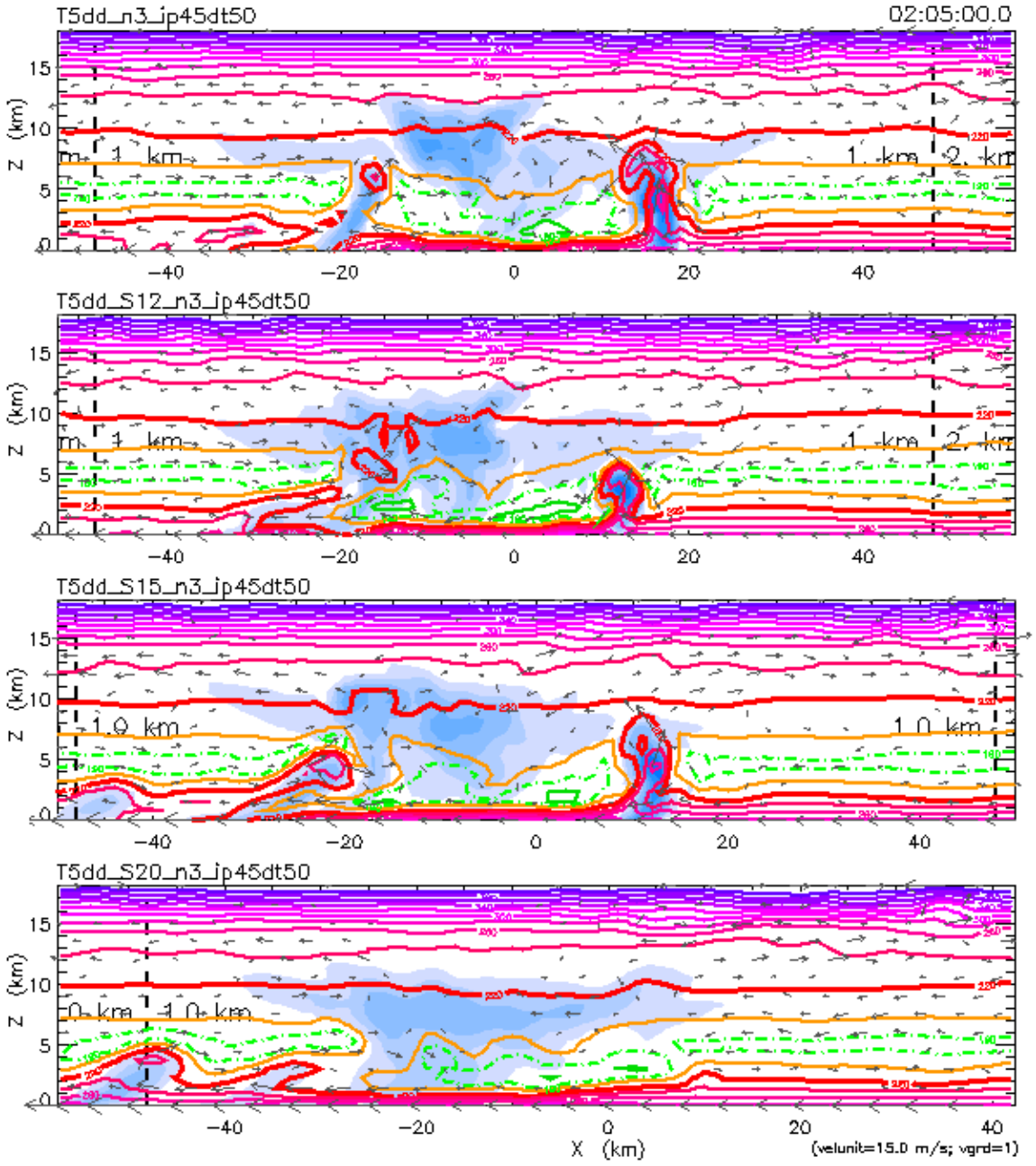

Figure 4.12g: Simulations for initial shears of 10, 12, 15, and 20 m s^{-1} for $z_s = 1$ km, at 2h 05m.

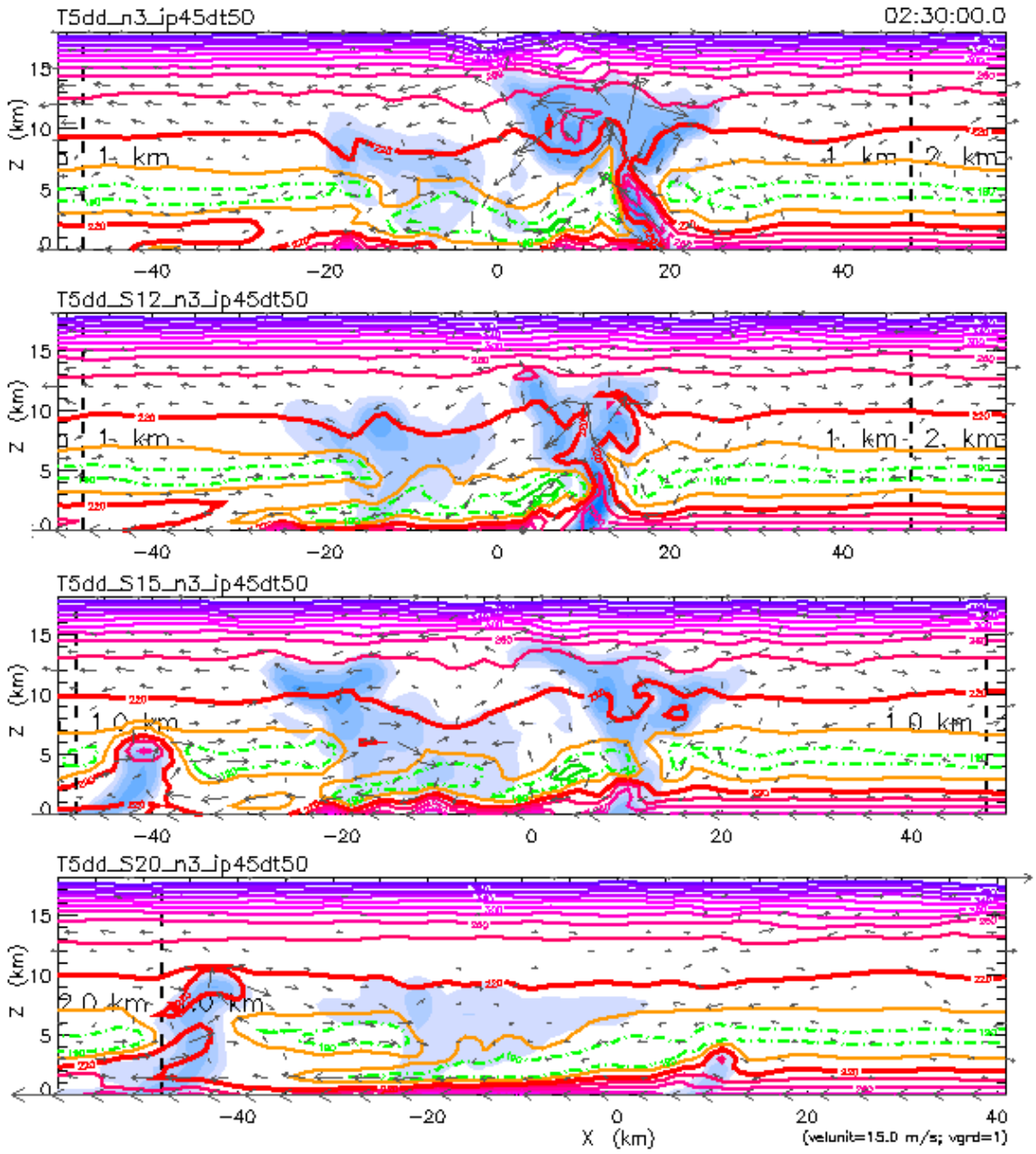

Figure 4.12h: Simulations for initial shears of 10, 12, 15, and 20 m s^{-1} for $z_s = 1$ km, at 2h 30m.

which may have formed solely under the influence of a small-scale low-level temperature perturbation after the descent and evaporation of debris downshear from the initial convective event. At this time, the moderately-sheared simulations display the development and propagation of a low-level convective outflow, along with the development of subsequent convection on the leading edge of the outflow region. Stronger low-level shear seems to have held the development of secondary convection close to the remains of the initial convection in the 12 m s^{-1} simulation, while convection forms on the leading edge and surface of the convective outflow slightly farther ahead of the main region of mid- and upper-level moisture in the 10 m s^{-1} simulation.

By 5h 00m (Figure 4.12j), a stronger low-level cold pool and downshear convective outflow has developed in the 12 m s^{-1} simulation, along with more independent secondary convective disturbances on the surface of the outflow region. Although the leading edge of the low-level convective outflow has long since passed the interface with the next coarser domain by this time, the low-level outflow and consequent derivative convection are just reaching that interface by this time in the 12 m s^{-1} simulation. The strongly-sheared simulations display more of a degeneration of convective activity by this time, rather than a propagation of convective elements and motions as in the moderately-sheared simulations.

4.4.9 The 10 m s^{-1} Shear Simulation: A Small-Scale Tropical Squall Line System?

The simulation with an initial near-surface shear of the horizontal wind of 10 m s^{-1} has been examined from various perspectives, most notably on a moderate-resolution domain ($\Delta x = 1.0$ km) in Figures 4.11 and 4.12 for comparison with stronger and weaker shear layers, and on a high-resolution domain ($\Delta x = 0.5$ km) in Figure 4.7 for comparison

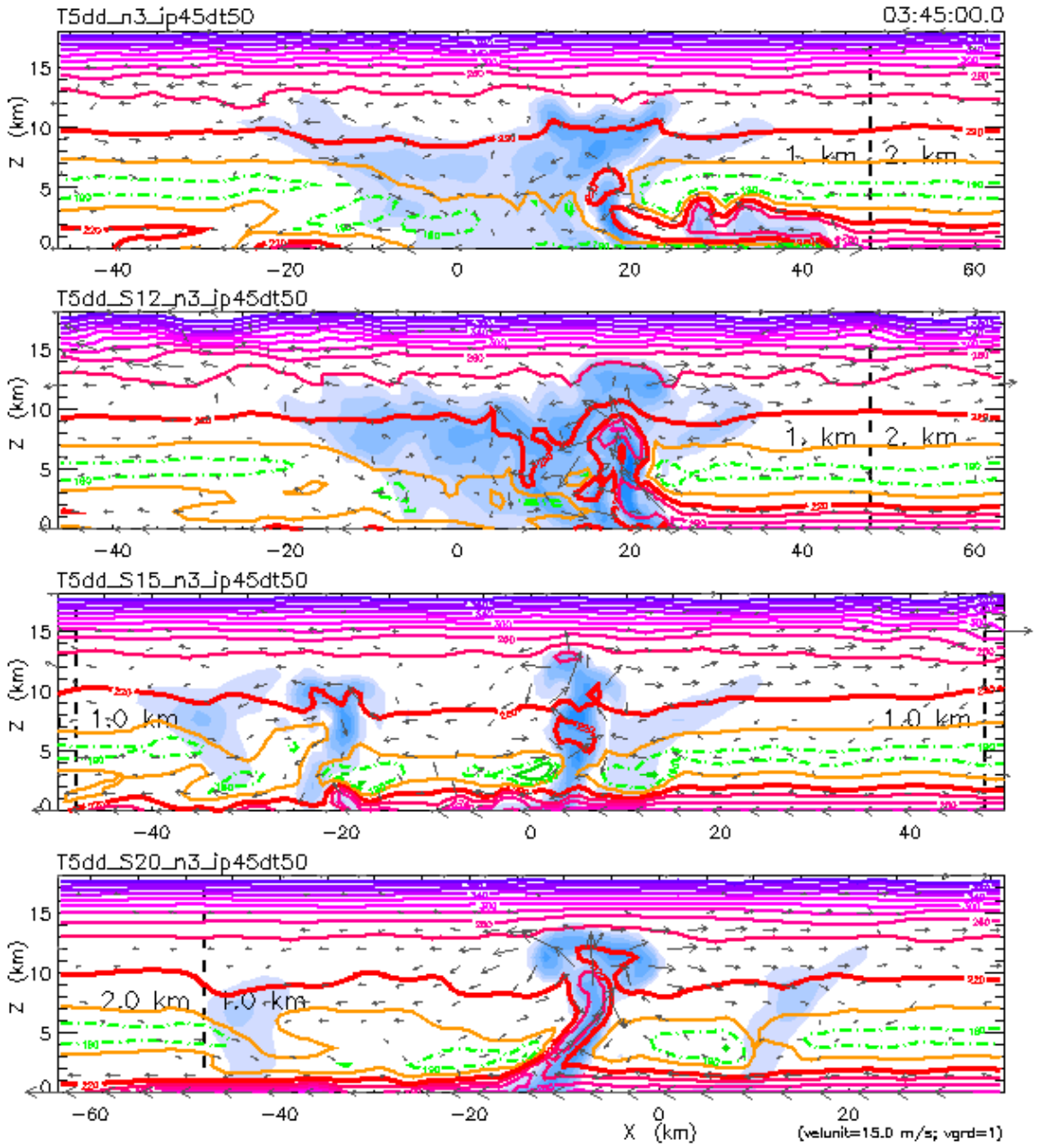

Figure 4.12i: Simulations for initial shears of 10, 12, 15, and 20 m s^{-1} for $z_s = 1$ km, at 3h 45m.

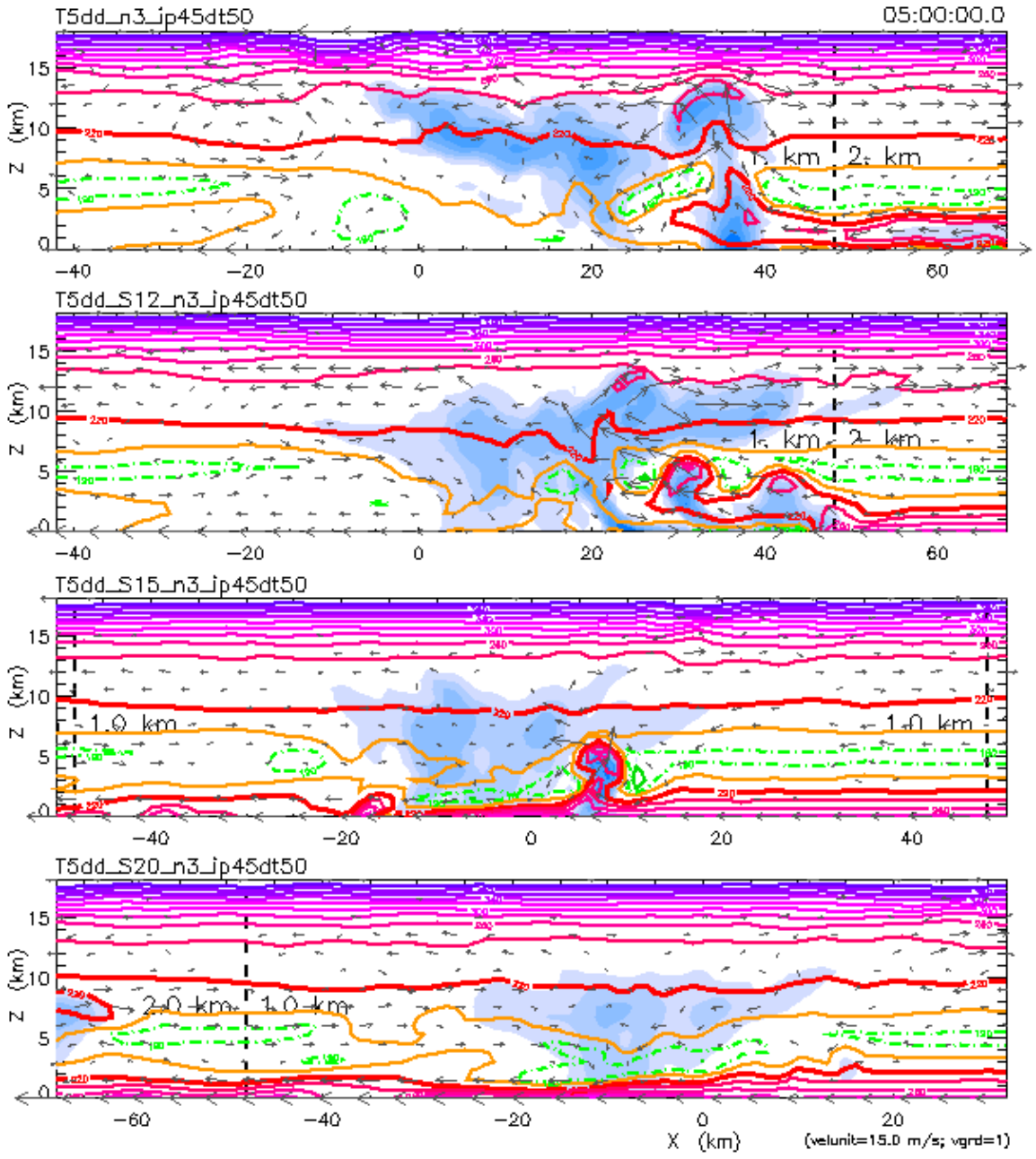

Figure 4.12j: Simulations for initial shears of 10, 12, 15, and 20 m s^{-1} for $z_s = 1$ km, at 5h 00m.

with simulations on a coarser domain. The convective structure which develops in the 10 m s^{-1} simulation in each of these examples is eventually self-sustaining, and at some point in its life cycle closely resembles the optimum long-lived squall line systems discussed in detail in Chapter 2. To illustrate these convective features and flow structures, several expanded-view snapshots of the fine-resolution 10 m s^{-1} simulation are included here in Figure 4.13.

Due to the strong surface winds, as demonstrated in Figure 4.2, the initial convective updraft begins just downstream (upshear) of the intended initial convective point as prescribed by the location of a warm bubble at the surface. This initial convection tilts noticeably downshear with height under the influence of the low-level vorticity produced by the ambient shear profile, and develops a familiar plume-and-cap structure which has been demonstrated in other simulations. Strong vortical flow structures develop on the outer edges of this cap which will be examined in closer detail later, with examples from the non-sheared simulations discussed earlier. By 0h 30m (Figure 4.13a), a sharp downdraft has formed immediately upshear of the cap, and is working to cut off the outer edge of the upshear side of the convective cap. Upward-directed inflow is stronger on the upshear side of the convective plume, providing a sharper demarcation between cloudy and clear air there than on the downshear side of the convection. Significant low-level inflow to the convection is provided only on the downshear side, although the lowest levels of inflow nearly reach the upshear side of the initial convective point before turning upward into the growing convective plume.

By 1h 10m (Figure 4.13b), a large field of mid- and upper level precipitation has developed both upshear and downshear of the initial convective point. Strong mid-level inflow from both ahead of and and behind the system has also developed, while rotor-like

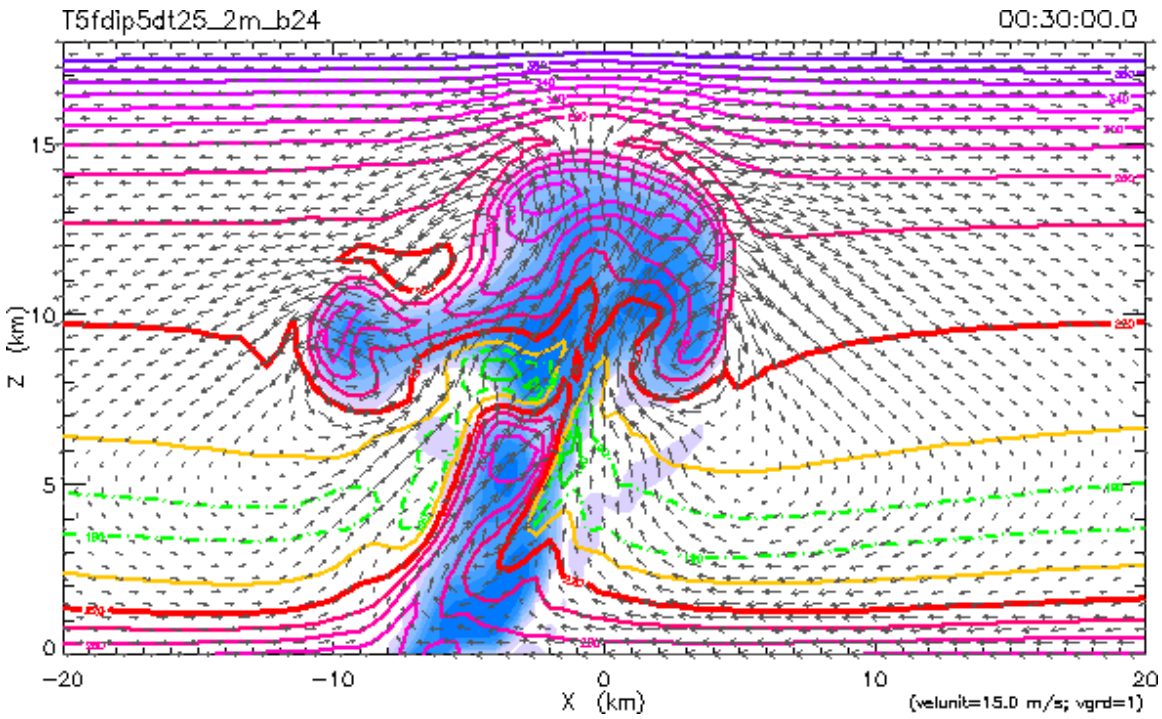

Figure 4.13a: The convective and moisture fields for the simulation with shear of 10 m s^{-1}, $z_s = 1$ km, at 0h 30m.

circulations, possibly due to gravity waves, in the mid- and upper levels of the precipitation system seem to propagate away from the initial convective point at regular intervals of approximately 10-12 km.

Weaker precipitation on the upshear side of the initial convective point seems to allow stronger lateral and rising inflow from the rear of the system, while stronger precipitation immediately downshear of the initial convective point significantly affects inflow from ahead of the system in the forcing and creation of downdrafts which reach the surface and could be expected to move upshear, forced by the strong low-level winds. However, by 1h 10m these convective downdrafts are beginning to turn more downshear upon nearing the surface, possibly indicating the onset of the propagating phase of the convective system.

Downshear motions of the convective downdrafts become more prominent by 2h 30m

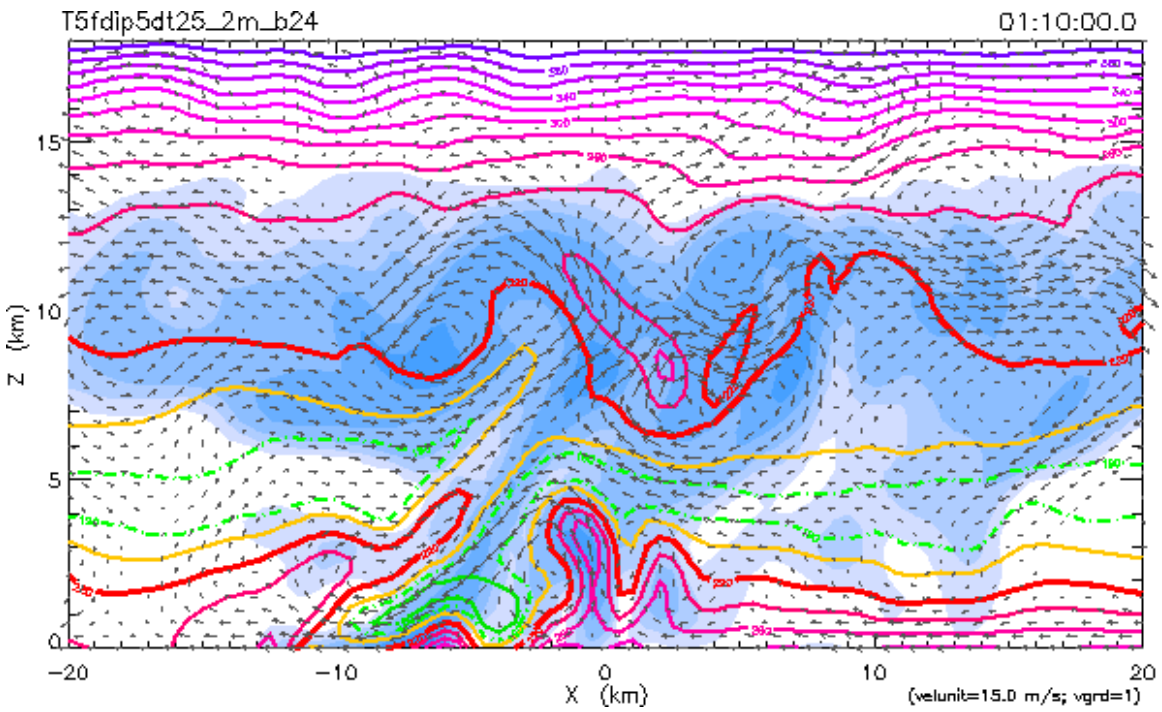

Figure 4.13b: The convective and moisture fields for the simulation with shear of 10 m s^{-1}, $z_s = 1$ km, at 1h 10m.

(Figure 4.13c). By this time, the upshear (post-squall) precipitation region has developed over a deeper layer of the troposphere than previously, and has developed more horizontally-oriented characteristics which are indicative of the post-squall stratiform precipitation region. A midlevel deformation zone has been established approximately 11-15 km behind the main convective updraft, within the nascent stratiform precipitation region.

Downshear convective outflow is supported primarily by mid-level inflow from behind the convective region, and may be forced significantly by water loading and evaporation in the heavy precipitation of the convective updraft region. Pre-squall midlevel inflow is joined by a newly-formed low-level jump updraft, forced by the low-level downshear convective outflow, on ascent through the convective region.

Horizontal upper level outflow from the convection occurs primarily in the downshear direction, while upshear upper level outflow experiences sharp descent immediately behind

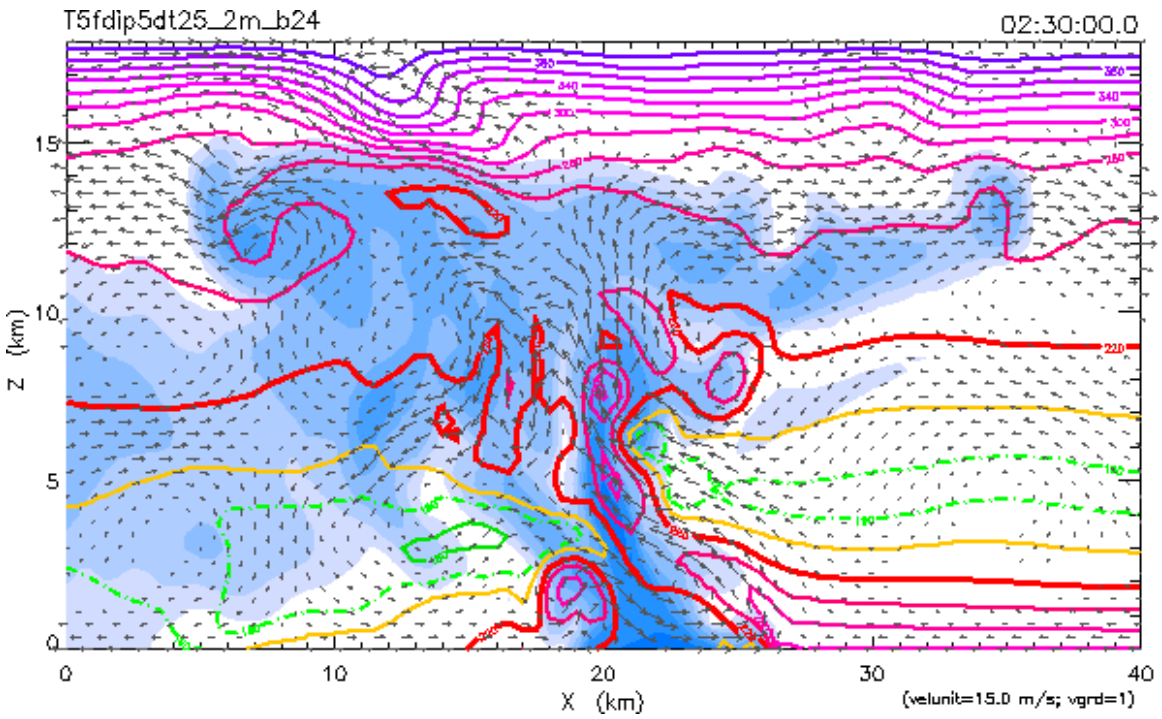

Figure 4.13c: The convective and moisture fields for the simulation with shear of 10 m s^{-1}, $z_s = 1$ km, at 2h 30m.

the convection. This subsidence may define the post-squall transition region, where precipitation is noticeably absent from the mid- and low-level moisture fields displayed in Figure 4.13c. Downdrafts through the transition region eventually turn horizontal and provide inflow to the midlevel post-squall deformation zone, which also receives inflow from behind the nascent squall line system. The stratiform region deformation zone provides outflow in the vertical directions, establishing a large region of weak subsidence in the low levels of the post-squall precipitation region and ascent in the upper levels. This region of post-squall ascent eventually turns to the horizontal, providing upshear upper level outflow from the convective and post-squall regions.

The typical structure of a tropical squall line system has become more evident by 3h 04m (Figure 4.13d), by which time a downshear surface bore has fully developed from

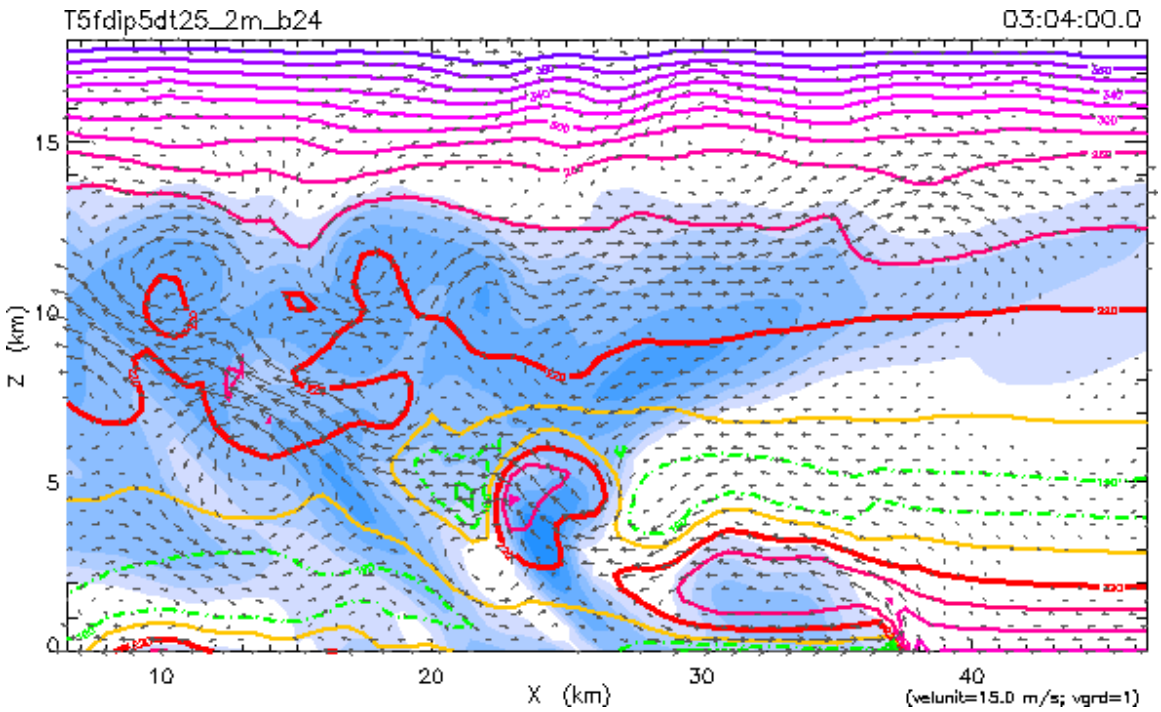

Figure 4.13d: The convective and moisture fields for the simulation with shear of 10 m s^{-1}, $z_s = 1$ km, at 3h 04m.

convective outflows, and continually forces a jump updraft in the pre-squall low-level inflow region. By estimating the position of the leading edge of the surface outflow during animations of these results, the surface-relative propagation speed of the convective outflow over this period can be estimated at approximately 7.3 m s^{-1} in the downshear direction at the time of the snapshot in Figure 4.13d. At this time, the downshear surface outflow is supported by a strong descending flow which originates in the midlevels behind the squall line system.

Strong downshear convective outflow has also developed in the upper levels, where precipitation and evaporation seemingly contribute to sharp downdrafts immediately downshear of the convective region. Further contributions to this pre-convective downdraft may arise from local circulations which may have developed about the most recent convective bubble, which is clearly evident in Figure 4.13d. The upshear tilt of this latest convec-

tive bubble indicates that it is being advected rearward by the midlevel pre-squall inflow during its ascent. Upper level outflow toward the rear of the squall line system is less coherent at this time, and is dominated by numerous rotor-like circulations which demonstrate significant diabatic motions immediately beneath the tropopause.

The midlevel deformation zone which was identified in the trailing stratiform region of the previous figure is less evident by this time, and may have translated rearward such that it is no longer clearly evident within the scale of the figures presented here. More significant, however, is the establishment of a midlevel minimum of vertical velocity in the convective region immediately above and behind the latest convective bubble. The "transition region" which was identified in the previous figure has disappeared, such that no post-convective region of sharp downdrafts is clearly evident. However, a region of suppressed low-level moisture, usually associated with the strong downdrafts of the transition region, is found immediately below the midlevel convective vertical velocity minimum.

By 3h 54m (Figure 4.13e), the domain of the display has advanced such that only the primary convective region and the downshear outflow bore are visible. However, in Figure 4.7e it is clearly evident that a large post-squall stratiform precipitation region has developed and extends approximately 60 km rearward from the main convective region. In Figure 4.13e, the upper level flow above and ahead of the convective region is dominated by rear-to-front flow, while the pre-squall overhanging precipitation region has contracted significantly since 3h 04m (Figure 4.13d) with little evidence of weak downdrafts produced by the evaporation of precipitation. Midlevel pre-squall inflow to the convective region remains strong, and above approximately 7 km is seemingly unaffected by convective development in the low levels.

By an estimation similar to those performed for the earlier figures, the gust front, at

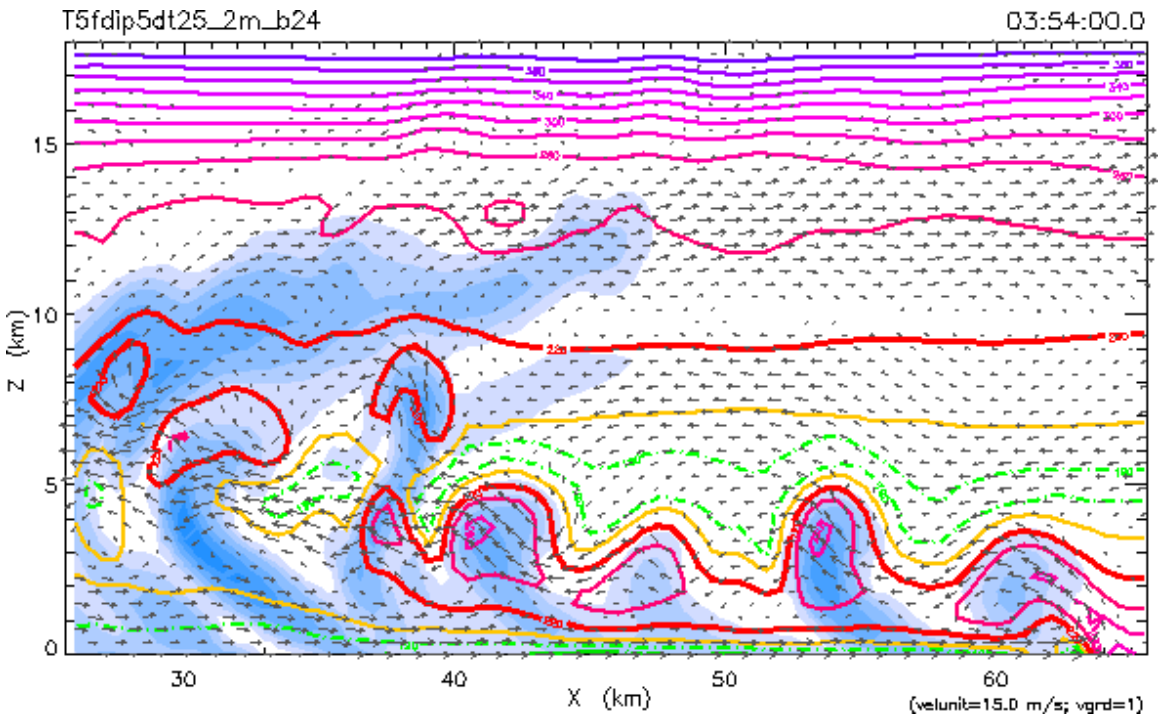

Figure 4.13e: The convective and moisture fields for the simulation with shear of 10 m s^{-1}, $z_s = 1$ km, at 3h 54m.

the head of the downshear surface outflow bore, has accelerated to approximately 11.5 m s^{-1} around the time of the snapshot in Figure 4.13e. The downshear surface bore is still supported by strong flow from the rear of the convective region which seemingly is affected only by the loading and evaporation of precipitation in the main convective region. The bore maintains an undular surface (approximately the 220 K isentropic surface, apparently) along the majority of its length at an altitude of approximately 1.5 km, while its head extends to a depth of approximately 3.0 km due to a collision interaction with the continued strong low-level pre-squall inflow. The undular surface of the downshear surface outflow bore seemingly forces a quasi-periodic interval of convective regeneration, with the formation of new cells separated by approximately 6-7 km along the bore surface. It is also apparent that, if the weak convective plume at approximately $x = 38$ km is discounted, buoyant

convective strength is concentrated in alternating new cells, such that a complex periodic behavior of convective cell generation has been established on the outflow surface. These considerations will be discussed in greater detail in analysis of a new squall line system experiment in Chapter 5.

4.4.10 The "Optimum" Shear Strength for a Long-Lived Squall Line System

By inspection of the 10 m s^{-1} simulation which was presented in the previous section, we may conclude that the convective structure and character and the longevity of the squall line system were such that the simulation represented near-optimal conditions for a long-lived tropical squall line. In fact, we may speculate that the difference bewteen the initial low-level wind strength (10 m s^{-1}) and the subsequent propagation speed of the convective line (approximately constant at 12 m s^{-1}) may help us to deduce the optimal initial low-level wind strength and shear and the subsequent convective propagation speed. We may conclude, tentatively, that the "optimal" strength of the initial low-level shear, in otherwise consistent initial environmental conditions, is approximately 11 m s^{-1}, and that these initial conditions would result in a long-lived squall line system with a convective region which propagates, against the low-level environmental winds, at approximately 11 m s^{-1}.

Such a conclusion is supported by an analysis presented in RKW88, although for their experiments "the squall line, in its optimal state, exhibits no significant propagation relative to the winds above the low-level shear layer." In a ground-relative frame of reference, and in this "optimal" state, the surface outflow layer is also found to be stagnant, a condition upon which much of the analysis presented in RKW88 rests. A propagating gust front indicates unbalanced conditions, though RKW88 found that "only when the simulated squall line enters the phase where it is dominated by the cold-pool circulation is there upper-level

wind relative to the leading edge of the system." We may identify this "relative" wind with deep-layer pre-squall inflow, as is observed in most tropical squall line systems (see discussion in Chapter 2). Later work by Weisman (1992) refined the balance conditions expounded in RKW88 with further consideration of a propagating surface outflow layer (relative to the ground) under the influence of strong descending rear-to-front flow as observed in tropical and midlatitude squall line systems.

Although no simulations have been provided here as examples for 11 m s^{-1} of initial low-level shear, several other precedents support this conclusion. An examination of the results presented in O95 revealed that an initial low-level shear of 12 m s^{-1} produced the most coherent and farthest-reaching squall line system, although the 10 m s^{-1} simulation produced results which were only slightly behind the 12 m s^{-1} simulation in these respects. Results for an intermediate case (11 m s^{-1}) were not provided, and may not have been examined at all. Features which could denote jumps in the forward propagation of the squall line system were found in the precipitations traces for both the 10 m s^{-1} and 12 m s^{-1} simulation in Figure 4.4. In the examination of these results, it has been noted that the 12 m s^{-1} simulation also demonstrated reductions in the forward speed of the propagating squall line system which alternated with the forward jumps of the convective line. This quasi-periodic alternation between jumps and reductions of the forward propagation speed of the squall line system was considered as a demonstration of the oscillatory nature of convective development on the downshear convective outflow of the squall line system. This oscillatory nature of convective growth and propagation was examined in great detail in FD95.

As discussed above in reference to the simulations which employed moderate-to-strong initial low-level shear, convection which forms on the surface and the leading edge of the

downshear convective outflow develops some distance ahead of the main convective region in the 10 m s^{-1} at advanced stages of the simulation, while a similar convective structure requires a slightly longer time period to develop in the 12 m s^{-1} simulation and, once this structure has developed, new convection which forms on the low-level outflow does so quite close to the main convective region such that the discrimination of new and pre-existing convection is sometimes difficult.

The effects of an initial low-level shear strength of 11 m s^{-1} would likely resolve several differences between the 10 m s^{-1} and 12 m s^{-1} simulations. It is likely that this "optimal" strength of the initial low-level shear would not only force new convective formation on the downshear outflow bore surface slightly closer to the main convective region than in the 10 m s^{-1} simulation, but would allow the formation of new convection on the surface and leading edge of the downshear convective outflow slightly further from the main convective region than in the 12 m s^{-1} simulation. Additionally, we may expect that the speed of the forward propagation of the low-level convective outflow is partially regulated by the initial low-level wind strength and, hence, by the initial low-level shear in the configuration chosen here. The forward propagation speed of the convective outflow which was found in the examination of the 10 m s^{-1} simulation would be restricted slightly by a stronger low-level inflow, while snapshots of the 12 m s^{-1} simulation in Figures 4.12i and 3.14j demonstrate an already restricted low-level convective outflow region which could be relieved by a slightly weaker initial low-level wind strength than that employed for the 12 m s^{-1} simulation.

Additionally, we may consider observational and numerical evidence to support this conclusion for the "optimal" squall line system propagation speed. In an analysis of fast- and slow-moving convective lines over the tropical Atlantic Ocean during GATE, Barnes and Seickman (1984) found a average propagation speed for the fast-moving lines of ap-

proximately 11 m s^{-1}. These fast-moving convective lines exhibited westward propagation ahead of the accompanying tropical easterly wave trough, in a direction normal to the typical low-level wind shear vector. These fast-moving convective lines also exhibited more squall-type characteristics than their slow-moving counterparts, with deeper pre-squall low-level convective outflows and greater stability, i.e. greater convective inhibition, in the low-level wake region. Modeling efforts presented in CW98 produced a squall line system of optimum configuration and duration with a propagation speed of 11 m s^{-1} for the case in which only warm rain microphysics was considered, and a propagation speed of approximately 12 m s^{-1} for the case in which mixed-phase (rain and ice) microphysics were considered. The effects of mixed-phase microphysics on squall line system propagation speed were considered in detail in CFBM95, leading to the experiments and conclusions which were presented in CW98.

The conclusion presented here for an optimum initial low-level wind shear strength and squall line propagation speed will be employed in a new simulation which relies on initial conditions that are otherwise consistent with the simulations provided by Ooyama and presented here. Results of this new experiment are presented and analyzed in Chapter 5.

4.4.11 Cumulus Growth in an Environment at Rest

Cumulus growth in an environment which is initially at rest poses an interesting problem in the model framework presented here. At the highest resolution utilized thus far in the simulations provided by Ooyama, motions which act on a scale of, typically, 1 km or less are not explicitly resolved by the model numerics. However, some interesting details of solitary cumulus growth can still be found in simulations which were performed at this res-

olution, providing some direction in the formulation of subsequent experiments with higher resolution to provide greater insight into cumulus growth processes. Because the model has been formulated using first principles of both dynamics and thermodynamics, and includes realistic mixed-phase microphysics of widely accepted originations (Kessler, 1969; KW78), it may be postulated that the model presented here is well-suited for the simulation not only of mesoscale atmospheric phenomena, but also of convective scale dynamical processes. In a larger domain, it has already been shown that the numerical foundation of Ooyama's model is appropriate for the simulation of phemomena on the meso- and synoptic scales (Shapiro and Ooyama, 1990; DeMaria et al., 1992).

Figure 4.8 demonstrated the growth of cumulus clouds in an unsheared environment, and compared the growth of convection in the center of the model domain of highest spatial resolution with growth on the interface with an adjacent coarser domain. As discussed earlier, in the presentation of Figure 4.8, convective growth in the center of the model domain proceeds symmetrically about the initial convective point, while the difference in spatial and temporal resolution between domains induces asymmetric growth and eventual propagation in the simulation for which convection was initiated on a domain interface.

Detailed snapshots of the growth stages of a solitary unsheared cumulus in the center of the model domain of highest resolution are included in Figure 4.14. Some aspects of the simulation retain artifacts of the numerical methods employed, particularly the symmetric cloud formation which extends diagonally from the surface at 0h 25m. This cloud formation is likely a Gibbs effect, brought about by the adjustment of the model to strong gradients in dynamic and thermodynamic fields at the onset of convection. At 0h 25m, the plume-and-cap structure of the initial convective development is already visible, and expands significantly by 0h 26m. Since the onset of convection, toroidal motions have been present

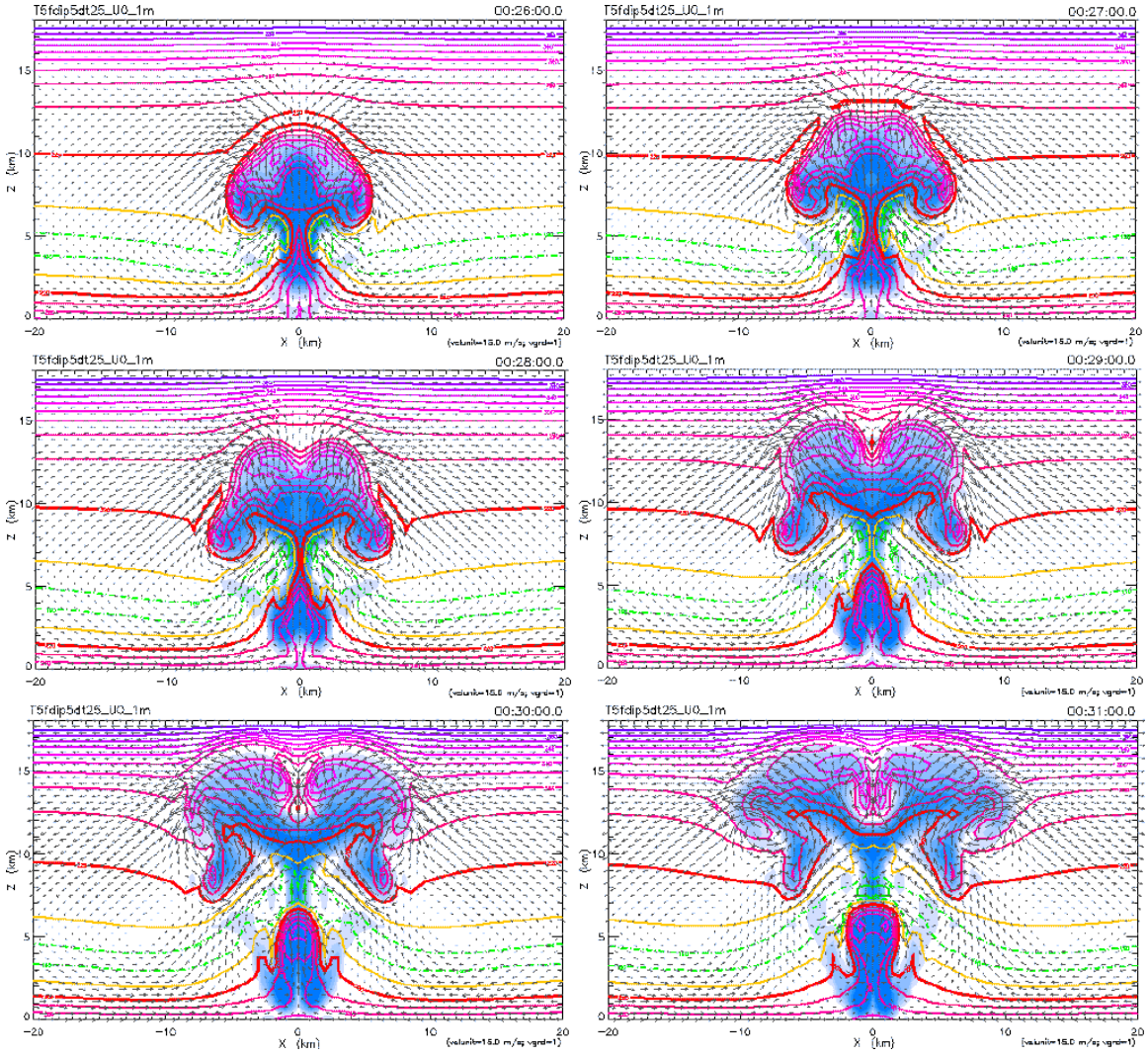

Figure 4.14: Close-up of unsheared simulation for demonstration of cap instabilities.

at the outer edges of the cap. These motions contribute to the compensating outflow and downdrafts which exist along the surface of the cap, as well as the lateral entrainment of environmental air into the region where the plume merges into the growing convective cap.

By 0h 27m, slight undulations along the surface of the cap are visible between the edges, which exhibit stronger toroidal motions than earlier snapshots, and the center of the cap, which by this time shows a weakness in upward vertical motions and a slight decrease in moisture content and temperature from the previous snapshot. Significant lateral inflow continues around the edge toroids and into the convective plume and the backside of the cap through 0h 28m, by which time the cap shows evidence that it has begun to shed the existing edge toroids in favor of intense vertical growth, which remains symmetric about the central weakness which has developed in the surface of the cap.

By 0h 29m, a secondary toroid has begun to form on the surface of the convective cap in two places, in addition to the primary edge toroid which shows signs of stagnation and weakening by this time. One weak secondary toroid has formed on the surface of the cap about midway between the edge toroid and the still-growing upper surface of the cap, and seems to be propagating downward with the compensating outflow and downdrafts along the surface of the cap toward the edge toroid. A slightly stronger toroid has begun to form about the central depression in the upper surface of the cap, induced by the weakness of updrafts along the central axis and continued growth in the adjacent regions. By 0h 30m (also shown in Figure 4.8a), the edge toroid shows signs of continued weakening despite significant lateral flow into the region where the plume merges into the growing cap. The toroid on the surface of the cap has intensified under the influence of continued convective growth, while the central surface toroid has contributed to a central downdraft which, by 0h 30m, has become isolated in the cloudy region by continued symmetric convective growth

of the upper cloud surface.

This central upper-level downdraft continues under the influence of the adjacent surface toroid through 0h 31m, developing a dry (unsaturated) region within the cumulus at upper levels of the growing cloud. The toroid on the outer surface of the cap has grown and intensified, while the earlier edge toroid has disappeared entirely, such that a new edge toroid has formed above and outside of the earlier structure. The location, size, and intensity of this new edge toroid will contribute to the lateral upper level outflow from the cloudy region, as seen in Figure 4.8b. Growth of the low-level cumulus structure over this time continues slowly, but is impeded by the development of a somewhat stable region in the center of the plume. At 0h 31m, this midlevel stable layer exhibits moderate downdrafts about the central cloud axis, indicating that the stable region may have formed from the evaporation of moisture which had been carried into the cloud and condensed and frozen in off-axis updrafts associated with the strong lateral inflow. The frozen precipitation then settled out of the off-axis updrafts into the central plume region where it could melt and evaporate, cooling the surrounding weak updrafts and turning them to downdrafts. Such a process would indicate that the upper and lower levels of the cumulus have, by 0h 31m, become somewhat decoupled, such that only a strong resurgence of the low-level updraft could again couple the motion and moisture fields in the upper and lower regions of the cloud.

The development of nodes and toroids on the surface of the growing cap of a simulated cumulus has been examined in detail by several researchers. Klaassen and Clark (1985) employed a high-resolution two-dimensional model with interactive nested grids to simulate the formation of "center-concave" and "center-convex" cumuli. In the consideration of several possibilities for the mechanism of formation of these cloud surface instabilities, it

was concluded by Klaassen and Clark that, for center-concave cumuli such as that examined here in Figure 4.14, the baroclinic generation of vorticity and the amplification of local shear instabilities in the layer which spans the cloud-environment interface is most likely the cause of these nodes on the surface of the cloud. Although the characteristic scale of the surface nodes found by Klaassen and Clark were approximately 125 m, much smaller than the resolvable scales of the simulations shown here, we may still see indications of these processes on a larger scale in Figure 4.14.

Conclusions similar to those discussed by Klaassen and Clark (1985) were found using three-dimensional simulations by Clark et al. (1988) and by Grabowski (1989). The process of baroclinic generation of vorticity, and subsequently the intensification of the shear layer, at the cloud-environment interface was recognized in these experiments and in experiments performed by Grabowski and Clark (1991, 1993) as the precursor to entrainment of environmental air through the cloud top by mixing of the cloud surface with its dry environment. Grabowski (1993) further proposed that this mixing, if intense and sustained, may lead to buoyancy reversals at select locations on the surface of the cloud and the formation of penetrative downdrafts within the cloudy region.

4.5 Discussion

Given the simplicity of formulation of the dynamic and thermodynamic aspects of this model, and the explicit reliance of these formulations on first principles of atmospheric dynamics and thermodynamics, this model is ideally suited for realistic representations of atmospheric motions and conditions. It may be prudent to consider more detailed formulations of the model microphysics in later work, as well as special dynamic aspects of realistic atmospheric representation such as boundary layer processes and special thermodynamic

aspects such as nonequilibrium processes, including supersaturation. Nevertheless, it has been found that this model quite accurately represents the life cycle of a tropical squall line system, qualitatively and quantitatively, in exquisite detail. Although we should expect that the representation of isolated cloud generation is sensitively dependent on the initial conditions and the method of convective preconditioning and triggering chosen, it has also been found that the evolution of an isolated cloud is simulated in realistic detail by Ooyama's model at even the maximum resolution demonstrated here.

Consideration of the experiments and simulations analyzed in this chapter quite naturally lead us to the formulation of new experiments which will further determine the accuracy of this model in the simulation of convective and mesoscale dynamic, thermodynamic and microphysical processes. An interest in high-resolution ($\Delta x = 0.5$ km or less) simulations is prompted by the results presented here, in Figures 4.6 and 4.7, and the work of Weisman et al. (1997), who found in a similar comparison of squall line experiments in domains of different resolutions that the coarse-resolution simulations exhibited stronger large-scale circulations but later development of the convective system and subsequent cold pool circulations. These deficiencies were attributed by Weisman et al. to the inability of the model to properly resolve nonhydrostatic effects and microphysical processes, such as the evaporation of precipitation, on a coarse domain. The subsequent degradation of the model results to a hydrostatic regime under the influence of large grid spacing was found to reduce the nonhydrostatic limiting of vertical mass transports, as compared to an explicitly hydrostatic simulation, and under this de facto hydrostatic approximation produced motions with greater time scales of evolution. Several new experiments will be performed with the model, with minimal alterations to the model formulation, which will examine the optimal conditions for a long-lived squall line system on a domain of the highest resolution

already demonstrated here, as well as the evolution of isolated clouds under alternate initial conditions on scales much finer that those employed in the simulations shown here. These new experiments are outlined and discussed in Chapter 5.

Chapter 5

FURTHER MODELING STUDIES OF TROPICAL CONVECTION

5.1 Squall Line Experiments

Several simulations of squall line systems were discussed in the previous chapter, in which efforts presented in O95, O97, and in the production of unpublished simulations were reported. For this thesis, a single new squall line experiment was performed in order to evaluate the hypothesis presented earlier that an "optimum" shear strength for the initiation and propagation of a long-lived squall line system may be found between the 10 and 12 m s^{-1} simulations which were presented. This conclusion was supported by the findings of several researchers (Barnes and Seickman, 1985; CW98) that the optimum speed of propagation for a fast-moving tropical maritime squall line system may be around 11 m s^{-1}. For ease of understanding, the construction of the model domain and the initial conditions will be noted in explicit terms here. Following this short re-introduction to the operational structure of the model, results for the 11 m s^{-1} simulation will be presented and discussed in detail, and will be related to previous squall line system modeling efforts as were presented in Chapter 2.

5.1.1 Domain Construction and Initial Conditions

For consistency of results and for ease of comparison, the model domain employed for the 11 m s^{-1} squall line system experiment is equivalent to that employed in unpublished shear experiment simulations formulated by Ooyama, which were described in the previous chapter, and will be described in brief here. The discussion of model numerical constructs and procedures, presented in Chapter 2, applies equally to the recent experiments, and will not be repeated here.

The model domain consists of five nested mesh in the x–z plane, each centered on $x = 0$. The mesh of the highest resolution is also the smallest, consisting of 192 grid points at a constant spacing of 0.5 km, for a total width of 96 km for the finest mesh. Each successively coarser mesh, except for the outermost, also contains 192 grid points in width, but with twice the grid spacing of the next finer mesh. The coarsest mesh, which is the fifth and outermost in the model domain, contains 144 grid points at a spacing of 8 km, for a total model domain size of 1152 km. The domain is periodic at the lateral boundaries. Thus, over longer time periods, horizontally-propagating waves may cycle through one end of the model domain and appear at the other end, possibly causing wave interference and growth which could be detrimental to the model results.

Each mesh in the model domain retains the vertical resolution of the finest mesh, which consists of 24 grid points with a constant spacing of 750 m for a total height of 18 km in an unstretched vertical coordinate system. The upper and lower boundaries of the domain are rigid and impermeable. The method of time integration employed in all new experiments discussed here is the Leapfrog scheme, tilted forward to reduce the contribution of high-wavenumber solutions and with an Asselin filtering parameter of $\nu = 0.3$, as discussed in Section 3.2.4. The length of time steps on the finest mesh is 2.5 seconds, and doubles with

each coarser mesh except for the outermost, such that the length of a time step on the coarsest and next-coarsest meshes is 20 seconds for both. The CFL condition for explicit methods of time integration in numerical models has been discussed in Chapter 3.

The microphysical formulations incorporated into the model originated in the work of Kessler (1969) and KW78, and were described in a short discussion in Chapter 3. The microphysical formulation of KW78 is selected for all of the simulations to follow. The thermodynamical formulations employed here were developed and refined by Ooyama (1989, 1990, 1991, 1995), and were also discussed in Chapter 3. The combination of these thermodynamical and microphysical formulations allows the appropriate assignment of thermodynamical properties to vapor, liquid and solid airborne moisture, and liquid and solid precipitation particles. The freezing zone, which may be defined by the user and is applied to various calculations, including the hyperbolic smoothing of the water-ice vapor pressure function via equation (3.31) and in the determination of precipitation terminal velocity via equations (3.40) and (3.41), is 2°C wide and is centered on 0°C. These formulations will be employed in all of the new experiments and simulations discussed here.

The thermodynamic profile employed in the initialization of the model physical domain is based on the mean West Indies (Caribbean) "hurricane season" sounding compiled from ten years of July-through-October data by Jordan (1958). This original profile was modified by Ooyama to include interpolated data, for a higher-resolution dataset, greater relative humidity in the lower layer up to approximately 600 hPa, and was extended in total height to 10 hPa to accomodate the upper levels included in the model domain. The resulting thermodynamic profile, up to 100 hPa, is displayed in Figure 5.1.

The initial wind profile employed in the current squall line system simulation is similar to that employed in O95, shown earlier in Figure 4.2. A wind profile possessing a shear of

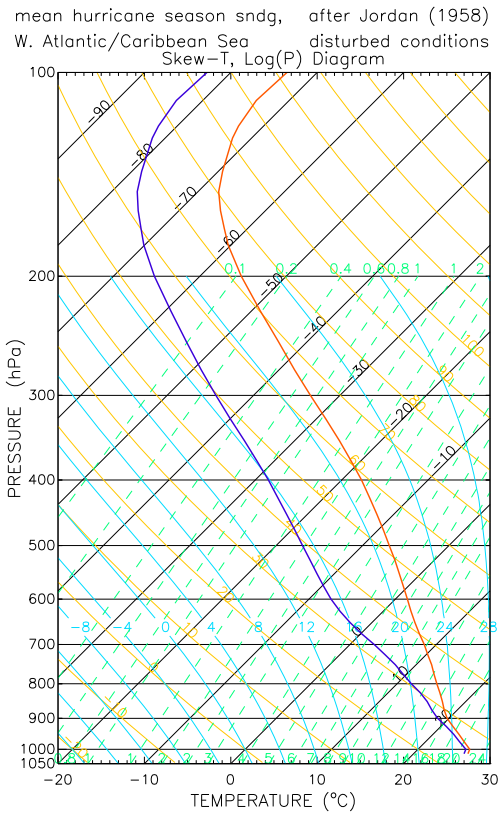

Figure 5.1: Initial thermodynamic profile for the 11 m s^{-1} tropical squall line system experiment, modified from Jordan (1958).

11 m s^{-1} over a layer scale height of $z_s = 1$ km, as demonstrated by the use of equation (3.42), produces a sheared lower layer with an actual depth of approximately 3 km. Figure 5.2 demonstrates this initial wind profile for the lower layer of the model physical domain.

The model was run on a Cray J916 supercomputer located at The National Center for Atmospheric Research (NCAR) in Boulder, Colorado, using the Fortran77 programming language. The current squall line system simulation was performed over an integration time of six hours. A detailed discussion of the 11 m s^{-1} squall line system simulation follows.

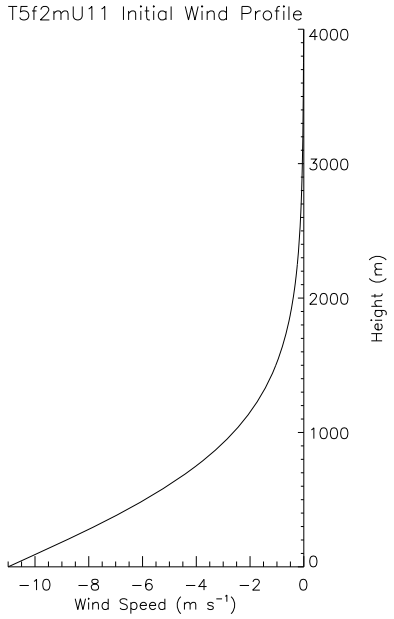

Figure 5.2: Initial wind profile for the 11 m s^{-1} tropical squall line system experiment.

5.1.2 Initial Sheared Development

This experiment was initialized with a $+3K$ temperature perturbation, also known as a "warm bubble," near the surface in order to generate convective activity as quickly as possible. The bubble was of elliptical shape in the x–z plane, with a major axis length of 32 km in the horizontal (x) direction and a minor axis length of 6 km in the vertical (z) direction, and was centered 24 km left of the center of the finest mesh. The center of the bubble was elevated to 500 m above the surface. Following the initial convective development, which was not likely to be representative of the organized convective structures of interest, convective motions settled into a regenerative phase which evolved into the tropical squall line system of interest. The discussion in this section will consider convective motions after the ascent of the initial thermal bubble but prior to the formation of a significant surface cold pool and pre-squall outflow, which will be considered in the next

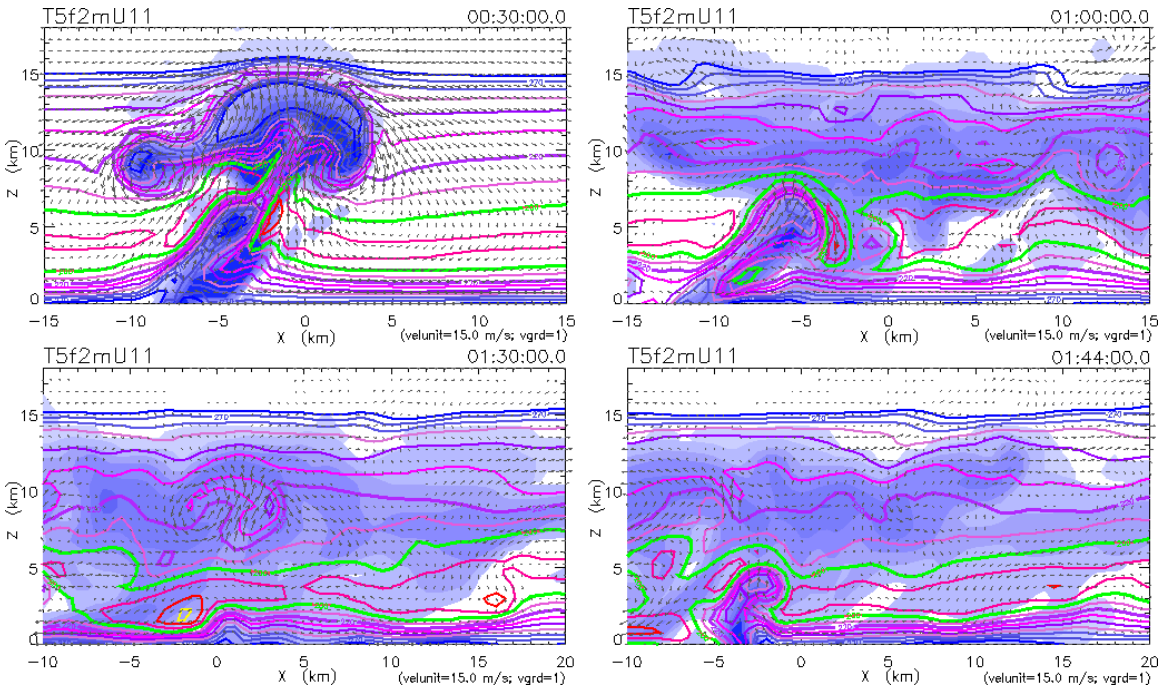

Figure 5.3: Initial convective development in the 11 m s^{-1} tropical squall line experiment.

section.

By 0h 30m, the initial convective bubble has reached the tropopause, at approximately 16 km in height, and the convective plume and cap demonstrate a strong tilt downshear (to the right) with height, as demonstrated in Figure 5.3. The reader should note that the closely-packed entropy contours in the stratosphere (above a height of approximately 15 km) have been omitted in these and later snapshots of convective development in this simulation in order to reduce cluttering of the images. Prominent toroidal motions are present on the up- and downshear sides of the bubble cap, supporting strong downdrafts adjacent to the convective cloud and strong inflow beneath and into the bottom of the convective cap. As demonstrated earlier, in Figures 4.7a and 4.13a, downdrafts in the upper levels and updrafts in the middle levels have begun to isolate a portion of the convective cap immediately upshear of the central convective plume. By 1h 00m, some convective motions near the surface have been generated by forcing from moist downdrafts meeting the surface

nearby. These downdrafts are products of the prominent stratiform cloud and precipitation region in the layer between 6 km and 16 km in height which was formed from moisture lofted by the initial convective motions.

The deep stratus layer is still present at 1h 30m, and by this time extends from near the surface to approximately 15 km in height over a large area of the region of interest (note the shift of the visible portion of the domain 5 km to the right for this snapshot). Convective motions are still present in the precipitating cloud mass at this time. While the intensity of convective motions within the stratiform cloud and precipitation region decreases significantly by 1h 44m, regenerative surface convective development persists through this time under the continued influence of large moist downdraft regions in the vicinity of the initial convection.

5.1.3 Surface Outflow and Gust Front Development

Moist stratiform downdrafts and surface flows which assisted in the regeneration of convective activity upshear of the initial convective point in the early development of the convective system can also be witnessed moving downshear. By 2h 00m, despite the lack of a coherent surface flow structure such as a density current or gust front, the meeting of two surface flows, one forced by a large stratiform downdraft region in the mid-levels near the initial convective point, another the initial surface flow which is still present far upstream of the initial convection, produces a seemingly discrete movement of the primary convective activity to the downshear side of the initial convective point, as demonstrated in Figure 5.4. Again, the reader should note that the contours of total entropy in the stratosphere have been omitted here, and that the visible portion of the domain is shifted 10 km to the right between the first and second snapshots in this sequence. The upshear tilt of this new

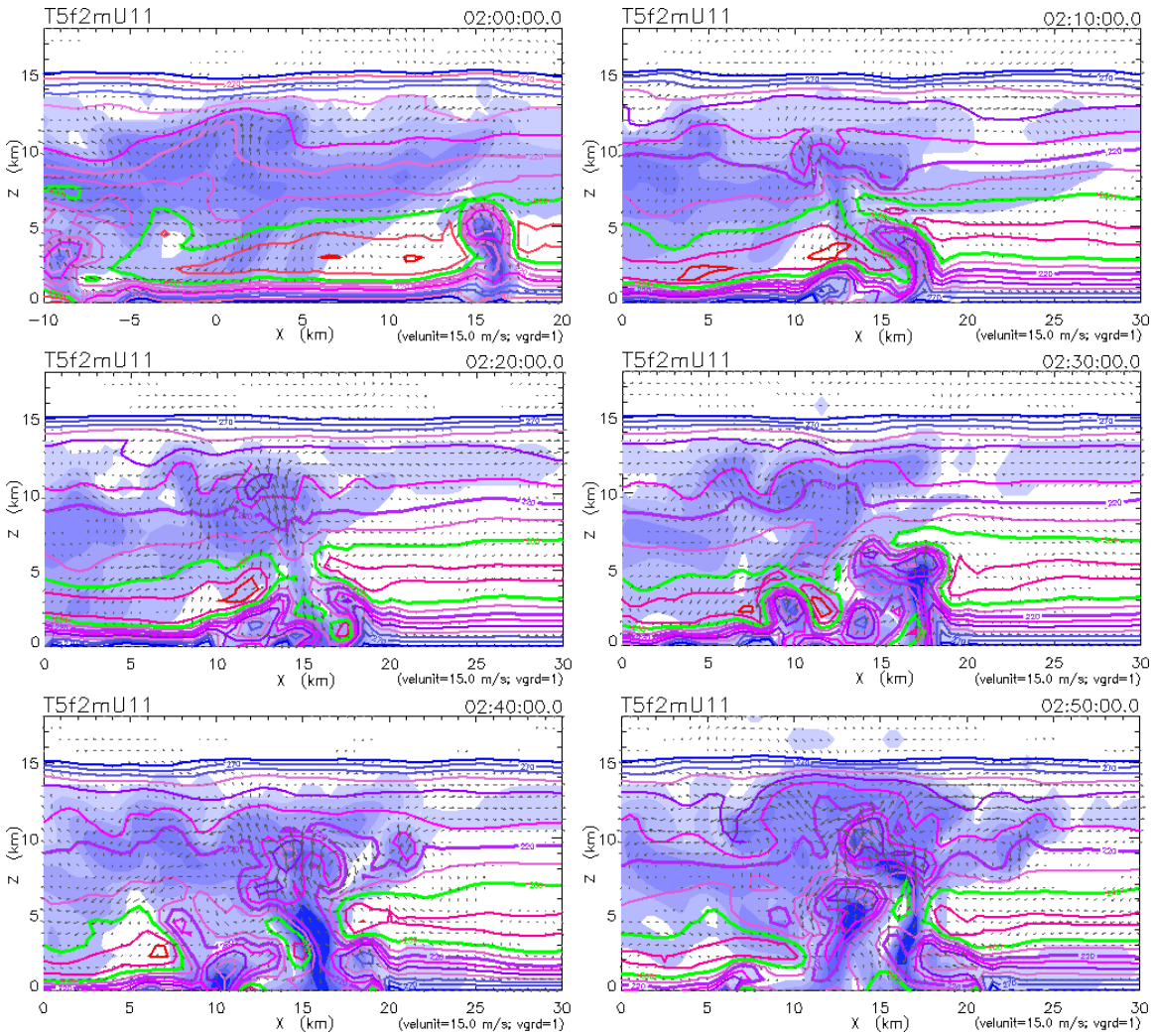

Figure 5.4: Surface outflow and gust front development in the 11 m s^{-1} tropical squall line experiment.

convection becomes more evident by 2h 10m, by which time the convective motions in the lower and middle levels have begun to draw cool mid-level air downward upshear of the latest convective plume. Through this period in the development of the convective system against the low-level winds, the stratiform cloud and precipitation region downshear of the region of primary convective motions evolves such that mid-level moisture dissipates slowly, and is eventually replaced by an overhanging stratiform region which persists through the life of the convective and squall line system. This evolution is apparently completed by 2h 20m, by which time more vertically-oriented convective motions in the middle and upper levels have begun to drive a strong downdraft of cool mid-level air, drawn into the strong convective precipitation immediately beneath the convective plume by the toroidal motions of the convection itself, toward the surface. Because of the placement of a remnant warm region at the surface slightly upshear of the new convection, the cool convective downdraft is forced downshear against the low-level winds.

This convective downdraft is initially hindered by new convective development in the remnant warm regions near the surface by 2h 30m, as a portion of the nascent cold pool becomes pinched off from its source of cool mid-level air upshear of the primary convection. However, the formation of the downdraft and surface outflow is regenerated by the toroidal motions of a new convective plume by 2h 40m. Upon reaching the surface, the downdraft forms a cold pool there and begins to spread downshear. Importantly, at this early stage in the formation of a surface outflow layer, the cold pool which spreads under its own weight is further forced against the low-level winds by continual inflow of precipitation-cooled convective downdrafts from the mid-levels and is mechanically forced by toroidal convective motions produced in a new convective plume immediately downshear. By 2h 50m, the regeneration of convection on the front of the spreading cold pool and the

subsequent precipitation-cooling of air which continually flows into the primary convective region from the mid-levels upshear of the primary convective region leads to the development of a sustained circulation which feeds the downshear propagation of the pre-squall surface outflow current and gust front.

5.1.4 Dynamic and Thermodynamic Squall Line Structures

Following the development and re-orientation of the primary convective region and the development of a surface cold pool and outflow region via precipitation-cooled convective downdrafts, the simulated tropical squall line system eventually reaches the peak of its life cycle around approximately 4h 56m. A view of nearly the entire squall line system at this time is shown in Figure 5.5, for which entropy contours in the stratosphere have again been omitted. Using this cross-sectional view of the convective system, we may divide the system into several regions which will facilitate the discussion of dynamic, thermodynamic and microphysical processes occurring within the system.

Pre-Squall Region

We may consider the pre-squall region as being that part of the system in Figure 5.5 which is entirely downshear of the primary convective region of the squall line system. This region encompasses the area in Figure 5.5 from approximately $x = 50$ km to $x = 70$ km. In this region of the system, beginning at the time of surface outflow and gust front formation as shown in Figure 5.4, warm and moist environmental air is lifted by the advancing cold and dense gust front at it meets the low-level inflow provided by the initial wind profile, which was demonstrated earlier. For the thermodynamic profile which was provided in Figure 5.1, the lifting condensation level (LCL) resides at approximately 1000 hPa, or approximately 150 m above the surface. Thus, a parcel which is lifted to the lowest resolvable height

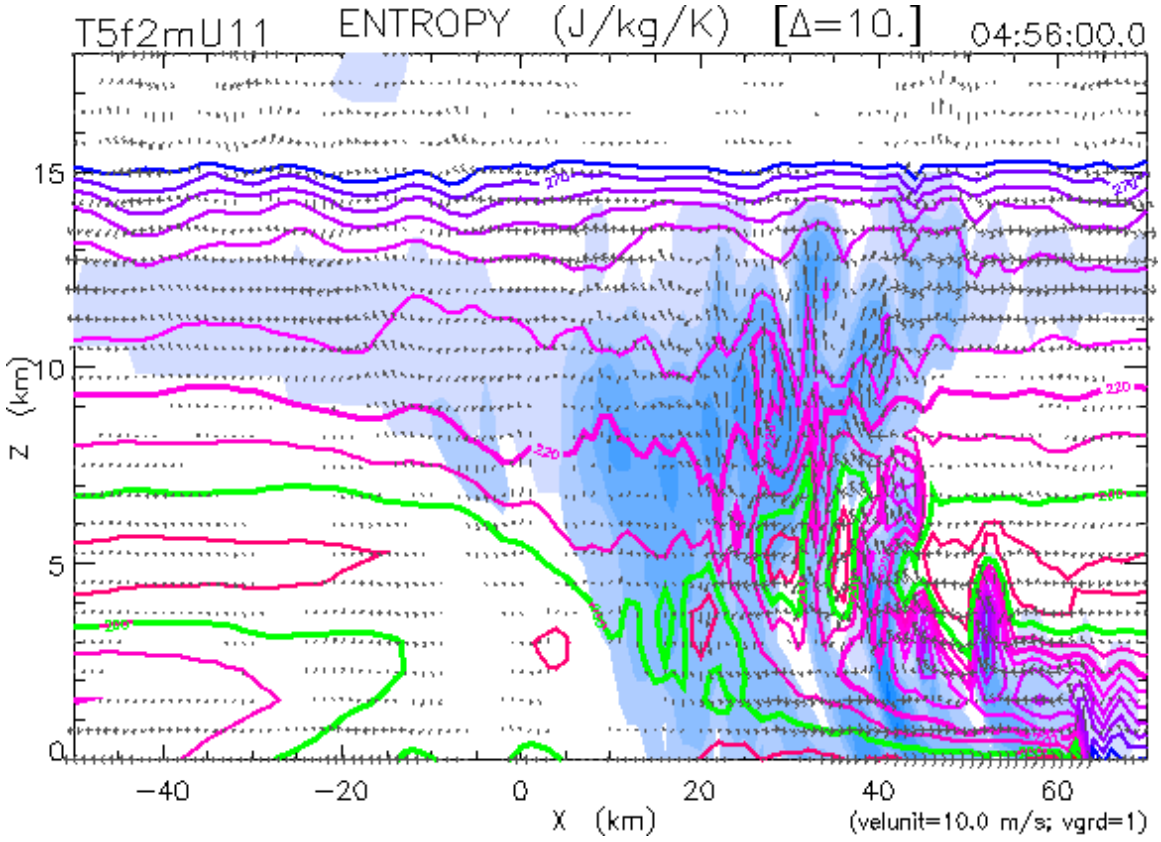

Figure 5.5: Large-scale view of squall line system organization in the 11 m s^{-1} tropical squall line experiment.

above the surface in the model, 200 m, would already have exceeded its LCL and would produce condensation and, subsequently, would be warmed to a temperature greater than dry-adiabatic ascent from the surface to this level would have provided. It is for this reason, and because no layers of convective inhibition (CIN) exist in the profile in Figure 5.1, that the level of free convection (LFC) also resides at approximately 1000 hPa in this simulation, such that the same parcel will will acquire a significant amount of buoyancy from this condensation warming. Through these processes, a moist convective updraft will likely form above the advancing gust front and surface outflow layer.

This process is demonstrated in Figure 5.6a, which is a snapshot of the surface outflow region in this simulation at 2h 56m. This snapshot denotes the time at which the surface

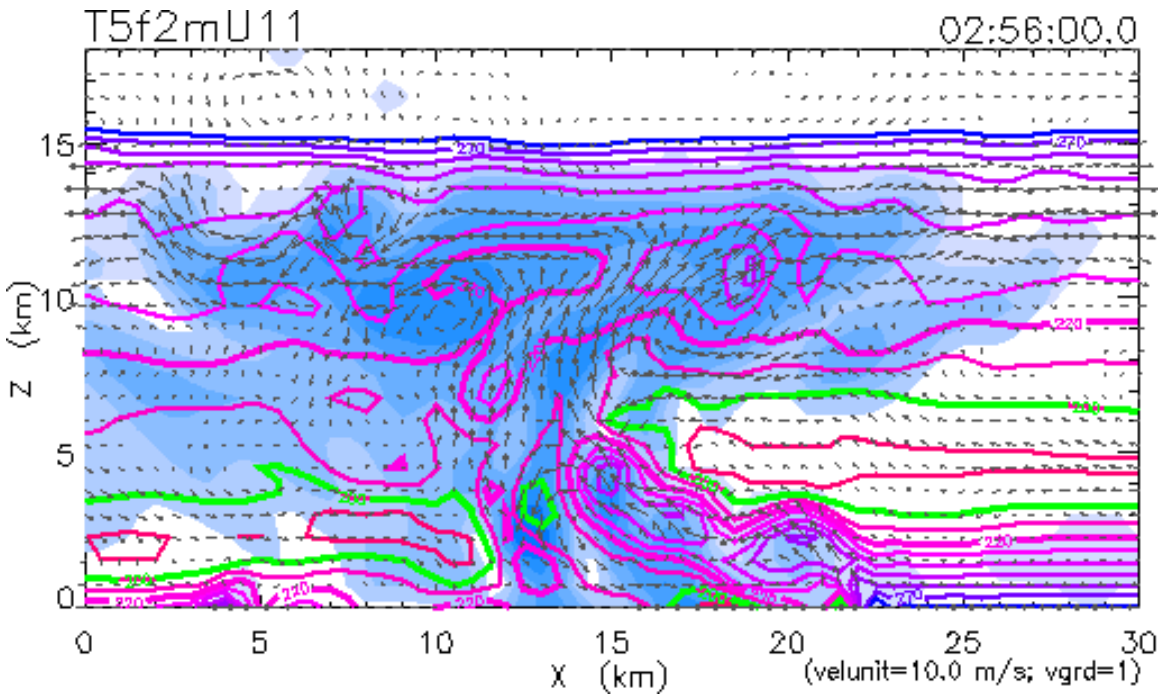

Figure 5.6a: Squall line system convective and transition regions at 2h 56m in the 11 m s^{-1} tropical squall line experiment.

cold pool begins to propagate forward, against the low-level environmental winds. At this early stage in the life of the surface outflow layer, it is clearly evident that toroidal motions in the new convective plumes assist the strength and propagation of the surface outflow layer. However, the strength of these new buoyant updrafts is somewhat hampered by stability in the middle and upper layers created by the evaporation of an overhanging pre-squall stratiform region which resulted from earlier convective outflow aloft. Later in the life of the gust front and surface outflow layer, the new convective plumes become more vertical in their initial ascent, as demonstrated in the simulation snapshot at 4h 30m in Figure 5.6b, but will still be forced to delay their full development until they are joined by the convective region of the squall line system, which will provide a more conducive environment through the depth of the troposphere for full development of the buoyant updrafts.

Figures 5.6b and 5.6c contain profile snapshots of the squall line system at 4h 30m

and 4h 56m, respectively, for which each frame contains the shaded cloud and precipitation content and wind vectors at that time as defined in Section 4.1.3. The frames for Figures 5.6b and 5.6c are differentiated by the contoured quantity: Figure 5.6bI and cI show isolines of the dry-air-specific entropy of moist air, as calculated by equation (4.2); Figures 5.6bII and cII demonstrate the perturbation temperature, as calculated by $T' = T - \bar{T}(z)$; Figures 5.6bIII and cIII demonstrate the horizontal vorticity structure about the squall line system. The parts of Figure 5.6d follow the same organization, but include close-up snapshots of the pre-squall surface outflow and gust front region at the simulation time of 5h 02m.

After the initial direct assistance to gust front propagation by convective circulations, the surface outflow layer is constantly replenished by moist convective downdrafts in the primary convective region, such that the forward speed of the gust front consistently increases over the interval between the snapshots in Figures 5.6a and 5.6b, and by 4h 30m has a forward speed of approximately 8.3 m s^{-1} against a low-level wind speed of 11 m s^{-1}. By this time, the gust front has reached approximately $x = 55$ km, still within the finest mesh of the model domain, and has begun to slow and decrease in intensity with regard to the cool surface layer within the outflow. The regular spacing of new convective plumes above the surface outflow layer at this time resembles a similar aspect of the 10 m s^{-1} simulation, as shown in Figure 4.13e. Within the initial surface outflow and gust front region, a secondary gust front has begun to form by 4h 30m, and can be seen at approximately $x = 43.5$ km as a more intense, cooler surface outflow layer.

Over the period between 4h 30m (Figure 5.6b) and 4h 46m, the primary gust front and surface outflow layer slows in its forward motion to approximately 3.1 m s^{-1} during this interval and reaches an ultimate distance of $x = 60$ km from the initial convective point, while the more intense secondary outflow boundary has accelerated to approximately

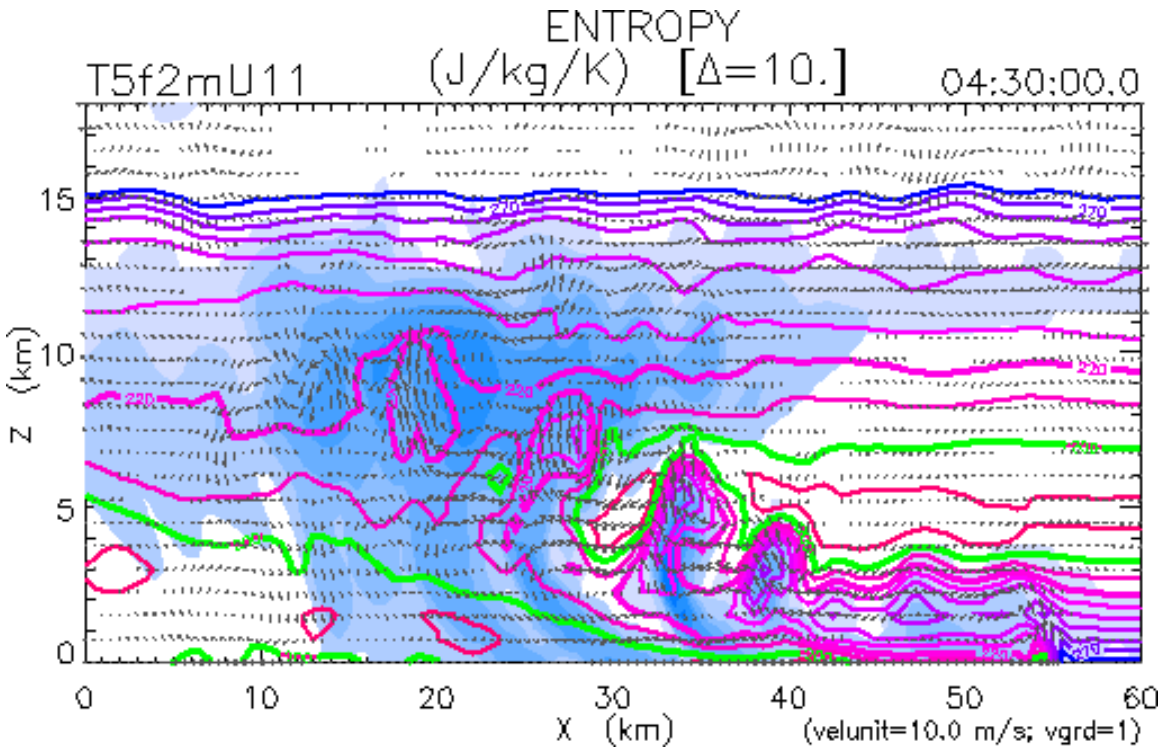

Figure 5.6bI: Squall line system outflow, convective and transition regions at 4h 30m in the 11 m s^{-1} tropical squall line experiment. Contours are of the dry-air-specific entropy of moist air, at intervals of 10 J kg^{-1} K^{-1}.

13.5 m s^{-1} and by 4h 46m has reached $x = 55$ km. This secondary outflow continues to accelerate to a speed of approximately 16.7 m s^{-1} before crossing the maximum extent of the primary outflow region, at $x = 60$ km, around 4h 52m. Upon meeting the undisturbed pre-squall boundary layer air, the outflow layer begins to form a head at its leading edge which ultimately extends to approximately 1 km in depth, about 25% deeper than the main region of the surface outflow layer, and slows to an approximately 6.3 m s^{-1} over the interval between 4h 52m and 4h 56m. Snapshots of the squall line system at 4h 56m are shown in the large scale view of Figure 5.5 and here in Figure 5.6c.

By 5h 00m, the gust front has accelerated again to approximately 10.4 m s^{-1} under the influence of continued convective outflows and flows from the rear of the squall line system through and beneath the convective line, and maintains an average forward speed

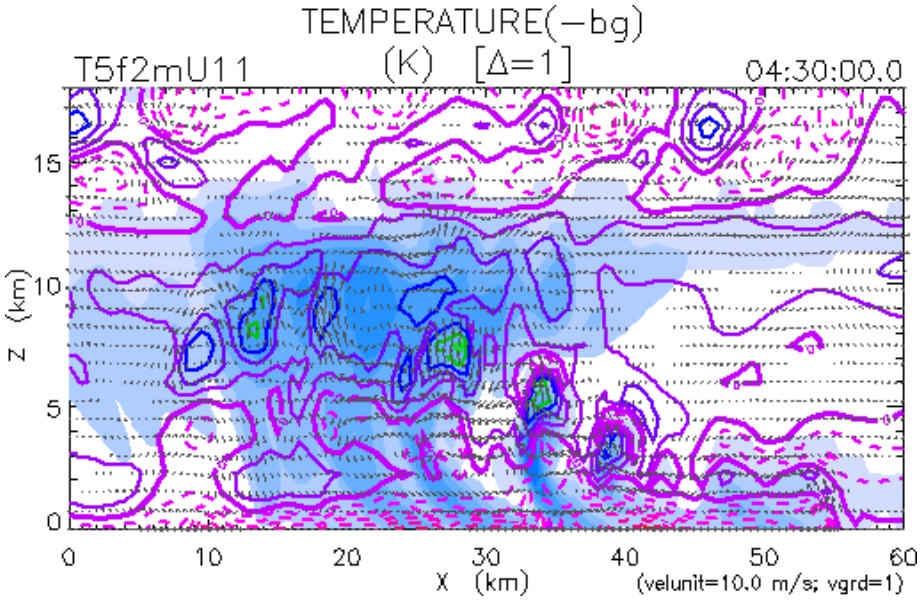

Figure 5.6bII: Squall line system outflow, convective and transition regions at 4h 30m in the 11 m s^{-1} tropical squall line experiment. Contours are of perturbation temperature ($T' = T - \bar{T}(z)$), at intervals of 1 K.

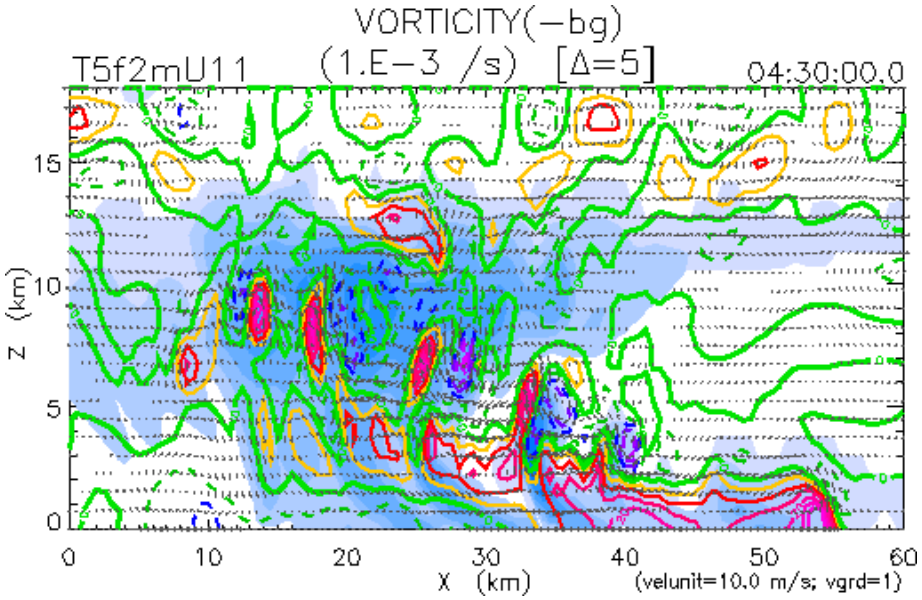

Figure 5.6bIII: Squall line system outflow, convective and transition regions at 4h 30m in the 11 m s^{-1} tropical squall line experiment. Contours are of horizontal vorticity, at intervals of 5×10^{-3} s^{-1}.

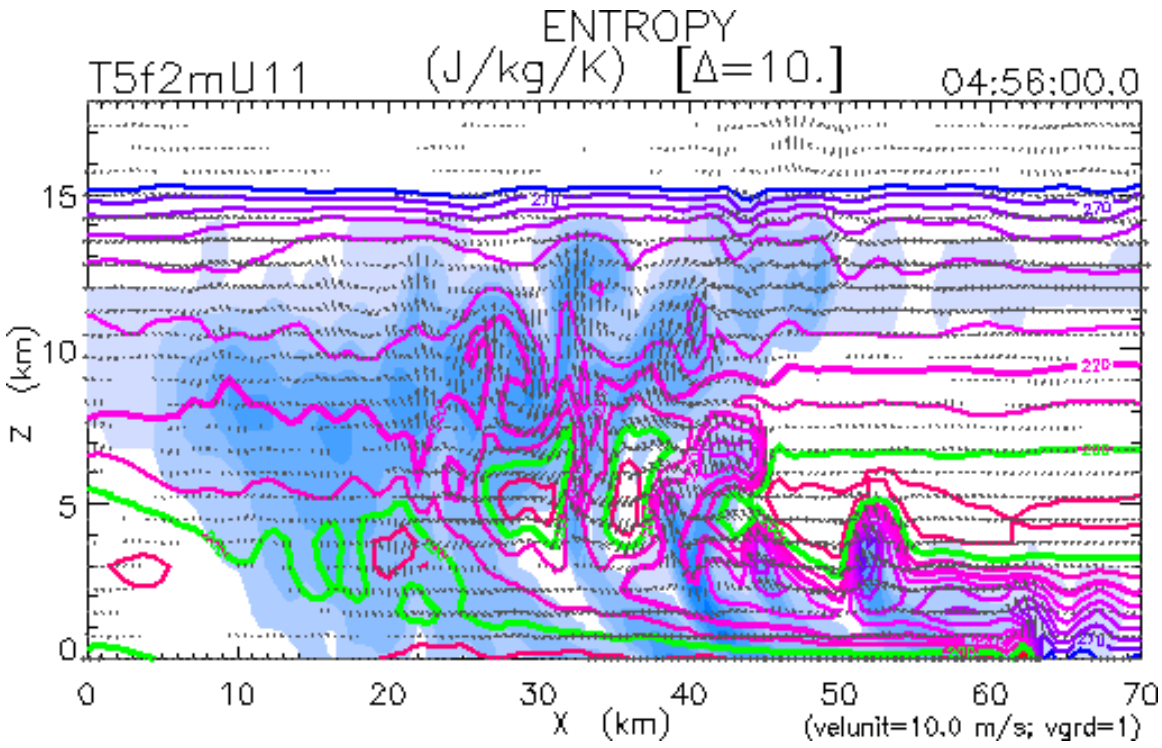

Figure 5.6cI: System structure at 4h 30m in the 11 m s^{-1} tropical squall line experiment. Contours are of the dry-air-specific entropy of moist air, at intervals of 10 J kg^{-1} K^{-1}.

of 10.3 m s^{-1} over the interval between 5h 00m and 5h 30m before beginning to diminish in strength near $x = 83.5$ km, already having entered the next coarser mesh of the model domain. Over this period, convection is generated on the gust front and upper surface of the outflow layer in a quasi-periodic manner which can be viewed in detail in Figure 5.6d. The gust front reaches $x = 100$ km, well into the second mesh of the model domain, before fizzling out near the end of the model simulation at 6h 00m with an average forward speed over the last 30m of approximately 9.2 m s^{-1}.

Convective Region

While the surface outflow and gust front regions may provide some of the more interesting and complex aspects of the tropical squall line system in its developing and mature phases, these structures would not exist without strong, tilted convective updrafts

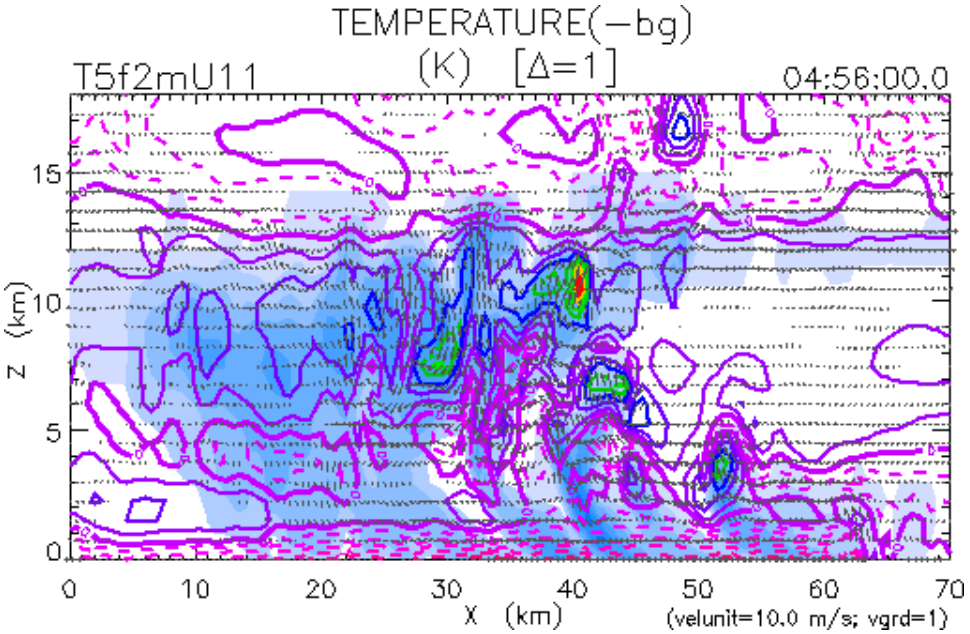

Figure 5.6cII: System structure at 4h 30m in the 11 m s^{-1} tropical squall line experiment. Contours are of perturbation temperature ($T' = T - \bar{T}(z)$), at intervals of 1 K.

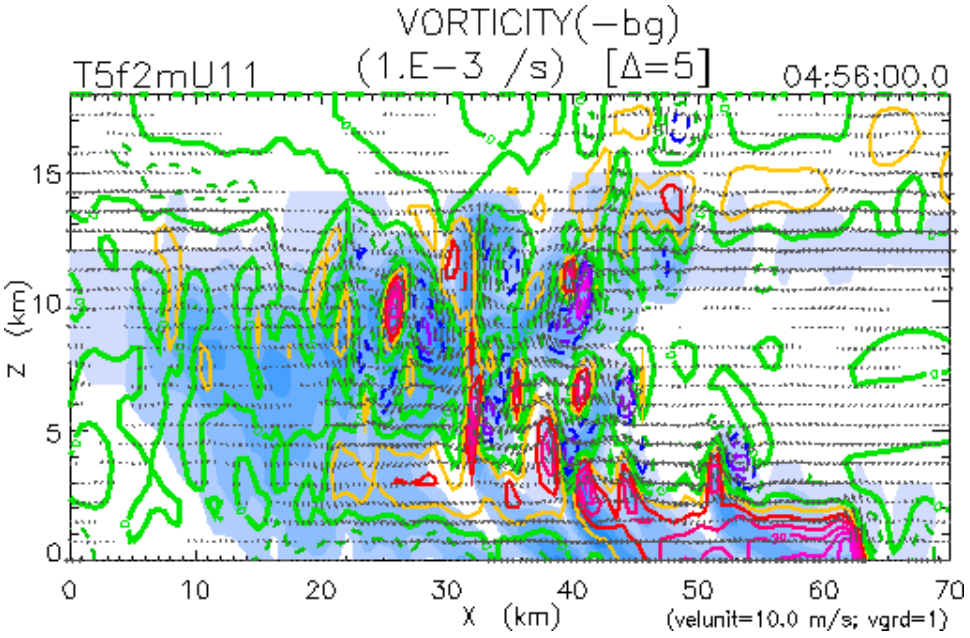

Figure 5.6cIII: System structure at 4h 30m in the 11 m s^{-1} tropical squall line experiment. Contours are of horizontal vorticity, at intervals of 5×10^{-3} s^{-1}.

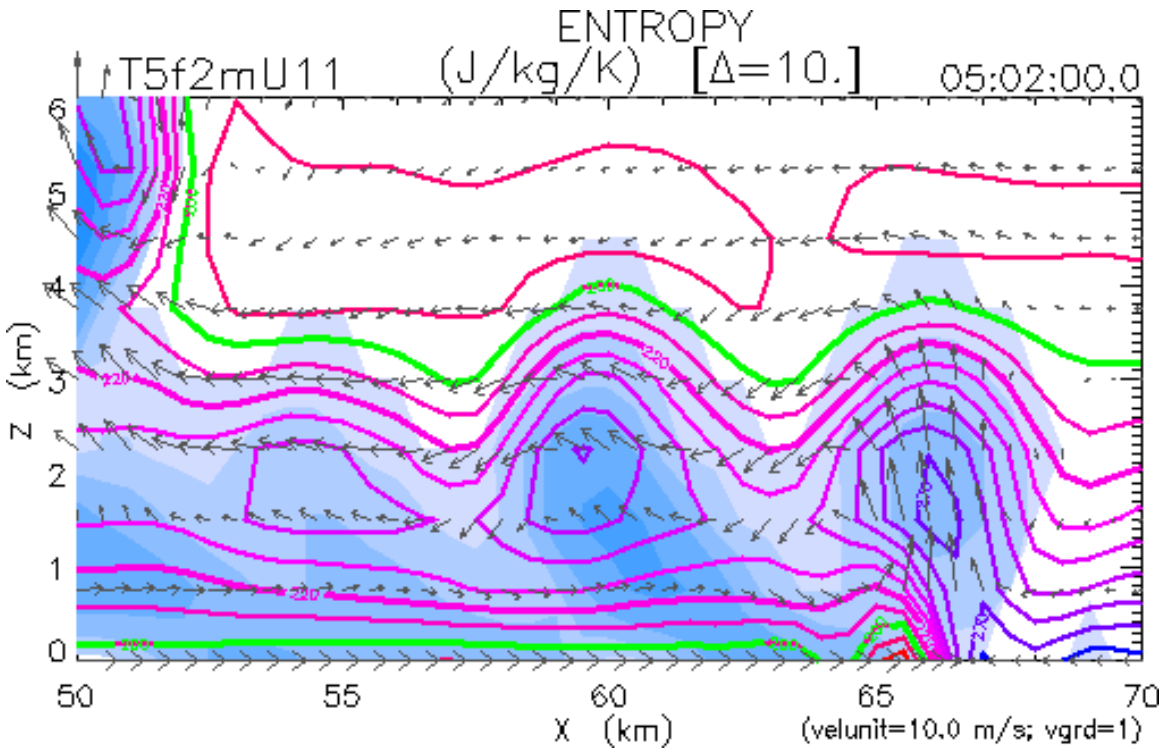

Figure 5.6dI: Pre-squall surface outflow region at 5h 02m in the 11 m s^{-1} tropical squall line experiment. Contours are of the dry-air-specific entropy of moist air, at intervals of 10 J kg^{-1} K^{-1}.

and precipitation-cooled convective downdrafts. These processes occur in a region which, in Figure 5.5, may be defined between $x = 35$ and $x = 50$ km, and is characterized by deep overturning updrafts, strong absolute vertical velocities, and heavy precipitation which reaches the surface. The convective region is maintained by updrafts which result from the low-level forcing of undisturbed pre-squall environmental air into shallow, near-surface "jump" updrafts, which subsequently condense and are warmed upon attaining a level of saturation, and form buoyant updrafts which ascend to their level of equilibrium within the immediate environment of the already-disturbed convective region.

Early in the life of the squall line, as shown in Figure 5.6a, convective outflows are directed toward several important areas of the system. Because of the rearward tilt of the convective updrafts in the lower levels, surface outflows are directed forward, against the en-

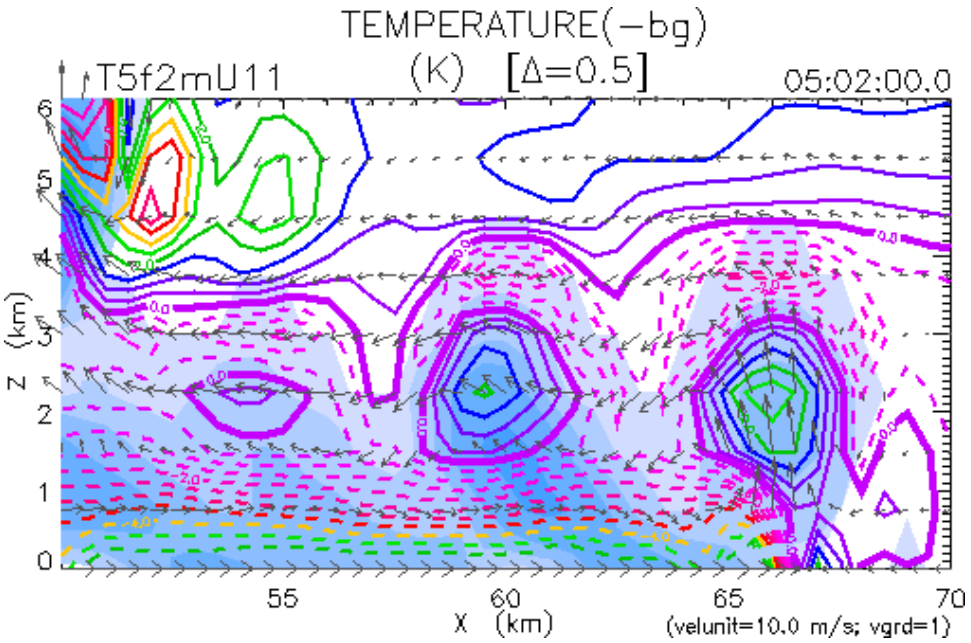

Figure 5.6dII: Pre-squall surface outflow region at 5h 02m in the 11 m s^{-1} tropical squall line experiment. Contours are of perturbation temperature ($T' = T - \bar{T}(z)$), at intervals of 0.5 K.

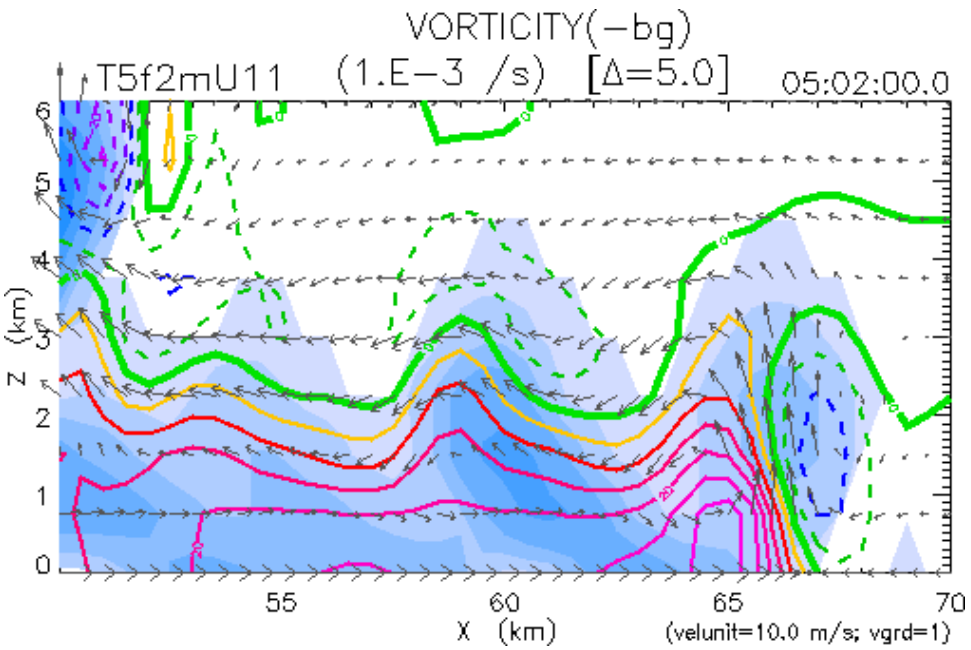

Figure 5.6dIII: Pre-squall surface outflow region at 5h 02m in the 11 m s^{-1} tropical squall line experiment. Contours are of horizontal vorticity, at intervals of 5×10^{-3} s^{-1}.

vironmental wind and downshear. The evolution of these flows was demonstrated in Figure 2.4. Because the convective updraft is relatively vertical in the upper levels, and because the system has yet to begin propagating with any significant speed, ouflow aloft is directed toward both the front and rear of the system upon reaching the tropopause. Outflow aloft which is directed forward, into the pre-squall region, forms a persistent stratiform region which inhibits the growth of new convective plumes on the surface of the pre-squall outflow layer ahead of the established convective region.

As the region of primary convective activity begins to shift slowly toward the new convective cells forming on the surface outflow layer ahead of the squall line, a relative flow of pre-squall environmental air through the convective line is established in the middle levels. Because of this new front-to-rear flow, more convective outflow aloft is directed toward the rear of the system, as shown in Figure 5.6b, such that the inhibitive effects of the slowly-dissipating pre-squall upper-level stratiform region are diminished. This allows greater development of the new pre-squall convective plumes ahead of the primary convective region, which begins to shift forward more quickly with the stronger development of new buoyant convective updrafts. This further directs the outflow of convective debris aloft toward the rear of the system. With stronger forward propagation of the convective region, and the squall line system as a whole, comes the possibility that convective cells may not reach their fullest development before finding themselves already at the rear of the convective region. Additionally, forward propagation of the system forces the development of storm-relative flow which is directed through the pre-squall and convective regions toward the rear of the system, further assisting the advection of cumulonimbus debris and still-active cumulus cells out of the convective region and into a trailing stratiform region.

In Figure 5.6b, it may seem as though the convective region extends from $x = 10$ km

to $x = 40$ km. However, closer inspection reveals that the forward cells may develop more slowly than in the undisturbed atmosphere due to some inhibitive effects of the upper-level pre-squall stratiform region, while cells which are nearest to the rear of the convective region exhibit residual convective motions in the middle and upper levels only, and therefore cannot be considered an active cumulonimbus which typically extends through the full depth of the troposphere. Considering these caveats, the actual convective region may be defined, in Figure 5.6b, as extending from $x = 25$ km to approximately $x = 35$ km. The convective region expands again slightly by 4h 56m, as shown in Figure 5.6c, and by this time extends from $x = 30$ km to approximately $x = 45$ km.

The increased forward speed of the squall line system has a visible effect on the thermodynamics of the convective region by this time in the isolation of unsaturated regions between strong convective updrafts. These mid-level "dry" regions have the ability to reduce the potential instability of the convective region by mixing into adjacent updrafts, evaporating precipitation and cloud droplets and cooling the air there, when one considers that a cooling of the middle levels in the convective region would suppress convective development from below and further ascent and rearward flow of convective debris into the upper-level trailing stratiform region. In association with the strong convective updrafts and with the convective downdrafts which have commenced in the presence of such a dry region, a rotor-like circulation has developed within the squall line by 4h 56m and is centered around $x = 37$ km at a height of approximately 3 km.

Transition Region

The post-squall transition can be distinctly identified only in the mature phase of the simulated squall line system evolution, and can be seen in the cross-section of Figure

5.5 immediately behind (to the left of) the primary convective updrafts in the lower levels and beneath residual convective activity to the rear of the main updraft region in the upper levels. This area is quite small, extending from approximately $x = 25$ km to about $x = 35$ km and from the surface of the model domain to approximately $z = 7.5$ km in height. This region, as discussed in Chapter 2, may be characterized by weak compensating (forced) and negatively buoyant downdrafts and low, or nonexistent, liquid water contents owing to the evaporation of precipitation in the downdraft air. In the middle levels behind the primary convective updrafts, the transition region receives precipitation and downdraft air from residual convective circulations which have been advected rearward out of the convective region and toward the trailing stratiform region.

In Figure 5.6b, we see that moist downdraft air of the transition region contributes significantly to low-level flow from the rear of the convective region into the surface outflow layer and, ultimately, to the advancing gust front. Near the surface, downdraft air in the transition region is forced beneath the convective updrafts and toward the pre-squall region by a cool and dense airmass near the surface beneath the forward edge of the trailing stratiform region. The intensification of this surface cold pool and its dynamical effects on the direction of downdrafts and outflows in the transition region are more clearly evident in Figure 5.6c. In this way, a rear-to-front (RTF) flow is established within the convective circulations without a source external to the system. We may expect that, if a flow were to originate from behind the squall line system in the mid-levels and advance to the front of the system while descending, due to precipitation-cooling beneath the trailing stratiform region, that it may carry stratiform precipitation forward in the system as well as enhancing near-surface flows beneath the transition region.

Pre-Squall and Trailing Stratiform Regions

Convective debris which is transported aloft and rearward by flow through the convective line induced by the forward motion of the squall line system eventually forms the trailing stratiform region, which can be identified in Figure 5.5 as an area which extends rearward from approximately $x = 35$ km, the location of the post-squall transition region, to $x = -50$ km, beyond the left end of the snapshot. The stratiform region is primarily characterized by a persistent cloud layer in the middle and upper levels of the troposphere which commonly extends several tens of kilometers behind the convective region. The trailing stratiform region is also commonly characterized by steady precipitation near the convective and transition regions which is less intense in surface accumulation rate than beneath the convective region and may or may not reach the surface.

At the early stages of squall line system evolution, as shown in Figure 5.6a, we see the initial formation of middle- and upper-level stratiform cloud and precipitation regions forward and rearward of the primary convective region. As the squall line begins to propagate with the discrete formation of new convective cells on its surface outflow layer, the pre-squall upper-level stratiform region diminishes in size while convective cells are forced rearward, establishing a persistent post-squall cloud mass in the mid-levels and above, as shown in Figure 5.6b. With the dissipation of convective activity in this cloud mass, and the release of convective precipitation in the squall and post-squall regions, the cloud mass is carried further rearward by flows through the convective line while microphysical processes, which are described in Section 3.2.3, allow the continued formation of precipitation as long as the region remains saturated.

As this stratiform precipitation is released from the cloud mass, more slowly than by active condensation precipitation formation mechanisms such as in the convective region,

the cloud mass is slowly diminished while being carried further rearward from the convective region. It may be seen, in Figure 5.6c, that the amount of stratiform precipitation which reaches the surface is quite steady in a region which extends for approximately 15 km behind the convective region, including a small area immediately beneath the post-squall transition region, but then decreases rapidly with distance from the convective region. It may also be noted at 4h 56m into the simulation, at the time of Figure 5.6c, that although some residual convective activity persists in the forward portion of the upper levels of the stratiform cloud and precipitation region, the enhanced precipitation formation in these upper-level convective cells adds little to the intensity of precipitation which actually reaches the surface beneath the transition and stratiform regions.

If we consider the initial thermodynamic profile which was used in the formulation of the model atmosphere for this simulation, the level at which condensation and precipitation particles freeze and melt is located at approximately 3.9 km in height. In the convective region, if we consider simulation results at 4h 30m (Figure 5.6b) and 4h 56m (Figure 5.6c), the most intense precipitation occurs below the freezing level in the updrafts. However, in the trailing stratiform region the most intense precipitation contours are located above the melting level. This phenomenon may be explained with reasoning similar to radar bright-band formation in the stratiform precipitation region of midlatitude and tropical squall line systems: liquid precipitation particles experience greater terminal fall speeds, and thus accelerate through the melting level. This acceleration, as well as a greater reflectivity for water-shrouded ice particles, lends to the increased radar return which is denoted as a bright band near the melting level. The acceleration of particle fall speeds also leads to the attenuation of precipitation densities in these levels, such that lower precipitation densities would be found immediately below the melting level than immediately above. This effect

is most prominently evident in Figure 5.6c, a snapshot of the precipitating regions of the squall line system near the end of the mature phase of its life cycle.

5.1.5 Comparison with Observed Squall Line System Structure

In association with the numerous observations of squall lines presented in Chapter 2, the current 11 m s^{-1} simulation may be evaluated on the basis of its qualitative representation of the fundamental features of tropical squall line system structure. Relevant observational studies through which these squall line system features may be verified are included where appropriate, and those studies which are abbreviated may be referenced through Appendix A. Many numerical modeling efforts oriented toward the simulation of squall lines systems have been validated with the help of observational studies, and provide greater spatial and temporal resolution of important squall line system structures which are not often found in the observational data. A comparison of the current 11 m s^{-1} simulation with previous modeling efforts may be found in the next section. A comparison of the current simulation with observations of squall line systems, the focus of this section, begins with an examination of the fundamental requirements for squall line formation and development, accepting the convective instability of the environment as an unstated precondition. The comparison then proceeds through an examination of dynamic, thermodynamic and microphysical attributes of the squall line system as divided into significant regions, as discussed above, and as a system in its entirety.

It was discussed in Chapter 4 that simulations which included no initial low-level vertical shear of the horizontal wind produced convective systems which either dissipated quickly or produced weak convective regeneration on sporadic low-level ouflow boundaries, neither of which would produce a persistent and regenerative convective system such as a

squall line. In the current simulation, the low-level shear which is required for an adequate intensity of low-level inflow (TMM82) and for the linear organization of the squall line system (Moncrieff and Liu, 1999) is certainly present. The squall line is observed to develop as a multicellular system, such that the system life cycle encompasses multiple individual cumulonimbus life cycles. New cumuli are initiated on the gust front and surface of a low-level inflow layer as jump updrafts (Moncrieff and Liu, 1999), but remain somewhat suppressed in their vertical development due to an overhanging pre-squall stratiform region which was formed by convective outflows aloft (Grady and Verlinde, 1997).

Although the overhanging pre-squall precipitation region may be considered "self-destructive" through the suppression of pre-squall convective development (Houze and Rappaport, 1984), a small degree of pre-squall inflow at all levels is achieved upon the forward propagation of the system (RKW88), which assists in the development of rearward-tilted convective updrafts and the release of precipitation behind the squall line front. The rearward tilt of the squall updrafts assists not only in the deposit of precipition behind the updrafts and the development of convective downdrafts and a surface cold pool and outflow region (Z77), but also in the rearward detrainment of convective cells and debris aloft and the development of a trailing stratiform precipitation region. Convective downdrafts and associated precipitation assist in the longevity of the squall line through the partial drying of cumulonimbus mid-levels, and a moistening of the adjacent non-cloud regions through evaporation of precipitation, both of which promote existing and new convection through the preconditioned region (Nakajima and Matsuno, 1988).

The orientation of convective updrafts and downdrafts ensures the development of a cumulonimbus cell which propagates continuously over a short time (Takeda, 1971), while the development of a surface cold pool and outflow region ensures the development of a

system which propagates discretely over longer time periods (Moncrieff and Liu, 1999). The discrete propagation of the convective line occurs much more quickly than the slower propagation of single cumulus cells in the same environment, such that new convective cells born on the gust front outflow boundary are assimilated into the convective line within one hour of their formation (Matejka and Stossmeister, 1986). The discrete propagation of the convective system commonly reaches 11 m s^{-1} for systems of such a configuration (Barnes and Seickman, 1984), in which the convective line is organized perpendicular to the low-level shear vector. The surface outflow layer is approximately 1.5 km deep, more than adequate for the initiation of new convective cells by the mechanical lifting of pre-squall low-level environmental air, and owes its existence to a combination of convective and stratiform precipitation-laden downdrafts and the formation of a significant cold pool near the surface beneath the system.

Low-level maxima in the vertical velocity field may be found, in Figure 5.5, immediately above the level of the surface convective outflow layer at the gust front, due to mechanically-forced lifting of environmental air by the dense cold pool layer, and near the base of the forward portion of the convective region, by which point buoyant convective updrafts have begun to develop. A third convective maximum may be observed in the upper levels of the convective region, and is likely attributed to additional buoyancy created on the release of latent heat during the freezing of cloud and precipitation droplets. The two convective vertical velocity maxima are separated by a mid-level minimum (JLT97) which occurs, in the case of the 11 m s^{-1} simulation, at a height of approximately 7 km in Figures 4.6c and 5.5. This vertical velocity minimum is located between convective cells both vertically and laterally, in a region of the convective line which is heavily influenced by compensating downdrafts aside the convective cells, by the freezing of cloud and precipitation

particles, and by mid-level lateral inflow from the pre-squall region (Z77).

Although several of the convective updraft cores appear to remain undiluted by mid-level entrainment during ascent (Heymsfield et al., 1978), their eventual aging and demise to the rear of the convective region in the upper levels leads to a release of precipitation and the formation of moisture-laden downdrafts there (Sun et al., 1993) and evaporatively-cooled downdrafts in the mid- and low-level post-squall transition region (Z77; Smull and Houze, 1987a; RHBM88). The upper-level vertical velocity maxima associated with consecutive aging convective cells are observed to ascend with distance from the front of the convective region (JLT97), indicating the advection of aging cells rearward by the upper branch of a front-to-rear system flow (GH82) which originated in the mid-levels of the pre-squall region (Betts et al., 1976; Z77). The advection of aging cells out of the convective region seems to occur quickly and without regard for instability which may remain in the upper levels of the region, as indicated by the residual convective motions which are evident in the forward portion of the upper-level stratiform cloud and precipitation region in Figures 5.6b and c (H77). Precipitation contours which indicate the large amount of moisture released by these aged convective cells into the stratiform precipitation region are separated from the strong precipitation of the convective region by significantly drier transition region downdrafts (Smull and Houze, 1987a).

A significant RTF flow in the mid-levels of the stratiform precipitation region (Betts et al., 1976; Z77) cannot be easily discerned in Figure 5.5, although some evidence of such a flow is evident in the weak wind field within the stratiform precipitation region near $z = 5$ km in Figure 5.6c. Such a RTF inflow through the stratiform region experiences sharp descent as it approaches the post-squall transition region (RHBM88) under the influence of precipitation loading, evaporative cooling, and mechanical forcing by transition region

downdrafts. The formation of a surface cold pool by the evaporation of heavy precipitation in the forward portion of the trailing stratiform region and the existing momentum of the sharply descending RTF flow through the stratiform region serve to force stratiform precipitation near the surface beneath the post-squall transition region, which correspondingly forces some low-level transition region downdraft air beneath the squall line convective region (Smull and Houze, 1987b). These forced flows, along with the convective updrafts, mid-level front-to-rear flow, and transition region downdrafts, close the rotor circulation observed in the lower levels of Figure 5.6c, as discussed above.

The branch of mid-level pre-squall inflow which was carried aloft by convective updrafts to form the upper-level front-to-rear flow may also, as discussed earlier, form a branch which bypasses the convective region and is forced downward, by interactions with transition region downdrafts and the sharply descending RTF flow, to form a low-level front-to-rear flow (Z69; Betts et al., 1976; Z77). Such a low-level flow structure may be observed in Figure 5.5, from approximately $x = -10$ km to the left edge of the snapshot, and on the far left side of Figures 5.6b and c. Although this flow seems to affect the lateral extent of the stratiform region surface cold pool toward the rear of the squall line system, the simulation examined here was not run for a long enough period, and at a great enough vertical resolution, to allow for an analysis of cold pool dissipation and the recovery of the post-squall boundary layer to convectively neutral or unstable conditions as examined by Nicholls and Johnson (1984). Also, it is expected that surface sensible and latent heat fluxes, absent from the present model formulation, are essential to such a recovery process.

5.1.6 General Comparisons with Previous Squall Line System Modeling Efforts

Several efforts at the numerical modeling of squall line systems which were presented in Chapter 2 offer valuable insight into the structure of squall line simulations which may not be resolved, in a spatial or temporal sense, in efforts to observe squall line system dynamic and thermodynamic structure. Since various models, methods of analysis, methods of initialization, and regions and structures of interest were employed in those efforts, the comparison of the 11 m s^{-1} tropical squall line system simulation presented here with any large group of these efforts, even only the tropical maritime squall line systems, could become quite complicated and lengthy. For this reason, a select few of the efforts presented in Chapter 2 have been chosen for comparison with the present simulation because they involved efforts at the analysis of specific and crucial structures involved in squall line system generation, propagation and maintenance, and eventual decay. Many earlier efforts included in the discussion here are abbreviated, and may be referenced through Appendix A.

In Y86, one of the earliest and most ambitious efforts at the modeling of a tropical squall line system was presented. As for many modeling efforts to follow, the initial conditions employed were derived from the environment of the 12 September, 1974, GATE squall line system. In Y86, stretched horizontal and vertical coordinates were employed in a two-dimensional system for which the mixed phase microphysical formulation involved a complex determination of cloud and precipitation mixing ratios, fall velocities and conversion rates. The simulated system was found to reach a steady, mature state approximately 2 hours after initialization with a warm bubble near the surface. In this case, the thermal employed to initiate convection was constructed from a disturbance in the potential temperature (θ) field, which is equivalent to the near-surface initial temperature (T) perturbation employed

in the present 11 m s^{-1} simulation. In the mature stage of the simulated squall line system in Y86, the convective region was found to be approximately 20 km wide and propagated toward the east, as did the observed GATE squall line system, at an average speed of approximately 7 m s^{-1}, which was significantly slower than the observed GATE squall line system propagation speed of approximately 13.5 m s^{-1}, while the simulated surface outflow pool and gust front was found to propagate at an average speed of approximately 12 m s^{-1}.

The current simulation, although not initialized with the same thermodynamic sounding, wind profile and large-scale forcing as employed in Y86, produced a surface outflow layer and gust front which propagated at approximately 10.3 m s^{-1} in the interval between 5h 00m and 5h 30m. The results presented in Y86 demonstrated a pre-squall overhanging stratiform precipitation region which diminished with the forward propagation of the squall line system, as was found for the 12 September, 1974, GATE squall line system by Leary and Houze (1979a), and a layered wind structure in the trailing stratiform precipitation region which included front-to-rear system-relative flows in the upper and lowest levels and RTF inflow in the low- and mid-levels, as was observed for the GATE system and reported in GH82. Both of these tropical squall line system structures were successfully reproduced in the current 11 m s^{-1} simulation.

Using Colorado State University's RAMS, in N87 a two-dimensional simulation of the same 12 September, 1974, GATE squall line system was reported. Throughout the propagation of the developing and mature squall line system, a persistent "daughter cloud" was found to reside in the lowest levels just above the lifting condensation level (LCL) several kilometers ahead of the gust front, a feature which was also found in the current 11 m s^{-1} simulation. The simulated system presented in N87 reached a mature phase by 5 hours in a similar initial thermodynamic and wind profile to that employed in Y86. This

wind profile was a composite of pre-squall observations during GATE, and included only 2 m s^{-1} of westerly shear in the low levels beneath the African Easterly Jet (AEJ), at a level of approximately 700 hPa, and the weaker Tropical Easterly Jet at approximately the 200 hPa level. By contrast, the squall line system simulation presented here was produced in an environment with LLS of 11 m s^{-1}, while simulations of a construction similar to the current results were performed earlier by Ooyama and have been presented in O95.

In the results of O95, reproduced in Figure 4.4, convection initialized in an environment of extremely light shear ($\leq$ 5 m s^{-1}) was found to develop sporadically and did not propagate coherently for a significant distance, but still persisted for several convective life spans before dissipation. However, the results presented in N87 seem to indicate that the initial low-level shear was of little immediate importance in the determination of system longevity, as the wind profile employed was dominated by MLS due to the height and strength of the AEJ, which caused tilted updrafts to develop. The effects of a tilted updraft have been reviewed here extensively, but it bears repetition that a more strongly-tilted updraft produces a stronger surface cold pool and outflow which, in the case of the results presented in N87, produced a convective system which propagated at approximately 12.3 m s^{-1}, a speed much closer to that of the observed system than the results presented in Y86. During the mature stages of the simulated squall line system, the mid-level RTF flow was assisted by the presence of the AEJ, and was forced to descend by the cooling effects of precipitation melting and evaporation in the trailing stratiform region until it reached the surface immediately behind the convective region.

A similar structure is found here, without the presence of the AEJ or a comparable midlevel jet in the initial wind profile. That such a rear inflow may be initiated by the convective system itself was hypothesized by Smull and Houze (1987b). Such descending

rear inflow "jets" have been observed in numerous tropical and midlatitude squall line systems, as discussed in detail in Chapter 2. Weisman (1992) examined the variability of rear inflow jet configurations and their contributions to updraft strength in the main convective region and the longevity of the convective system. In the terminology employed by Weisman in the analysis of simulations performed there, the current 11 m s^{-1} demonstrates a descending rear inflow through the trailing stratiform region which is thought to allow the squall line system to achieve a much weaker maximum strength than an elevated rear inflow would support. This difference was attributed to the additional contribution of a descending rear inflow to the vorticity production in the surface outflow layer ahead of the squall line, thereby creating an unbalanced condition in the region of new convective development as examined earlier in RKW88 and revised by Weisman. This balance condition as it applies to the current simulation is discussed below.

In N87, the surface outflow layer and gust front were simulated more accurately with a high-resolution region, in which $\Delta z = 350$ m, in order to discern small-scale pressure and temperature structures. High pressure was found at the surface beneath the head of the convective outflow layer, and a strong negative pressure perturbation was found immediately behind the gust front and head at the upper surface of the convective outflow layer. Both of these small-scale pressure structures may be found to a lesser degree in the current simulation (not shown). Strong negative temperature perturbations of approximately $T' = -5$ K were found near the surface beneath the head of the outflow layer and gust front in the simulated squall line system of N87. These cold regions are also successfully reproduced in the current simulation, as shown in Figure 5.6dII which demonstrates an absolute temperature perturbation, relative to the undisturbed pre-squall environment, of approximately $T' = -5$ K beneath the surface outflow layer and a perturbation relative to

the higher temperatures beneath the forced updraft ahead of the gust front of approximately $T' = -7$ K.

5.1.7 The Mechanism and Periodicity of Convective Cell Generation

In FO89, a squall line system was simulated which maintained a discrete regeneration of convective cells on the forward surface outflow region during an infinite mature phase (i.e., no natural decay of the system was found in the simulation). Such discrete production of convective cells was discussed in FO89 and later in FT95, and will be discussed below in the context of the simulation presented by FT95. The simulations presented in FO89 and FD95 focused on the variation of initial environmental parameters, specifically the strength of the LLS and the depth of the shear layer and the effects of these conditions on the periodicity of new cell generation. Since many of these simulations incorporated vastly different initial shear strength and depth conditions, with correspondingly different results, only the results presented in FO89 and FD95 for simulations in which the shear strength and layer depth were similar to the current simulation, as well as some general results, will be discussed. Specifically, the FO89 and FD95 simulations in which the shear strength $\Delta u = 10$ m s^{-1} and the shear layer depth $D = 2.5$ km are similar to the current simulation, in which $\Delta u = 11$ m s^{-1} and $D = \sim 3$ km.

In the simulations presented in FO89 and FD95, the basic period of convective cell regeneration on the surface gust front was approximately 16 minutes, with a possible harmonic period of 32 minutes at which time a weaker cell was formed at a greater distance behind the gust front than the primary convective updrafts. Each cell of this cycle was formed by, and carried with it, high-θ_e (i.e. warm and moist) air from the boundary layer. However, it was found in FO89 that the primary cell of the cycle was subjected to the

mid-level pre-squall inflow in greater amounts, and was affected in its later development by the entrainment of large amounts of this low-θ_e (i.e. cool and dry) mid-level air, while the secondary cell generally formed in or near some remaining updraft which continually fed the primary cell and protected the secondary cell from entrainment of the mid-level inflow. These secondary, protected cells were found to entrain air mostly from the surface outflow region during their initial development and were therefore observed to experience a longer mature updraft phase, decayed more slowly in the rear of the convective region, and produced weaker convective downdrafts.

The current 11 m s^{-1} also produced a complex periodic regeneration of new convective cells on the gust front and surface outflow layer, but at a different and more variable fundamental period than that found in FO89 and FD95. It should be explicitly noted that, although a regenerative mature phase is reached in the current experiment and simulation, this phase is by no means steady, and eventual decay of the system does occur as the surface outflow enters the next coarser grid of the model domain. Various aspects of the mature phase of the squall line system simulated here have been demonstrated in the snapshots in Figures 5.5, 5.6, and 5.7. As noted in the above discussion which compared this squall line system with previously observed systems, the propagation speed of the gust front itself experienced a temporal oscillation over its life span which seemed to result from two successive and strong surface outflow pools. A more detailed analysis of the simulated system, at a time resolution much finer than that represented by the included figures, demonstrates oscillations in both the gust front propagation speed and the convective regeneration period.

For the current simulation, the fundamental period of convective cell generation falls between 10 minutes and 16 minutes, and oscillates within this range over the period of the mature phase of the squall line system along with the gust front propagation speed. The

time of cell generation is measured as the time at which the vertical velocity within the nascent cell at the $z = 1.5$ km level becomes strongly positive, indicating a transition of the convective cell from ascent forced by the propagating gust front to ascent by buoyant convective motions. The $z = 1.5$ km level was chosen because the convective surface outflow commonly occupies the layer between this level and the surface, because the LCL was calculated to reside at approximately 150 m (1000 hPa), and because the wind vectors at this level were more easily discernable above and behind the gust front, where buoyant convection would be expected to occur, than in the gust front itself, where forced ascent would still be expected to dominate the convective dynamics.

After an intial, somewhat chaotic generation of strong primary cells between the advent of the mature phase, as represented by Figure 5.6a, and approximately 3h 58m, the simulated squall line system settled into a state of complex oscillation in the generation of new convective cells on the surface outflow and gust front. Secondary cells were formed within the fundamental oscillation period of 10 to 16 minutes at between 6 and 10 minutes after the generation of the primary cell, depending on the length of the primary cell cycle. Over the period between 3h 58m and 5h 02m, beyond which time the gust front passed out of the grid of highest resolution within the model domain, the average fundamental cell regeneration period was 12.8 minutes, while the average lag of secondary cell generation behind that of the primary cell was 8.8 minutes. As the lag-time of secondary cell generation increased, along with the period between primary cell generation events, the gust front was observed to accelerate from approximately 6.3 m s^{-1} at 3h 20m to approximately 8.3 m s^{-1} at 4h 30m, after which time the primary gust front was observed to diminish in strength and was followed by a resurgent gust front several minutes later, marking an acceleration of the surface outflow layer to an average speed over the interval between 5h 00m and 5h

30m of approximately 10.3 m s^{-1}.

It may be possible to relate the average lag of secondary cell generation behind that of the primary cell to the Brunt-Vaisälä period, $\tau = 2\pi/N$, for which N is the Brunt-Vaisälä frequency calculated by

$$N^2 = g\frac{d(\ln\theta)}{dz}.$$

For the thermodynamic profile demonstrated in Figure 5.1, the Brunt-Vaisälä frequency in the 950 to 700 hPa layer, in which the generation of new convective cells is expected to occur in the region of the surface outflow layer gust front and head, is approximately $N = 0.0119$ s^{-1}, which provides a period of approximately $\tau = 8.8$ minutes. This value is exactly that of the average lag of secondary cell generation in the complex periodic oscillations described here. We may hypothesize a process by which the release of the primary cell in a convective cycle generates a gravity wave on the surface of the outflow layer. This gravity wave would be expected to oscillate on the surface of the cold pool with a frequency equal to the ambient Brunt-Vaisälä frequency, such that a peak amplitude of this gravity wave oscillation is again achieved in the vicinity of the location of primary cell generation at a lag time equal to the Brunt-Vaisälä period for the surrounding environment.

As well, this gravity wave on the surface of the outflow layer is expected to propagate away from the location of primary cell generation with some finite velocity. Given the typical depth of the surface outflow layer in the current simulation, approximately 1 km, we may calculate the velocity of a gravity wave on the surface of the outflow layer using the shallow-water approximation, for which the speed of an external gravity wave is given by

$$c_g = \sqrt{gH\frac{\delta\rho}{\rho_{outflow}}}.$$

For $H = 1000$ m and an approximation to the density differential between the outflow and enviromental air of $\delta\rho/\rho_{outflow} = 0.01$, we find that $c_g = 9.9$ m s^{-1} on the surface

of the outflow layer. Using this with the previously-determined Brunt-Vaisäla period, a characteristic spacing of cell generation points on the surface of the outflow layer may be determined as

$$\lambda = c_g \tau,$$

such that the characteristic cell spacing for this system is approximately $\lambda = 5.2$ km. This calculation is supported by the simulation results presented earlier in Figure 5.6d, at 5h 02m, and below in Figure 5.7 at various times through the current simulation.

That secondary cells also formed farther behind the gust front was not found in the current simulation, although the finding presented in FO89 and FD95 that secondary cells ascend within or very near the updraft of the primary cell is strongly supported here. In the 11 m s^{-1} simulation, between 3h 50m and 5h 00m, primary cells were generated at an average distance of 7.6 km behind the gust front on the upper surface of the outflow layer, commonly just behind the head, while secondary cells were found to form at an average distance of 7.8 km behind the gust front. Given the translation of the primary cell updraft with the cell itself, rearward toward the main convective region, this small distance between generation points relative to the location of the gust front would certainly allow a secondary updraft to ascend within the protective and preconditioned confines of the primary cell's wake. The distance of primary and secondary cell generation behind the gust front was found to diminish rapidly after 4h 46m, as the secondary surface outflow layer began to move beyond the maximum extent of the primary gust front after accelerating in its preconditioned region near the surface. By 5h 02m, the last primary convective cell regeneration event visible within the finest grid of the model domain had occurred immediately above the gust front. This does not imply that the surface outflow and the near-surface environmental shear had finally come into balance, which will be discussed

later, as the entire convective region was found to propagate beyond the finest grid in the model domain by 6h 00m, at the prescribed end of the simulation.

The process of new cell generation on the surface outflow and gust front was the primary focus of discussion in FT98. The hypotheses presented there were formulated after a careful analysis of the vorticity balance argument for "optimal" conditions which was presented in RKW88 and summarized below. In FO89 it was found, through numerical simulation of various convective systems arising from equally various shear strengths within a constant shear layer depth, that supercell-type systems which result from strongly sheared conditions maintain a continual updraft, such as that which would result from cold pool and ambient shear vorticity balance as prescribed in RKW88, and allow mid-level environmental air to enter the system only through entrainment. However, multicell systems such as the squall line simulated here, which result from moderately sheared conditions, experience intermittent convective updraft and cell formation. By this intermittency, pre-squall mid-level inflow is allowed to enter the convective region as pockets of low-θ_e air which mix with the precipitation-laden convective downdrafts, strengthening these downdrafts and the resulting surface cold pool and convective outflow region by evaporative cooling. In order to rectify the inconsistencies between the RKW88 theory and the convective mode found by most squall line modeling efforts, in FT98 a more refined conceptual model of convective cell generation was proposed based on the theories presented in RKW88 and new modeling experiments.

According to the theory presented in RKW88, vorticity balance between a cold pool gust front and the near-surface environmental shear would support a vertical updraft, which develops toroidal circulations about its core according to external buoyancy pressure gradient forces (FT98), the baroclinic generation of vorticity, and an updraft-compensating

subsidence couplet about the condensing updraft core. Such a columnar configuration is demonstrated in Figure 5.6dI, a close-up snapshot of the surface outflow gust front in the 11 m s^{-1} simulation at 5h 02m, at which time a new cell has begun to form atop the forced updraft but has not yet been advected rearward by the cold pool vorticity or the environmental flow. If the updraft is removed from this column aloft, specifically in the up-LLS direction, by some finite and opposing MLS, then precipitation will be deposited about the convective cell opposite the low-level inflow, forming a cold pool there which will continue to oppose the LLS, as demonstrated in Figure 2.4. In this way, a continuously convecting system such as a supercell storm (Browning, 1964) may be produced.

However, in a mature squall line system for which the cold pool gust front dominates the environmental LLS in an imbalance of vorticity production, the gust front is allowed to propagate against the low-level wind, as observed in all types of squall line systems. This vorticity imbalance also causes a new convective cell to be displaced rearward, over the head of the surface outflow layer, where it may still receive some inflow from the undisturbed pre-squall boundary layer but also begins to draw some of its inflow and updraft air from the surface cold pool itself. This source of convective core moisture was found in the simulations presented in FT98, which demonstrated that more moisture than the undisturbed pre-squall environmental boundary layer could provide was being condensed during the developing stages of the new convective updraft.

One of the other important aspects of new convective cell generation found through simulations presented in FT98 concerned the eventual cut-off of the new cell from its high-θ_e boundary layer source of inflow, which is the basis for convective intermittency in multicellular systems. In FT98 it was explained that, as the new convective cell is displaced rearward over the head of the surface outflow layer, the toroidal circulations which have

developed outside the convective core will begin to oppose the underlying forced updraft, such that a flow of boundary layer air from the surface over the leading edge of the outflow layer is effectively pinched off above the outflow head. Beyond this point, much of the inflow to the convective core consists of entrained moist cold pool and low-θ_e mid-level air, leading to the stabilization of residual convective instability in the updraft core and the eventual dissipation of the convective cell as it is advected rearward by the system-relative front-to-rear flow.

Interestingly, all of these processes are reproduced quite well in the current 11 m s^{-1} simulation. Figure 5.6bI, a snapshot of the squall line system in its mature stage at 4h 30m, demonstrates the formation of a new cell at approximately $x = 52$ km which has approached the maximum height of the outflow-forced updraft but has not yet begun to ascend buoyantly. It is also shown, in Figure 5.6bV, that the compensating (relative) downdrafts on the upstream side of the new convective cell lie immediately above the forced lower level updraft, causing a small region of intense convergence at approximately $x = 55$ km, the location of the surface outflow gust front at that time. This opposition effectively isolates the new cell from its high-θ_e boundary layer inflow ahead of the gust front, forcing the cell to draw upon the low-θ_e air of the surface outflow layerfor moisture during ascent and later condensation and precipitation production.

5.1.8 A "Balanced" State?

In FO89 the vorticity balance prescribed in RKW88 for the "optimal" state of a squall line system was examined. This is a state in which the generation of positive (negative) horizontal vorticity near the leading edge of the surface outflow layer is balanced by the generation of negative (positive) vorticity by the ambient LLS, as demonstrated in Figure

2.5. The condition for this balanced state as given in RKW88 may be written as

$$u_{g,c}^2 = \Delta u^2, \tag{5.1}$$

for which $u_{g,c}$ represents the observed propagation velocity of the gust front relative to some uniform flow speed aloft, and Δu^2 the near-surface shear of the (squared) environmental winds with height, i.e. $\Delta u^2 = u_0^2 - u_H^2$. In a state of balance, as prescribed in RKW88, the gust front may not propagate relative to the surface, else some finite propagation speed would imply an imbalance in the vorticity field in which the surface outflow layer likely dominates. Conversely, a downshear-tilted updraft, as shown in Figure 2.4, would be a result of stronger vorticity production by the ambient low-level shear, as if a gust front were not present at all, and would deposit its precipitation in its own inflow region, effectively cutting off its source of boundary layer air and convective instability.

In the "optimal" state, a balance between these two sources of vorticity production is thought to exist, and a continual forced updraft is linked to its subsequent buoyant updraft immediately above the gust front throughout the mature phase of the system. However, such a structure is rarely observed in association with developing multicellular tropical squall line systems. Weisman (1992, hereafter W92) considered the additional contribution of the observed and simulated rear-to-front (RTF) flow into the pre-squall outflow region and its effects on this vorticity balance. It may be concluded from the current simulation that this near-surface jet contributes significantly to the production of strong vorticity at the gust front, ensuring a large vorticity imbalance, according to the RKW88 analysis, in that region and the subsequent ground-relative propagation of the cold pool. In W92 an amended balance condition was provided, which may be written as

$$u_g^2 = \Delta u_{rtf}^2 + \Delta u^2, \tag{5.2}$$

for which u_g represents the ground-relative propagation velocity of the gust front, and Δu^2_{rtf} the difference in (squared) horizontal winds between the base and upper surface of the outflow layer some distance behind the gust front, i.e. $\Delta u^2_{rtf} = u^2_{rtf,H} - u^2_{rtf,0}$. The case of an elevated RTF flow, and its effects on the orientation and strength of the convective region, was examined in detail in W92.

For the case of a descending RTF flow through the system, as is observed for most tropical squall lines and has been discussed in Chapter 2, we may consider that this flow reaches the surface some distance behind the gust front and remains at the surface until reaching the head of the surface outflow layer. Therefore, with the horizontal wind within the cold pool greater at the ground than at the upper surface of the outflow layer, i.e. $u_{rtf,0} > u_{rtf,H}$, we would find $\Delta u^2_{rtf} < 0$. For $\Delta u^2_{rtf} < -\Delta u^2$, (5.2) becomes invalid: for descending RTF flow, we must write (5.2) as

$$u_g^2 = -\Delta u^2_{rtf} - \Delta u^2 \tag{5.3}$$

in order to provide a realistic u_g. Given the observed overturning of the flow within the gust front head, as shown in Figure 5.6d, we would expect the gust front to propagate at a speed less than the speed of the RTF inflow which feeds the cold pool, i.e. $u_g < u_{rtf,0}$.

Snapshots of the surface outflow head and gust front region at several times during the current 11 m s^{-1} simulation are shown here. Figure 5.7a demonstrates the state of the surface outflow at 4h 30m, at which time the system may be considered to be in a quasi-stable multicell phase of its life cycle. At this time, the primary gust front (see Section 5.1.4 for further explanation of the "primary" and "secondary" gust fronts in this simulation) is found to propagate at approximately 8.3 m s^{-1}. For a surface outflow layer of height $H = 1$ km, at this time the surface outflow is nearly in balance with the environmental low-level flow under the RKW88 condition (5.1), despite the obvious vorticity imbalance near the

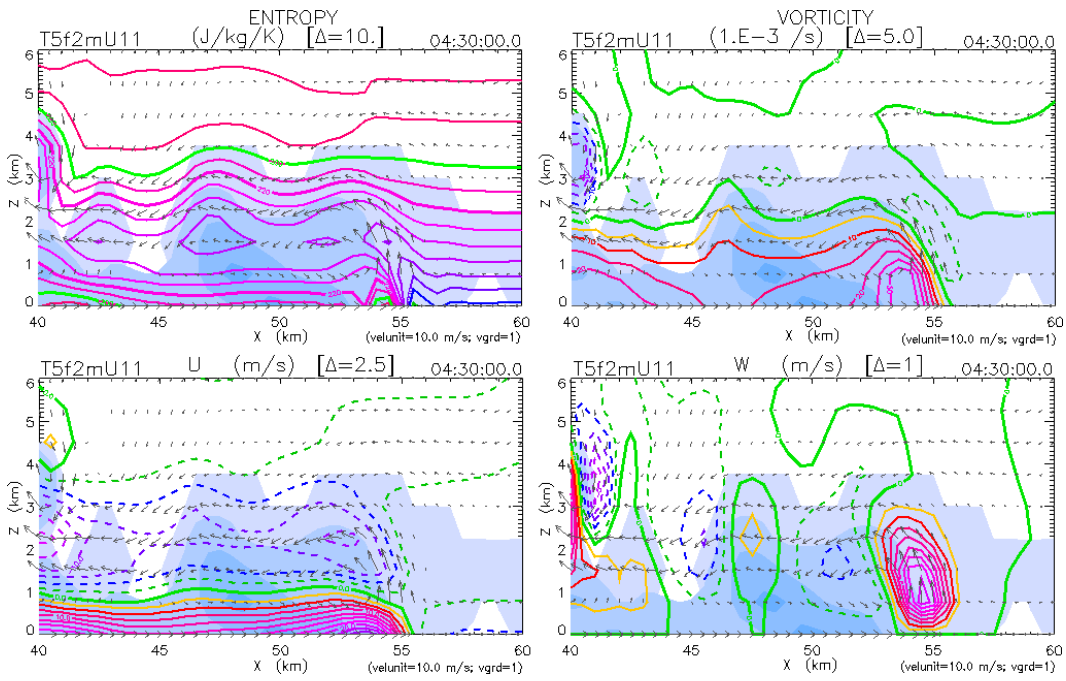

Figure 5.7a: Surface outflow layer and gust front for the 11 m s^{-1} simulation at 4h 30m. The contoured quantities are: the dry-air-specific entropy of moist air, at intervals of 10 J kg^{-1} K^{-1}, at upper left; horizontal vorticity, at intervals of 5×10^{-3} s^{-1}, at upper right; the horizontal component of the wind, at intervals of 2.5 m s^{-1}, at lower left; the vertical component of the wind, at intervals of 1 m s^{-1}, at lower right.

gust front and the collateral ground-relative propagation of the gust front as demonstrated here.

At this point, we must recall the reason for the formulation presented in W92: in RKW88, the surface outflow layer was considered stagnant and the system remained stationary relative to the mean wind above the low-level shear layer, which may be considered negligible in this case. However, using $u_{rtf,H} = 0$ and $u_{rtf,0} = 16$ m s^{-1}, as shown here, the W92 condition (5.3) for a descending RTF flow demonstrates a large imbalance in the flow near the gust front, despite the seemingly quasi-steady nature of the system at this time.

For these reasons, we must reconsider the conditions (5.1) and (5.3) if we are to find "balance" in a propagating surface outflow which is continually forced by a descending RTF

flow through the squall line system. In RKW88, the notion of a stagnant surface outflow layer required only a balance of the vorticity field in the vicinity of the gust front. In the formulation of the balance condition provided by that work, given in (5.1) above, the flux of mass by updraft through the top of the control volume which encompasses the gust front and its immediate surroundings was balanced by inflow through the right (environment) side of the control volume. Because of this theoretical mass balance, the result of speed balance as related to the initially-considered vorticity balance is rather sound, and is still well-accepted. In W92, RTF flow into the surface outflow layer was thought to provide an additional source of vorticity which contributes to the balance desired in the control volume. However, a couple of important aspects of this theory were not adequately considered in W92.

Most importantly, RTF flow into the surface outflow layer contributes mass to the control volume which is not properly considered in the formulation of (5.2). In RKW88, the mass contributed to the volume by the winds closest to the surface is considered exported by an updraft, such that a theoretical mass balance exists and need not have been explicitly considered in the formulation of (5.1). However, the idea of mass balance is important in a consideration of the mechanism of vertical transport for the export of mass contributed to the volume by the RTF flow. Although the vorticity provided by the RTF flow may contribute to the forward propagation (stagnation) of the gust front by dominating (contributing to) the vorticity produced by the ambient low-level shear in the case of descending (elevated) RTF flow, in an attempt to balance the vorticity production in the vicinity of the gust front, the concept of mass balance was ignored in W92. That the top of the control volume was thus eliminated is inconsistent with the export of mass from that volume by a vertical jet, which is important in the development of new convection on or near the gust

front.

That the elevated RTF flow in W92 was considered similar in dynamical structure to a surface cold pool formed by a descending RTF flow is inconsistent with the common identification of the surface outflow layer with a density current, in which the dynamics are rather self-contained. Such a consideration allows us to define the top of the control volume about the gust front region at the upper surface of the outflow layer, facilitating measurements of horizontal and vertical velocity and the fluxes of mass and vorticity through the sides of the volume.

Simply stated, the analysis which leads to the balance condition (5.1) provided in RKW88 is inconsistent with observations of squall line systems and surface outflow layers which propagate at some finite (non-zero) speed relative to the ground, while the balance condition (5.2) provided in W92 is inappropriately formulated for application to systems in which the RTF flow descends toward the surface some distance behind the gust front. Upon consideration of the modified W92 condition as given in (5.3), we may hypothesize a new formulation of this balance condition which accounts for a descending RTF flow, as in W92, and its contribution to the mass balance of the system which was originally established in RKW88. We may write this condition as

$$u_g^2 = -\Delta u_{rtf}^2 - \Delta u^2 - w_{max}^2, \tag{5.4}$$

for which w_{max} represents the maximum updraft velocity in the vicinity of the gust front head. This term is included in order to account for the export of mass contributed by the RTF flow, and is commonly found at the height of the upper surface of the outflow layer. This formulation relies on the vorticity balance postulated in W92 and revised here in (5.3), in which the RTF flow plays a contributing factor, and the necessity of a mechanism for the export of mass contributed by that flow, which was not considered in W92, by a forced

Table 5.2: Evaluation of "balance" conditions for the surface outflow region and gust front in the 11 m s^{-1} tropical squall line simulation. For the prediction of u_g using (5.1), $u(H)$ from (4.1) was employed as a constant wind above the low-level shear layer, such that the prediction could be corrected to provide a ground-relative u_g given here.

Time	4h 30m	4h 40m	4h 56m	5h 02m	5h 08m
$u_{rtf,0}$ (m s^{-1})	16.0	12.5	22.5	22.0	20.0
H at $u_{rtf} = 0$ (m)	1000	800	1000	1200	1200
$u(H)$ by (4.1) (m s^{-1})	-2.6	-3.7	-2.6	-1.8	-1.8
Δu^2 for H (m^2 s^{-2})	114.2	107.3	114.2	117.8	117.8
w_{max} (m s^{-1})	8.5	6.1	8.8	12.5	8.4
u_g by (5.1) (m s^{-1})	8.1	6.7	8.1	9.1	9.1
u_g by (5.3) (m s^{-1})	11.9	7.0	19.8	19.1	16.8
u_g by (5.4) (m s^{-1})	8.3	3.4	17.7	14.5	14.5
Observed u_g (m s^{-1})	8.3	6.3	6.3	10.3	14.6
Balance by (5.4)?	Yes	No	No	No	Yes
Predicted Trend of u_g	—	decel	accel	accel	—
Observed Trend of u_g	—	decel	accel	accel	—

updraft which is commonly observed in the region of the squall line gust front near the surface.

All of the data necessary for the evaluation of terms on the right side of (5.4) may be found in the snapshots included here and in analyses presented earlier in this work. These data, and the results of balance assessments at the time of each snapshot included here in Figure 5.7, are summarized in Table 5.1. Further evaluation of the surface outflow region in the current simulation at 4h 30m, as shown earlier in Figure 5.7a, reveals that the gust front is nearly in balance with its environment via the RKW88 condition (5.1), and is exactly in balance under the new condition (5.4). This conclusion is reached through a comparison between the observed (simulated) gust front propagation velocity and that predicted by the balance condition. This balance, at 4h 30m, is expected upon consideration of the observed quasi-steady nature of gust front propagation and convective cell development around this time in animated results of the current simulation.

A short time later, however, this quasi-steady phase deteriorated as the primary gust front was found to diminish in strength and forward speed, eventually reaching a maximum

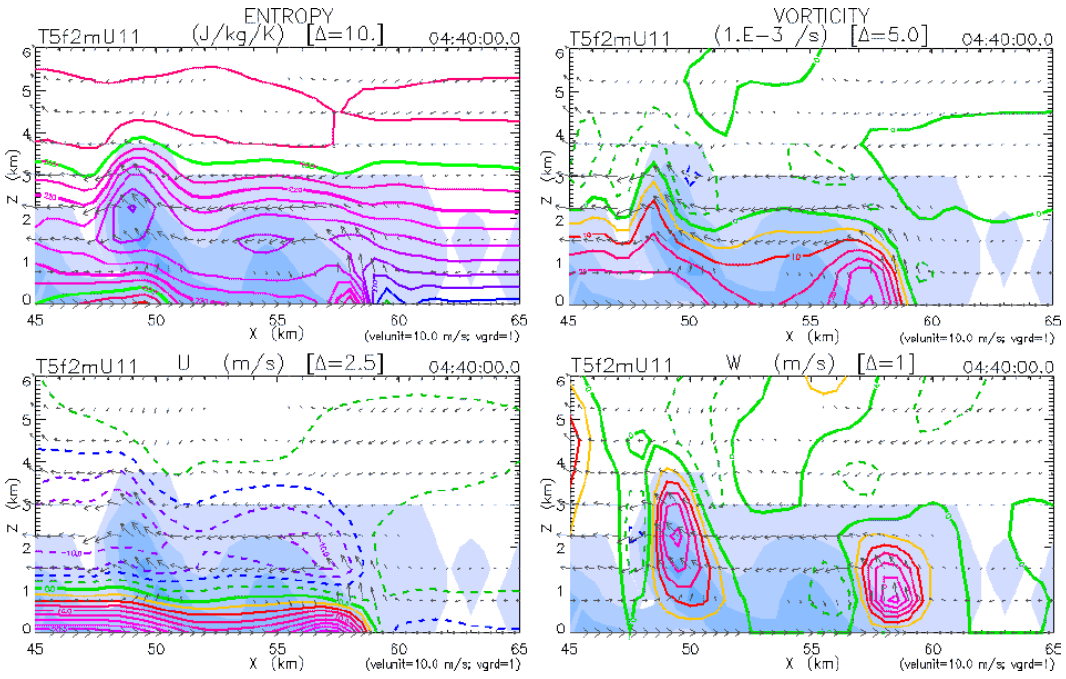

Figure 5.7b: Surface outflow layer and gust front for the 11 m s^{-1} simulation at 4h 40m. The contoured quantities are as described in Figure 5.7a.

extent at $x = 60$ km around 4h 50m. During this deterioration, the gust front was analyzed as out of balance with its environment at 4h 40m (Figure 5.7b). At this point in our analysis, it was determined that the sign and amount of imbalance between the predicted and observed gust front propagation velocities may be used to qualitatively predict the future behavior of the gust front. If u_g predicted by (5.4) is less than that observed, as at 4h 40m in the current simulation, we could expect the gust front to decelerate over the next several minutes. This predicted trend was verified in the rapid deterioration of the gust front by 4h 50m and its eventual demise before being replaced by a stronger secondary surface outflow layer. The opposite result is also valuable, as shown below.

This secondary outflow layer is observed to pass the maximum extent of the primary gust front ($x = 60$ km) at 4h 52m, after which time the surface outflow layer exited the preconditioned region of the primary surface outflow region and was observed to adjust to

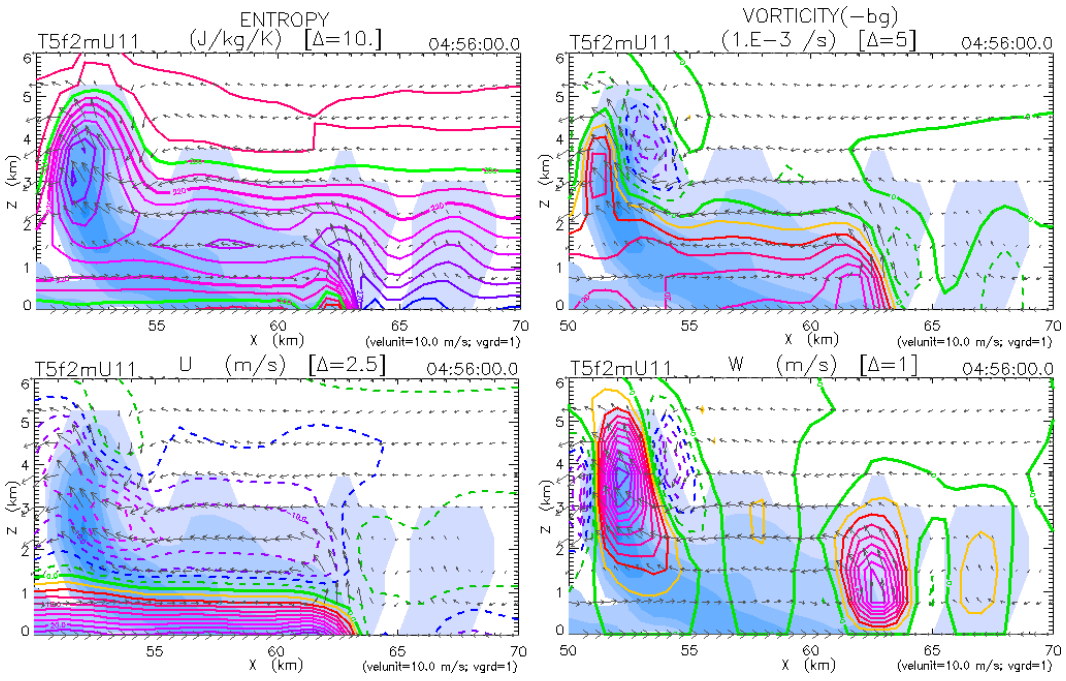

Figure 5.7c: Surface outflow layer and gust front for the 11 m s^{-1} simulation at 4h 56m. The contoured quantities are as described in Figure 5.7a.

its environment over a period of approximately 16-20 minutes. At 4h 56m, as shown in Figure 5.7c, the gust front was observed to propagate at approximately 6.3 m s^{-1}, while (5.4) provided a predicted speed of 17.7 m s^{-1} as shown in Table 5.1. This large disparity led us to predict that the gust front would accelerate rapidly during its adjustment to the environment ahead of the squall line system. Such adjustment was observed, as the speed of the gust front was found to increase by 4 m s^{-1} between 4h 56m and 5h 02m, shown in Figure 5.7d. By this time, the gust front has not yet recovered balance with its environment, but seems to approach this state as evidenced by the smaller difference between the predicted and observed values for u_g. This smaller difference led to a prediction of continued gust front acceleration over the following several minutes.

Over an interval equal to that between the snapshots in Figures 5.7c and d, the gust front was again observed to increase in speed by approximately 4 m s^{-1}, while the

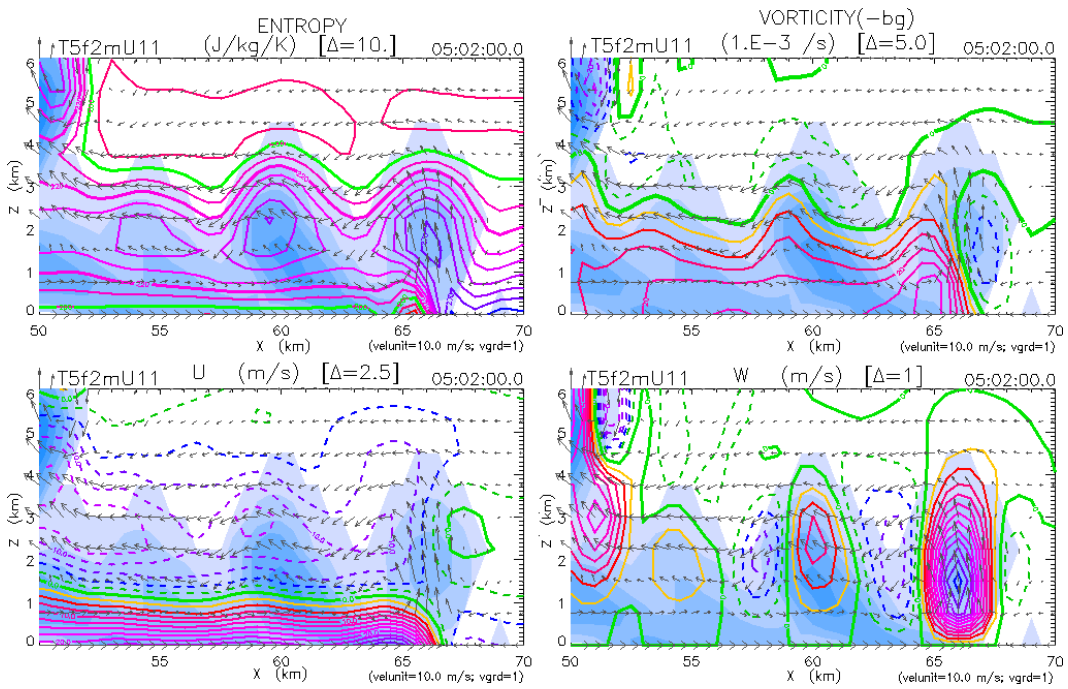

Figure 5.7d: Surface outflow layer and gust front for the 11 m s^{-1} simulation at 5h 02m. The contoured quantities are as described in Figure 5.7a.

predicted gust front speed did not change, such that the surface outflow was observed to finally approach a balanced state around 5h 08m as shown in Figure 5.7e. Beyond this time, small fluctuations in the gust front speed were observed through 5h 30m, over which period the surface outflow layer maintained an average propagation velocity of approximately 10.3 m s^{-1} as demonstrated in earlier analyses. A slow weakening of the RTF flow, which contributes to the strength of the surface outflow layer, and a slight thinning of the layer as it spreads under its own weight could account for this slightly lower average speed over the period between 5h 00m and 5h 30m while still under such a condition of balance, such that the squall line system could be expected to maintain a quasi-steady phase of gust front propagation and convective development as observed.

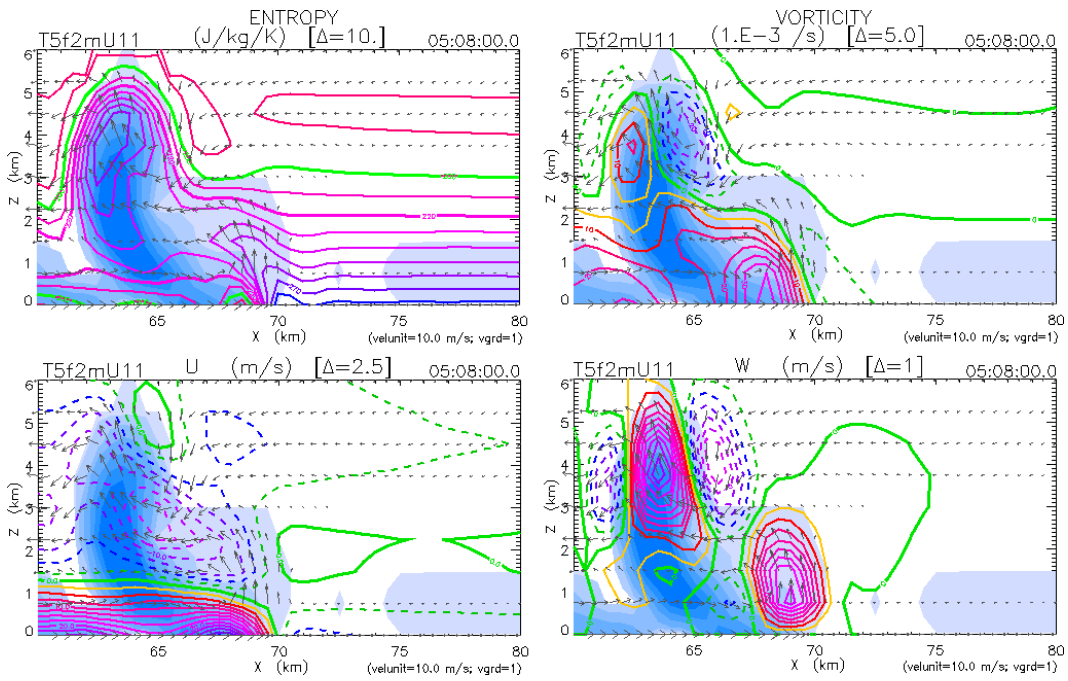

Figure 5.7e: Surface outflow layer and gust front for the 11 m s^{-1} simulation at 5h 08m. The contoured quantities are as described in Figure 5.7a.

5.2 Using the SCSMEX Data

The author was generously granted the opportunity to participate in the South China Sea Monsoon Experiment (SCSMEX) during the summer of 1998. The SCSMEX program, carried out in conjunction with the GEWEX Asian Monsoon Experiment (GAME), was designed to explore the preconditioning and onset of yearly monsoonal flow in East and Southeast Asia. The author participated in the SCSMEX program as an atmospheric scientist aboard the R/V *Kexue 1* during the first intensive observation period (IOP1), which began on May 5, 1998, and extended through May 25, 1998. During both IOP1 and IOP2 (June 5-25, 1998), the *Kexue 1* was stationed at 6.25°N, 110°E. During IOP1, the author maintained and managed the surface meteorology station, which was mounted at various locations about the ship, and participated in radiosonde ("sounding") management and launches along with the shipboard NASA scientist. Soundings were launched each day

Figure 5.8: A precipitating cumulus in the vicinity of the *Kexue 1* during SCSMEX, photographed by M. Garcia.

of IOP1 at 00, 06, 12, and 18 UTC, which corresponded to 08, 14, 20, and 02 local time (LST), respectively.

Little precipitating convection was observed in the vicinity of the *Kexue 1*, especially during the first half of IOP1. The cloud structures during this period were dominated by scattered shallow cumulus and cirrus, cirrostratus and some altostratus, consistent with the high humidity of the lower and upper levels of the troposphere and the relative dryness of the middle levels. During the second half of IOP1, scattered cumulus and isolated cumulonimbus were observed in the vicinity of the *Kexue 1*. An example of these isolated, sometimes precipitating cumulus is shown in Figure 5.8, for which a rainshaft extending to the ocean surface is visible beneath the center of the cloud base. Similar convective cells were observed prior to the passage of a squall line system, discussed below, over the position

of the *Kexue 1* during the (local) afternoon of 21 May, 1998. The only precipitation recorded at the position of the *Kexue 1* during IOP1 occurred during the passage of pre-squall arcus at that time. After this time, numerous cumulus, altostratus, and cirrus were observed in the vicinity of the *Kexue 1* through the end of IOP1.

Pursuant to participation in the SCSMEX program, the author and several colleagues at CSU were granted unlimited permission to employ data obtained during the program in analyses and publication. The simulations which are discussed below employed thermodynamic and wind profiles obtained during the following soundings: 18 May, 1998, at 00 and 06 UTC, and 21 May, 1998, at 00 and 06 UTC. Each of these soundings and wind profiles is analyzed below.

5.2.1 Model Resolution

For the experiments which follow, the same model as described in Chapter 3 and evaluated in Chapter 4 is employed, and several alterations to the experimental domain structure are made in order to facilitate analysis of convective events of a smaller spatial and shorter temporal extent than the tropical squall line system examined above. Since the object of these new experiments is the examination of individual convective events, the model grid spacing required for relatively accurate results must be somewhat less than the $\Delta x = 0.5$ km and $\Delta z = 750$ m grid spacings employed above. Additionally, since convective motions operate on much faster time scales than meso- and synoptic scale events, a shorter numerical time step is employed in the integration of the following experiments.

The domain of the following simulations employs four nested grids, oriented with $x = 0$ at the center of the finest grid. The central grid of the domain employs a constant spacing of $\Delta x = 0.2$ km over a span of 48 km, such that the outermost grid of the model

domain employs a constant spacing of $\Delta x = 1.6$ km with boundaries at $x = \pm 172$ km. In the vertical direction, a constant grid spacing of $\Delta z = 0.2$ km is employed throughout the domain. The base time step, employed on the finest domain, is $\Delta t = 1.5$s, such that the time step on the outermost grid of the domain is $\Delta t = 12$s. Numerical boundary conditions are the same as those employed for the experiments discussed in Chapter 4.

Most of the experiments discussed below were integrated for 3h of model time, although convective motions commonly remained within the finest grid of the model domain and dissipated before 1h 30m could be reached. An exception to this convective system life span will be noted in discussion of the 21 May, 06 UTC experiment, below.

5.2.2 Convective Initiation

Two types of convection commonly occur in the atmosphere. Forced, or mechanical, convection commonly occurs near the surface of the Earth and is initiated by an external forcing mechanism such as a gravity wave or convergent flows, quite often by the convergence of a warm flow and a cold pool of air such as a synoptic cold front or a mesoscale cold outflow pool. Convective motions in a moist atmosphere which occur in the boundary layer, which is often well-mixed with respect to vertical temperature gradients, are often considered forced because of negligible temperature differences between a lifted parcel and its immediate environment before condensation occurs. As condensation occurs, the parcel is warmed by the release of latent heat and becomes warmer than its immediate surroundings. At this point, free, or buoyant, convection commences, and the parcel is accelerated upward until it reaches thermal equilibrium with its environment and has depleted its vertical momentum. A similar process occurs in the initiation of convective downdrafts, which become cooler than their environment at some point while experiencing evaporation of a

water load, inducing negatively buoyant motions and a downward acceleration of the parcel until thermal equilibrium, or the Earth's surface, is reached.

Given these descriptions of convective motions, several mechanisms for the initiation of moist convection might be postulated. The initiation of buoyant convection with a near-surface positive temperature perturbation, or "bubble," is most common in published numerical modelling efforts. Because of its significance and favor, the thermal bubble will be discussed last. Methods for the initiation of convection which employ forcing mechanisms have been proposed in TMM82, and include orographic forcing, which is of little significance over regions of flat terrain or over the ocean, and the development of a cold pool, as described above. In TMM82, a cold pool was employed to initiate convection, and was constructed using a localized heat sink or cooling function.

The reasoning provided in TMM82 for such a choice finds its basis in the characteristics of nocturnal thermodynamic soundings over continental tropical regions, which commonly demonstrate a near-saturated boundary layer. In order to develop a surface outflow layer on which the development and propagation of subsequent convection will depend, a sowewhat dry surface layer is required to evaporate precipitation from the initial convective cell, to consume the latent heat available in the boundary layer parcels, and to form a cold pool on which the low-level flow will impinge, causing forced and eventually buoyant convection on its upstream side and the subsequent regeneration and propagation of the cold pool. A cooling of the lower levels induces subsidence and drying of the cooled air, such that a surface cold pool is formed.

This method for the initiation of convection by a surface forcing mechanism was proposed in TMM82 and was supported by similar use in the simulation of nocturnal continental squall line systems in DMS87, LM89, and CY93. Such a method may be appropriate

for the thermodynamic profile shown in Figure 5.1, for which the boundary and lower layers are near-saturated. Such a method is available in the model, for which a cold "bubble" perturbation may be prescribed. However, such an experiment was not performed with the sounding shown in Figure 5.1. The initiation of an experiment with a cold bubble was performed with other soundings, without the development of convective motions. These will be mentioned later.

With regard to buoyant convection, we may consider the process through which a rising thermal is developed. If solar heating is concentrated in particular regions at the surface, due to any number of reasons including vegetation, cloud cover, etc., a localized heat source is introduced in the radiation of sensible heat from the Earth's surface. Differential heating of the near-surface air introduces baroclinicity and the baroclinic generation of horizontal vorticity, which causes convergence of moist air over the warm region. The combination of warmed moist air, convergence, and vertical forcing from baroclinic vorticity induces the development of a thermal which, upon reaching its level of condensation, becomes warmer than its immediate surroundings and accelerates upward in free convection.

Thus, several possibilities exist for the initiation of such convection, which follow from the structure of the thermal during its development: 1. differential surface heating; 2. baroclinic vorticity production; 3. moist convergence; 4. a near-surface thermal bubble; 5. an elevated thermal bubble. It should be noted by the reader that the process of buoyant convective development includes mechanical forcing mechanisms in the 2d and 3d steps, and that the initiation of convection with a stationary cold pool, or an orographic obstruction, in low-level relative flow would most closely resemble the 3d step. During the propagation of a squall line system, the initiation of convection by convergence of the cold pool and the low-level inflow would resemble both the 2d and 3d steps, despite a different source

of horizontal vorticity in consideration of the outflow related shear flow which have been discussed above and were examined in great detail in RKW88 and FT98.

In the model employed here, differential surface heating and vertical velocity fields cannot currently be included in the initialization. In this model, perturbations may be specified which allow the initiation of convective motions by a convergence region or by a thermal bubble. Brief experiments in which thermal bubbles, centered at the surface of the domain and at slightly elevated heights, were introduced as the initial perturbation developed significant convective motions in nearly all cases in which convection was expected, given a careful examination of the applied environmental thermodynamic profile.

However, the initiation of convective motions with a convergence field provided slightly more complicated results. Figure 5.9 demonstrates the differences between the initiation of convection with an elevated convergence perturbation, shown on the left, and a convergence perturbation which is centered at the surface of the domain, shown on the right. Although detail of the near-surface wind field may not be discernible in Figure 5.9, the elevated perturbation allows updrafts to form on the edges of the perturbation, while the elevation of the convergence region allows subsidence to occur in the center of the perturbation. In this case, relatively weak convective motions form at the edges of the initial convergence perturbation region, while no significant forced convective motions develop at the desired location. In the case of a surface-centered convergence perturbation, significant convective motions develop as expected at the location desired, with additional consideration of the low-level wind field in the particular experiment shown in Figure 5.9.

Thus, the preferred mode of convective initialization employed in the experiments to be discussed below is derived from one of three methods: 1. surface convergence; 2. a near-surface thermal bubble; 3. a superposition of the two perturbations. A cursory examination

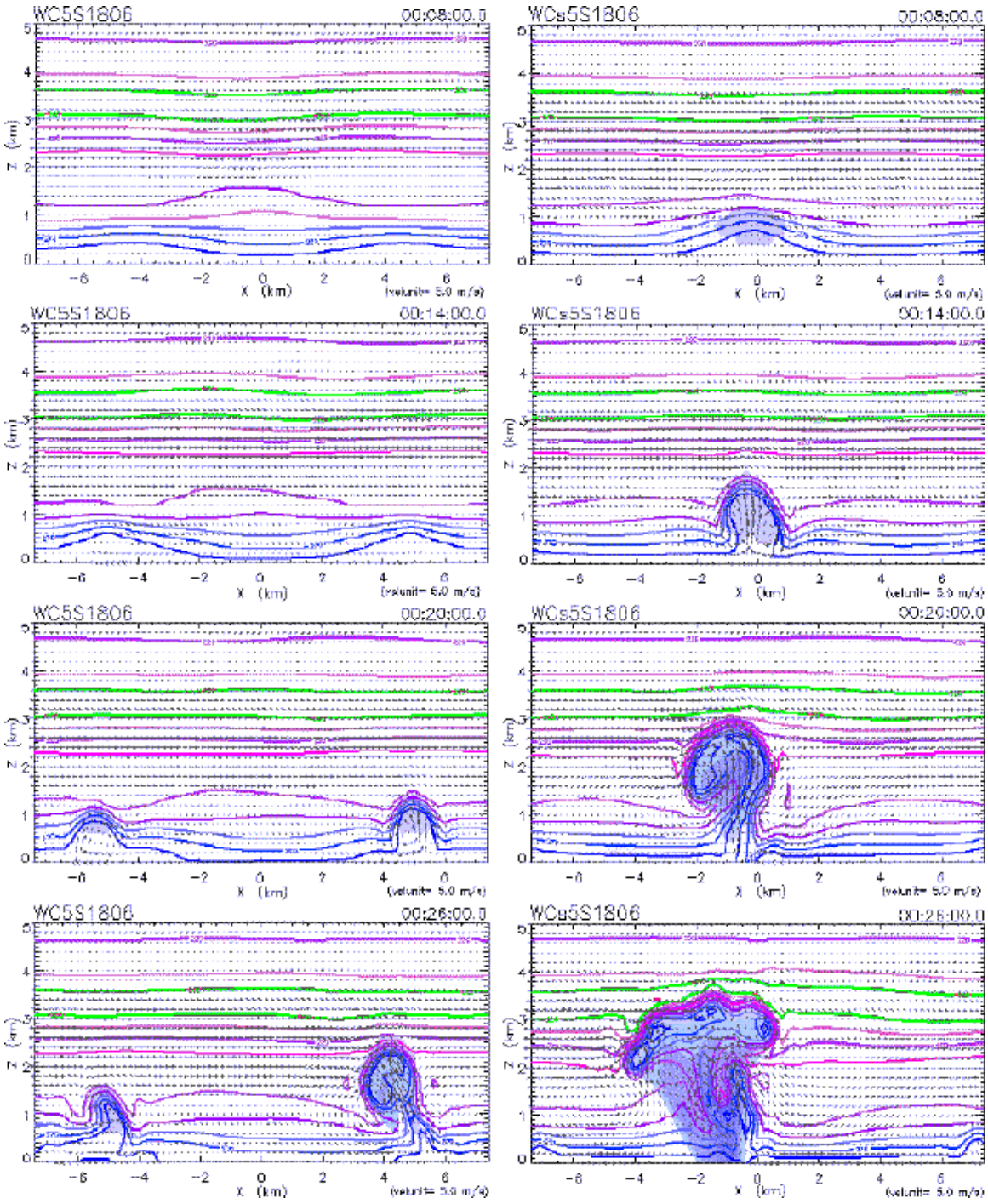

Figure 5.9: Comparison of convective development for experiments with different initial convergence perturbations.

of these methods reveals that a surface convergence perturbation corresponds with the 3d step in the process described above, and that a near-surface thermal bubble corresponds to the 4th step above. A combination of the two methods, such as a slightly-elevated thermal bubble supported by a surface convergence field, would correspond closely to the entire process of near-surface convective development up to the 4th step as described above. It is significant to note that such a structure for a convective cell corresponds well with the starting-plume model of moist convection as proposed by Turner (1962), a combination of the convective jet analogy drawn by Stommel (1947) and the convective bubble analogy drawn by Scorer and Ludlam (1953) and by Levine (1959).

5.2.3 Initial Soundings and Wind Profiles

The SCSMEX soundings and wind profiles employed in the experiments performed and discussed here are demonstrated in Figures 5.10 through 5.21. Convective indices, calculated by the author during analysis, are also included with the thermodynamic profiles. For use in the numerical model, thermodynamic profiles were sampled at the surface and at intervals of 10 hPa between 1000 hPa and approximately 30 hPa. Given this interval and the vertical grid spacing of the model domain ($\Delta z = 0.2$ km in all experiments), at least 98 levels of thermodynamic data are provided to the model, which employs only 90 grid points on the vertical axis, ensuring that most features of the thermodynamic profiles discussed below are easily resolved. Because thermodynamic data is provided at specific pressure levels and not at actual physical heights, wind profiles associated with the thermodynamic data are approximated from the actual sounding data, as will be discussed below, and are adjusted to fit the model domain according to the actual and model-defined heights of certain pressure levels. Whereas the model was originally constructed to accomodate

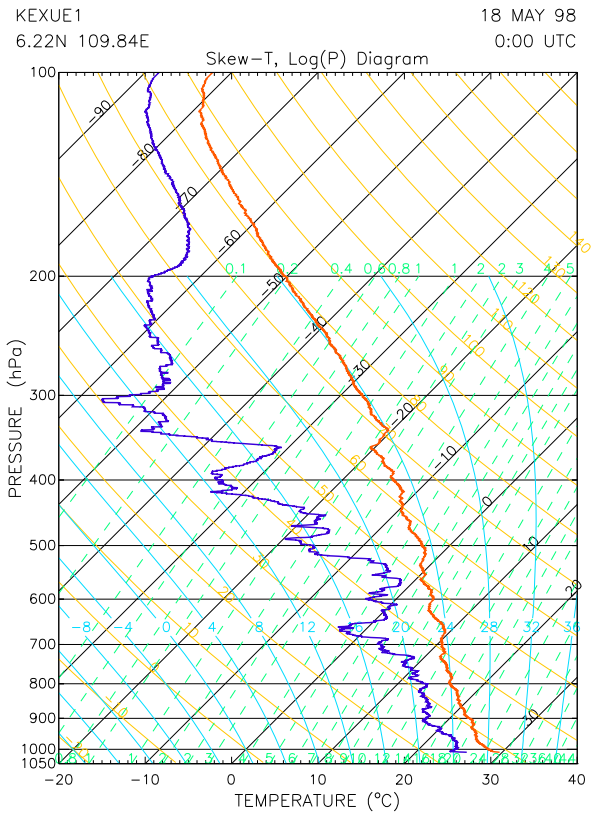

Figure 5.10: 18 May, 1998, 00 UTC SCSMEX thermodynamic profile.

a single, simple initial wind profile, in order to accomodate the constructed wind profiles which will be discussed below, the input structure of the model employed here was modified slightly to allow combinations of simple mathematically-defined profiles. The model domain is initialized as a horizontally homogeneous atmosphere, as discussed above.

The 18 May, 1998, 00 UTC thermodynamic profile is demonstrated in Figure 5.10. The thermodynamic profile at this time demonstrates a lifting condensation level (LCL) at 0.5 km (956 hPa) and an equilibrium level (EL) at the approximate height of the tropical tropopause of 16.4 km (105 hPa). The freezing (0°C) level resides at a height of 5.2 km, and an isothermal layer is found between heights of 8.5 km and 8.9 km. Hodographs derived from the wind profile obtained during this sounding are included in Figure 5.11,

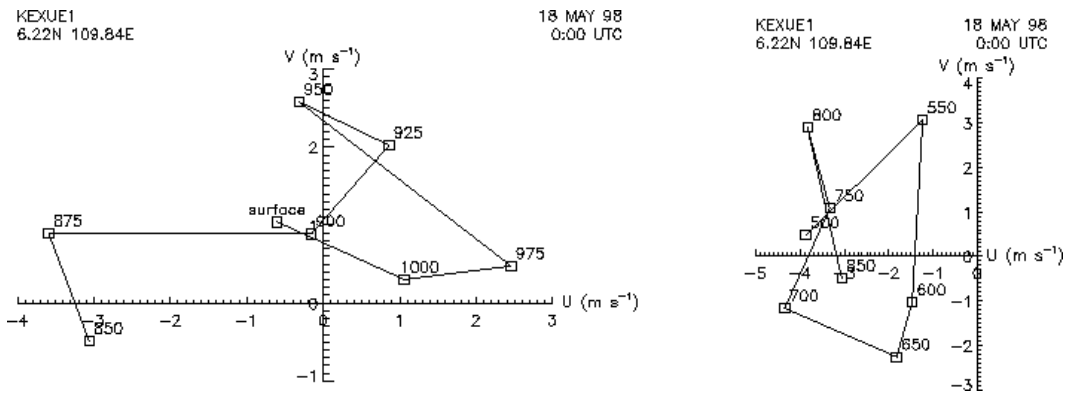

Figure 5.11: 18 May, 1998, 00 UTC SCSMEX surface-to-850 mb (left) and 850-to-500 mb (right) hodographs.

and demonstrate light shear toward the southwest in the surface-to-850 hPa layer and nearly negligible shear toward the northwest in the 850-to-500 hPa layer. The model wind profile for this sounding was chosen along a 90° azimuth, such that a zonal wind profile was produced and is demonstrated in Figure 5.12. The actual zonal wind profile is shown on the left side of Figure 5.12, and includes no-data gaps in the layers between approximately 7 km and 9.5 km and between approximately 14 km and 16 km. The actual wind profile is approximated by the dash-dot line, a piecewise combination of smooth mathematical functions. This approximation was adjusted to fit the model domain, a process involving the recalculation of shear layers according to the scale height of the model domain and the heights of the corresponding pressure levels in the actual sounding, the end result of which is demonstrated on the right side of Figure 5.12.

Similar analyses were performed with the 21 May, 1998, 00 UTC sounding. This thermodynamic profile, which is displayed in Figure 5.13, is quite similar to that of 18 May, 00 UTC, and demonstrates an LCL at approximately 0.6 km (947 hPa) and an EL at 15.75 km (118 hPa) which does not necessarily coincide with the tropopause. The 0°C level is found at a height of 5.0 km, and the thermodynamic profile exhibits no significant

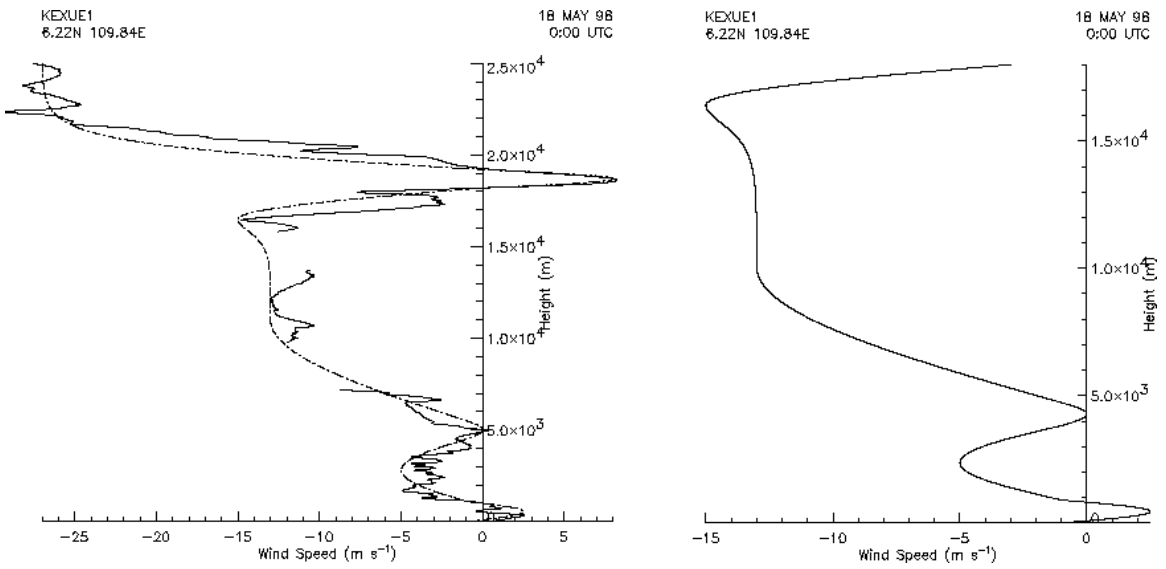

Figure 5.12: 18 May, 1998, 00 UTC SCSMEX actual and approximate zonal wind profiles (left), and approximate zonal wind profile, adjusted to fit the model domain (right). Note that the adjusted profile extends only to a height of 18 km, which represents only a portion of the sounding data.

isothermal or stable layers. Hodographs of the surface-to-850 hPa and 850-to-500 hPa winds are shown in Figure 5.14, and demonstrate nearly opposite shear in the two layers. A wind profile along a 240° azimuth was chosen for this sounding so as to examine the dynamics of cloud formation along a line which would be nearly perpendicular to both of the shear vectors. This profile is demonstrated on the left side of Figure 5.15, and is approximated by a nearly smooth piecewise mathematical wind profile which is then adjusted to fit the model domain, in the same manner as the 18 May, 00 UTC approximate wind profile, the results of which are shown on the right side of Figure 5.15.

The two soundings described above were chosen on the basis of their relation to the following two soundings, during which time convection was prevalent in the region of the *Kexue 1* in the form of isolated cumulus of moderate cloud top height, during the 18 May 06 UTC sounding, and a tropical squall line system, during the 21 May 06 UTC sounding. For these reasons, the 00 UTC soundings might be considered representative of

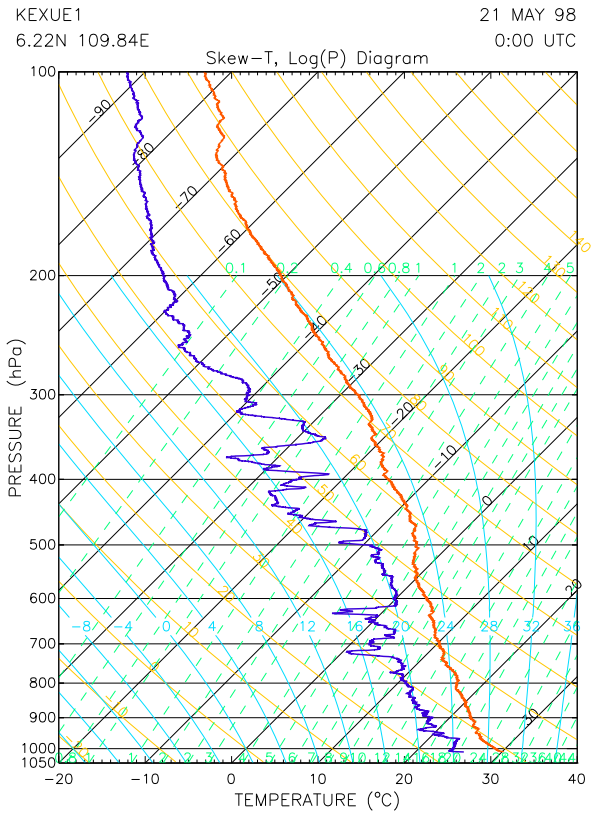

Figure 5.13: 21 May, 1998, 00 UTC SCSMEX thermodynamic profile.

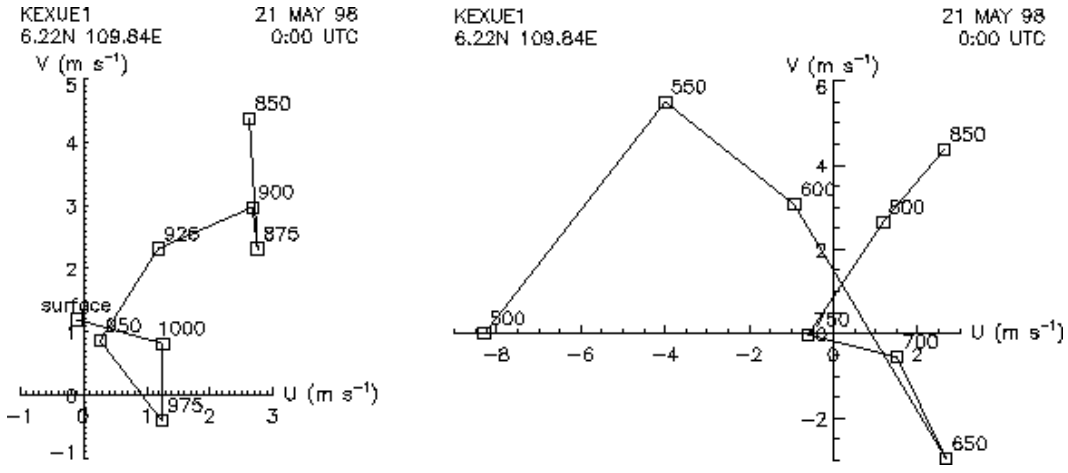

Figure 5.14: 21 May, 1998, 00 UTC SCSMEX surface-to-850 mb (left) and 850-to-500 mb (right) hodographs.

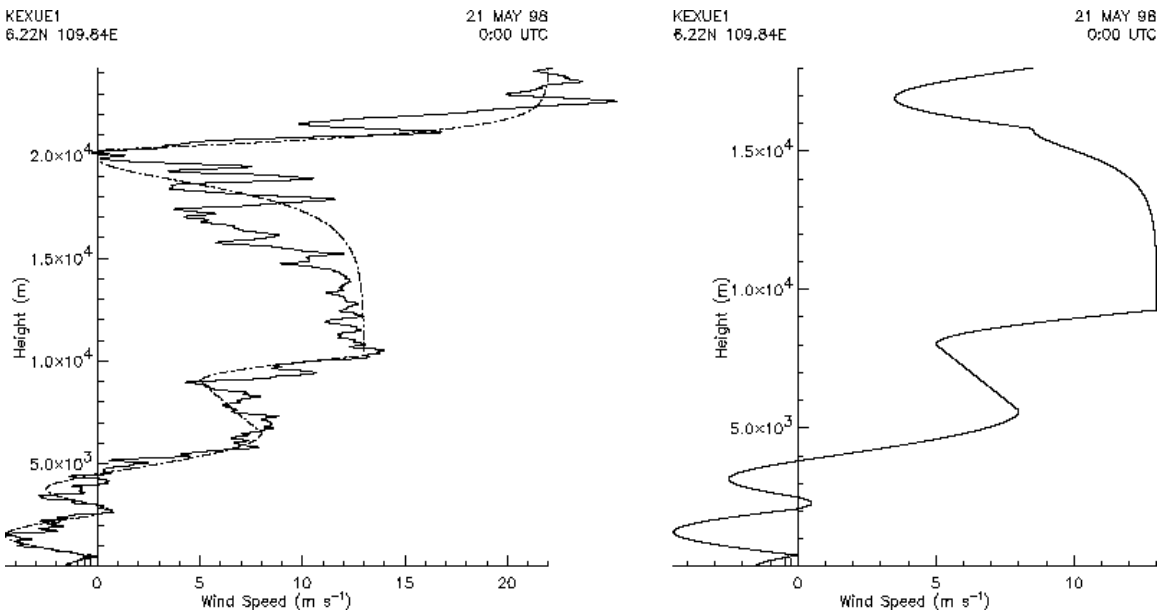

Figure 5.15: 21 May, 1998, 00 UTC SCSMEX actual and approximate zonal wind profiles along a 240° azimuth (left), and approximate zonal wind profile along a 240° azimuth, adjusted to fit the model domain (right). Note that the adjusted profile extends only to a height of 18 km, which represents only a portion of the sounding data.

the "preconditioning" or "pre-convective" state of the atmosphere for each day, and might therefore be conducive to buoyant convection themselves. Modeling results for the two 00 UTC sounding environments proved otherwise, however, and will be explained briefly below. The two 06 UTC soundings, described below, were chosen on the basis of convective activity in the region of the *Kexue 1* during collection of the sounding data. It should be noted that none of the soundings described here was observed to enter an elevated cloud mass during its ascent, such that the thermodynamic profiles are, to a large degree, representative of the cumulus environment. The limitations of such an assumption will also be discussed in analysis of the modeling results.

The 18 May, 1998, 06 UTC thermodynamic and wind profiles provided the most successful cloud simulations of the soundings considered. This thermodynamic profile, shown in Figure 5.16, demonstrates an LCL at 0.75 km (928 hPa) and an EL at a height of approx-

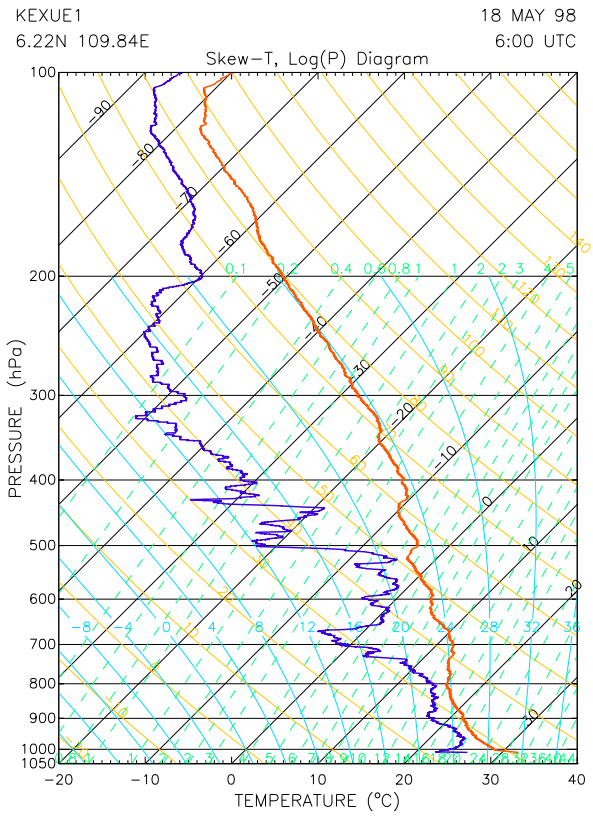

Figure 5.16: 18 May, 1998, 06 UTC SCSMEX thermodynamic profile.

imately 16.5 km (104 hPa). The 0°C level is located at a height of approximately 5.1 km, and shallow isothermal or stable layers can be found just below a height of 5.9 km and just above a height of 7.0 km. Moist layers may be found in this thermodynamic profile in the lower levels, between the surface and approximately 750 hPa, and in the midlevels between approximately 650 and 520 hPa. Hodographs constructed from winds in the surface-to-850 hPa and 850-to-500 hPa layers are shown in Figure 5.17. Nearly perpendicular shear vectors between these two layers may be found, as in the 18 May, 00 UTC wind data. Again, similar to the earlier sounding, a zonal wind profile is chosen and is shown on the left side of Figure 5.18. The piecewise mathematical wind profile constructed from the sounding data is shown with the actual data on the left side, and the adjusted profile for the use in

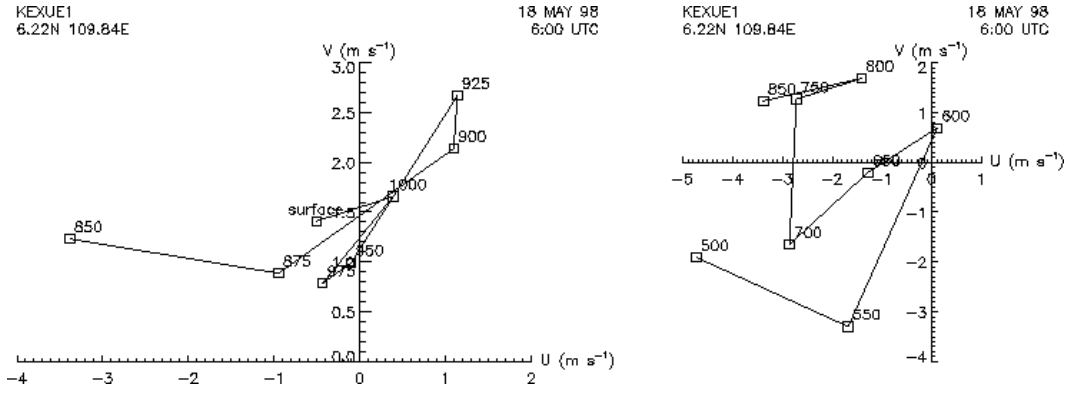

Figure 5.17: 18 May, 1998, 06 UTC SCSMEX surface-to-850 mb (left) and 850-to-500 mb (right) hodographs.

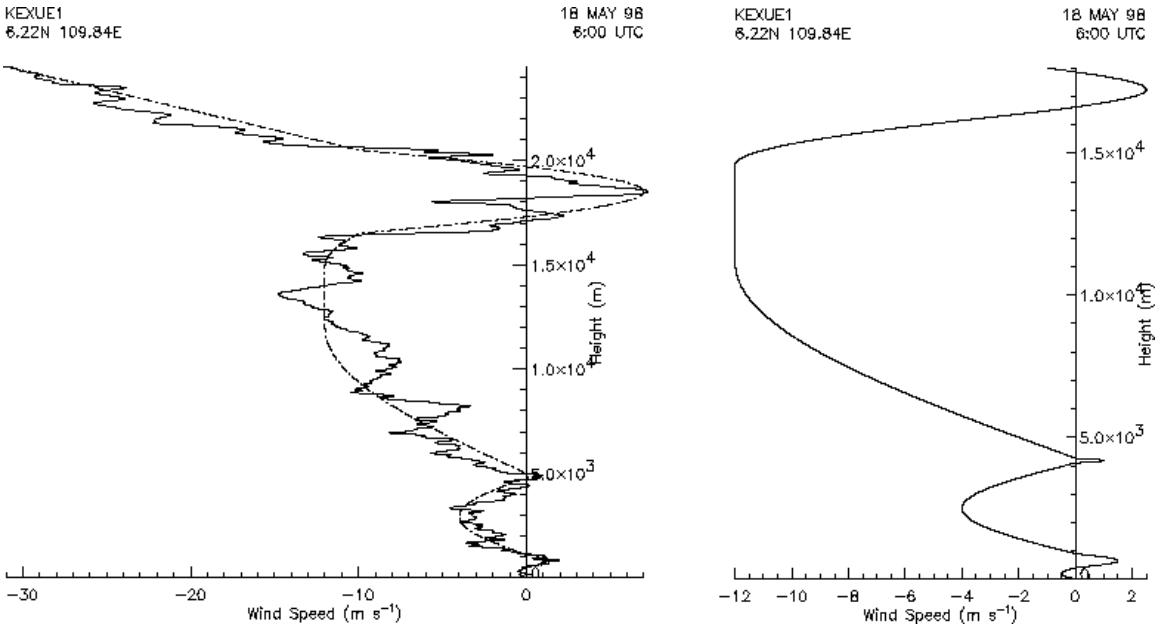

Figure 5.18: 18 May, 1998, 06 UTC SCSMEX actual and approximate zonal wind profiles (left), and approximate zonal wind profile, adjusted to fit the model domain (right). Note that the adjusted profile extends only to a height of 18 km, which represents only a portion of the sounding data.

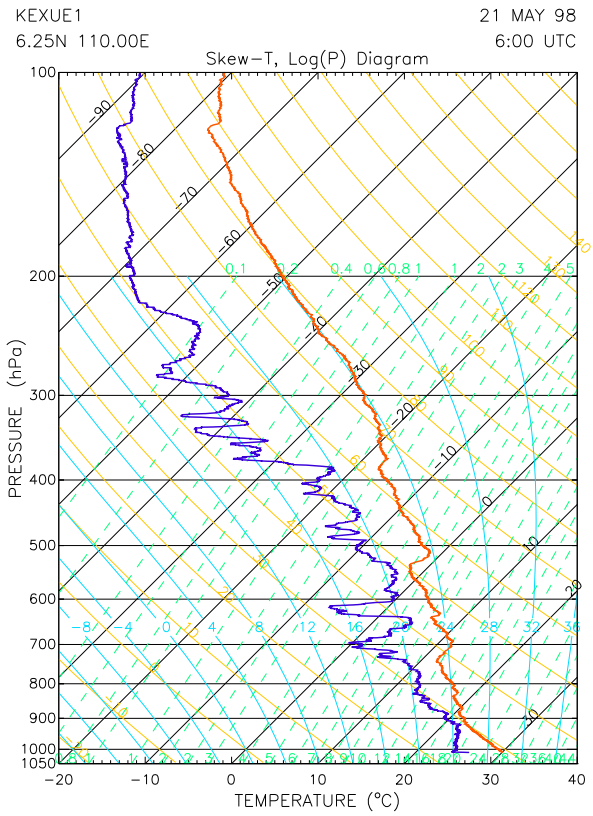

Figure 5.19: 21 May, 1998, 06 UTC SCSMEX thermodynamic profile.

the model domain is shown on the right side, of Figure 5.18.

The 21 May, 06 UTC thermodynamic profile is shown in Figure 5.19, and demonstrates an LCL at approximately 0.5 km (956 hPa) and an EL at an approximate height of 16.1 km (111 hPa). The 0°C level is located at a height of 5.0 km. Shallow isothermal layers are found between heights of 2.7 km and 3.1 km and around a height of 8.1 km, and shallow stable layers are found at an approximate height of 4.0 km and between heights of 5.4 km and 5.7 km. Again, moist layers may be found in the thermodynamic profile in the lower levels, between the surface and approximately 750 hPa, and in the midlevels around 650 hPa and between approximately 600 and 525 hPa. Hodographs of the winds in the surface-to-850 hPa and 850-to-500 hPa layer are shown in Figure 5.20, and demonstrate

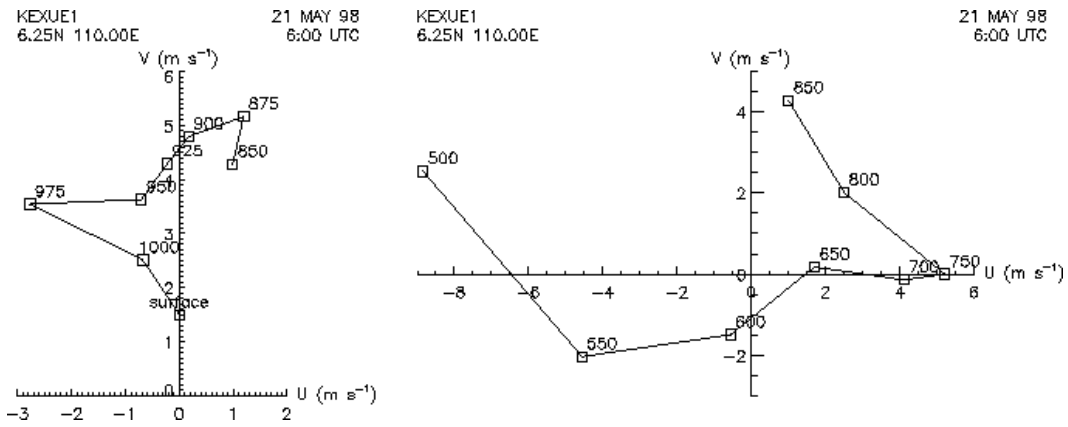

Figure 5.20: 21 May, 1998, 06 UTC SCSMEX surface-to-850 mb (left) and 850-to-500 mb (right) hodographs.

nearly perpendicular shear vectors between the two layers. A 230° azimuth was chosen for the wind profiles demonstrated in Figure 5.21, for which a nearly smooth piecewise mathematical wind profile was constructed and adjusted for the model domain, as shown on the right side of Figure 5.21.

5.3 Results of SCSMEX Cloud Experiments

For experiments initialized with thermodynamic and wind profiles under which conditions very little cumulus convection in the vicinity of the *Kexue 1* was observed by the shipboard scientists, only three experiments were performed. This includes the two 00 UTC soundings, on 18 and 21 May, 1998. For experiments initialized with the two 06 UTC soundings, again on 18 and 21 May, 1998, additional experiments were performed incorporating variations in thermal and convergence perturbation strengths. Many of these results are discussed below.

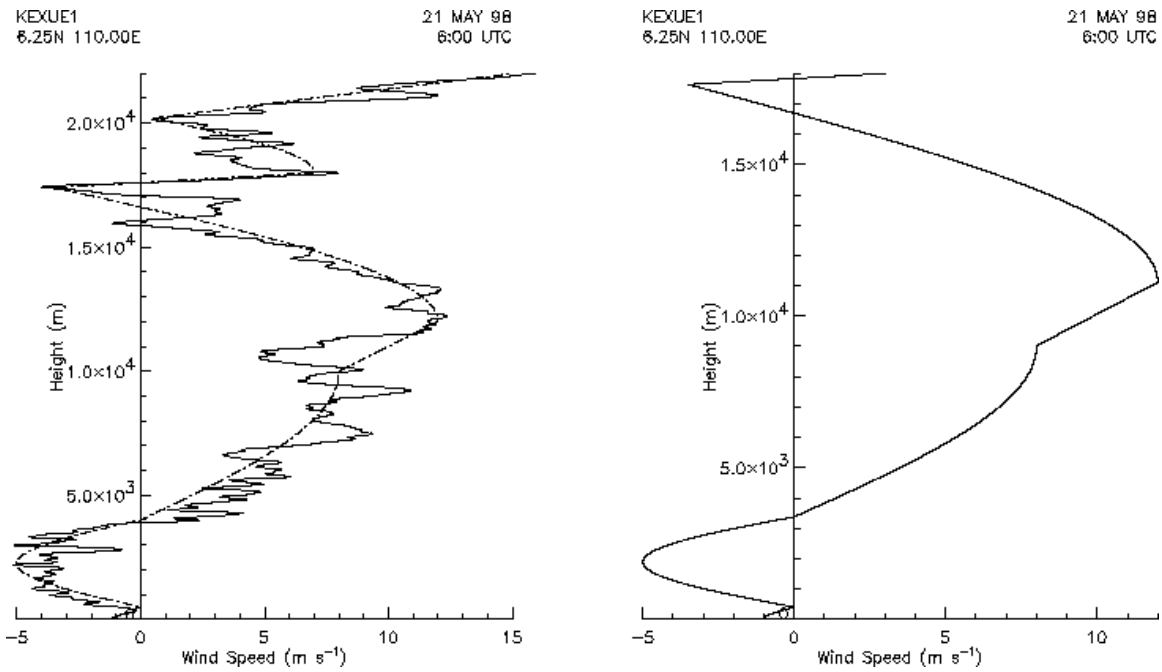

Figure 5.21: 21 May, 1998, 06 UTC SCSMEX actual and approximate zonal wind profiles along a 230° azimuth (left), and approximate zonal wind profile along a 230° azimuth, adjusted to fit the model domain (right). Note that the adjusted profile extends only to a height of 18 km, which represents only a portion of the sounding data.

5.3.1 18 and 21 May, 1998, 00 UTC Experiments

The wind profile which was employed for the 18 May, 00 UTC experiments, as shown on the right side of Figure 5.12, is characterized by strong easterly shear in the layers between approximately 0.5 km and 2.3 km and between approximately 4.1 km and 9.0 km. For the reason of the lower sheared layer, and for the reason of the relative dryness of the lower levels as evidenced by the lack of a pronounced humidity peak near the LCL, the experiments which were initiated with the thermodynamic and wind profile from the 18 May, 00 UTC sounding produced good results. No convective clouds were produced at all in the case of initiation with only a surface convergence zone of strength $u_{conv} = 5$ m s^{-1}, and only weak strongly-sheared convection was produced for the experiments which employed the other two forms of convective initialization discussed above. Convection in

these experiments reached an ultimate height of only 4 km, when the initial perturbation was only an elevated thermal bubble of strength $T' = +2$K, and 5 km, in the case of a combined convergence-and-thermal ($u_{conv} = 5$ m s^{-1}, $T' = +1$K) initial perturbation. These results are considered "good" because very little cumulus convection was observed in the vicinity of the *Kexue 1* by the shipboard scientists at the time of the sounding. The reluctance of the model employed here to produce persistent cumulus development with all but the strongest of initial perturbations is validated by the lack of convective development in the real atmosphere at the time of the sounding.

Quite different results were obtained for the 21 May, 00 UTC experiments, in which shallow layers of strong alternating shear dominate the wind profile up to approximately 9 km, as shown in Figure 5.15. This thermodynamic profile is also characterized by a lack of humidity in the lower levels, although a small peak is visible near the LCL in Figure 5.13. Experiments with this sounding, however, were much more successful in the development of cumulus convection. An experiment initialized with an elevated thermal, centered at 0.5 km and with a perturbation of $T' = +2$K, produced strongly-sheared convection of moderate strength which reached an ultimate height of approximately 10 km, while the experiment in which a combined perturbation ($u_{conv} = 5$ m s^{-1}, $T' = +1$K) was employed produced strongly-sheared weak convective development up to approximately 9 km. An experiment in which only a surface convergence zone was employed produced no convective development. A lack of low-level humidity helps to explain why this sounding produced little persistent convective development which did not exceed the height of the freezing level, while the strongly-sheared wind profile employed here helps to explain why that convection which did develop remained relatively weak and dissipated quickly. Again, the development of convection with only the strongest of perturbations provided good results when compared

with the lack of observed cumulus convection in the vicinity of the *Kexue 1* at the time of the sounding.

5.3.2 21 May, 1998, 06 UTC Experiments

Because of the persistent and prevalent convection observed in the vicinity of the *Kexue 1* during the gathering of data for the 21 May, 06 UTC sounding, several experiments were performed in an attempt to replicate the squall line convection which is demonstrated in Figure 5.22. The large-scale environment of the *Kexue 1*, located at 6.25°N 110°E, at 00 UTC on 21 May, 1998, is shown in the European Center for Medium-Range Weather Forecasting (ECMWF) analyses included in Figure 5.23a. The synoptic environment of the *Kexue 1* at 00 UTC was characterized by southeasterly flow through approximately 700 hPa with easterly flow aloft. At 12 UTC on the same date, included in Figure 5.23b, flow in the layers up to approximately 700 hPa contain a more southerly component, while the winds aloft remain easterly. As can be seen in the sequence of satellite photographs shown in Figure 5.22, a convective system similar to a tropical squall line passed over the location of the *Kexue 1*, marked with a white arrow, over the period between the 00 UTC and 12 UTC soundings. The squall line system was observed to approach the location of the *Kexue 1* slowly during the (local) morning of 21 May, 1998, from the southern horizon. At 06 UTC, it is clearly visible that the location of the *Kexue 1* is between the leading gust front cloud, or arcus, and the convective region of the squall line system. After this time, the squall line system was observed to dissipate rapidly, leaving in its wake small amounts of altostratus and cirrostratus clouds which are visible in the last frames of the sequence in Figure 5.22, several hours prior to the time of local sunset.

The timing of 06 UTC sounding, given the locations of the arcus and convective

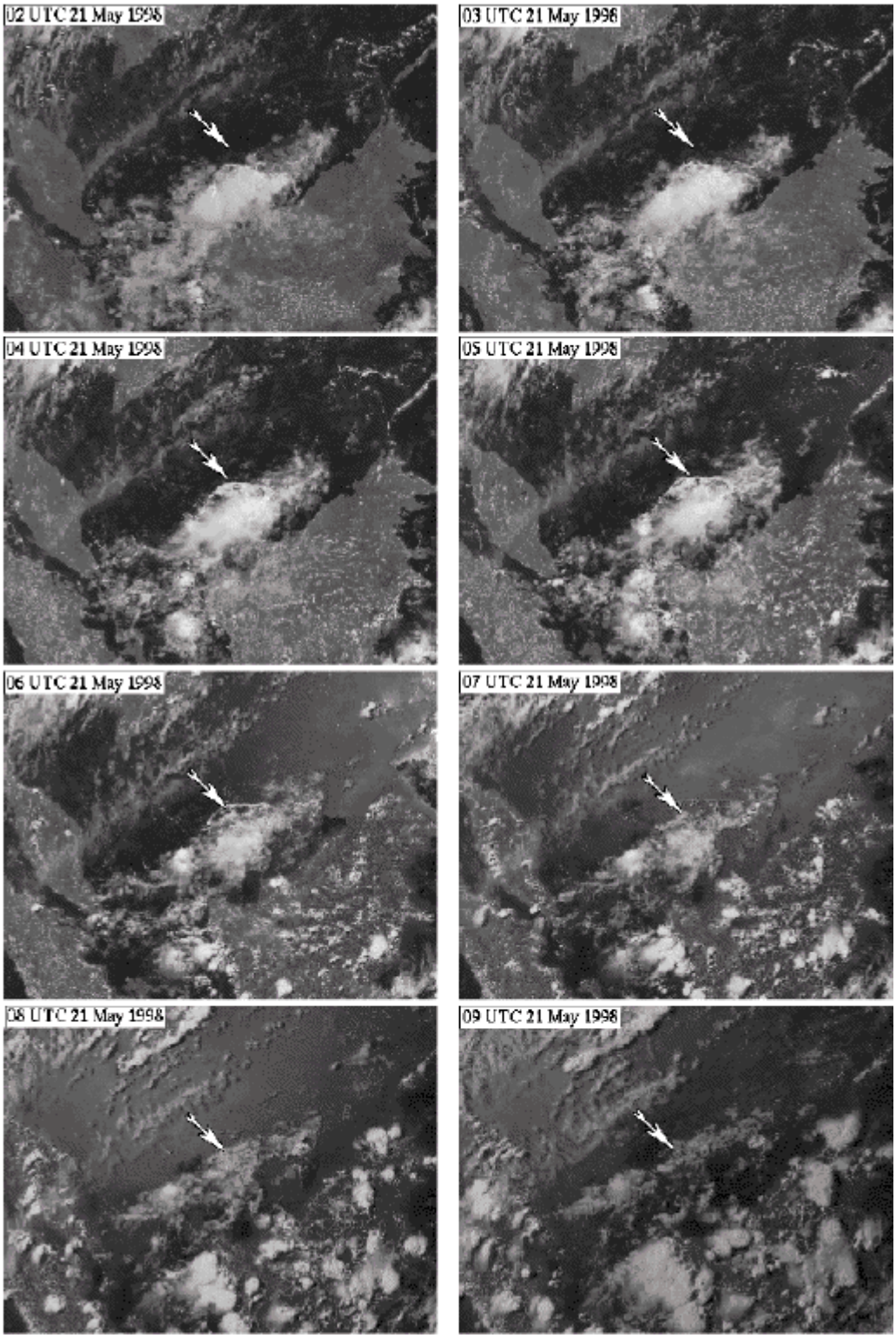

Figure 5.22: 21 May, 1998, GMS image sequence (visible channel) in the region of the R/V *Kexue 1* during SCSMEX. The island of Borneo is visible to the southeast, the Malaysian peninsula and the island of Sumatra are visible to the southwest, and the Vietnamese coast is visible to the north of the position of the *Kexue 1*.

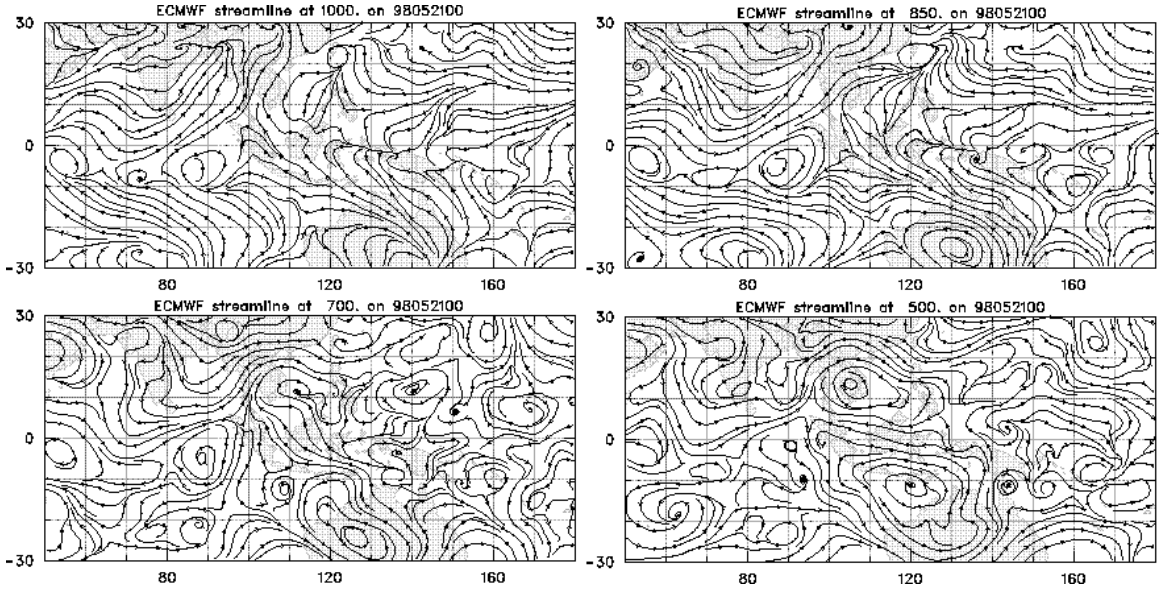

Figure 5.23a: 21 May, 1998, 00 UTC ECMWF streamline analyses. Numbers on the left of each frame indicate degrees of latitude (0° = Equator); numbers below each frame indicate degrees East longitude.

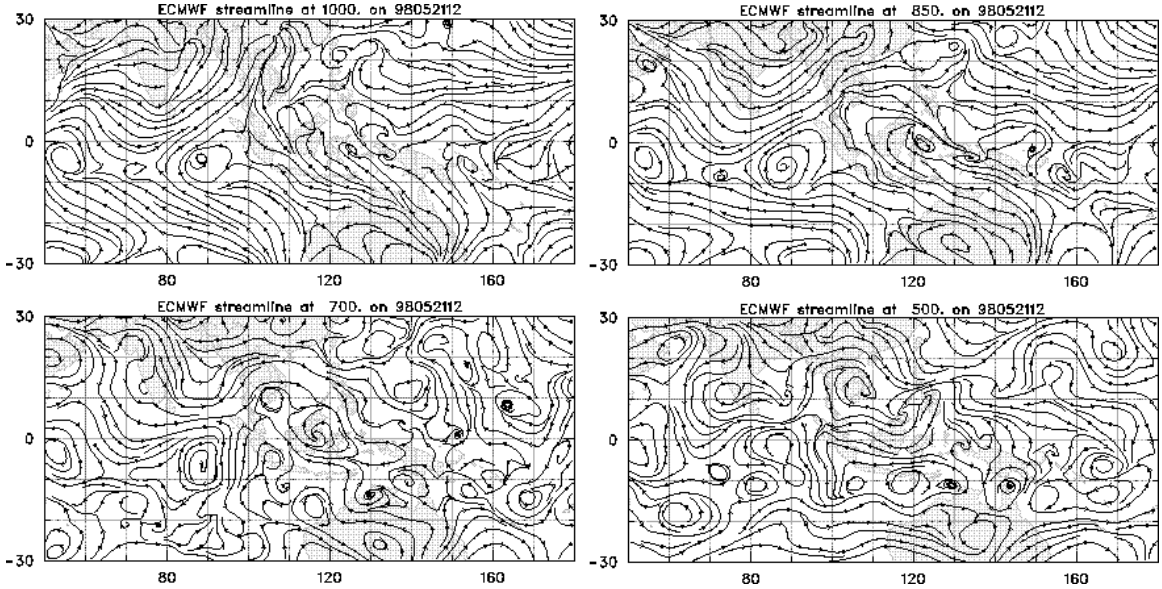

Figure 5.23b: 21 May, 1998, 12 UTC ECMWF streamline analyses. Numbers on the left of each frame indicate degrees of latitude (0° = Equator); numbers below each frame indicate degrees East longitude.

regions relative to the *Kexue 1*, likely caused a contamination of the thermodynamic and wind profiles obtained. These profiles seem to be hybrids of the pre-squall region, in the levels above approximately 3 km (∼700 hPa), and the convective outflow region of the squall line system below this level. Given the hodographs and the orientation of the wind profile for this sounding, as shown in Figures 5.20 and 5.21, respectively, there exists a significant northward component of the winds at low levels which is consistent with the direction of convective outflow for a northward-propagating squall line system.

Simulations in which these thermodynamic and wind profiles were employed as the environment produced little sustained convection, and then only with significant initial temperature perturbations which could penetrate the LCL at approximately 0.5 km (956 hPa) and the alternately moist and dry mid-levels of the environment to reach the relatively dry upper levels above 8 km (∼400 hPa). Convection in the simulation which is shown in Figure 5.24 was initiated with a combined convergence-and-temperature perturbation, for which the convergence perturbation of $u_{conv} = 5$ m s^{-1} was centered at the surface at $x = 0$ and had an initial overall width of 16 km, and the temperature bubble of strength $T' = +1.5$K was centered at $x = 0$ at a height of 0.5 km and also had an initial width of 16 km. The results of this experiment are shown in Figure 5.24 at intervals of 8m between 0h 24m and 1h 20m, demonstrating the development of strongly-sheared convection of moderate strength which reaches the upper levels of the model domain and is carried rearward (to the right) within the convective system toward the 230° azimuth used for the wind profiles in Figure 5.21. Precipitation, which may be classified as convective showers, persists through this portion of the simulation, falling from the remnant convective clouds which also persist in the more weakly-sheared environment of the layer between heights of approximately 7 km and 14 km. Convective clouds seem to dissipate quickly in the lower

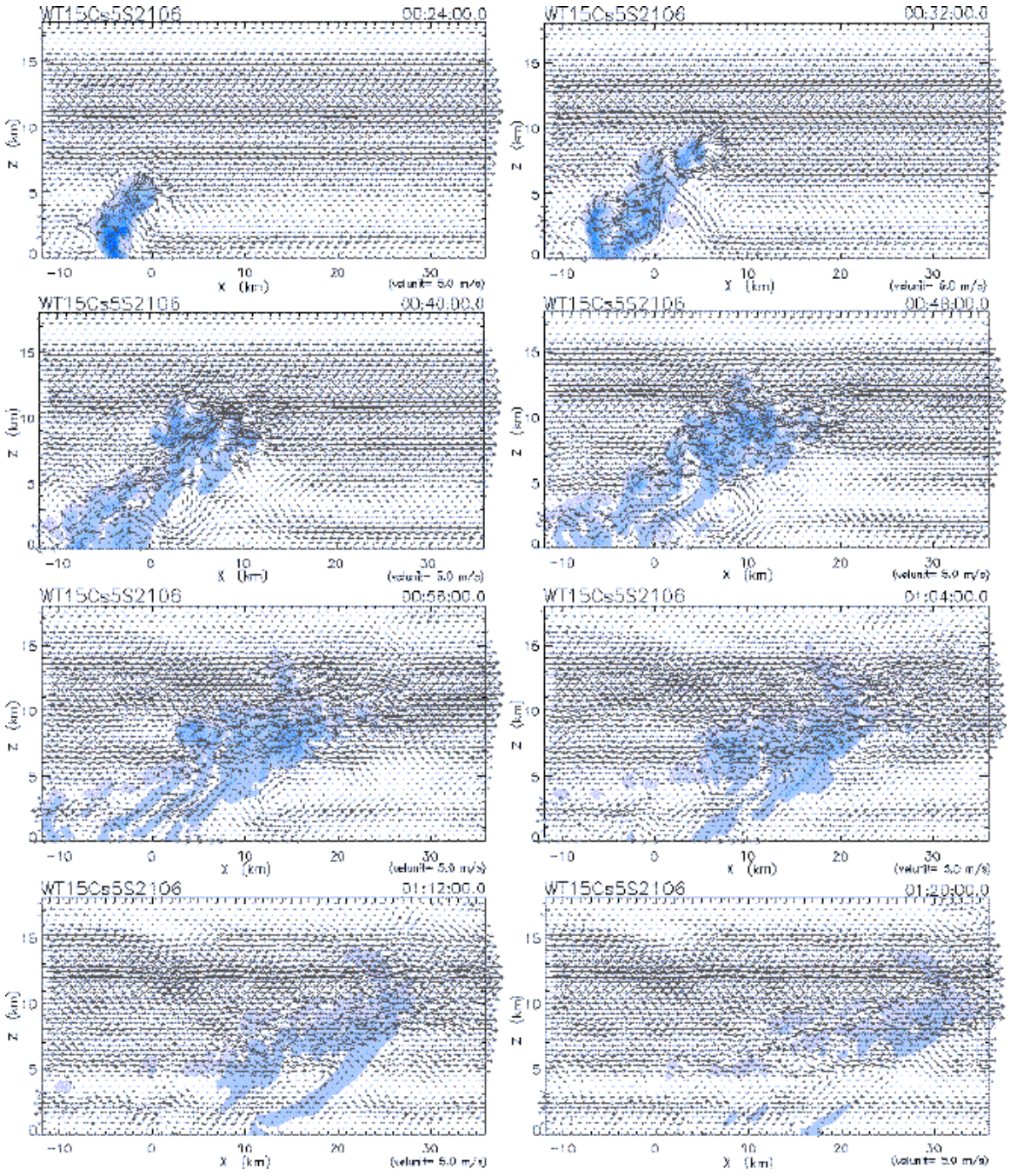

Figure 5.24: 21 May, 1998, 06 UTC SCSMEX temperature-and-convergence perturbation experiment. Cloud and precipitation contents are indicated by the shaded regions, and wind vectors are included.

levels, due to the greater initial environmental moisture and more concentrated shear layers present there.

A simulation employing the 06 UTC sounding environment in which only a temperature bubble was employed to initiate convection is demonstrated in Figure 5.25. The initial thermal bubble of strength $T' = +2$K was centered at $x = 0$ at a height of 0.5 km and had an initial width of 16 km, as in the previous experiment. Results from this experiment, displayed at regular intervals of 10 minutes between 0h 18m and 1h 28m, demonstrate a qualitative similarity to the previous experiment but with more persistent cloud mass in the mid-levels of the domain and a more significant formation of cirrostratus in the layer between 13 km and 16 km later in the simulation. These structures may likely be attributed to the additional buoyancy introduced with a stronger initial low-level thermal, which imported a greater amount of low-level moisture to the middle and upper levels of the atmosphere than weaker thermals in other simulations.

5.3.3 18 May, 1998, 06 UTC Experiments

Isolated convective cells, barely visible in the satellite images included in Figure 5.26, were prevalent about the *Kexue 1* during the early (local) afternoon of 18 May, 1998. The synoptic environment of the *Kexue 1* on this date may be deduced from the ECMWF analyses included in Figure 5.27. The analysis at 00 UTC on 18 May, shown in Figure 5.27a, demonstrates southeasterly to easterly flow at the approximate location of the *Kexue 1* in the layer between the surface and 500 hPa. This flow transitions to southerly in the lower levels near the location of the *Kexue 1* by 12 UTC, as shown in Figure 5.27b, with continued easterly flow in the layer between 700 hPa and 500 hPa. Isolated cumulus of moderate development, such as that shown in Figure 5.28, are representative of the convective activity

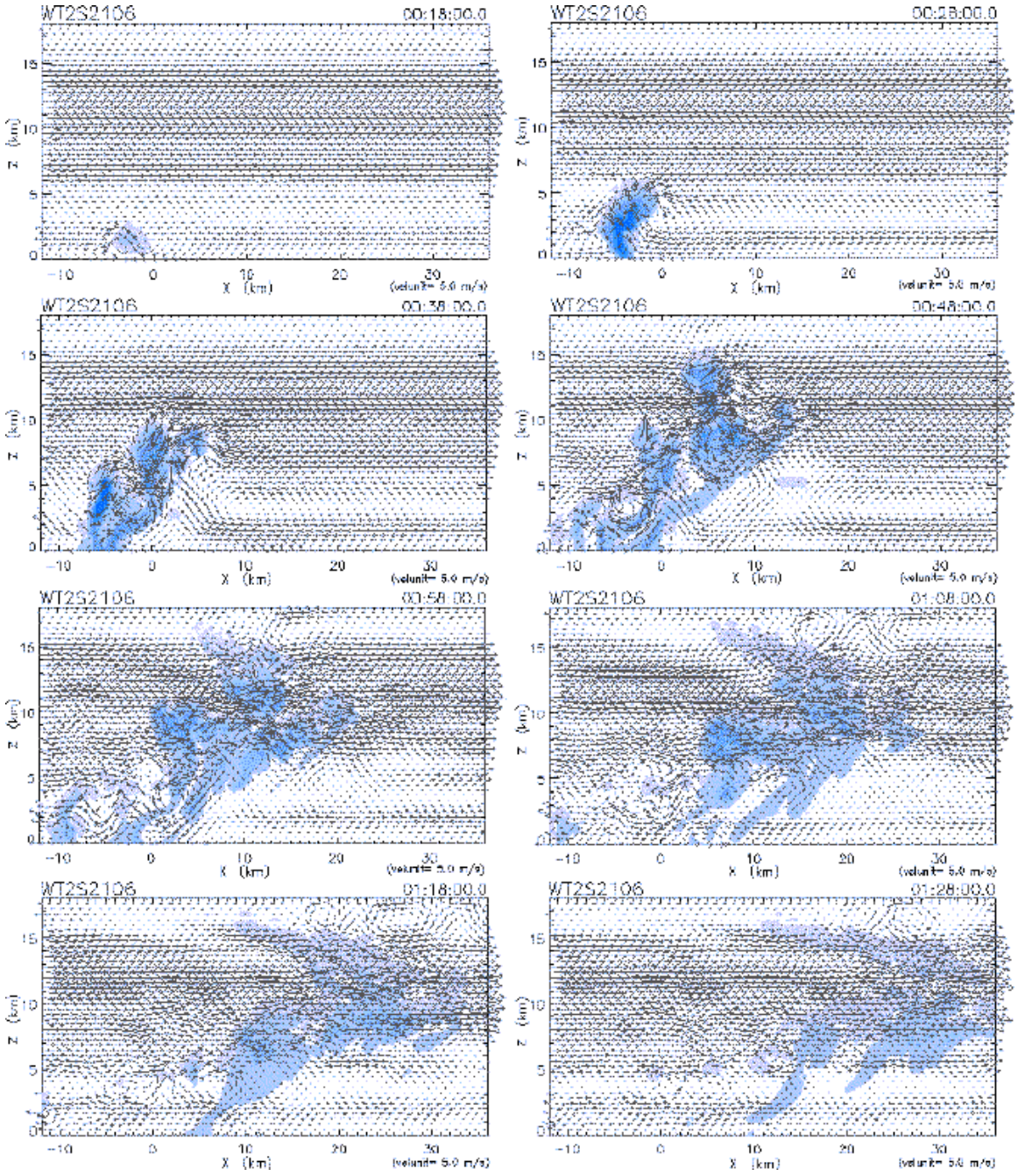

Figure 5.25: 21 May, 1998, 06 UTC SCSMEX temperature perturbation experiment. Cloud and precipitation contents are indicated by the shaded regions, and wind vectors are included.

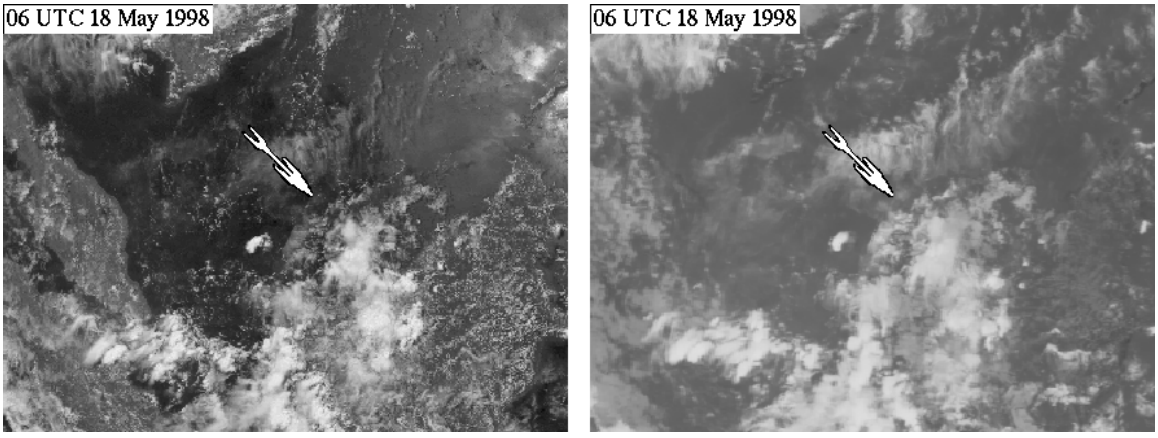

Figure 5.26: 18 May, 1998, coincident GMS images in the region of the R/V *Kexue 1* during SCSMEX. The visible-channel image is displayed on the left; the infrared-channel (IR) image at the same time is displayed on the right. In the visible-channel image at left, the island of Borneo is visible to the southeast, the Malaysian peninsula and the island of Sumatra are visible to the southwest, and the Vietnamese coast is visible to the north of the position of the *Kexue 1*.

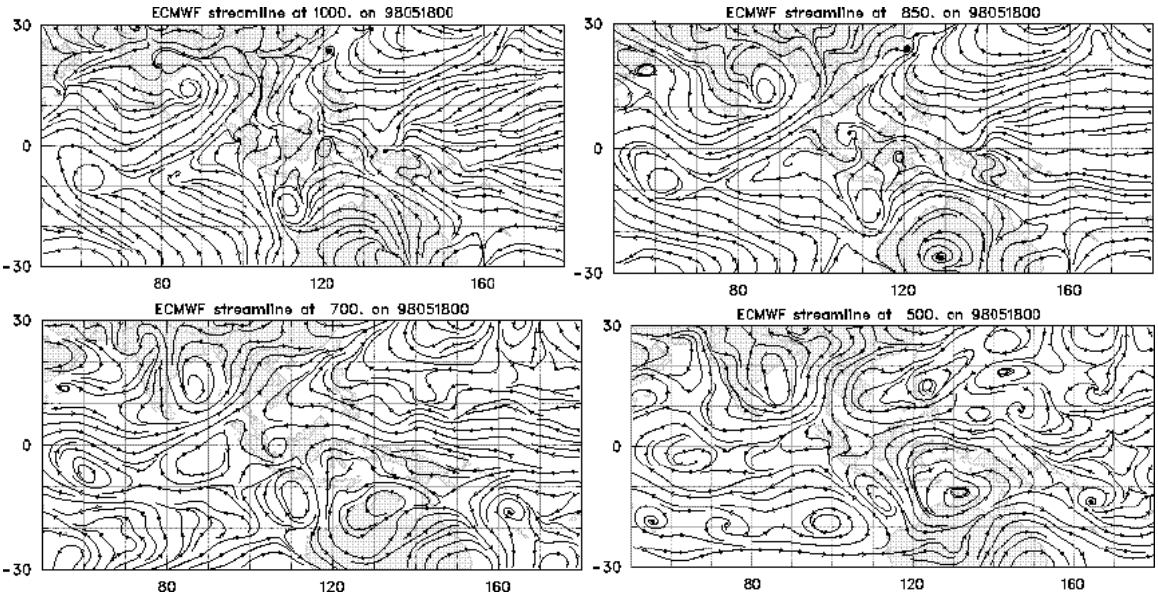

Figure 5.27a: 18 May, 1998, 00 UTC ECMWF streamline analyses. Numbers on the left of each frame indicate degrees of latitude (0° = Equator); numbers below each frame indicate degrees East longitude.

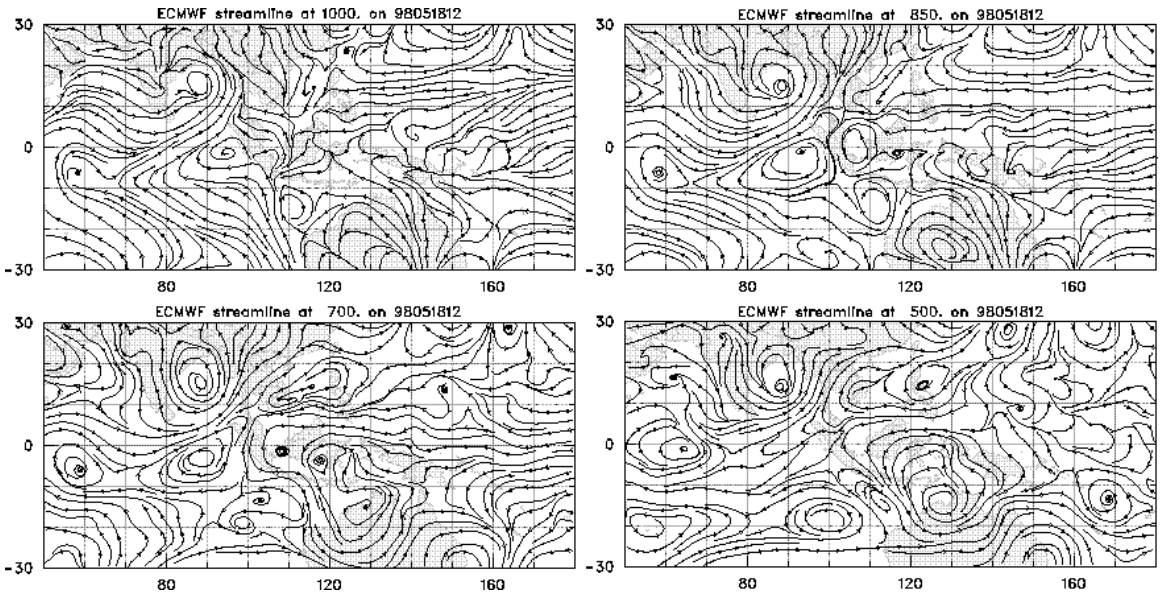

Figure 5.27b: 18 May, 1998, 12 UTC ECMWF streamline analyses. Numbers on the left of each frame indicate degrees of latitude (0° = Equator); numbers below each frame indicate degrees East longitude.

observed by the shipboard scientists around the time data was gathered during the 18 May, 1998, 06 UTC sounding. A lack of significant convective development is evident in the satellite photographs in Figure 5.26, in which the horizontal resolution is approximately 5 km per pixel. In the visible-channel photograph, on the left of Figure 5.26, very few clouds of a size larger than approximately 5 km in diameter are found in the vicinity of the *Kexue 1*, which is indicated by the large white arrow. The infrared-channel (IR) image, included on the right of Figure 5.26, demonstrates the lack of vertical development in many of these cumulus, such that few clouds in the immediate vicinity of the *Kexue 1* exhibit the cold cloud tops which commonly result from the freezing of cloud and precipitation droplets which occurs with vertical cloud development to the freezing level and above. Even with the vertical development of a single cumulus to a level which freezes the cloud droplets, leaving a signature on the IR photograph, such a cloud may still be far too small to be found on a photograph for which a pixel represents as much as 25 km^2.

Figure 5.28: An isolated precipitating cumulus in the vicinity of the *Kexue 1* during SCSMEX, photographed by M. Garcia.

Several experiments were performed with a background atmosphere provided by the 18 May, 06 UTC thermodynamic and wind profiles. Many of the experiments in which a near-surface thermal bubble, a surface convergence region, or a combination perturbation produced convective updrafts of some height and clouds with a typical life span of approximately 20m to 50m. Given the low LCL, though not as low as other soundings discussed here, and the convective activity observed by the scientists during the sounding, these results were expected. Two of these experiments are demonstrated here in Figures 5.29 and 5.31.

A Convergence Experiment

An experiment in which the initial perturbation included only a surface convergence region is demonstrated in Figure 5.29. This convergence region had a strength of $u_{conv} = 5$ m s^{-1} and an overall initial width of 16 km. The early portions of this experiment are also included on the right side of Figure 5.9 in an example of the possible convective formations which result from initial convergence perturbations centered at the surface of the model domain and at some elevated position. It is shown, in Figure 5.29, that the cloud top seems to break into three nodes during ascent past a height of approximately 4 km, and that two of the three updrafts persist in their vertical development while the third, which is the most upstream of the three, dissipates quickly. The most upstream of the two remaining nodes is then observed to dissipate more slowly than the first, followed by the eventual dissipation of the last updraft node. None of the updraft nodes develops beyond 8 km in height, seemingly due to the stronger shear present above a height of approximately 7 km. Again, some cloud mass does persist throughout the simulation in the midlevels due to the greater presence of ambient moisture there, as demonstrated earlier in a discussion of the thermodynamic profile. Except for the shapshot of cumulus development at 0h 31m, as shown in Figure 5.29, the cloud which is developed under these environmental and initial conditions little resembles cumulus observed in nature, including those observed by the shipboard scientists around the time of the 18 May, 06 UTC sounding.

It may be concluded that the reasons for this departure from expected cumulus growth stem from the early formation of a tri-nodal cloud top structure, although the reasons for the evolution of the single initial updraft structure to the tri-nodal structure are still somewhat unclear. A similar cloud-top structure can be seen in the photograph shown in Figure 5.30. Several recent experiments have employed two-dimensional models with high spatial

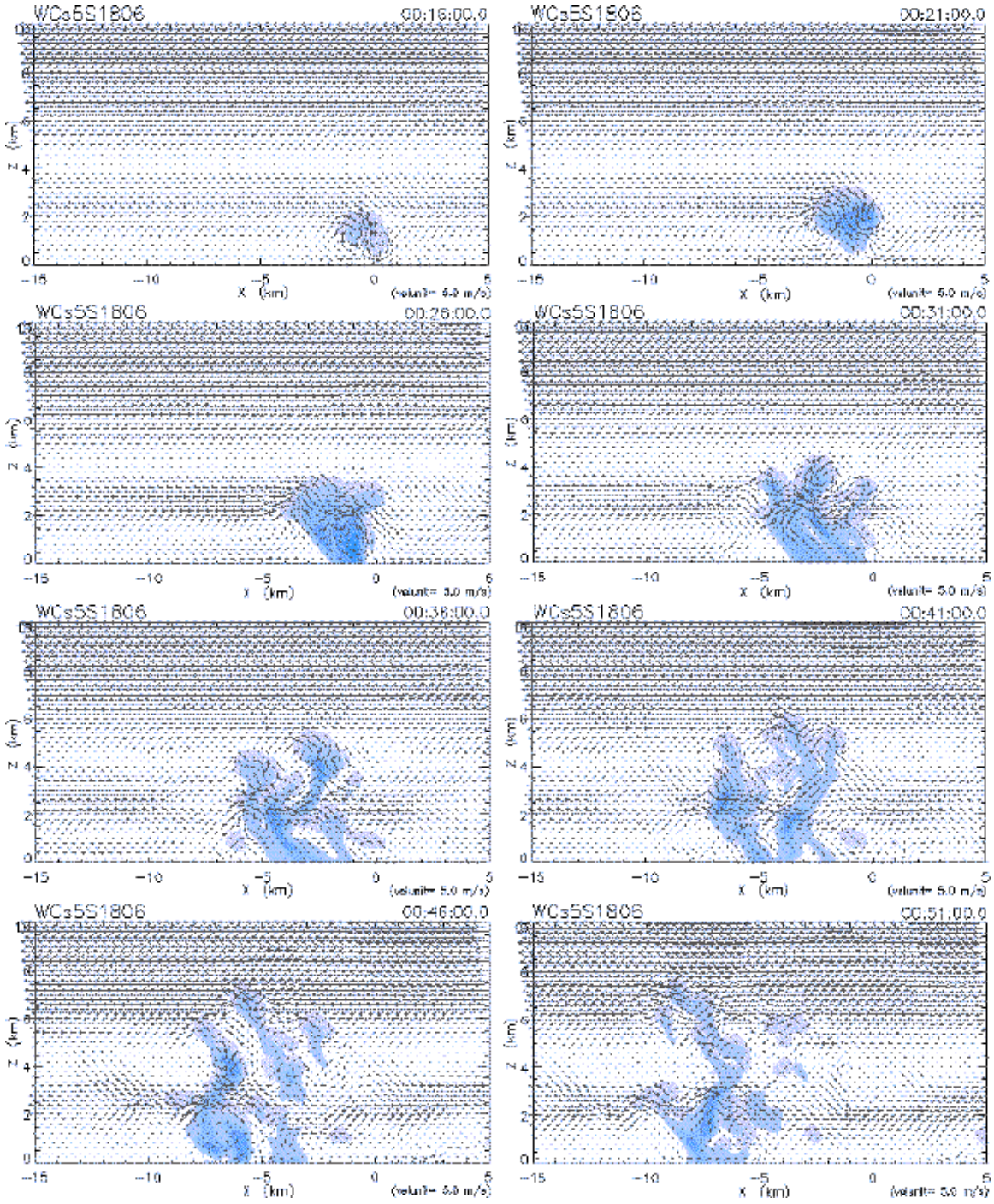

Figure 5.29: 18 May, 1998, 06 UTC SCSMEX convergence perturbation experiment. Cloud and precipitation contents are indicated by the shaded regions, and wind vectors are included.

Figure 5.30: A cumulus in the vicinity of the *Kexue 1* during SCSMEX demonstrating the growth of "turrets" at cloud-top, photographed by M. Garcia.

and temporal resolution to examine the cumulus growth and entrainment process. Klaassen and Clark (1985) simulated the growth of small cumulus and witnessed the development of nodes, such as those demonstrated here, along the upper cloud boundary. These nodes were found to assist in the entrainment of relatively dry environmental air above cloud top into the cloud (Paluch, 1979; Stith, 1992) and in the subsequent formation of penetrative downdrafts (Squires, 1958b) which reached the mid-level interior of the cloud. Although the work of Klaassen and Clark did not distinguish clearly between physical dynamic instabilities, e.g. aerodynamic, hydrodynamic and thermodynamic instabilities, and purely numerical instabilities, it was concluded that the penetrative downdrafts resulted from cloud-top instabilities on a small scale. The scale of these instabilities seemed more closely related to

Rayleigh-Taylor instabilities, in which perturbations caused by a flow which contains reversing shear, and thus opposing vorticity gradients, grow due to pre-existing instability across a surface at which low-density fluid lies below a heavier fluid, than to the evaporative cooling of entrained parcels. Several problems with the numerical approach of Klaassen and Clark were criticized by Grabowski (1989), and were somewhat corrected by Grabowski and Clark (1991, 1993) and Grabowski (1993), by which time it was concluded that the cloud-top instability was brought about by the baroclinic generation of vorticity in a thin layer of strong gradients in the potential temperature and liquid water fields near the cloud boundary.

A Combined-Peturbation Experiment

Another experiment was performed for which a combined initial perturbation was employed, producing far more realistic results. Convection in this simulation, shown in Figure 5.31, was initiated with a convergence-and-temperature perturbation, for which the convergence perturbation of $u_{conv} = 5$ m s^{-1} was centered at the surface at $x = 0$ and had an initial overall width of 16 km, and the temperature bubble of strength $T' = +1$K was centered at $x = 0$ at a height of 0.5 km and also had an initial width of 16 km. Snapshots of a portion of the model domain are shown in Figure 5.31 at intervals of 10m between 0h 24m and 0h 54m, demonstrating the development of a single convective updraft which reaches approximately 10 km in height through the strongly sheared lower levels of the troposphere. Again, some cloud mass persists in the midlevels due to the moisture in the background atmosphere there with which the model domain was initialized.

A close-up of the convective tower at 0h 34m is shown in Figure 5.32a, near the extent of its vertical development and as the upper portion of the cumulus was just beginning to

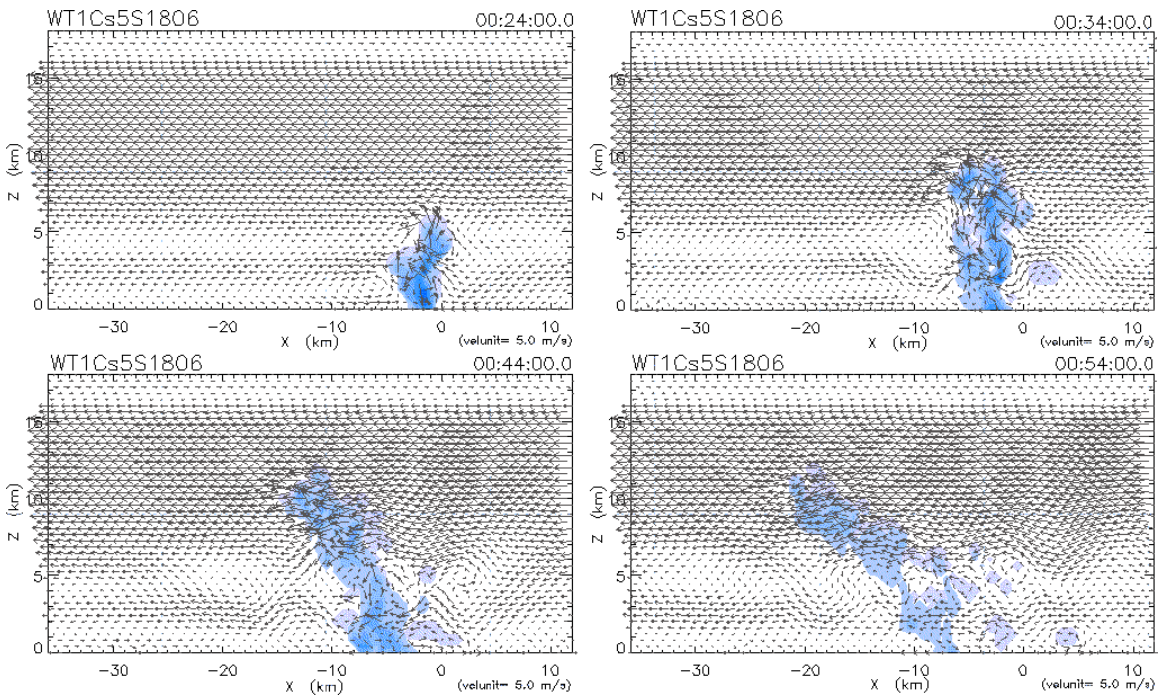

Figure 5.31: 18 May, 1998, 06 UTC SCSMEX temperature-and-convergence perturbation experiment. Cloud and precipitation contents are indicated by the shaded regions, and wind vectors are included.

lean downshear under the strong influence of the approximated wind profile in the middle and upper levels. The snapshot in Figure 5.32 is of a portion of the model domain for which the grid cell apsect ratio, i.e. the ratio of Δx to Δz, as shown in the figure is approximately 1, thus demonstrating the vertical development of the cumulus in relation to its narrow base and updraft region. The cumulus updraft core is tilted in sections, according to the vorticity production by the environmental shear profile: downstream in the surface-to-3 km layer, slightly upstream in the layer between 3 km and 5 km, and again downstream in the layer above 5 km. The vorticity which influences these tilted regions is clearly evident in the wind vectors adjacent to the cumulus region in Figures 5.31 and 5.32a. A photograph of a cloud of moderate vertical extent is included in Figure 5.32b for comparison. Although the shape of the simulated cloud in Figure 5.32a is somewhat different from that observed, as shown in Figure 5.32b, given the infinite number of cloud growth possibilities under

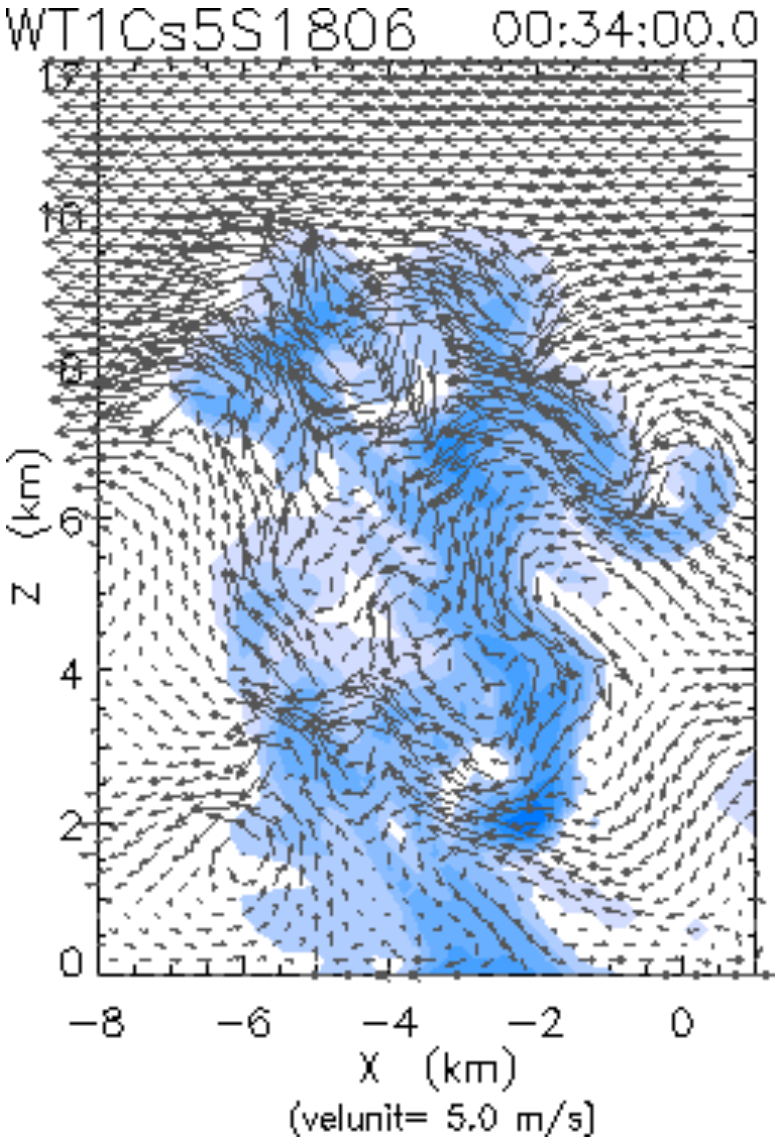

Figure 5.32a: 18 May, 1998, 06 UTC SCSMEX temperature-and-convergence perturbation experiment, at 0h 34m. Cloud and precipitation contents are indicated by the shaded regions, and wind vectors are included.

Figure 5.32b: An isolated cumulus of moderate development in the vicinity of the *Kexue 1* during SCSMEX, photographed by M. Garcia. The structure of this cloud may be favorably compared with that of simulated cumulus growth in Figure 5.32a.

seemingly similar environmental conditions, it may be concluded that the structure of the simulated cloud is well within the scope of those possibilities.

Stommel (1947) found that in-cloud temperature profiles were more similar to a clear air environmental sounding than to a moist adiabat, and hypothesized that the updraft in a convective cloud was analogous to a fluid jet, which in laboratory experiments had been found to entrain envionmental fluid laterally. Squires (1958a) proposed that the dilution of liquid water content in growing cumulus clouds comes about by the entrainment of environmental air through the top of the cloud. Numerous observational and numerical experiments have been performed since the time of these works which lend support to both concepts of cumulus entrainment. Many of these experimental efforts are reviewed by Reuter (1986).

A brief early review of cumulus updraft and entrainment theories was provided by Squires (1958b), who listed three possible mechanisms of cumulus entrainment: 1. dry environmental air enters the sides of the cloud, mixing laterally with the updraft; 2. dry air mixes in situ with cloudy air rising from below; 3. dry air parcels from just above the cloud top enter the cloud as penetrative downdrafts, which mix vertically with the cumulus updraft. The first mechanism may be considered a lateral entrainment mode, while the second and third mechanisms may be considered cloud-top entrainment modes. The process of convective downdraft formation at cloud top has been explored by Squires (1958a) and Telford (1975), and later by Randall (1980) and Deardorff (1980) as a possible mechanism for the breakup of stratocumulus clouds in subtropical maritime regions. Although many observational experiments employ a method developed by Paluch (1979) to determine the source region of entrained air in cumuli, this method was developed under the assumption of limited mixing of air entrained by the cloud-top mode without regard for the growth

stage of the cumulus.

Some researchers (Randall and Huffman, 1982; Cooper and Rodi, 1982) have suggested ideas by which the two modes of cumulus entrainment, cloud-top and lateral, may not be mutually exclusive. These ideas require consideration of the growth mode of the cumulus: is the cloud still growing vertically, and if so, how vigorously? Observational evidence presented by Stith (1992) suggests that small-scale circulations in the layer at the interface between cloud-top and the environment above the cloud may actually force air from above a growing cumulus down around the rising turret and then into the sides of the top portion of the cloud as laterally entrained parcels. At the top of a cumulus which is no longer growing vertically, radiative cooling may induce cloud-top entrainment and mixing, which may produce evaporative cooling and subsidence (Stith and Politovich, 1989) and the formation of penetrative downdrafts (Squires, 1958a). Mixing of the entrained air with its cloudy environment begins immediately upon entrainment through the production of turbulence kinetic energy (Randall, 1980), possibly resulting in evaporation of cloud droplets and cooling of the mixed parcel, which eventually achieves buoyancy equilibrium by way of mixing through the cloud in a sorting process proposed by Telford (1975) and developed further by Taylor and Baker (1991).

The entrainment of environmental air into the growing cumulus is well-simulated in this experiment. Figure 5.32a demonstrates the lateral entrainment of relatively dry air throughout the growth of the cloud. A closer look at the simulation reveals the growth of an instability on the upper cloud surface, the entrainment of cloud-top air, and the formation of a relatively dry penetrative downdrafts due to evaporative cooling within the interior of the cumulus over the period between 0h 30m and 0h 36m, while the cumulus is still growing vigorously. This sequence of events is demonstrated in Figure 5.33, which shows snapshots

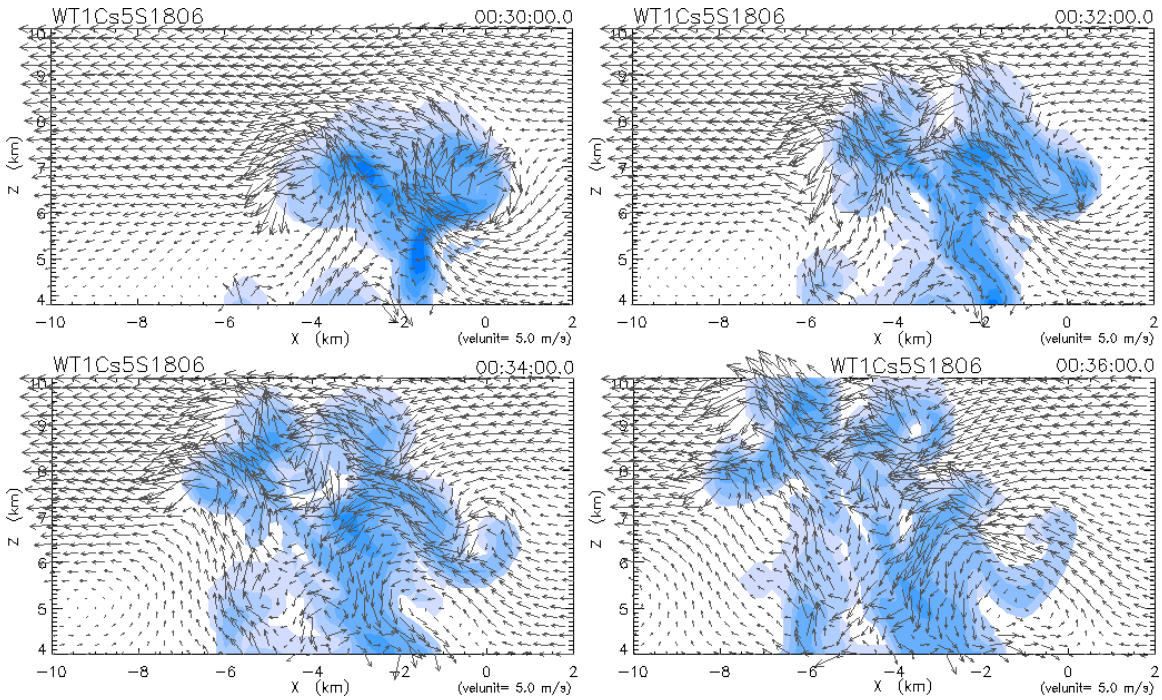

Figure 5.33: 18 May, 1998, 06 UTC SCSMEX temperature-and-convergence perturbation experiment, close-up of cloud-top entrainment. Cloud and precipitation contents are indicated by the shaded regions, and wind vectors are included.

of the cloud-top region at intervals of 2 minutes between 0h 30m and 0h 36m.

Chapter 6

CONCLUSIONS

6.1 Summary and Conclusions

The construction of a two-dimensional, nonhydrostatic, primitive equation model of the atmosphere, previously published in parts by Ooyama, has been described in detail. Physical and numerical constructs within this model have been discussed, and have been analyzed using previously performed experiments for that purpose. Supported by a detailed review of tropical squall line observations and modeling efforts, earlier simulations of squall line systems have also been analyzed at length. These were followed by an additional, recent, squall line simulation, which compares well with the previously described qualitative structure of tropical squall line systems and with various efforts at the analysis of specific squall line structures which invlove the regeneration and maintenance of convection. The dependence and nature of convective regeneration on the cold surface outflow layer and gust front is illustrated clearly in a discussion of this recent simulation and in the included figures. A new formulation of the "balance" between a propagating convective outflow layer near the surface, continually forced by a strong descending rear-to-front flow through the squall line system, and its environment is proposed and evaluated, providing physically realistic and relatively accurate prognoses of the balanced state and of gust front propagation speed trends when in an unbalanced state.

In order to further validate the utility of the described model, numerous additional experiments were performed which employed tropospheric thermodynamic and wind profiles obtained during the author's participation in SCSMEX. The use of these data in the two-dimensional model described earlier produced results which were widely supported by observations of convective activity around the time of data collection. A favorable assessment of these simulations was also supported by a brief review of cumulus growth and entrainment theoretical, observational and modeling studies, with specific well-accepted theories and observations appropriately referenced.

In conclusion, results provided by the two-dimensional, nonhydrostatic, primitive equation model are well-supported by previously published theoretical, observational, and computational efforts which have been designed to explore the fundamental processes involved in cumulus growth and propagation and tropical squall line system generation, development, maintenance, and propagation. The utility of this model in the successful simulation of convective systems as large as hundreds of kilometers in size, in the mesoscale regime, to hundreds of meters in size, well within the convective scale regime, has been shown repeatedly through analysis of previous results and in the formulation and analysis of new experiments.

6.2 Future Work

Numerous possibilities exist for the extension of simulation and analysis efforts presented here. The refinement of internal model processes holds the promise of future experimental efforts which produce more accurate results, both qualitatively and quantitatively, when compared with observed convective systems.

Simulation of the 4-5 September, 1974, GATE squall line system would provide a

promising avenue for the further validation of model construction and results, as well as some insight into the quantitative accuracy of model results, given the numerous observational and numerical efforts at analysis of that particular tropical maritime squall line system. Such an effort could also include an analysis of variations in initial environmental conditions and perturbations, following NJC88.

Refinements may be made in the implementation of inhomogeneous boundary conditions, as employed by Shapiro and Ooyama (1990). The use of analyzed data from other sources in this manner provides greater possibilities in defining the initial environment of observed convective systems. Radiation conditions may be considered, to lend even greater reality to the thermodynamic structure employed in this model and to facilitate a closer examination of radiative-convective equilibrium theory.

More careful treatment of the boundary layer, including surface friction, is of great importance, in consideration of the observational studies of Johnson and Nicholls (1983) and Nicholls and Johnson (1984). As well, the incorporation of surface fluxes demand particular attention, considering the general environment of both continental and maritime tropical squall line systems, the diurnally-varied surface radiative heat source in continental regions, and the widely-stressed importance of the ocean as a near-infinite source of latent and sensible heat (Wang et al., 1996; Trier et al., 1996).

More varied perturbations may be incorporated into the initialization procedures of the model, in order to provide greater freedom in the specification of an initial disturbance. Bulk microphysical parameterizations included in the current model may also be reconsidered, given the wealth of experimental data on such processes produced after the pioneering formulations of Kessler (1969) and Klemp and Wilhelmson (1978). All of these possibilities may provide significant further improvements in modeling efforts on any scale. Kessler and

Bumgarner (1971) employed a higher threshold and slower rate for the autoconversion of cloud droplets to precipitation than that employed by Kessler (1969), and an autoconversion rate which was slower by an order of magnitude than that employed in the later formulation of Klemp and Wilhelmson (1978) and here in Section 3.2.3. Employment of the autoconversion parameters formulated by Kessler and Bumgarner might successfully address the early and strong formation and release of precipitation by growing cumulus in the current model which is found to be of some consequence for continued cumulus development in recent experiments by the present author.

The simulation of processes on the convective scale would provide a wealth of information regarding cumulus and cumulonimbus initiation, development, propagation and demise which could be easly compared and constrasted with previous theoretical, observational and numerical efforts. Experiments such as these could provide greater insight into the internal growth, instability, entrainment, and mixing processes of clouds.

The simulation of near-surface density current dynamics would also provide an interesting avenue of research. New simulations may be compared with the early laboratory and numerical experiments of Simpson (1969) and Simpson and Britter (1980) and detailed examinations of density current surface dynamics by Droegemeier and Wilhelmson (1985, 1986, 1987) and Straka et al. (1993). Along these lines, further work must be undertaken in order to properly assess the condition of "balance" between a propagating gust front and its environment as proposed in Section 5.1.8.

Finally, the extension of this model to a quasi-three-dimensional and fully three-dimensional framework follows the natural progression of model development given these recent efforts. Quasi-three-dimensional simulations have already been performed in other incarnations of this model, including an axisymmetric framework for the simulation of

atmospheric vortices such as tropical cyclones. Simulations of convective clouds with this version of the model may be compared with the work of Murray (1970) and Soong and Ogura (1973). The extension of the model to a fully three-dimensional framework for the simulation of systems such as developing and mature tropical cyclones would complement the earlier efforts of Ooyama (1969a, b) and the efforts of subsequent collaborators (Shapiro and Ooyama,1990; DeMaria et al., 1992).

Given the inherent three-dimensionality of cumulus development, the simulation of small-scale process would obviously benefit from an expansion of the current model geometry to a fully three-dimensional framework. While the energetics of the model may improve significantly with such a transition, such that the energy cascade of three-dimensions is explicitly and fully treated, we may not necessarily denigrate the current framework as representative of classical two-dimensional turbulence, for which kinetic energy is thought to experience only upscale transfer, creating an "anti-cascade" of turbulent energy (Fjørtoft, 1953; Lilly, 1969; Deardorff, 1975). In two-dimensional, homogeneous, nondivergent, incompressible flows, turbulence energy is actually found to be *more likely*, but not always, to cascade upscale (Merilees and Warn, 1975). The model presented here includes few of those limiting assumptions: stratification, divergence and compressibility are certainly allowed in the current framework, as they are found if one analyzes a two-dimensional slice through the real atmosphere.

The conclusion at which most modelers arrive, that turbulent energy in their two-dimensional model cascades only upscale, is based on the observation that the processes of divergence and stretching are not present and that therefore the vorticity field in a region may not be forced to higher wavenumbers under their influence. Based on such an observation, the conclusion of simple anti-cascade is quite narrow-minded and is not neces-

sarily correct, and should be expected to invalidate the model results within some period of time. Under such strict conclusions, one might expect the upper-level rotor-like circulations found in the trailing stratiform precipitation region in Figure 4.13d to intensify, and possibly grow, over time through interactions with similar adjacent disturbances. Such a conclusion is not representative of the actual model results for the simulations presented here. We may conclude that the processes of compressibility and divergence allow the present model to treat two-dimensional turbulence in a somewhat rudimentary fashion, such that model results are not invalidated by the strict anti-cascade of turbulent energy. However, a full treatment of turbulent energy may only be accomplished in a three-dimensional framework, similar to the real atmosphere, such that the natural cascade of turbulent energy to higher wavenumbers is explicitly simulated.

REFERENCES

Ackerman, B., 1958: Turbulence around tropical cumuli. *J. Meteor.*, **15**, 69-74.

Arakawa, A., and W.H. Schubert, 1974: Interaction of a cumulus cloud ensemble with the large-scale environment, part I. *J. Atmos. Sci.*, **31**, 674-701.

Asai, T., and I. Nakasuji, 1977: On the preferred mode of cumulus convection in a conditionally unstable atmosphere. *J. Meteor. Soc. Japan*, **55**, 151-167.

Asai, T., and I. Nakasuji, 1982: A further study of the preferred mode of cumulus convection in a conditionally unstable atmosphere. *J. Meteor. Soc. Japan*, **60**, 425-431.

Asselin, R., 1972: Frequency filter for time integrations. *Mon. Wea. Rev.*, **100**, 487-490.

Baker, M.B., R.G. Corbin and J. Latham, 1980: The influence of entrainment on cloud droplet spectra: I. A model of inhomogeneous mixing. *Quart. J. Roy. Meteor. Soc.*, **106**, 581-598.

Barnes, G.M., and K. Sieckman, 1984: The environment of fast- and slow-moving tropical mesoscale convective cloud lines. *Mon. Wea. Rev.*, **112**, 1782-1794.

Betts, A.K., and B.A. Albrecht, 1987: Conserved variable analysis of the convective boundary layer thermodynamic structure over the tropical oceans. *J. Atmos. Sci.*, **44**, 83-99.

Betts, A.K., R.W. Grover, and M.W. Moncrieff, 1976: Structure and motion of tropical squall lines over Venezuela. *Quart. J. Roy. Meteor. Soc.*, **102**, 395-404.

Bluestein, H.B., and M.H. Jain, 1985: Formation of mesoscale lines of precipitation: Severe squall lines in Oklahoma during the spring. *J. Atmos. Sci.*, **42**, 1711-1732.

Böhm, J.P., 1992: A general hydrodynamic theory for mixed-phase microphysics. Part I: Drag and fall speed of hydrometeors. *Atmos. Res.*, **27**, 253-274.

Bond, N.A., 1992: Observations of planetary boundary-layer structure in the eastern equatorial Pacific. *J. Climate*, **5**, 699-706.

Brenguier, J.-L., and W.W. Grabowski, 1993: Cumulus entrainment and cloud droplet spectra: A numerical model within a two-dimensional dynamical framework. *J. Atmos. Sci.*, **50**, 120-136.

Browning, K.A., 1964: Airflow and precipitation trajectories within severe local storms which travel to the right of the winds. *J. Atmos. Sci.*, **21**, 634-639.

Caniaux, G., J.-P. LaFore, and J.-L. Redelsperger, 1995: A numerical study of the stratiform region of a fast-moving squall line. Part II: Relationship between mass, pressure, and momentum fields. *J. Atmos. Sci.*, **52**, 331-352.

Caniaux, G., J.-L. Redelsperger, and J.-P. LaFore, 1994: A numerical study of the stratiform region of a fast-moving squall line. Part I: General description and water and heat budgets. *J. Atmos. Sci.*, **51**, 2046-2074.

Chalon, J.P., G. Jaubert, F. Roux, and J.P. LaFore, 1988: The West African squall line observed on 23 June 1981 during COPT81: Mesoscale structure and transports. *J. Atmos. Sci.*, **45**, 2744-2763.

Chang, C.-Y., and M. Yoshizaki, 1993: Three-dimensional modeling study of squall lines observed in COPT81. *J. Atmos. Sci.*, **50**, 161-183.

Charba, J., 1974: Application of a gravity current model to analysis of squall-line gust

front. *Mon. Wea. Rev.*, **102**, 140-156.

Chin, H.-N.S., Q. Fu, M.M. Bradley, and C.R. Molenkamp, 1995: Modeling of a tropical squall line in two-dimensions: Sensitivity to radiation and comparison with a midlatitude case. *J. Atmos. Sci.*, **52**, 3172-3193.

Chin, H.-N.S., and Y. Ogura, 1989: The impact of the ice phase and radiation on a midlatitude squall line. *J. Atmos. Sci.*, **46**, 1440-1447.

Chin, H.-N.S., and R.B. Wilhemlson, 1998: Evolution and structure of tropical squall line elements within a moderate CAPE and strong low-level jet environment. *J. Atmos. Sci.*, **55**, 3089-3113.

Chong, M., P. Amayenc, G. Scialom, and J. Testud, 1987: A tropical squall line observed during the COPT81 experiment in West-Africa. Part I: Kinematic structure inferred from dual-Doppler radar data. *Mon. Wea. Rev.*, **115**, 670-694.

Clark, T.L., 1977: A small-scale dynamic model using a terrain-following coordinate transformation. *J. Comput. Phys.*, **24**, 186-215.

Clark, T.L., and R.D. Farley, 1984: Severe downslope windstorm calculations in two and three spatial dimensions using anelastic interactive grid nesting: A possible mechanism for gustiness. *J. Atmos. Sci.*, **41**, 329-350.

Clark, T.L., and W.D. Hall, 1991: Multi-domain simulations of the time-dependent Navier-Stokes equations: Benchmark error analysis of some nesting procedures. *J. Comput. Phys.*, **92**, 456-481.

Clark, T.L., and R. List, 1971: Dynamics of a falling particle zone. *J. Atmos. Sci.*, **28**, 718-727.

Cooper, W.A., and A.R. Rodi, 1982: Cloud droplet spectra in summertime cumulus clouds.

Preprints, Conference on Cloud Physics, Chicago, IL, Amer. Met. Soc., 147-150.

Cram, J.M., R.A. Pielke, and W.R. Cotton, 1992: Numerical simulation and analysis of a prefrontal squall line. Part II: Propagation of the squall line as an internal gravity wave. *J. Atmos. Sci.*, **49**, 209-225.

Cunning, J.B., 1986: Oklahoma-Kansas preliminary regional experiment for STORM-Central. *Bull. Amer. Meteor. Soc.*, **67**, 1478-1486.

Das, P., 1964: Role of condensed water in the life cycle of a convective cloud. *J. Atmos. Sci.*, **21**, 404-418.

Deardorff, J.W., 1975: The development of boundary-layer turbulence models for use in studying the severe storm environment. *Proc. SESAME Meeting*, Boulder, CO, NOAA-ERL, 251-264.

Deardorff, J.W., 1980: Cloud top entrainment instability. *J. Atmos. Sci.*, **37**, 131-147.

DeMaria, M., 1995: Evaluation of a hydrostatic, height-coordinate formulation of the primitive equations for atmospheric modeling. *Mon. Wea. Rev.*, **123**, 3576-3589.

DeMaria, M., S.D. Aberson, K.V. Ooyama, and S.J. Lord, 1992: A nested spectral model for hurricane track forecasting. *Mon. Wea. Rev.*, **120**, 1628-1643.

Droegemeier, K.K., and R.B. Wilhelmson, 1985: Kelvin-Helmholtz instability in a numerically simulated thunderstorm outflow. *Preprints, 14th Conference on Severe Local Storms*, Indianapolis, IN, Amer. Meteor. Soc., 151-154.

Droegemeier, K.K., and R.B. Wilhelmson, 1986: Kelvin-Helmholtz instability in a numerically simulated thunderstorm outflow. *Bull. Amer. Meteor. Soc.*, **67**, 416-417.

Droegemeier, K.K., and R.B. Wilhelmson, 1987: Numerical simulation of thunderstorm outflow dyanmics. Part I: Outflow sensitivity experiments and turbulence dynamics.

J. Atmos. Sci., **44**, 1180-1210.

Dudhia, J., M.W. Moncrieff, and D.W.K. So, 1987: The two-dimensional dynamics of West African squall lines. *Quart. J. Roy. Meteor. Soc.*, **113**, 121-146.

Dutton, J.A., 1986: *Dynamics of Atmospheric Motion*, 2d Ed. Dover Publications, 617 pp.

Fankhauser, J.C., 1971: Thunderstorm-environment interactions determined from aircraft and radar operations. *Mon. Wea. Rev.*, **99**, 171-192.

Firestone, J.K., and B.A. Albrecht, 1986: The structure of the atmospheric boundary layer in the central equatorial Pacific during January and February of FGGE. *Mon. Wea. Rev.*, **114**, 2219-2231.

Fjørtoft, R., 1953: On the changes in the spectral distribution of kinetic energy for twodimensional, nondivergent flow. *Tellus*, **5**, 225-230.

Fovell, R.G., 1991: Influence of the Coriolis force on two-dimensional model storms. *Mon. Wea. Rev.*, **119**, 606-630.

Fovell, R.G., and P.S. Dailey, 1995: The temporal behavior of numerically simulated multicell-type storms. Part I: Modes of behavior. *J. Atmos. Sci.*, **52**, 2073-2095.

Fovell, R.G., and Y. Ogura, 1988: Numerical simulation of a midlatitude squall line in two dimensions. *J. Atmos. Sci.*, **45**, 3846-3879.

Fovell, R.G., and Y. Ogura, 1989: Effect of vertical wind shear on numerically simulated multicell storm structure. *J. Atmos. Sci.*, **46**, 3144-3176.

Fovell, R.G., and P.-H. Tan, 1998: The temporal behavior of numerically simulated multicell-type storms. Part II: The convective cell life cycle and cell regeneration. *Mon. Wea. Rev.*, **126**, 551-577.

Frank, W.M., 1978: Life cycles of GATE convective systems. *J. Atmos. Sci.*, **35**, 1256-1264.

Franklin, J.L., S.J. Lord, L.J. Shapiro, and K.V. Ooyama, 1985: An objective analysis of Omega dropwindsonde data from hurricane Debby (1982). *Extended Abstracts, 16th Conference on Hurricanes and Tropical Meteorology*, Houston, TX, Amer. Meteor. Soc., 186-187.

Gamache, J.F., and R.A. Houze, Jr., 1982: Mesoscale air motions associated with a tropical squall line. *Mon. Wea. Rev.*, **110**, 118-135.

Grabowski, W.W., 1989: Numerical experiments on the dynamics of the cloud-environment interface: Small cumulus in a shear-free environment. *J. Atmos. Sci.*, **46**, 3513-3541.

Grabowski, W.W., 1993: Cumulus entrainment, fine-scale mixing, and buoyancy reversal. *Quart. J. Roy. Meteor. Soc.*, **119**, 935-956.

Grabowski, W.W., and T.L. Clark, 1991: Cloud-environment interface instability: Rising thermal calculations in two spatial dimensions. *J. Atmos. Sci.*, **48**, 527-546.

Grabowski, W.W., and T.L. Clark, 1993: Cloud-environment interface instability. Part II: Extension to three spatial dimensions. *J. Atmos. Sci.*, **50**, 555-573.

Grady, R.L., and J. Verlinde, 1997: Triple-Doppler analysis of a discretely propagating, long-lived, high plains squall line. *J. Atmos. Sci.*, **54**, 2729-2748.

Grover, R.W., 1974: Characteristics of tropical squall lines over Venezuela. *Atmospheric Science Report No. 228*, Colorado State University, Fort Collins, Colorado. 79 pp.

Haertel, P.T., 1998: The dynamics of MCS mesohighs and wake lows. *Atmospheric Science Report No. 649*, Colorado State University, Fort Collins, Colorado. 76 pp.

Haltiner, G.J., and R.T. Williams, 1980: *Numerical Prediction and Dynamic Meteorology*. John Wiley and Sons, New York, 477 pp.

Haman, K.E., and H. Pawlowska, 1995: Dynamics of nonactive parts of convective clouds.

J. Atmos. Sci., **52**, 519-531.

Hamilton, R.A., and J.W. Archibold, 1945: Meteorology of Nigeria and adjacent territory. *Quart. J. Roy. Meteor. Soc.*, **71**, 231-262.

Heymsfield, A.J., P.N. Johnson and J.E. Dye, 1978: Observations of moist adiabatic ascent in northeast Colorado cumulus congestus clouds. *J. Atmos. Sci.*, **35**, 1689-1703.

Heymsfield, A.J., and S. Schotz, 1985: Structure and evolution of a severe squall line over Oklahoma. *Mon. Wea. Rev.*, **113**, 1563-1589.

Hicks, E., C. Pontikis and A. Rigaud, 1990: Entrainment and mixing processes as related to droplet growth in warm midlatitude and tropical clouds. *J. Atmos. Sci.*, **47**, 1589-1618.

Holton, J.R., 1992: *An Introduction to Dynamic Meteorology*, 3d Ed. Academic Press, 511 pp.

Houze, R.A., Jr., 1977: Structure and dynamics of a tropical squall line system. *Mon. Wea. Rev.*, **105**, 1540-1567.

Houze, R.A., Jr., 1993: *Cloud Dynamics*. Academic Press, 573 pp.

Houze, R.A., Jr., and A.K. Betts, 1981: Convection in GATE. *Rev. Geophys. Space Phys.*, **19**, 541-576.

Houze, R.A., Jr., and E.N. Rappaport, 1984: Air motions and precipitation structure of an early summer squall line over the eastern tropical Atlantic. *J. Atmos. Sci.*, **41**, 553-574.

Johnson, R.H., P.E. Ciesielski, and K.A. Hart, 1996: Tropical inversions near the 0°C level. *J. Atmos. Sci.*, **53**, 1838-1855.

Johnson, R.H., and P.J. Hamilton, 1988: The relationship of surface pressure features to the

precipitation and airflow structure of an intense midlatitude squall line. *Mon. Wea. Rev.*, **116**, 1444-1472.

Johnson, R.H., and M.E. Nicholls, 1983: A composite analysis of the boundary layer accompanying a tropical squall line. *Mon. Wea. Rev.*, **111**, 308-319.

Jordan, C.L., 1958: Mean soundings for the West Indies area. *J. Meteor.*, **15**, 91-97.

Jorgensen, D.P., M.A. LeMone, and S.B. Trier, 1997: Structure and evolution of the 22 February 1993 TOGA COARE squall line: Aircraft observations of precipitation, circulation, and surface energy fluxes. *J. Atmos. Sci.*, **54**, 1961-1985.

Kamburova, P.L., and F.H. Ludlam, 1966: Rainfall evaporation in thunderstorm downdrafts. *Quart. J. Roy. Meteor. Soc.*, **92**, 510-518.

Kessler, E., 1969: *On the Distribution and Continuity of Water Substance in Atmospheric Circulation.* Meteor. Monogr. No. 32, Amer. Meteor. Soc., 84 pp.

Kessler, E., and W.C. Bumgarner, 1971: *Model of Precipitation and Vertical Air Currents.* NOAA Technical Memorandum ERL NSSL-54, NOAA/OAR/ERL/NSSL, 93 pp.

Kingsmill, D.E., and R.A. Houze, Jr., 1999: Kinematic characteristics of air flowing into and out of precipitating convection over the west Pacific warm pool: An airborne Doppler radar survey. *Quart. J. Roy. Meteor. Soc.*, **125**, 1165-1207.

Klaassen, G.P., and T.L. Clark, 1985: Dynamics of the cloud-environment interface and entrainment in small cumuli: Two-dimensional simulations in the absence of ambient shear. *J. Atmos. Sci.*, **42**, 2621-2642.

Klemp, J.B., R. Rotunno, and W.C. Skamarock, 1994: On the dynamics of gravity currents in a channel. *J. Fluid Mech.*, **269**, 169-198.

Klemp, J.B., and R.B. Wilhelmson, 1978: The simulation of three-dimensional convective

storm dynamics. *J. Atmos. Sci.*, **35**, 1070-1096.

Kloesel, K.A., and B.A. Albrecht, 1989: Low-level inversions over the tropical Pacific—thermodynamic structure of the bondary layer and the above-inversion moisture structure. *Mon. Wea. Rev.*, **117**, 87-101.

Knight, C.A., 1982: Cooperative convective precipitation experiment (CCOPE), 18 May–7 August, 1981. *Bull. Amer. Meteor. Soc.*, **63**, 386-398.

Kuettner, J.P., 1974: General description and central program of GATE. *Bull. Amer. Meteor. Soc.*, **55**, 712-719.

LaFore, J.-P., and M.W. Moncrieff, 1989: A numerical investigation of the organization and interaction of the convective and stratiform regions of tropical squall lines. *J. Atmos. Sci.*, **46**, 521-544.

Leary, C.A., and R.A. Houze, Jr., 1979: Melting and evaporation of hydrometeors in precipitation from the anvil clouds of deep tropical convection. *J. Atmos. Sci.*, **36**, 669-679.

LeMone, M.A., G.M. Barnes, E.J. Szoke, and E.J. Zipser, 1984: The tilt of the leading edge of mesoscale tropical convective lines. *Mon. Wea. Rev.*, **112**, 510-519.

LeMone, M.A., E.J. Zipser, and S.B. Trier, 1998: The role of environmental shear and thermodynamic conditions in determining the structure and evolution of mesoscale convective systems during TOGA COARE. *J. Atmos. Sci.*, **55**, 3493-3518.

Levine, J., 1959: Spherical vortex theory of bubble-like motion in cumulus clouds. *J. Meteor.*, **16**, 653-662.

Lewis, S.A., M.A. LeMone, and D.P. Jorgensen, 1998: Evolution and dynamics of a late-stage squall line that occurred on 20 February 1993 during TOGA COARE. *Mon.*

Wea. Rev., **126**, 3189-3212.

Lilly, D.K., 1969: Numerical simulation of two-dimensional turbulence. *Phys. Fluids Supplement: High-Speed Computing in Fluid Dynamics*, **2**, 240-249.

List, R.J., 1949: *Smithsonian Meteorological Tables*. Smithsonian Institution Press, 527 pp.

Liu, C., M.W. Moncrieff, and E.J. Zipser, 1997: Dynamical influence of microphysics in tropical squall lines: A numerical study. *Mon. Wea. Rev.*, **125**, 2193-2210.

Loehrer, S.M., and R.H. Johnson, 1995: Surface pressure and precipitation life cycle characteristics of PRE-STORM mesoscale convective systems. *Mon. Wea. Rev.*, **123**, 600-621.

Maddox, R.A., 1980: Mesoscale convective complexes. *Bull. Amer. Meteor. Soc.*, **61**, 1374-1387.

Mapes, B.E., 1993: Gregarious tropical convection. *J. Atmos. Sci.*, **50**, 2026-2037.

Matejka, T., and G. Stossmeister, 1986: Convective-mesoscale interaction in a squall line. *Preprints, 23rd Conference on Radar Meteorology and Conference on Cloud Physics, Volume 3: Joint Sessions*, Chicago, IL, Amer. Meteor. Soc., J135-138.

Merilees, P.E., and H. Warn, 1975: On energy and enstrophy exchanges in two-dimensional non-divergent flow. *J. Fluid Mech.*, **69**, 625-630.

Mesinger, F., and A. Arakawa, 1976: Numerical methods used in atmospheric models. *GARP Publications Series*, No. 17, 64 pp.

Miller, M.J., 1978: The Hampstead Storm: A numerical simulation of a quasi-stationary cumulonimbus system. *Quart. J. Roy. Meteor. Soc.*, **104**, 413-427.

Miller, M.J., and R.P. Pearce, 1974: A three-dimensional primitive equation model of cumulonimbus convection. *Quart. J. Roy. Meteor. Soc.*, **100**, 133-154.

Mitchell, K.E., and J.B. Hovermale, 1977: A numerical investigation of the severe thunderstorm gust front. *Mon. Wea. Rev.*, **105**, 657-675.

Moncrieff, M.W., and C. Liu, 1999: Convection initiation by density currents: Effect of shear on convergence. *Preprints, 23rd Conference on Hurricanes and Tropical Meteorology*, Dallas, TX, Amer. Meteor. Soc., 219-220.

Mueller, C.K., and R.E. Carbone, 1987: Dynamics of a thunderstorm outflow. *J. Atmos. Sci.*, **44**, 1879-1898.

Murray, F.W., 1970: Numerical models of a tropical cumulus cloud with bilateral and axial symmetry. *Mon. Wea. Rev.*, **98**, 14-28.

Nakajima, K., and T. Matsuno, 1988: Numerical experiments concerning the origin of cloud clusters in the tropical atmosphere. *J. Meteor. Soc. Japan*, **66**, 309-329.

Nicholls, M.E., 1987: A comparison of the results of a two-dimensional numerical simulation of a tropical squall line with observations. *Mon. Wea. Rev.*, **115**, 3055-3077.

Nicholls, M.E., and R.H. Johnson, 1984: A model of a tropical squall line boundary layer wake. *J. Atmos. Sci.*, **41**, 2774-2792.

Nicholls, M.E., R.H. Johnson, and W.R. Cotton, 1988: The sensitivity of two-dimensional simulations of tropical squall lines to environmental profiles. *J. Atmos. Sci.*, **45**, 3625-3649.

Nicholls, M.E., and M.J. Weissbluth, 1988: A comparison of two-dimensional and quasi-three-dimensional simulations of a tropical squall line. *Mon. Wea. Rev.*, **116**, 2437-2452.

Ogura, Y., Y.-L. Chen, J. Russel, and S.-T. Soong, 1979: On the formation of organized convective systems observed over the eastern Atlantic. *Mon. Wea. Rev.*, **107**, 426-441.

Ogura, Y., and M.-T. Liou, 1980: Structure of a mid-latitude squall line: A case study. *J. Atmos. Sci.*, **37**, 553-567.

Ooyama, K.V., 1969a: Numerical simulation of the life cycle of tropical cyclones. *J. Atmos. Sci.*, **26**, 3-40.

Ooyama, K.V., 1969b: Numerical simulation of tropical cyclones with an axisymmetric model. *Proc. WMO/IUGG Sympos. Numer. Wea. Pred., Tokyo.* pp. III 81-88.

Ooyama, K.V., 1971: A theory on parameterization of cumulus convection. *J. Meteor. Soc. Japan*, **49** (Special Issue), 744-756.

Ooyama, K.V., 1982: Conceptual evolution of the theory and modeling of the tropical cyclone. *J. Meteor. Soc. Japan*, **60**, 369-379.

Ooyama, K.V., 1984: A model for hurricane prediction. *Postprints, 15th Conference on Hurricanes and Tropical Meteorology*, Miami, FL, Amer. Meteor. Soc., 344-349.

Ooyama, K.V., 1987: Scale-controlled objective analysis. *Mon. Wea. Rev.*, **115**, 2479-2506.

Ooyama, K.V., 1989: Thermodynamics in the primitive form for modeling the moist atmosphere. *Extended Abstracts, 18th Conference on Hurricanes and Tropical Meteorology*, San Diego, CA, Amer. Meteor. Soc., 157-158.

Ooyama, K.V., 1990: A thermodynamic foundation for modeling the moist atmosphere. *J. Atmos. Sci.*, **47**, 2580-2593.

Ooyama, K.V., 1991: A dynamic test of the diagnostic pressure calculation. *Extended Abstracts, 19th Conference on Hurricanes and Tropical Meteorology*, Miami, FL, Amer. Meteor. Soc., 171.

Ooyama, K.V., 1995: A thermodynamic foundation for modeling the moist atmosphere, part II: Tests of microphysics in the formation of squall lines. *Preprints, 21st Conference*

on Hurricanes and Tropical Meteorology, Miami, FL, Amer. Meteor. Soc., 219-221.

Ooyama, K.V., 1997: The semi-implicit integration of a nested spectral model and the result of tests in squall-line simulation. *Preprints, 22nd Conference on Hurricanes and Tropical Meteorology*, Fort Collins, CO, Amer. Meteor. Soc., 531-532.

Paluch, I.R., 1979: The entrainment mechanism in Colorado cumuli. *J. Atmos. Sci.*, **36**, 2467-2478.

Payne, S.W., and M.M. McGarry, 1977: The relationship of satellite inferred convective activity to easterly waves over West Africa and the adjacent ocean during Phase III of GATE. *Mon. Wea. Rev.*, **105**, 413-420.

Perry, K.D., and P.V. Hobbs, 1996: Influences of isolated cumulus clouds on the humidity of their surroundings. *J. Atmos. Sci.*, **53**, 159-174.

Politovich, M.K., 1993: A study of the broadening of droplet size distributions in cumuli. *J. Atmos. Sci.*, **50**, 2230-2244.

Purdom, J.F.W., 1976: Some uses of high-resolution GOES imagery in the mesoscale forecasting of convection and its behavior. *Mon. Wea. Rev.*, *104*, 1474-1483.

Purdom, J.F.W., 1979: The development and evolution of deep convection. *Preprints, 11th Conference on Severe Local Storms*, Kansas City, MO, Amer. Meteor. Soc., 143-150.

Purdom, J.F.W., and K. Marcus, 1982: Thunderstorm trigger mechanisms over the Southeast United States. *Preprints, 12th Conference on Severe Local Storms*, San Antonio, TX, Amer. Meteor. Soc., 487-488.

Randall, D.A., 1980: Conditional instability of the first kind upside-down. *J. Atmos. Sci.*, **37**, 125-130.

Randall, D.A., and G.J. Huffman, 1982: Entrainment and detrainment in a simple cumulus

cloud model. *J. Atmos. Sci.*, **39**, 2793-2806.

Redelsperger, J.-L., and J.-P. LaFore, 1988: A three-dimensional simulation of a tropical squall line: Convective organization and thermodynamic vertical transport. *J. Atmos. Sci.*, **45**, 1334-1356.

Redelsperger, J.-L., and G. Sommeria, 1986: Three-dimensional simulation of a convective storm: Sensitivity studies on subgrid parameterization and spatial resolution. *J. Atmos. Sci.*, **43**, 2619-2635.

Reuter, G.W., 1986: A historical review of cumulus entrainment studies. *Bull. Amer. Meteor. Soc.*, **67**, 151-154.

Robert, A.J., 1969: The integration of a spectral model of the atmosphere by the implicit method. *Proc. WMO/IUGG Sympos. Numer. Wea. Pred., Tokyo.* pp. VII 19-24.

Rotunno, R., J.B. Klemp, and M.L. Weisman, 1988: A theory for strong, long-lived squall lines. *J. Atmos. Sci.*, **45**, 463-485.

Roux, F., 1984: West African squall line thermodynamic structure retrieved from dual-Doppler radar observations. *J. Atmos. Sci.*, **41**, 3104-3121.

Roux, F., 1985: Retrieval of thermodyanmic fields from multiple Doppler radar data, using the equations of motion and the thermodynamic equation. *Mon. Wea. Rev.*, **113**, 2142-2157.

Roux, F., 1988: The West African squall line observed on 23 June 1981 during COPT81: Kinematics and thermodynamics of the convective region. *J. Atmos. Sci.*, **45**, 406-426.

Rutledge, S.A., R.A. Houze, Jr., M.I. Biggerstaff, and T. Matejka, 1988: The Oklahoma-Kansas mesoscale convective system of 10-11 June 1985: Precipitation structure and single-doppler radar analysis. *Mon. Wea. Rev.*, **116**, 1409-1430.

Scorer, R.S., and F.H. Ludlam, 1953: Bubble theory of penetrative convection. *Quart. J. Roy. Meteor. Soc.*, **79**, 94-103.

Shapiro, L.J., and K.V. Ooyama, 1990: Barotropic vortex evolution on a beta plane. *J. Atmos. Sci.*, **47**, 170-187.

Simpson, J.E., 1969: A comparison between laboratory and atmospheric density currents. *Quart. J. Roy. Meteor. Soc.*, **95**, 758-765.

Simpson, J.E., and R.E. Britter, 1980: A laboratory model of an atmospheric mesofront. *Quart. J. Roy. Meteor. Soc.*, **106**, 485-500.

Skamarock, W.C., S.B. Trier, and M.A. LeMone, 1996: The dynamics of slow and fast-moving convective lines in TOGA COARE. *Preprints, 7th Conference on Mesoscale Processes*, Reading, UK, Amer. Meteor. Soc., 301-303.

Smull, B.F., and R.A. Houze, Jr., 1985: A midlatitude squall line with a trailing region of stratiform rain: Radar and satellite observations. *Mon. Wea. Rev.*, **113**, 117-133.

Smull, B.F., and R.A. Houze, Jr., 1987a: Dual-doppler radar analysis of a midlatitude squall line with a trailing region of stratiform rain. *J. Atmos. Sci.*, **44**, 2128-2148.

Smull, B.F., and R.A. Houze, Jr., 1987b: Rear inflow in squall lines with trailing stratiform precipitation. *Mon. Wea. Rev.*, **115**, 2869-2889.

Sommeria, G., and J. Testud, 1984: COPT81: A field experiment designed for the study of dynamics and electrical activity of deep convection in continental tropical regions. *Bull. Amer. Meteor. Soc.*, **65**, 4-10.

Soong, S.-T., and Y. Ogura, 1973: A comparison between axisymmetric and slab-symmetric cumulus cloud models. *J. Atmos. Sci.*, **30**, 879-893.

Soong, S.-T., and Y. Ogura, 1980: Response of trade-wind cumuli to large-scale processes.

J. Atmos. Sci., **37**, 2035-2050.

Soong, S.-T., and W.-K. Tao, 1980: Response of deep tropical clouds to mesoscale processes. *J. Atmos. Sci.*, **37**, 2016-2034.

Squires, P., 1958a: The spatial variation of liquid water and droplet concentration in cumuli. *Tellus*, **10**, 372-380.

Squires, P., 1958b: Penetrative downdraughts in cumuli. *Tellus*, **10**, 381-385.

Srivastava, R.C., 1967: A study of the effects of precipitation on cumulus dynamics. *J. Atmos. Sci.*, **24**, 36-45.

Stith, J.L., 1992: Observations of cloud-top entrainment in cumuli. *J. Atmos. Sci.*, **49**, 1334-1347.

Stith, J.L., and M.K. Politovich, 1989: Observations of the effects of entrainment and mixing on the droplet size spectra in a small cumulus. *J. Atmos. Sci.*, **46**, 908-919.

Stommel, H., 1947: Entrainment of air into a cumulus cloud. *J. Meteor.*, **4**, 91-94.

Straka, J.M., R.B. Wilhelmson, L.J. Wicker, J.R. Anderson, and K.K. Droegemeier, 1993: Numerical solutions of a non-linear density current: A benchmark solution and comparisons. *Int. J. Num. Meth. Fluids*, **17**, 1-22.

Sun, J., S. Braun, M.I. Biggerstaff, R.G. Fovell, and R.A. Houze, Jr., 1993: Warm upper-level downdrafts associated with a squall line. *Mon. Wea. Rev.*, **121**, 2919-2927.

Syōno, S., and M. Yamasaki, 1966: Stability of symmetrical motions driven by latent heat release by cumulus convection under the existence of surface friction. *J. Meteor. Soc. Japan*, **44**, 353-375.

Takeda, T., 1966: The downdraft in the convective cloud and raindrops: A numerical computation. *J. Meteor. Soc. Japan*, **44**, 1-11.

Takeda, T., 1971: Numerical simulation of a precipitating convective cloud: The formation of a "long-lasting" cloud. *J. Atmos. Sci.*, **28**, 350-376.

Tao, W.-K., and J. Simpson, 1989: Modelling study of a tropical squall-type convective line. *J. Atmos. Sci.*, **46**, 177-202.

Tao, W.-K., and S.-T. Soong, 1986: The study of the response of deep tropical clouds to mesoscale processes: Three-dimensional numerical experiments. *J. Atmos. Sci.*, **43**, 2653-2676.

Taylor, G.R., and M.B. Baker, 1991: Entrainment and detrainment in cumulus clouds. *J. Atmos. Sci.*, **48**, 112-121.

Telford, J.W., 1975: Turbulence, entrainment, and mixing in cloud dynamics. *Pure Appl. Geophys.*, **113**, 1067-1084.

Telford, J.W., and S.K. Chai, 1980: A new aspect of condensation theory. *Pure Appl. Geophys.*, **118**, 720-741.

Thorpe, A.J., M.J. Miller, and M.W. Moncrieff, 1980: Dynamical models of two-dimensional downdrafts. *Quart. J. Roy. Meteor. Soc.*, **106**, 463-484.

Thorpe, A.J., M.J. Miller, and M.W. Moncrieff, 1982: Two-dimensional convection in non-constant shear: A model of midlatitude squall lines. *Quart. J. Roy. Meteor. Soc.*, **108**, 739-762.

Tipler, P.A., 1991: *Physics for Scientists and Engineers*, 3d Ed. Worth Publishers, 1171 pp.

Trier, S.B., W.C. Skamarock, M.A. LeMone, D.B. Parsons, and D.P. Jorgensen, 1996: Structure and evolution of the 22 February 1993 TOGA COARE squall line: Numerical simulations. *J. Atmos. Sci.*, **53**, 2861-2886.

Turner, J.S., 1962: The "starting plume" in neutral surroundings. *J. Fluid Mech.*, **13**, 356-368.

Wakimoto, R.M., 1982: The life cycle of thunderstorm gust fronts as viewed with Doppler radar and rawinsonde data. *Mon. Wea. Rev.*, **110**, 1060-1082.

Wang, Y., W.-K. Tao, and J. Simpson, 1996: The impact of ocean surface fluxes on a TOGA COARE convective system. *Mon. Wea. Rev.*, **124**, 2753-2763.

Webster, P.J., and R.A. Houze, Jr., 1991: The equatorial mesoscale experiment (EMEX): An overview. *Bull. Amer. Meteor. Soc.*, **72**, 1481-1505.

Webster, P.J., and R. Lukas, 1992: TOGA COARE: The coupled ocean-atmosphere response experiment. *Bull. Amer. Meteor. Soc.*, **73**, 1377-1416.

Weckwerth, T.M., and R.M. Wakimoto, 1992: The initiation and organization of convective cells atop a cold-air outflow boundary. *Mon. Wea. Rev.*, **120**, 2169-2187.

Weisman, M.L., 1992: The role of convectively generated rear-inflow jets in the evolution of long-lived mesoconvective systems. *J. Atmos. Sci.*, **49**, 1826-1847.

Weisman, M.L., W.C. Skamarock, and J.B. Klemp, 1997: The resolution dependence of explicitly modeled convective systems. *Mon. Wea. Rev.*, **125**, 527-548.

William, K.M., 1994: The South China Sea Monsoon Experiment (SCSMEX): scientific rationale. *Eos*, **75**, 42.

Xu, Q., 1992: Density currents in shear flows: A two-fluid model. *J. Atmos. Sci*, **49**, 511-524.

Xue, M., Q. Xu, and K.K. Droegemeier, 1997: A theoretical and numerical study of density currents in nonconstant shear flows. *J. Atmos. Sci.*, **54**, 1998-2019.

Yamasaki, M., 1968: A tropical cyclone model with parameterized vertical partition of

released latent heat. *J. Meteor. Soc. Japan*, **46**, 202-214.

Yamasaki, M., 1984: Dynamics of convective clouds and 'CISK' in vertical shear flow, with its applicability to easterly waves and squall line systems. *J. Meteor. Soc. Japan*, **62**, 833-863.

Yamasaki, M., 1988: Towards an understanding of the interaction between convection and the larger scale in the tropics. *Aust. Meteor. Mag.*, **36**, 171-182.

Yasunari, T., 1994: Scientific strategy of GEWEX Asian Monsoon Experiment. *Eos*, **75**, 31.

Yoshizaki, M., 1986: Numerical simulations of tropical squall line clusters: Two-dimensional model. *J. Meteor. Soc. Japan*, **64**, 469-491.

Zipser, E.J., 1969: The role of organized unsaturated convective downdrafts in the structure and rapid decay of an equatorial disturbance. *J. Appl. Meteor.*, **8**, 799-814.

Zipser, E.J., 1977: Mesoscale and convective-scale downdrafts as distinct components of squall-line structure. *Mon. Wea. Rev.*, **105**, 1568-1589.

Zipser, E.J., R.J. Meitín, and M.A. LeMone, 1981: Mesoscale motion fields associated with a slowly moving GATE convective band. *J. Atmos. Sci.*, **38**, 1725-1750.

Appendix A

PUBLICATION ACRONYMS

C94	Chin (1994)	JCH96	Johnson et al. (1996)
CFBM95	Chin et al. (1995)	JLT97	Jorgensen et al. (1997)
CLR95	Caniaux et al. (1995)	JN83	Johnson and Nicholls (1983)
CRL94	Caniaux et al. (1994)	KW78	Klemp and Wilhelmson (1978)
CW98	Chin and Wilhelmson (1998)	LH79	Leary and Houze (1979)
CY93	Chang and Yoshizaki (1993)	LM89	LaFore and Moncrieff (1989)
DAOL92	DeMaria et al. (1992)	LMZ97	LaFore et al. (1997)
DMS87	Dudhia et al. (1987)	N87	Nicholls (1987)
F91	Fovell (1991)	NJC88	Nicholls et al. (1988)
FD95	Fovell and Dailey (1995)	NW88	Nicholls and Weissbluth (1988)
FO88	Fovell and Ogura (1988)	O87	Ooyama (1987)
FO89	Fovell and Ogura (1989)	O90	Ooyama (1990)
FT98	Fovell and Tan (1998)	O95	Ooyama (1995)
GH82	Gamache and Houze (1982)	O97	Ooyama (1997)
H77	Houze (1977)	RHBM88	Rutledge et al. (1988)

RKW88	Rotunno et al. (1988)	TSLPJ96	Trier et al. (1996)
RL88	Redelsperger and LaFore (1988)	W92	Weisman (1992)
TMM82	Thorpe et al. (1982)	Y86	Yoshizaki (1986)
TS89	Tao and Simpson (1989)	Z69	Zipser (1969)
TSFS95	Tao et al. (1995)	Z77	Zipser (1977)

Appendix B

FIELD EXPERIMENTS

CCOPE	Cooperative Convective Precipitation Experiment: eastern Montana, 1981 (Knight, 1982)
COPT	Convection Profonde Tropicale: tropical western Africa, 1981 (Sommeria and Testud, 1984)
EMEX	Equatorial Mesoscale Experiment: tropical western Pacific, 1987 (Webster and Houze, 1991)
GAME	Global Energy and Water Cycle Experiment (GEWEX), Asian Monsoon Experiment: eastern Asia and adjacent Pacific oceanic regions, 1994-? (Yasunari, 1994)
GATE	Global Atmospheric Research Program (GARP), Atlantic Tropical Experiment: tropical eastern Atlantic, 1974 (Kuettner, 1974; Houze and Betts, 1981)
PRE-STORM	Preliminary Regional Experiment for the Stormscale Operational and Research Meteorology Program, Central Phase: Oklahoma and Kansas, 1985 (Cunning, 1986)

SCSMEX	South China Sea Monsoon Experiment:
	South China Sea and Southeast Asia, 1998 (William, 1994)
TOGA COARE	Tropical Ocean-Global Atmosphere
	Coupled Ocean-Atmosphere Response Experiment:
	tropical western Pacific, 1993 (Webster and Lukas, 1992)
VIMHEX-1972	2d Venezuelan International Meteorological and Hydrological Experiment:
	tropical South America, 1972 (Grover, 1974; Betts et al., 1976)

Appendix C

VARIABLE LISTING

Coordinates and Distances

x	horizontal coordinate	z	vertical coordinate

Prognostic Variables

$\boldsymbol{u}$	vector velocity	ρ	total density
u	horizontal velocity component	ρ_a	dry air density
w	vertical velocity component	ρ_m	total airborne moisture density
σ	total entropy	ρ_r	precipitation density

Operators

$\frac{D}{Dt}$	total (Lagrangian) derivative
∂_t	partial (Eulerian) derivative, with respect to time
$\partial_{(x,z)}$	partial (Eulerian) derivative, with respect to (x,z)
$\boldsymbol{\nabla}$	gradient
$\boldsymbol{\nabla\cdot}$	divergence

Physical Constants

f	Coriolis parameter	g	gravitational acceleration

Source/Sink (Q) and Diffusion (D) Terms

$Q_{\rho u}$, $D_{\rho u}$	horizontal momentum density	Q_{ρ_a}, D_{ρ_a}	dry air density
$Q_{\rho w}$, $D_{\rho w}$	vertical momentum density	Q_{ρ_m}, D_{ρ_m}	airborne moisture density
Q_σ, D_σ	total entropy density	Q_r, D_{ρ_r}	precipitation density

Numerical Quantities

$\Delta(x,z)$	length of grid point interval in the appropriate coordinate	c	acoustic velocity, commonly measured at T_0
Δt	length of model time step	ν	Asselin parameter

Diagnostic Quantities

T	temperature	θ	potential temperature
T'	perturbation temperature	θ_e	equivalent potential temperature
T_1	temperature w/o condensate	s	dry-air-specific entropy of moist air
T_2	temperature of condensate	s_r	precipitation partial entropy
p	total pressure	ρ	total density
p'	perturbation pressure	ρ_v	vapor density
p_a	dry air partial pressure	ρ_c	condensate density
p_v	vapor partial pressure		

Thermodynamic Constants

R_a	gas constant for dry air	R_v	gas constant for water vapor
c_{pa}	dry air specific heat, constant pressure	c_{pv}	vapor specific heat, constant pressure
c_{va}	dry air specific heat, constant volume	c_{vv}	vapor specific heat, constant volume

Defined Functions of Temperature

p_v	vapor pressure	L	latent heat of vaporization for water
ρ_*	saturation vapor density	Λ	entropy increase due to evaporation
E	saturation vapor pressure	c_c	specific heat of condensate
E_w	saturation vapor pressure over water	c_w	specific heat of water
E_i	saturation vapor pressure over ice	c_i	specific heat of ice
C	entropy of condensate	D	saturation entropy due to evaporation
Ω_w	entropy weighting factor for water	Ω_i	entropy weighting factor for ice

Thermodynamic and Microphysical Quantities

ΔT_f	width of freezing zone	T_f	freezing zone central temperature
w_r	terminal velocity of precipitation	Q_{auto}	autoconversion of condensate
f_{vent}	precipitation ventilation factor	Q_{coll}	collection of condensate by precipitation
f_{ice}	terminal velocity reduction factor	Q_{evap}	evaporation of precipitation

Reference Quantities

T_0	reference temperature, 273.15K
θ_0	reference potential temperature, 273.15K
p_0	reference pressure, 1013.25 hPa
ρ_{a0}	dry air density at T_0
ρ_{*0}	saturation vapor density at T_0
Λ_0	reference entropy of water at T_0
E_{w0}	saturation vapor pressure over water at T_0
E_{i0}	saturation vapor pressure over ice at T_0
T_b	water boiling point temperature
p_b	water boiling point pressure
T_t	water triple point temperature
p_t	water triple point pressure

Other Dynamical Quantities

ϵ	hydrostatic imbalance
u_c	constant uniform flow aloft
Δu	strength of shear layer, as employed in FO89 and FD95
z_s	scale height of surface shear layer
D	actual depth of shear layer, as employed in FO89 and FD95
u_{conv}	strength of initial convergence perturbation
N, τ	Brunt-Vaisälä frequency and period
H	depth of surface outflow layer
$\delta\rho$	change in air density across the upper surface of the outflow layer
$\rho_{outflow}$	density of air within the urfac outflow layer
c_g	speed of external gravity waves on the outflow layer surface
λ	characteristic cell spacing on surface of outflow layer
$u_{g,c}$	gust front velocity relative to uniform flow aloft
u_g	gust front velocity, relative to Earth
u_0	surface environmental wind
u_H	environmental wind at height $z = H$
Δu_{rtf}	strength of shear within surface outflow layer due to rear-to-front flow
$u_{rtf,0}$	surface wind within outflow layer due to rear-to-front flow
$u_{rtf,H}$	wind at surface of outflow layer due to rear-to-front flow
w_{max}	maximum updraft velocity in vicinity of surface outflow head

Appendix D

EQUIVALENT POTENTIAL TEMPERATURE

The dry-air-specific entropy of moist air, $s = \sigma/\rho_a$, is analogous to the equivalent potential temperature, θ_e, defined by

$$s = c_{pa} \ln\left(\frac{\theta_e}{T_0}\right), \tag{D.1}$$

in the exact form as in Section 6 of Ooyama (1990). The constant T_0 appearing in (D.1) has been chosen so that (D.1) is consistent with the dry part of (3.20) and (3.28) in the limiting case of a completely dry atmosphere. In order to validate this substitution, we may consider this special case, for which

$$\theta_e \to \theta = T\left(\frac{p_0}{p}\right)^{\frac{R_a}{c_{pa}}},$$

which can be used in the more general form of the dry-air-specific entropy of moist air, for which the T_0 in (D.1) is replaced by θ_0, such that we may write

$$\begin{aligned} s &= c_{pa} \ln\left[\frac{T}{\theta_0}\left(\frac{p_0}{p}\right)^{\frac{R_a}{c_{pa}}}\right], \\ &= c_{pa} \ln\left(\frac{T}{\theta_0}\right) - R_a \ln\left(\frac{p}{p_0}\right). \end{aligned}$$

For this to be consistent with the dry parts of (3.20) and (3.28), we must have $\theta_0 = T_0$. Equation (D.1) can also be written as

$$\theta_e = T_0 \exp\left(\frac{s}{c_{pa}}\right), \tag{D.2}$$

which is a more exact form of the equivalent motential temperature than traditional, approximate formulations, i.e. (in notation used here)

$$\theta_e \sim \theta \exp\left(\frac{L\rho_*}{\rho_a c_{pa} T}\right),$$

for saturated air (Houze, 1993). This allows us to relabel contours of dry-air-specific entropy of moist air, s, in the Figures presented in Chapters 4 and 5 as contours of equivalent potential temperature, θ_e.

In Figures 5.3, 4, 6a, 6bI, 6cI, and 6dI, near-surface values of the dry-air-specific entropy of moist air in excess of $s = 280$ J kg^{-1} K^{-1} may be found in undisturbed regions ahead of the squall line gust front. A value of $s = 280$ J kg^{-1} K^{-1} corresponds to $\theta_e \approx 361$K by (D.2). Values of $s = 190$ J kg^{-1} K^{-1} found in the midlevels of several of these Figures correspond to $\theta_e \approx 330$K. These regions demonstrate higher θ_e values in the lower levels than those found for the tropical boundary layer of the central (Firestone and Albrecht, 1986; Betts and Albrecht, 1987; Kloesel and Albrecht, 1989) and eastern Pacific (Bond, 1992). For each of these efforts, the analyzed midlevel values of θ_e are approximately equal to those displayed in the Figures here. A similar relationship may be found between the values of θ_e displayed in the Figures included here and analyses of the environments of fast-moving tropical squall line systems during GATE presented by Barnes and Seickman (1984). However, the environments analyzed by LeMone et al. (1998) in the vicinity of TOGA COARE convective systems demonstrate lower (higher) values of θ_e in the low (middle) levels than the environment employed here for simulations of tropical squall lines. We suspect that these differences may stem from the modification of the original Jordan (1958) tropical thermodynamic profile by Ooyama (1995, 1997), for which the relative humidity in the lower (middle) levels was arbitrarily increased (decreased) in order to facilitate squall line-type convective development and motions and the formation of a significant surface

outflow layer and gust front (Nicholls et al., 1988).

If we consider the model described in Section 3.2.1, neglecting precipitation and other non-conservative processes (e.g., radiation, diffusion, etc.), we may write (3.5) and (3.8) as, in flux form,

$$\partial_t \rho_a + \boldsymbol{\nabla}\cdot(\boldsymbol{u}\rho_a) = 0, \tag{D.3}$$

$$\partial_t \sigma + \boldsymbol{\nabla}\cdot(\boldsymbol{u}\sigma) = 0, \tag{D.4}$$

respectively. In advective form, these may be written as

$$\frac{D\rho_a}{Dt} + \rho_a \boldsymbol{\nabla}\cdot\boldsymbol{u} = 0, \tag{D.5}$$

$$\frac{D\sigma}{Dt} + \sigma \boldsymbol{\nabla}\cdot\boldsymbol{u} = 0, \tag{D.6}$$

respectively. Performing ρ_a(D.7) $-$ σ(D.6) produces

$$\rho_a \frac{D\sigma}{Dt} - \sigma \frac{D\rho_a}{Dt} = 0, \tag{D.7}$$

or

$$\frac{D}{Dt}\left(\frac{\sigma}{\rho_a}\right) = \frac{Ds}{Dt} = 0. \tag{D.8}$$

Using (D.1), we may write

$$\frac{D}{Dt}\ln\theta_e = 0. \tag{D.9}$$

In this way, a complete analogy between s and θ_e may be drawn, such that the dry-air-specific entropy of moist air s is also conserved following reversible dry (i.e., unsaturated) adiabatic motions and is approximately conserved following irreversible pseudoadiabatic motions of a parcel (Dutton, 1986; Holton, 1992; Houze, 1993). Under the influence of precipitation processes, such as those described in Section 3.2.3, the conservation principle (D.8) is only approximate, but is still very useful in the analysis of model results.